Laser Cladding of Ti-6Al-4V with Carbide and Boride Reinforcements using Wire and Powder Feedstock

Peter Kayode Farayibi, MSc.

Thesis submitted the University of Nottingham
for the degree of Doctor of Philosophy

Department of Mechanical, Materials and Manufacturing Engineering

June 2014

Preface

This thesis is submitted for the degree of Doctor of Philosophy at the University of Nottingham. The research work was carried out under the supervision of Professor D.G. McCartney, Dr. A.T. Clare and Late Dr. J.A. Folkes in the Department of Mechanical, Materials and Manufacturing Engineering.

It is certified that the work presented in this thesis is original and suitable references are made to any work from the literature or carried out elsewhere.

The list of publications from the work presented in this thesis is listed here:

- P. K. Farayibi, J. W. Murray, L. Huang, F. Boud, P. K. Kinnell, A. T. Clare; Erosion resistance of laser clad Ti-6Al-4V/WC composite for waterjet tooling; *Journal of Materials Processing Technology*; 214(3):710-721, 2014
- P. K. Farayibi, J. A. Folkes, and A. T. Clare; Laser Deposition of Ti-6Al-4V Wire with WC Powder for Functionally Graded Components; *Materials and Manufacturing Processes*; 28(5):514-518, 2013.
- P. K. Farayibi, J. Folkes, A. Clare, and O. Oyelola, Cladding of pre-blended Ti-6Al-4V and WC for wear resistant applications; *Surface and Coatings Technology*; 206(2-3):372-377, 2011.
- P. K. Farayibi, A. T. Clare, J. A. Folkes and D. G. McCartney; Laser Deposition of Ti-6Al-4V Wire with Varying WC composition for Functionally Graded Components. Paper No. 3157. *In Conference Proceedings* at *37th MATADOR Conference* at The University of Manchester, UK, 2012.
- P. K. Farayibi, J. Folkes, and A. Clare, Influence of Process Parameters and Energy Density on the Microstructure of Ti-6Al-4V wire/ WC powder Cladding. Paper ID: 37010. *In Conference Proceedings* at *The 30th International Congress on Application of Lasers and Electro-Optics (ICALEO)*, Florida, USA held from 23rd-27th October, 2011.

Peter Kayode Farayibi

June, 2014

Acknowledgements

I would like to express my most sincere gratitude to my supervisors, Dr Adam Clare and Prof D.G. McCartney for their guidance and immense support during the course of this research. The successful completion of this work would not have been achieved without their great assistance. I am highly indebted to Late Dr **Janet Folkes** who died at the end of my year one into the research programme. Her guidance is well appreciated and has helped me throughout the course of this work. I would also like to express my gratitude to Dr Joel Segal for acting as my internal examiner during the course of this study, I am grateful for his advice and support in the yearly reviews during the course of this work. I would like to appreciate Prof Stewart Williams from the Cranfield University, UK, who acted as my external examiner. I am grateful for his valuable comments at during the PhD examination. I would like to acknowledge Dr Paul Goodwin and Laser Cladding Technologies for the provision of some of the materials used in the course of this work.

I would like to thank Mr Stuart Branston and Mr Barry Holdsworth for their invaluable technical contributions during the laser and waterjet experiments in the course of this research. I would also like to acknowledge Dr Nigel Neate, Mr Tom Buss and Mr Keith Dinsdale for their inestimable assistance during the material characterisation in the course of this work.

I am grateful to my family, parents, brothers, sisters, colleagues and friends in the University of Nottingham and also special thanks to my house mates and wonderful families I met here in Nottingham for their encouragements and support.

Thanks to the management of the Federal University of Technology, Akure, (FUTA) Nigeria and the entire members of staff of the department of Mechanical Engineering for granting me the secondment to study at the University of Nottingham, UK.

I would like to acknowledge the office of the Dean of Engineering, the University of Nottingham, who sponsored my PhD programme through the Dean of Engineering Scholarship for International Excellence. I am very grateful.

Above all, thanks be to GOD for the privilege to achieve this milestone.

Abstract

The growth in the use and wear of Ti-based alloy components in mining and offshore explorations has led to a search for techniques to re-engineer such components for reuse. The most desirable method of restoring/protecting the component surfaces is by hard-facing to enhance longevity in service.

Laser cladding is one of the viable techniques to achieve a thick coating on such components which involves the addition of reinforcing particulates to improve surface properties such as hardness, wear and erosion resistance amongst others. A fundamental study and understanding of the resultant microstructure-property of the laser clad, hard-facing composite becomes necessary.

In this study, laser cladding of Ti-6Al-4V wire with Spherotene particulate reinforcement and laser cladding of modified pre-blend of Ti-6Al-4V and TiB_2 powder were undertaken. The resulting physical and microstructural characteristics, hardness, and performance characteristics of laser clad composites were investigated. Samples from the as-deposited laser clad composites were characterised using optical microscopy, scanning electron microscopy (with chemical microanalysis) and X-ray diffraction. Performance characteristics were examined via erosion testing of the laser clad Ti-6Al-4V/Spherotene using plain and abrasive water jetting, and tensile testing of the laser clad Ti-6Al-4V/TiB_2 composite.

The results showed that a crack and pore free clad containing as high as 76±1 wt.% Spherotene in the Ti matrix was achieved at an energy density of 150±10 J.mm^{-2}, 275±25 mm/min traverse speed, 700 mm/min wire feed rate and 30 g/min powder feed rate. The microstructure of the laser clad Ti-6Al-4V/Spherotene is characterised by nano-sized precipitates of reaction products (W and TiC) uniformly distributed in a β-Ti solid solution matrix. Matrix hardness is enhanced by the presence of the reaction products in the Ti ranging between 410-620 kgf.mm^{-2}. Moreover, the modification made to the 90 wt.% Ti-6Al-4V/10 wt.% TiB_2 feedstock by attaching the TiB_2 to Ti-6Al-4V allowed uniform distribution of reinforcing element in the deposited composite. The composite microstructure on solidification is characterised by TiB eutectic needle-like features uniformly distributed in a Ti-rich primary phase. The hardness of the composite ranged between 440-480 kgf.mm^{-2}. Tensile tests showed that the mean elastic modulus of Ti-6Al-4V/TiB_2 composite is 145 GPa, which is a 27% improvement when compared to that of Ti-6Al-4V. Erosion test indicated that the Ti-6Al-4V/Spherotene composite offered as high as 13 and 8 times resistance of that of Ti-6Al-4V when subjected to PWJ and AWJ impacts respectively.

Contents

List of Figures

List of Tables

Abbreviations

AFR	**A**brasive **F**low **R**ate
ANOVA	**A**nalysis **O**f **V**ariance
AWJ	**A**brasive **W**ater **J**et
BSE	**B**ack **S**cattered **E**lectron
CW	**C**ontinuous **W**ave
DoE	**D**esign **o**f **E**xperiments
EDX	**E**nergy **D**ispersive **X**-ray
HAZ	**H**eat **A**ffected **Z**one
HCP	**H**exagonal **C**lose- **P**acket
ICDD	**I**nternational **C**entre **D**iffraction **D**atabase
LASER	**L**ight **A**mplication by **S**timulated **E**mission of **R**adiation
LC	**L**aser **C**ladding
LMI	**L**aser **M**elt **I**njection
MMC	**M**etal **M**atrix **C**omposite
MPD	**M**elt **P**ool **D**epth
MRR	**M**aterial **R**emoval **R**ate
Nd:YAG	**N**eodymium **Y**ttrium **A**luminium **G**arnet
PFR	**P**owder **F**low **R**ate
P-value	**P**ercentage contribution of a factor
PWJ	**P**lain **W**ater **J**et
RoM	**R**ule **o**f **M**ixture
S'	**S**um of squares
SE	**S**econdary **E**lectron
SEM	**S**canning **E**lectron **M**icroscopy
SOD	**S**tand **O**ff **D**istance

Ti$_{ss}$	**T**itanium solid solution
VAM	**V**acuum **A**rc **M**elting
WEDM	**W**ire **E**lectrical **D**ischarge **M**achine
WFR	**W**ire **F**eed **R**ate
W$_{ss}$	Tungsten solid solution
XRD	**X**-**R**ay **D**iffraction
3-D	**T**hree **D**imensional

Symbols

A_p	effective particle area irradiated	m^2
c_p	specific heat capacity of particle material	$J.(kg\text{-}K)^{-1}$
C_s	water droplet shock velocity	$m.s^{-2}$
d	distance travelled by particle in laser beam	m
E	laser energy density	$J.mm^{-2}$
F	Variance ratio	
$I_{x,y}$	laser power density	$W.mm^{-2}$
m_p	mass of particle	kg
P_h	waterjet pressure head	Pa
P_L	laser power	$W(J.s^{-1})$
P_w	water hammer pressure	Pa
r_b	laser beam spot radius	mm
T	particle temperature	K
T_o	initial particle temperature	K
V	laser traverse speed	$mm.min^{-1}$
V_j	waterjet traverse speed	$mm.min^{-1}$
v_p	projected particle speed	$mm.min^{-1}$
τ	laser material interaction time	s
η	laser absorptivity of particle material	

Chapter 1

Introduction

Laser surface engineering is a rapidly developing research area which is capable of enhancing component performance in a range of applications. A variety of laser assisted surface modification processes have evolved, these include: laser surface melting [1], laser surface alloying [2] and laser surface cladding [3] amongst others. These approaches have demonstrated the use of lasers to improve surface properties and laser cladding (LC) may be considered as the most versatile of these surface modification techniques. It involves consolidation of materials with desired properties fed into a laser generated melt pool which cools to form a clad layer on a component surface as it solidifies [4]. LC offers advantages over other surface engineering techniques, such as, minimal heat input, precise energy control to a localised region, excellent material utilisation, microstructural control with tailored properties and a well-bonded clad layer [3, 5].

Whilst laser-clad layers can be manufactured from materials in powder, wire and sheet strip form, the wire and sheet strip depositions have been given less attention. Wire-based LC process may be considered economical, as material utilisation approaches 100% with a cleaner process environment. As the applications of laser-clad layers are to protect against wear, corrosion, thermal degradation and contact deformation amongst others [3], it is common to use ceramics as reinforcements in laser-clad layers prepared towards wear and impact applications. Various metal matrix ceramic composite (MMC) laser-clad layers have been developed such as Fe-based, Ni-based, Al-based and Ti-based MMCs amongst others, principally for wear applications.

However, owing to the excellent properties of Ti and its alloys, such as high strength to weight ratio, excellent toughness and good corrosion resistance, there is an increase in their demand and use for different industrial applications. These applications range from aerospace to ground transport, military, marine, mining, food processing and biomedical. Hence, there is a need to either protect the surface of new components or re-engineer the surfaces of worn Ti-base components which can be achieved via laser surface cladding with ceramic reinforcements. The inclusion of reinforcements helps to prolong the working lives of the engineering components.

Among the various types of ceramics, carbide-based and boron-based ceramics are proposed as suitable reinforcements in Ti-based laser-clad layers for wear and impact resistant applications. Carbide-based ceramics such as WC are known to possess high hardness (1300-2200 kgf.mm^{-2}) and excellent abrasive resistance. While the boron-based ceramic such as TiB_2 is also well known for its high stiffness and hardness (3650 kgf.mm^{-2}). Thus, based on these properties, both ceramics are potentially good choices of reinforcing phase.

Prior work has shown that composites of Ti-6Al-4V with carbide reinforcements produced via laser surface engineering possess improved wear resistance. However, the resultant microstructure has been found to be dependent on the type of laser employed and mostly commonly used are CO_2 and Nd:YAG lasers, owing to the difference in their photon energies. Moreover, most of the reported work on laser processed Ti alloy with carbide reinforcement has employed laser melt injection technique i.e particle injection into the surface of component. However, the application of this technique is restricted to protect the surface of new components and not suitable for component surface repair purposes. Hence the work in this thesis deals with laser cladding of Ti-6Al-4V with carbide reinforcements using a diode-pumped fibre laser which is suitable for surface modifications and component repairs. The previous work is yet to establish whether the dissolution of the carbide reinforcement is beneficial to the properties of the composites and the erosion resistance characterisation of these composites under high energy jet impacts is yet to be studied. All these are covered in this work.

TiB_2 and TiB have also been reported as suitable reinforcements in Ti and its alloys. These can be in-situ synthesized via laser cladding of boron-based ceramics with Ti. From prior work, the resultant microstructure is dependent on laser process conditions

employed. However, composite clad layers produced have been reported without necessarily having consideration for the influence of substrate dilution on the overall melt pool composition and the resulting microstructure on cooling. Moreover, the boride reinforced-Ti alloy composites have been either produced using a preplaced deposition of the preblended material or using two powder feeders with a cyclone for the laser processing. However, these deposition methods require careful control. In this work, a new method of using modified feedstock in which an agglomerated feedstock is produced is developed.

Hence, the overall aim of this work is to produce laser clads of carbide-based (Spherotene WC/W_2C) and boride-based (TiB_2)-Ti-6Al-4V matrix composite coatings using a fibre laser and to investigate the relationship between process parameters, microstructure formation and selected mechanical performance characteristics.

1.1 Aim and Objectives of the research

The overall aim of this work is to investigate laser clad composites formed using Ti-6Al-4V wire and Spherotene (WC/W_2C) particles and a modified pre-blend of Ti-6Al-4V/TiB_2 powder. The following specific objectives, which are further discussed in detail in the thesis chapters, are:

- To deposit Ti-6Al-4V wire with Spherotene (WC/W_2C) powder on a Ti-6Al-4V substrate, identify suitable processing parameter ranges and determine the influence of laser processing parameters on the physical characteristics (width and height) of beads and the efficiency of Spherotene deposition (Chapter 4).
- To study the microstructural features of composite beads and determine the influence of Spherotene particle dissolution on the composite microstructure formed. Also to characterise the overlap cladding of Ti-6Al-4V/Spherotene composite beads in terms of microstructure and microhardness, and also to demonstrate the suitability of the wire-powder process for the development of 3-D functionally graded structures (Chapter 4).
- To prepare a suitable powder feedstock for one stage laser cladding process by agglomeration of Ti-6Al-4V and TiB_2 powders (Chapter 5).

- To study the microstructural evolution of the Ti-6Al-4V/TiB_2 composite bead produced, assess the formation of ceramic phases with respect to changes in laser processing parameters, substrate dilution and influence on composite microhardness. Also to identify the microstructural changes in multilayer deposition of the Ti-6Al-4V/TiB_2 feedstock and its influence on multilayer microhardness (Chapter 5).

- In the case of Ti-6Al-4V/Spherotene, to study the erosion wear performance of the composite clad with different reinforcement fraction when subjected to both plain water jet and abrasive water jet erosion. Also, in the case of Ti-6Al-4V/TiB_2 3-D composite multilayers to investigate their tensile properties at room temperature.

1.2 Organisation of the Thesis

The thesis has been structured into 7 chapters with all the set objectives covered. Each chapter starts with an introduction stating the contents of the chapter and ends with a summary detailing the key findings. Moreover, a list of references cited in the entire research work is provided at the end of the thesis. Also, some additional information, which may be important to the reader, but not included in each chapters are provided in the appendices section before the list of references. The thesis overview is as follows:

- Chapter 1 provides an introduction and the rationale to the entire research work.

- Chapter 2 details a review on materials (Ti-6Al-4V, WC, TiC and TiB_2) and different laser surface engineering with focus on laser processing of Ti-6Al-4V with carbide and boride reinforcements. Based on the reviews, research opportunities are identified and research objectives formulated.

- Chapter 3 provides information on experimental methods and procedures including material characterisation, cladding and testing procedures employed to carry out the research work.

- Chapter 4-6 present the results obtained from the experimental study with each chapter containing the discussions of the relevant results.

- Chapter 4 reports the results of laser clad Ti-6Al-4V reinforced with Spherotene particles, and contains discussion on the microstructural characterisation of the composite deposits.

- Chapter 5 reports the result of laser clad Ti-6Al-4V/TiB_2 composites with discussion on the microstructural characterisation of the composite deposit and the tensile properties of the laser clad Ti-6Al-4V/TiB_2 composite walls.

- Chapter 6 provides information on the erosion performance of laser clad Ti-6Al-4V reinforced with Spherotene particles subjected to high impact plain and abrasive water jets.

- Chapter 7 gives a summary of the entire results in the research work. Also, areas of future work are presented.

Chapter 2

Literature Review

This section discusses laser processing technologies and laser surface engineering with extensive details on a variety of processing techniques and the characteristics of the process. Materials (Ti-6Al-4V, WC and TiB_2) to be used in the research work are discussed in terms of their properties, crystal structures and phase diagrams to aid the understanding of material characterisation. Since this thesis focusses on laser based surface engineering of Ti-6Al-4V with carbide and boride reinforcement, previous research work on laser processing of Ti alloys is also explored and discussed to identify where the present research work overlaps with previous work on cladding of Ti alloys. The theories of liquid and solid impacts on materials with previous research work on erosive wear testing of composite are also covered in this chapter.

2.1 Laser

Since 1960, when the first working laser was developed by Theodore Maiman [6, 7], an annual growth of about 10-20% has been observed in laser industry. The growth is driven by the increasing applications of laser light, a form of optical energy [8]. Over the years, laser applications have ranged from metrology to photography, material processing, medicine, communications, and electronics amongst others [8, 9]. In manufacturing, this optical form of energy is transformed into heat energy by focussing the laser beam using an optics arrangement to a required spot-size and profile. The interaction of the laser energy with materials during processing, results in the structural vibration of the

material. The vibration is detected as heat which could be high enough to melt the material, hence causing the optical energy to be transformed into heat energy [8]. Laser as a form of energy can be easily automated, thus making its use flexible for various applications. Laser applications in manufacturing may include: welding, drilling, cladding, peening, cleaning of material surfaces, surface treatment, micromachining, bending, 3D marking and cutting [4, 8, 10].

Laser is an acronym for Light Amplification by Stimulated Emission of Radiation, and it is generated by exciting an active medium which can either be in the form of solid, liquid or gas with an energy source (light, electricity, heat, etc). The excitation causes the electrons of the active medium to move from the ground state - low energy level (inner shell) to a higher energy level (outer shell). However, as the electrons relax and return back to their ground state, photons are released by the electrons. The photons, which are a form of light energy, are made to reflect with the medium between two mirrors (one fully reflecting mirror and another partially reflecting mirror) as in the case of a CO_2 laser or between two Bragg gratings as in the case of a fibre laser. The interaction of these photons with other excited atoms of the active medium give rise to increase in the population of the photons. As the population of the photons increase, a certain wavelength is reached, such that a coherent, monochromatic laser beam is generated which passes through the partially reflected mirror or the Bragg grating. The laser beam is then passed through an optical arrangements which would include a collimating lens and a focussing lens amongst others for the beam to be applied for various manufacturing processes. More information about laser evolution, its operating principle, classifications and operational mode, industrial type of lasers, and laser beam characteristics are well documented in the literature [3, 11] as this section does not aim to describe these in details.

2.2 Laser Process Technologies

Direct laser deposition is a novel technique for fabrication of metallic parts and engineering of metallic surfaces. The process involves melting of additive material in the form of either wire or powder using a focussed laser beam to deposit single beads on a substrate. Repeated bead passes with specified overlap pitch results in an area coating, while a controlled repetitive multilayer allows the fabrication of 3-dimensional (3-D) structures [5].

Figure 2.1 gives a schematic diagram of direct metal deposition using either powder or wire. This process has been developed and given different names which may include; direct metal deposition (DMD), direct light fabrication (DLF), laser engineered net shaping (LENS), and laser based flexible fabrication (LBFF) [12]. The LENS^{TM} process was developed at Sandia Laboratories and commercialised by Optomec Design Company in New Mexico; and DLF process was developed at Los Alamos National Laboratories; all these systems work by the same solid freeform fabrication principle which is achieved using a focussed laser beam with enough energy density to melt metallic powder and generate a solid, three dimensional component [13]. It is also possible to have a combined use of both wire and powder as this method has been previously used for development of functionally graded materials[14, 15]. Figure 2.2 gives an illustration of a DMD system with powder-wire combination.

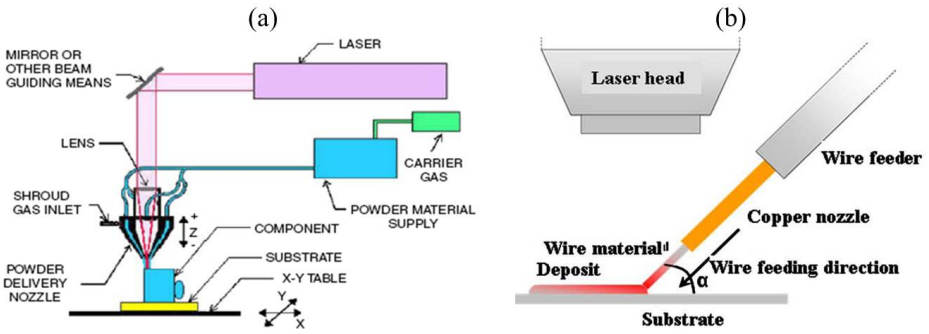

FIGURE 2.1: Schematic diagram of Direct Metal Deposition using (a) powder metal [16] (b) metallic wire [17].

2.3 Laser Surface Engineering

Laser surface engineering is a novel approach for surface modification of metals to enhance their performance when subjected to severe environmental and industrial conditions. It involves using the concentrated energy of lasers with material interaction to re-engineer a metallic surface. There are different approaches by which laser surface engineering can be deployed, these may include; laser surface melting, laser surface alloying, and laser surface cladding amongst others.

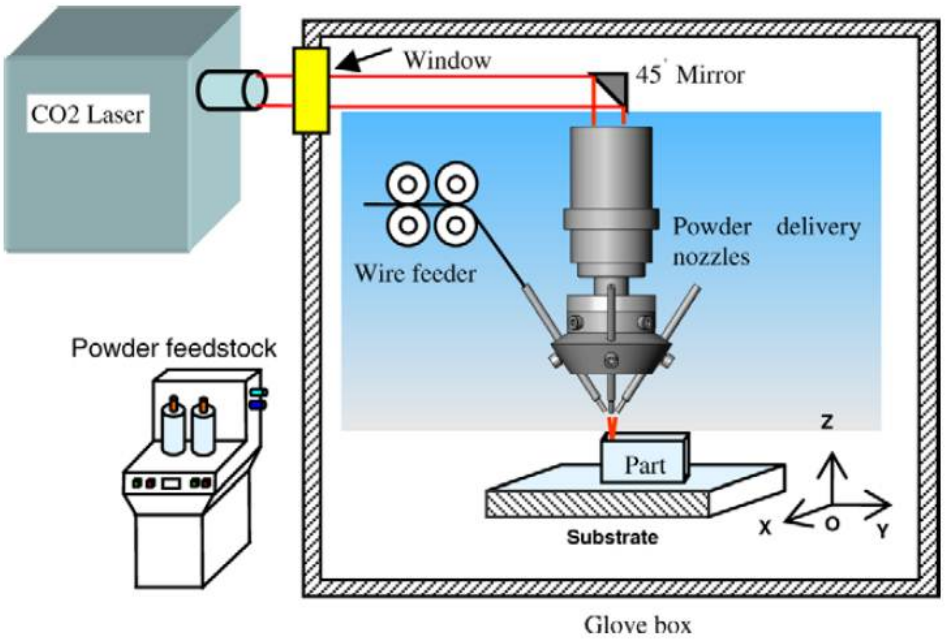

FIGURE 2.2: Schematic diagram of DMD system with concurrently fed powder and wire material [15].

Figure 2.3 shows different classifications of laser based surface engineering of metallic components. Route "A1-B1-C1" corresponds to laser surface melting technique, "A2-B1-C1" corresponds to a laser surface melting with a preplaced alloying material and "A1-B2-C3" correspond to laser surface alloying technique. "A1-B (2 or 3)-C2" and "A2-B1-C2" corresponds to laser surface cladding via a side-fed material system and a preplaced material respectively and "A1-B (2 or 3)-C (4 or 5)" corresponds to laser composite surfacing technique [1, 18, 19]. These techniques are further discussed to understand their process features. With any of these techniques employed, resistance against surface failure mechanisms, which may include wear, corrosion, erosion and high temperature oxidation; may be enhanced.

2.3.1 Laser Surface Melting

Laser surface melting is a surface modification process which involves the use of sufficient laser energy to irradiate the component surface in the presence of air, nitrogen or an inert gas. The laser irradiation causes a thin layer of the surface to melt, followed by a rapid solidification process within a short interaction time. This results into a

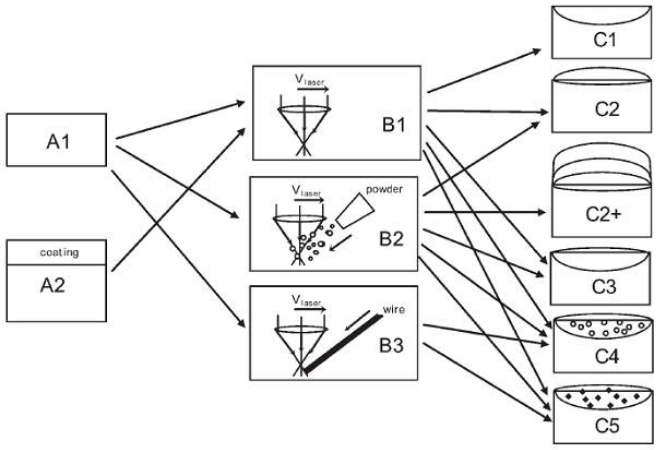

FIGURE 2.3: Classification of laser surface engineering approaches [18].

thin layer of a fine and near homogenous microstructure on the component surface. The surface hardness, corrosion, wear properties are enhanced based on the resulting fine microstructure [1, 4]. Figure 2.4 shows the schematics for laser surface melting processes. The surface modification process has been applied to different engineering materials; and applications based on Ti alloys are further discussed.

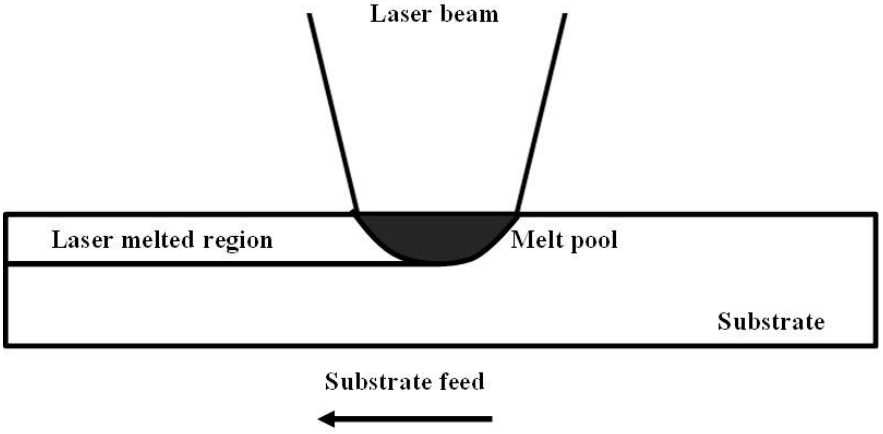

FIGURE 2.4: Schematics of Laser Surface Melting process showing the melted region [1].

The laser surface nitriding of Ti-6Al-4V alloy was investigated to improve the surface properties of the alloy which may include; hardness, wear and erosion resistance, using a CO_2 laser [20]. The investigation was carried out via laser surface melting process with the melt pool shrouded with nitrogen gas to prevent oxidation of the melt pool and also to react with titanium to give a TiN rich layer. Figure 2.5 shows the microstructure

of the nitrided layer on the titanium which was dendritic. The surface hardness was reported to be 500-800 HV up to a depth of 0.5-0.8 mm. In a similar study, the Ti nitrided layer was observed to appear as a golden colour with δ-TiN and ε-TiN phases dominating the treated surface. Also, similar hardness results were obtained to a depth of 400μm [21].

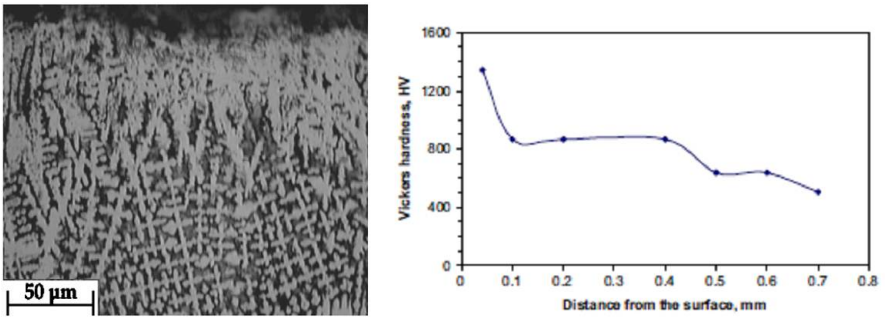

FIGURE 2.5: Dendritic microstructure of laser surface nitriding on Ti-6Al-4V alloy with the hardness profile [20].

In another complementary study, laser surface melting of Ti-6Al-4V in the presence of nitrogen shroud was carried out using a diode laser. The microstructure of the laser treated layer was characterised to contain TiN dispersed in α-Ti matrix. Figure 2.6 shows that low laser power was observed to increase the mass fraction of the TiN precipitates in the matrix. The residual stress of the layer was reported to be compressive at a laser power of 800 W and at all applied nitrogen gas flow rates, which is beneficial to hinder surface fatigue failure. Moreover, improvement of pitting corrosion resistance in Hanks solution was reported for the laser treated nitrided Ti-6Al-4V surface when compared to the untreated alloy [22]. The wear behaviour of the surface nitrided Ti-6Al-4V alloy was investigated using a pin-on-disc (two-body abrasive wear test using SiC abrasive paper) and a block-on-ring dry sliding wear rigs(Specimen sliding on hardened steel). The laser treated surface, rich in hard TiN phase, was reported to possess enhanced wear resistance which was inversely dependent on the scanning speed of the laser treatment as indicated by the relative wear values, which is the ratio of the wear weight loss of Ti-6Al-4V to that of the laser surface nitrided Ti-6Al-4V, in Figure 2.7 [23].

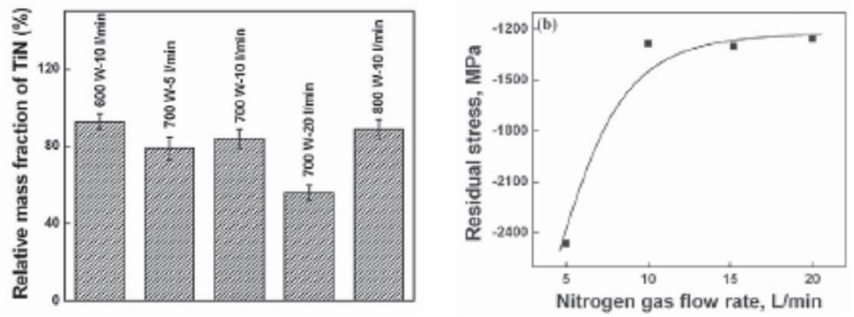

FIGURE 2.6: TiN fraction in Ti matrix and the residual stress as a function of nitrogen gas flow rate [22].

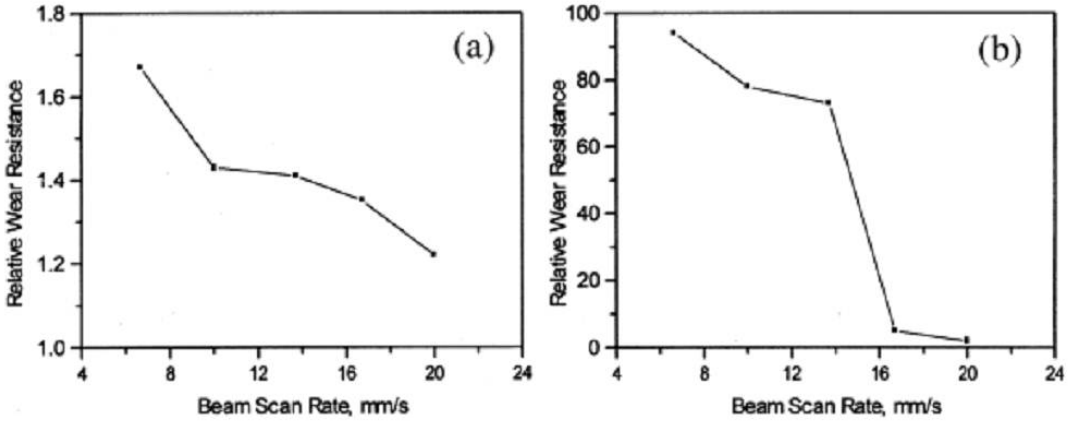

FIGURE 2.7: Relative wear performance of laser surface nitrided Ti-6Al-4V (a)pin-on-disc wear,(b)block-on-ring wear [23].

2.3.2 Laser Surface Alloying

Laser surface alloying is another surface modification technique whereby the laser beam irradiates the component surface with a simultaneous injection of alloying elements into the melt pool. The process can also be achieved by preplacing the alloying element on the component surface before laser scanning. The absorbed laser energy raises the surface temperature above the melting points of both the alloying element and the work-piece. This results in an alloyed melt pool composition with uniform solute redistribution owing to the thermo-capillary convection acting in the pool. On rapid cooling and solidification, an alloyed surface is generated which possesses enhanced surface properties from refined microstructure, solid solution strengthening, formation of metastable hard phases [2, 19]. Figure 2.8 shows the schematics of laser surface alloying process with alloying elements injected. The application of this process for Ti alloy surface modification is further

discussed.

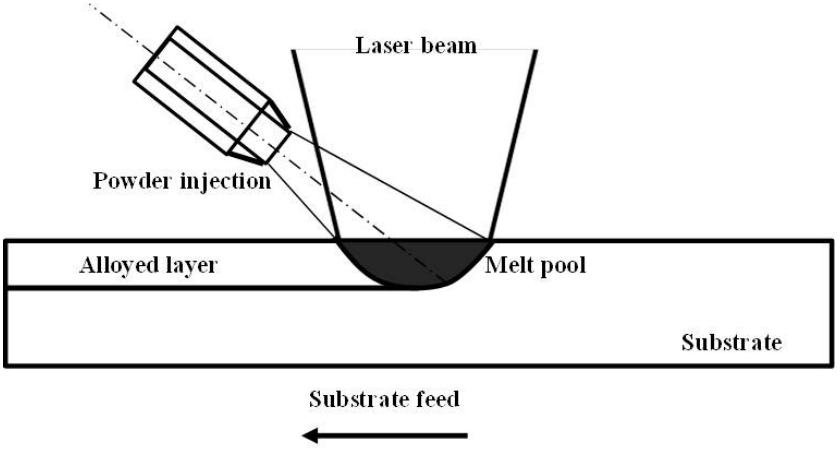

FIGURE 2.8: Schematics of Laser Surface Alloying process by direct injection of the alloying element [2].

The laser surface alloying technique was used to generate a carburised surface on a Ti-6Al-4V alloy. This was achieved by preplacing graphite powder with polyvinyl alcohol as a binder, up to a thickness of 200μm on a Ti-6Al-4V surface. The preplaced layer was irradiated with a multipass of laser beam using both CO_2 and Nd-YAG lasers [24]. A layer containing TiC precipitates was formed on the surface to some depth into the bulk Ti-6Al-4V. The carburised depth was reported to be deeper when Nd-YAG laser was used with 0.5 mm depth, while, 0.4 mm depth was reported as maximum when CO_2 laser was used. Figure 2.9 shows the microstructure of the top part of the alloyed surface cross section. TiC precipitates were formed as dendrites in the surface treated layer and the layer hardness was found to lie between 500-1050 HV.

In another study, laser surface alloying of Ti-6Al-4V with preplaced boron nitride, BN, was carried out using a CO_2 laser to improve the surface hardness of the alloy. The surface hardness of the boronised layer was found to lie between 1500-1700 HV and a cross sectional hardness of 700-900 HV to a depth of 0.4 mm. The surface improvement was attributed to the formation of TiB/TiN white needles and dendritic precipitates. This improvement was anticipated to enhance the wear and corrosion resistance, load bearing capability/contact deformation resistance and high temperature stability of the surface [25]. Thus, from previous works, laser surface melting and alloying are found to enhance the surface properties of Ti-6Al-4V alloy with the component dimensions retained.

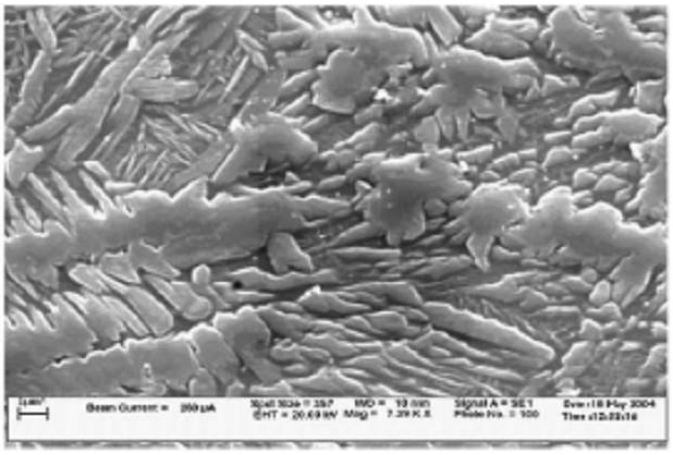

FIGURE 2.9: Ti-6Al-4V laser surface alloying using preplaced graphite powder showing TiC dendrites [24].

2.3.3 Laser Surface Cladding

Laser cladding is another key surface engineering technique. It is a melting process which involves the use of a laser beam to fuse an alloy addition onto a substrate. Materials with desirable properties such as corrosion and wear resistance are chosen for the cladding process [3]. In contrast to previously discussed laser surface engineering techniques, laser cladding is capable of re-engineering of component surfaces with the addition of a new material layer. This new layer of material is metallurgically bonded onto the component surface, hence allowing production of surface coatings and fabrication of functional components in a layered manner. More recently, the term laser cladding has also been applied to the layer additive manufacturing technique where three dimensional, fully dense metal components are generated from a CAD model without the use of moulds or tools [26, 27].

The process involves controlled and localised delivery of alloying material which can either be in the form of a powder or a wire into a laser generated melt pool on a substrate. The material becomes molten and solidifies on the substrate on cooling. During the process, surface melting of the substrate occurs as it absorbs laser energy which raises its temperature above its melting point. The molten clad solidifies rapidly with the surface melting of substrate to give a strong metallurgical bonding at their interface [3]. Most common materials used as substrate may include; carbon-manganese and stainless steel, titanium, aluminium, nickel and copper alloys; while the cladding powder could be an alloy of cobalt, nickel, iron, titanium, tungsten and silicon [3]. Wear

resistant surfaces which are strongly bonded to the substrate, with minimal heat input and distortion may be generated via this cladding process [3]. Laser cladding with alloying material in form of powder can be achieved in two ways namely;

- Pre-deposition (a two-stage process)
- Co-deposition (a one-stage process)

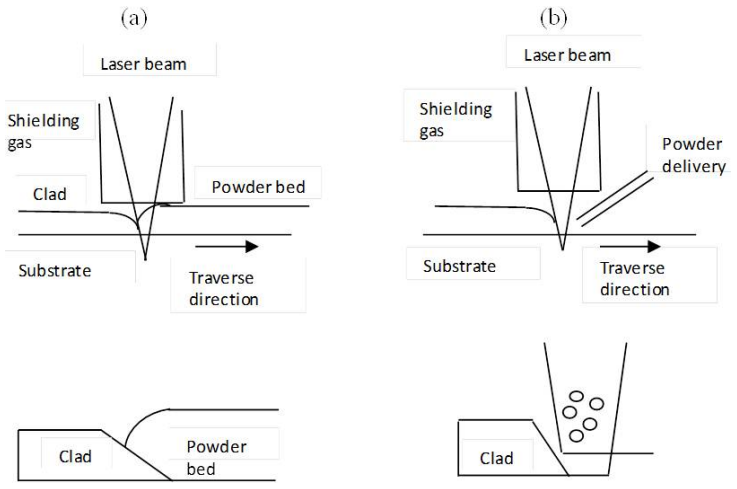

FIGURE 2.10: Schematics diagram of laser cladding processes (a)Pre-deposition(b)Co-deposition [3].

Figure 2.10 gives an illustration of these stage processes. Pre-deposition is a two-stage process which involves preparation of powder bed on substrate before the laser passes are made to melt the bed. The melt front moves rapidly through the powder, as the laser beam is moved over the bed until it reaches the interface. A small part of the substrate melts to dilute the clad and should result in a strong bond between the preplaced materials and the substrate. However, co-deposition is a one-stage process in which powder is injected into the laser generated melt pool on the substrate either by a coaxial or a side-feeding system [3].

2.3.4 Cladding Process Characteristics

Figure 2.11 shows a typical single clad bead cross section with its dimensional characteristics. These dimensional physical characteristics are regarded as some of the outputs which are observed in the cladding process. These outputs are being influenced by different variable input parameters associated with the laser cladding process.

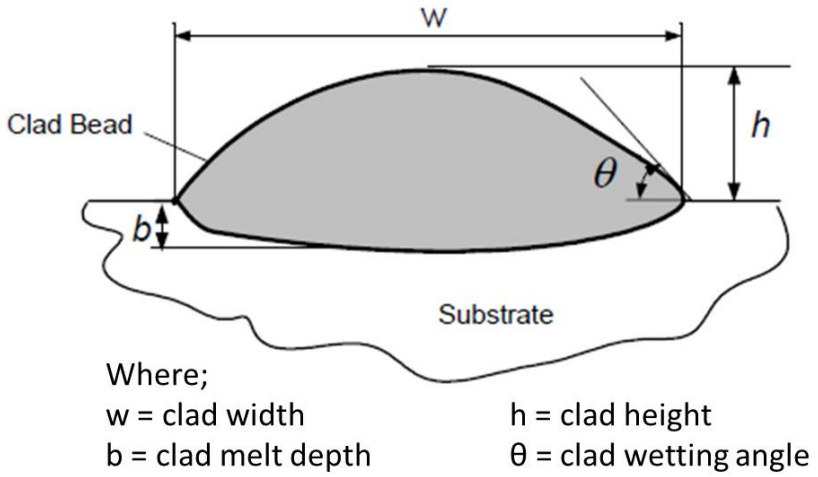

FIGURE 2.11: A typical cross section of a single clad bead [10]

These input parameters include: laser power and its mode (continuous wave or pulsed), traverse speed, spot diameter, material properties, material feed rate, feeding direction, angle of feed, preheating and delivery gas flow rate [10]. The desired outputs which are commonly observed include: physical characteristics (clad width, height, and dilution or melt depth), microstructural characteristics and performance characteristics amongst others. The influence of the laser input variables on different outputs characteristics is further discussed.

Laser power

Laser power is an extremely important factor that provides the heat to drive the cladding process. The power density of the laser beam is determined by the laser power and the spot area where the laser beam is focussed. For a circular laser beam profile, as would be used in this study, Equations (2.1) and (2.2) give expressions for power density and interaction time respectively, and the product of these two gives energy density relation for the process [3]. It can be noted that another important parameter to fully characterise the laser processing is the specific point energy (Equations (2.3)) since the same energy densities could result in having different energies delivered to the workpiece [28].

$$I_{(x,y)} = \frac{P_L}{\pi . r_b^2} \tag{2.1}$$

$$\tau = \frac{2.r_b}{v} \tag{2.2}$$

$$E_{sp} = \int\int I_{(x,y)}.\tau dxdy = I_{(x,y)}.\tau.(\pi.r_b^2) = P_L.\tau \tag{2.3}$$

Where; $I_{(x,y)}$ = power density in W.mm^{-2}, P_L = laser power in W, r_b = beam radius in mm, τ = interaction time or heating time in second, s, v = traverse speed of substrate in mm.s^{-1} and E_{sp} = specific point energy in J.

Laser power density influences the geometry of the melt pool and it has a positive relationship with clad height, width and melt pool depth [29–31]. The power employed during processing must be enough to eliminate limited melting of materials, poor metallurgical bonding at clad-substrate interface, and incomplete homogenisation of materials in the melt pool [32]. The relative position of the focal plane of laser beam has a direct influence on the processing energy density as shown in Figure 2.12. Hence, this may alter the microstructure of deposited track, as a uniform microstructure is reported to be achieved at under-focus position [33, 34]. Whilst using Nd:YAG laser, Dubourg and St-Georges [35] noted that the effect of out-of focus distance (defocus) on the clad size is less significant, but an increase in laser beam spot size promotes increasing quantity of materials assimilated into the pool when operating powder systems.

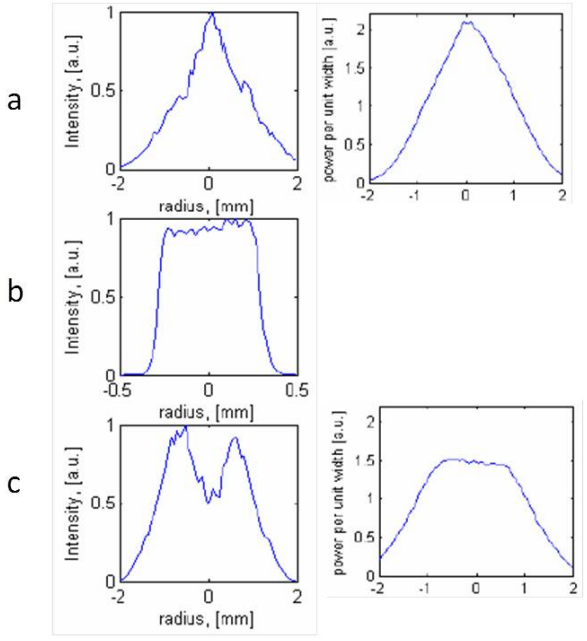

FIGURE 2.12: Laser beam intensity and power distribution at;(a)under-focus, (b) focus, (c) defocus [33].

Traverse speed

With all other independent parameters constant, as traverse speed increases, material delivery per unit length decreases, and this result in an inverse relationship with clad width, melt pool depth and clad height both in powder and wire based deposition [29, 36, 37].

Shielding and delivery gas flow rate

The carrier gas flow assists the steady delivery of powder material into the melt pool. This also serves to locally protect the melt pool from oxidation. Gases such as argon, Ar, helium, He, and nitrogen, N can be used for shielding and as carrier gas depending on the process and the desired output characteristics. Ar is the most commonly used gas because it is denser and cheaper [38]. However, carrier gas flow rate may cause a pool surface perturbation and a negative effect on clad width and surface roughness, as the melt pool experiences high cooling rate when the carrier gas rapidly flow over the melt pool surface [30, 39]. The rate of carrier gas flow determines the powder particle velocity and time spent in the laser beam before the deposition. As particle velocity increases laser power attenuation is reduced and this promotes increased laser energy reaching the substrate [40, 41].

Powder feed rate, wire feed rate and feeding strategy

In the cladding process, material can either be in the form of powder or wire. Moreover, in the powder based cladding process, the powder can either be fed through a coaxial nozzle or laterally fed through a dedicated feeding nozzle into the melt pool. The lateral feeding nozzle can be used to feed materials specifically to leading edges, trailing edges or centre of the melt pool. Figure 2.13 shows powder feeding mechanisms for both feeding scenarios [42].

Material delivery and interaction with the laser beam to generate clad tracks is influential on clad characteristics. With all other factors constant, an increase in material feed rate, either powder or wire, promotes increase in clad height, width and may as well improve deposition efficiency to a limit which depends on the viscosity of the melt pool and rate of solidification [35, 36, 43]. In powder based deposition systems, greater flexibility can be achieved in laser cladding with the use of lateral feeding nozzles to deliver different materials into the pool for generation of compositionally graded parts or coatings [32, 42]. A higher powder efficiency has been reported when the powder

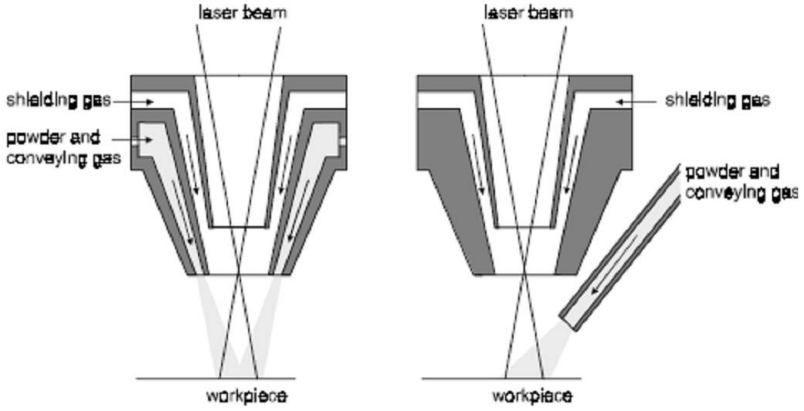

FIGURE 2.13: Coaxial (left) and lateral (right) feeding strategies [42].

is laterally and rear-fed from the side where substrate moves than being front-fed [40]. However, wire deposition can help to overcome shortcomings of powder deposition which may include: high cost of powder, low deposition efficiency, and poor surface finish [39]. In wire based deposition, it is best to adopt front feeding strategy, by delivering the wire at angle 45^o into the leading edge of the melt pool. The wire melts by absorbing the radiant heat as it approaches the melt pool. This delivers a bead with a better surface quality and dimensional control [17, 39, 44].

Preheating

Preheating of materials before laser cladding can be beneficial in some cases. It depends on the metallurgy of the materials used and how easy they are to weld. For example, a uniform preheating of the stainless steel substrate to 527^oC (800K) reduced residual stress by 22% during steel deposition. This residual stress could lead to crack formation, delamination, distortion and porosity [37, 45]. Preheating reduces the cooling rate during the process. Also in some situations, the surface oxide layer of substrate metal can be broken down by increasing preheating temperature [46]. Moreover, preheating of powder feedstock enhances the flowability of powder into the melt pool [43], while improved deposition efficiency is achievable by preheating wire feedstock before deposition [12].

2.4 Materials

The section discusses the materials to be used in this research work. The materials include; a titanium alloy, tungsten carbide (WC), titanium carbide (TiC) and titanium

(di) boride (TiB_2). Their chemical characteristics, properties, crystal structure and phase diagrams are discussed.

2.4.1 Titanium and its alloys (α, α/β, β-Ti)

Titanium alloy exists in three types which include: alpha (α), beta (β), and two phase alpha-beta (α-β). The α-Ti phase has a hexagonal closed pack (HCP) crystal structure, while the β-Ti phase has a body centred cubic (BCC) crystal structure. Figure 2.14 shows the crystal structure of the α-Ti and β-Ti phases. Ti-6Al-4V is a non-magnetic, α-β phase type alloy of titanium as shown in Figure 2.15. It has a beta transus temperature of 999±15^{o}C. It derives strength from substitutional and interstitial alloying of elements in solid solution in alpha and beta phases when it is in the annealed condition [47]. The composition range of Ti-6Al-4V can be found in Table 2.1. Interstitial alloying elements increase its strength and decrease ductility, such elements may include: carbon, hydrogen, oxygen and nitrogen.

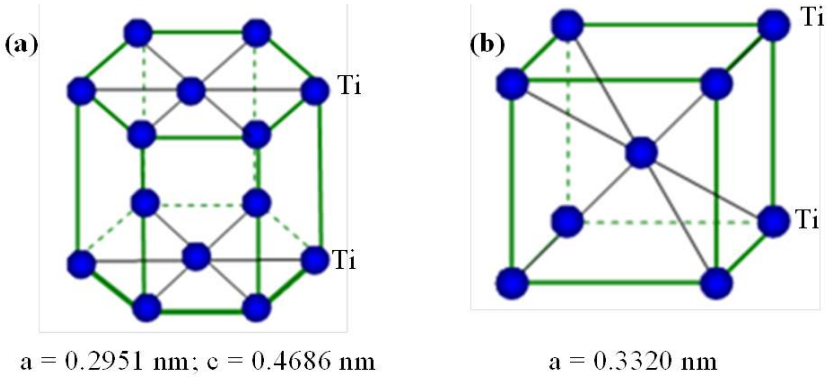

FIGURE 2.14: Crystal structure of titanium (a)α-Ti phase;(b)β-Ti phase [48].

TABLE 2.1: Composition of Ti-6Al-4V sheet Grade 5 in wt% [49]

Element	C	Fe	N_2	O_2	Al	V	H_2	Ti
wt.%	<0.08	<0.25	<0.05	<0.2	5.5-6.76	3.5-4.5	<0.015	Balance

Table 2.2 and Table 2.3 give the physical and mechanical properties of Ti-6Al-4V respectively. Ti-6Al-4V is responsive to heat treatment and the amount of beta phases can be manipulated in the alloy to increase strength [47].

Applications of Ti-6Al-4V alloy

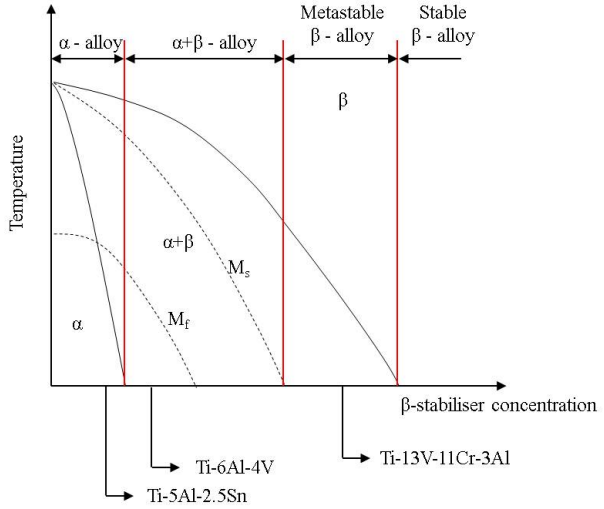

FIGURE 2.15: A pseudo-binary titanium phase diagram showing Ti-6Al-4V as $\alpha + \beta$ alloy and non-equilibrium martensitic phase lines, M_s and M_f (s = start; f = finish) [47].

TABLE 2.2: Physical properties of Ti-6Al-4V [49]

Property	Typical value
Density (kg/m^3)	4420
Melting point (^{o}C)	1649±15
Specific heat (J/kg.K)	560
Volume electrical resistivity (Ω.m)	1.7
Thermal conductivity (W/m.K)	7.2
Mean thermal expansion co-efficient (^{o}C^{-1})	8.6 x 10^{-6}
β-transus temperature (^{o}C)	999±15

Ti-6Al-4V alloy accounts for 60% of the industrial use of titanium and can be subjected to various processing stages to yield different product forms which may include: forgings, bar, castings, foils, sheet, plate, extrusions, tubing and fasteners [51]. Ti-6Al-4V alloy is good for applications at room temperature and up to a temperature range of 315-400^{o}C and also having a good weight saving and excellent corrosion resistance when compared to aluminium and steels [47, 51]. The alloy is widely used for aerospace applications for both gas turbine engines and aircraft structures. Other applications of Ti alloys may include: power generation, chemical processing, automotive, marine, oil gas and petroleum processing, medicine and architectural structures [51, 52].

TABLE 2.3: Mechanical properties of Ti-6Al-4V Grade 5 [49, 50]

Property	Typical value
Tensile strength (UTS) (MPa)	950
Elongation (%)	14
Area reduction (%)	36
Elastic modulus (GPa)	114
Poisson's ratio	0.342
Fatigue strength (MPa)	240
Fracture toughness (MPa.m$^{0.5}$)	75
Shear modulus (GPa)	44
Shear strength (MPa)	550
Vickers hardness (HV)	349

2.4.2 Tungsten carbide, WC

Tungsten carbide, WC, is a refractory, transitional, metallic carbide with hexagonal closed pack (HCP) crystal structure, and has excellent chemical and thermal stability, high hardness excellent oxidation resistance, low coefficient of thermal expansion, and good wettability [53]. Figure 2.16 shows the crystal structure of HCP WC where the lattice parameters are; a = 0.2906 nm and c = 0.2837 nm [54].

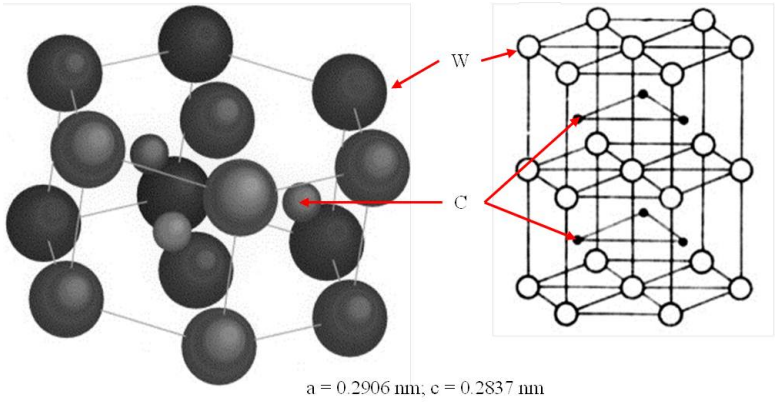

FIGURE 2.16: Crystal structure of WC [55, 56].

2.4.2.1 Mechanical and Physical properties

Table 2.4 shows the mechanical and physical properties of WC. This material has a high melting point, high hardness and high density. These properties promote its use as a refractory material and as matrix reinforcement in composites.

TABLE 2.4: Mechanical and Physical properties of WC [57–59]

Density ($kg.m^{-3}$)	Hardness (HV)	Thermal coefficient of expansion ($10^{-6}\ ^oC^{-1}$)	Melting point (^oC)	Tensile strength,UTS (MPa)	Elastic modulus (GPa)
15700	1300-2200	5.2	2800-2870	344	669-696

2.4.2.2 Thermal properties

Table 2.5 shows the thermal properties of WC. This includes specific heat capacity, enthalpy and Gibbs free energy of formations.

TABLE 2.5: Thermal properties of WC [60]

Specific heat capacity,C_p (J/kg.K) at 298K	Enthalpy of formation, ΔH_f (kJ/kg) at 298K	Gibbs free energy of formation, $\Delta\ G_f$ (kJ/kg) at 298K
181.12	-193.88	-188.78

2.4.2.3 W-C phase diagram

Figure 2.17 shows the W-C phase diagram. Phases of tungsten carbide which exist may include: WC, WC_{1-x} and W_2C. The mutual existence of all these phases can be attributed to the solidification mechanism of the carbide during preparation. The formation of WC and W_2C as composition and temperature vary, can be seen on the W-C phase diagram in Figure 2.17. The crystallisation of the two phases (WC and W_2C) are found to prevail under a moderate to high cooling rates (10^4-10^6 $K.s^{-1}$) when a non-isothermal analysis was employed [58]. This gives the possibility of having WC and W_2C phases co-existing as WC phase only exists on a narrow region at 50 at.% C in the phase diagram. WC is the most preferred carbide, as it retains its stability at temperatures up to 3049 K, while W_2C is a metastable reaction product which is not expected to be stable at temperatures below 1523 K [54, 58].

2.4.3 Titanium carbide, TiC

Titanium carbide, TiC, is a refractory ceramic material with a face centred cubic crystal (FCC) structure, exhibiting good resistance to high temperature oxidation, corrosion and

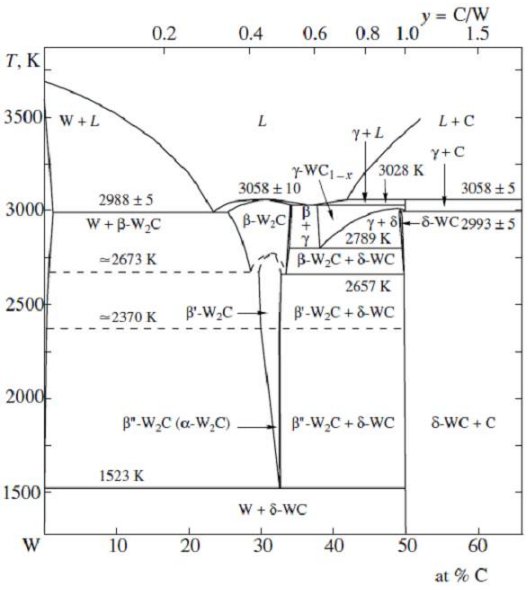

FIGURE 2.17: Phase diagram of W-C system [54].

wear [61]. Figure 2.18 shows the crystal structure of TiC which is similar to the FCC, NaCl-type structure with the Ti and C atoms octahedrally coordinated and the lattice constant for the cell, a = 0.4327 nm [62]. It is used as reinforcement in metals to form cermets and cutting tools. Also, it is used for high temperature applications such as heat exchangers and engines for oxidation and corrosion resistance purposes [61].

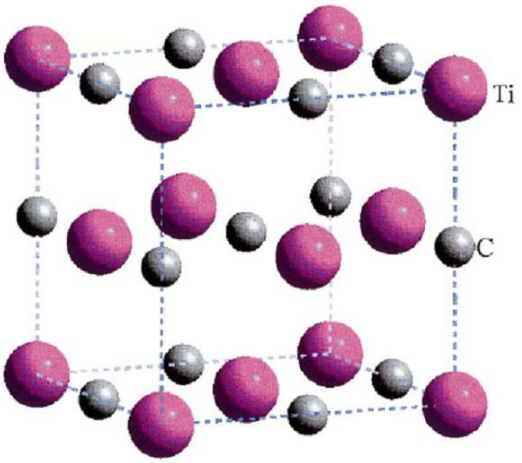

FIGURE 2.18: Crystal structure of TiC [62].

2.4.3.1 Mechanical and Physical properties

Table 2.6 shows the mechanical and physical properties of TiC. It has a lower density, high hardness and high melting point when compared to WC properties, which make it a desirable material for reinforcement and high temperature applications.

TABLE 2.6: Mechanical and Physical properties of TiC [61, 63]

Density ($kg.m^{-3}$)	Hardness (HV)	Thermal coefficient of expansion ($10^{-6}\ ^oC^{-1}$)	Melting point (^oC)	Elastic modulus (GPa)
4930	3200	8.5	3065	448-451

2.4.3.2 Thermal properties

Table 2.7 shows the specific heat capacity, enthalpy of formation and the Gibbs free energy of formation for TiC.

TABLE 2.7: Thermal properties of TiC [64]

Specific heat capacity,C_p (J/kg.K) at 298K	Enthalpy of formation, ΔH_f (kJ/kg) at 298K	Gibbs free energy of formation, ΔG_f (kJ/kg) at 298K
560.93	-3055.09	-3021.7

2.4.3.3 Ti-C binary phase diagram

Figure 2.19 shows the Ti-C binary phase diagram with TiC phase formed with carbon content lying between 30-50 at% [65]. This means that TiC phase exists over a wide composition range. However, other non-stoichiometric phases can be formed in a Ti-C system, these may include TiC_x with 0.56<x<0.98 ($TiC_{0.59}$, $TiC_{0.62}$, $TiC_{0.6}$) and Ti_2C. The Ti_2C phase is considered as a stoichiometric reaction product in a Ti-C system [61, 62, 66]. Wanjara et al. [66] reported that the percentage composition of carbon in TiC_x influences the lattice parameter of the TiC unit cell, as shown in Figure 2.20. The figure indicates an increase in lattice parameter as the carbon content increases from 0.3-1.0.

Considering the Ti-C binary phase diagram in Figure 2.19, there are no intermediate phases existing between the TiC and the Ti phases (α and β-Ti). Also, two eutectic and

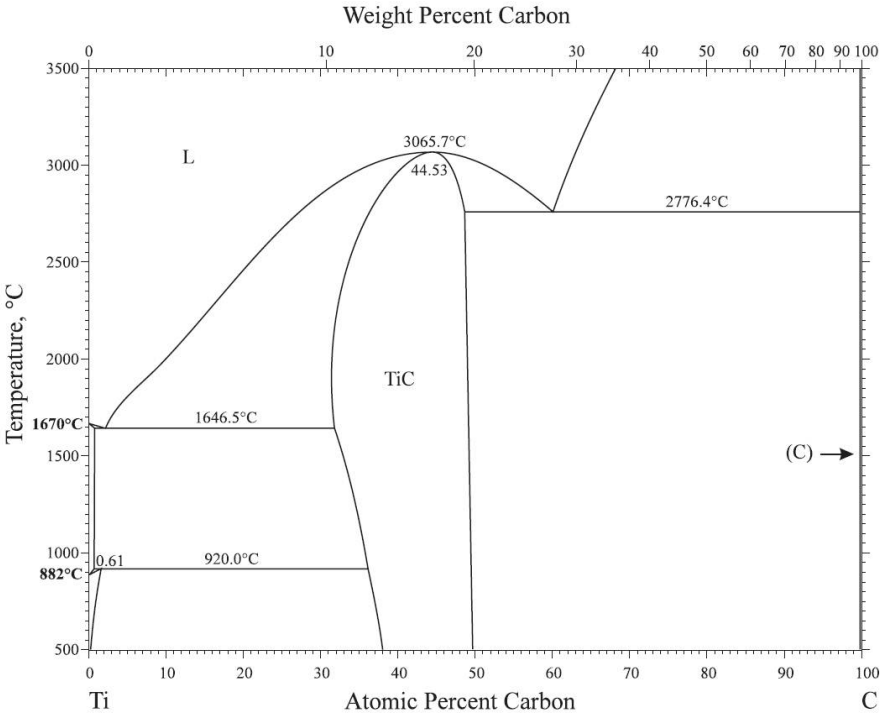

FIGURE 2.19: Ti-C binary phase diagram [65].

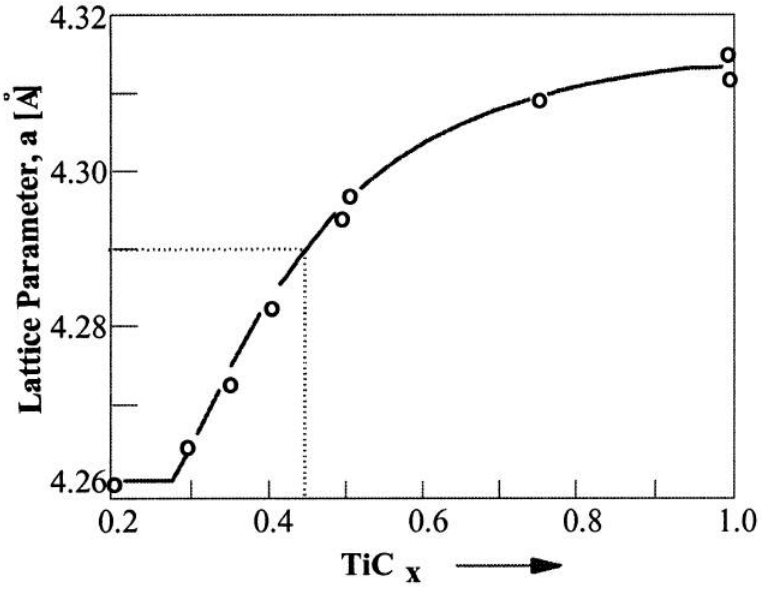

FIGURE 2.20: Room temperature lattice parameter changing as a function of carbon content in TiC_x [66].

one peritectoid reactions exist in the phase diagram at temperatures 2776^{o}C, 1646^{o}C and 920^{o}C respectively. The atomic content of carbon in Ti must exceed 30% for TiC phase to be formed under an equilibrium condition. It was observed that the maximum temperature for the TiC phase to go into liquid phase is about 3065^{o}C.

2.4.3.4 Ti-W phase diagram

Figure 2.21 shows a phase diagram for Ti-W system. In this system, the dissolution of W into a Ti matrix results in a β-stabilised continuous isomorphous, BCC, (Ti,W) solid solution at high temperature. On cooling, a monotectoid decomposition is expected to occur to produce α-Ti and W phases. It was reported that Ti can be stabilised as α-phase under equilibrium conditions when the terminal solid solution of the Ti phase does not contain more than 0.3 at.% W. However, Ti solid solution would be β-stabilised with W content ranging from 0-100 at.%. Also, W solid solution which contain 100 at.% Ti is possible [65].

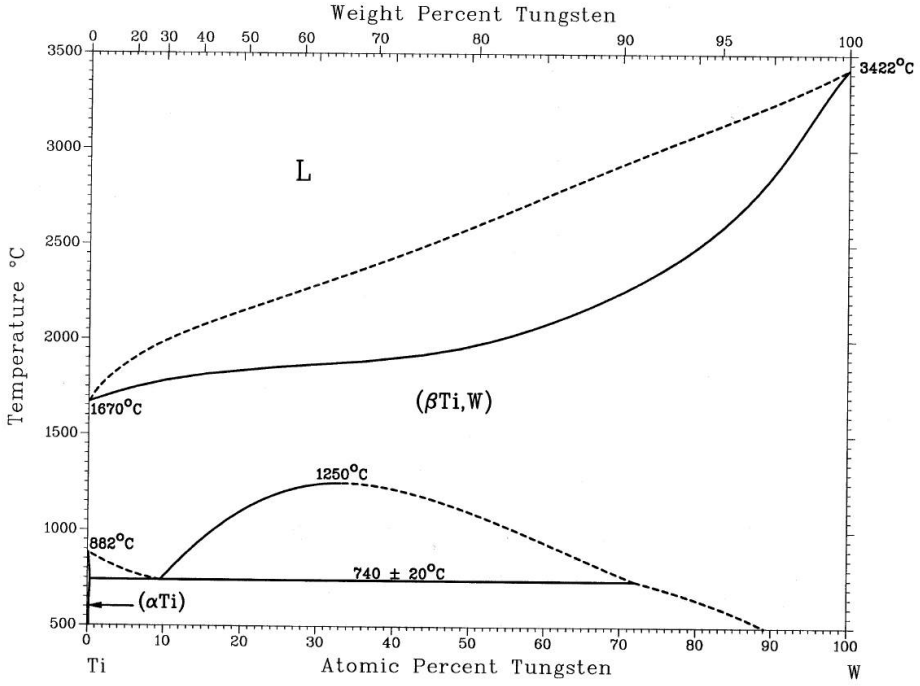

FIGURE 2.21: Ti-W binary phase diagram [65].

The combination of the two previous discussed binary phase diagrams resulted into a Ti-W-C ternary phase diagram. This gives the different phases that could be formed when these three elements interplay under equilibrium conditions. Figure 2.22 shows the

liquidus projection of the ternary phase diagram for the Ti-W-C system. Intermediate phases reported to be formed in the Ti-W-C system are TiC, WC, W_2C, WC_{1-x} and Ti solid solutions. It was reported that there is a great possibility of having a complete miscibility of TiC and WC_{1-x} phases at temperatures greater than 2530^{o}C, and the melting point of the resulting solid solution is about 3130^{o}C. Also, the solubility of TiC and WC_{ss} was reported to be dependent on temperature.

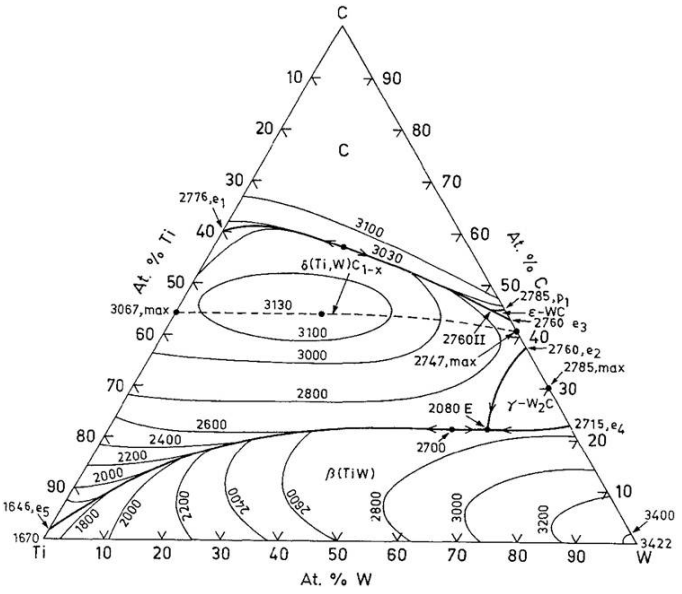

FIGURE 2.22: Liquidus projection of the Ti-W-C ternary phase diagram [65].

2.4.4 Titanium (di) boride, TiB_2

Titanium diboride, TiB_2, is another important refractory material, with a hexagonal closed pack (HCP) crystal structure. It is characterised by a high melting point (3225^{o}C), low specific weight, high hardness, high strength to density ratio, good wear resistance, excellent thermal and chemical stability, and superior electrical and thermal conductivities [61, 67]. It has found use in nuclear industry, as well as in the production of impact resistant armour, cutting tools, wear resistant coatings, and electrodes among many others [68]. Figure 2.23 shows the crystal structure of TiB_2. It is a hexagonal AlB_2-type structure with trigonal prism formed by the titanium atoms and boron atoms fill the space between Ti atoms. The lattice parameter for the TiB_2 hexagonal structure are a = 0.3028 nm and c = 0.3228 nm [61].The lattice parameters of a TiB_2 single crystal is reported to vary with temperature as shown in Figure 2.24 [68].

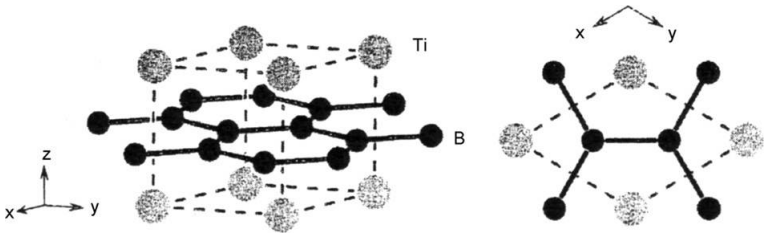

FIGURE 2.23: Crystal structure of TiB_2 [61].

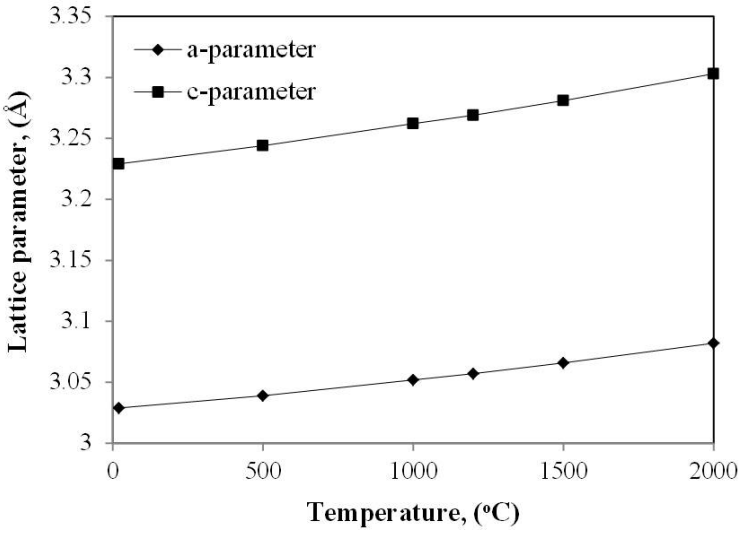

FIGURE 2.24: Change in lattice parameters of TiB_2 single crystal as a function of temperature [68].

2.4.4.1 Mechanical and Physical properties

Table 2.8 shows the mechanical and physical properties of TiB_2. It has a slightly lower density, higher hardness and melting point when compared to TiC.

TABLE 2.8: Mechanical and physical properties of TiB_2 [61, 68]

Density ($kg.m^{-3}$)	Hardness (HV)	Thermal coefficient of expansion (10^{-6} $^oC^{-1}$)	Melting point (^oC)	Compressive strength, (MPa)	Elastic modulus (GPa)
4520	3650	6.4-9.2	3225	1800	565

2.4.4.2 Thermal properties

Table 2.9 shows the thermal properties of TiB_2 in terms of specific heat capacity, enthalpy and Gibbs free energy of formation. Figure 2.25 shows that the specific heat

capacity of TiB_2 increases with increase in temperature [68].

TABLE 2.9: Thermal properties of TiB_2 [60, 64]

Specific heat capacity,C_p (J/kg.K) at 298K	Enthalpy of formation,ΔH_f (kJ/kg) at 298K	Gibbs free energy of formation,ΔG_f (kJ/kg) at 298K
640.29	-4647.48	-4589.93

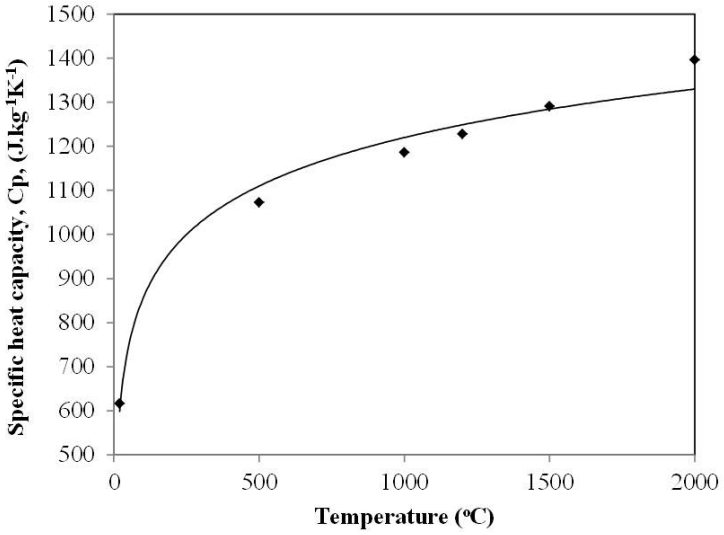

FIGURE 2.25: Change in specific heat capacity of TiB_2 as a function of change in temperature [68].

2.4.4.3 Ti-B binary phase diagram

In the Ti-B binary phase diagram (Figure 2.26), there exist 3 phases of the Ti boride, these may include: TiB, Ti_3B_4 and TiB_2. TiB_2 is found to exist over a wide composition range, while other boride phases exist over a narrow range. Thus, with the diffusion of boron atoms, TiB_2 may be transformed into Ti_3B_4 or TiB phase. TiB_2 has found application in nuclear industry, military (impact resistant armours), foundry (lining of crucibles), and machining (cutting tools) [61]. TiB whiskers are most chemically stable in Ti alloy which helps to overcome the limitations of poor wear resistance, low specific strength, at elevated temperature, and low specific fatigue resistance [69, 70]. It was reported that higher stiffness comparable to high strength steel with minimal residual stress was observed for Ti/TiB MMCs due to thermodynamic and mechanical stability of TiB whiskers in Ti matrices. The chemical stability of TiB can be supported by the

Ti-B binary phase diagram in Figure 2.26, where it can be seen that there is no other formation of an intermediate phase between the TiB and the α or β Ti phase [70].

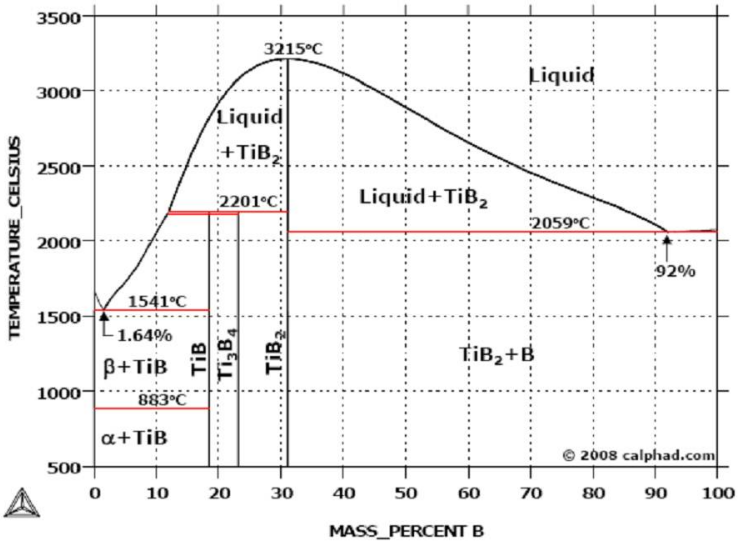

FIGURE 2.26: Titanium Boron phase diagram [71].

2.5 Laser Cladding of Titanium Alloys

Having reviewed the surface engineering techniques made by laser processing and materials, this section further discusses laser cladding applications to improve surface properties of Ti alloys as this research work focuses on laser cladding of Ti-6Al-4V. Previous work is as well reviewed to highlight the significance of the laser processing technique to improved surface properties and also to identity new research opportunities.

The laser processes which result in the formation of modified metallic surfaces have been discussed earlier in Section 2.3. These laser-based, surface modification processes include: laser surface melting, laser surface alloying by injection of alloying elements or reinforcing particles, and laser cladding. However, for repair purpose and 3-dimensional component manufacture, laser cladding is considered as the most suitable laser processing technique. This technique is favourable for surface modification of titanium alloy for coatings and structural purposes. Though, pure titanium has excellent toughness, corrosion resistance, and high strength to weight ratio, it possesses poor tribological properties which has been associated with its high c/a lattice dimensional ratio as a hexagonal closed pack (HCP) metal [72]. This has prompted researchers to improve Ti

alloy wear properties with ceramic reinforcements by employing surface engineering approaches such as laser melt injection/surface alloying or laser cladding. Also, improved stiffness of Ti alloys can be achieved by production of fibre-reinforced Ti MMC with comparable strength to steels which could make it more useful for specific applications [73]. Since, this research work looks at enhancing the properties of Ti-6Al-4V with carbide and boride reinforcements using laser cladding, previous works on this subject are further reviewed.

2.5.1 Laser processing of Ti alloys with carbides

Research work has been conducted in the area of laser processing of Ti alloys with various carbides to produce a coating on metallic substrates. Ayers [74] studied the wear behaviour of aluminium- and titanium alloy surfaces that were subjected to the laser melt injection process with TiC and WC particles. The process was conducted by having a laser beam focused to a spot diameter of 3 mm with the injection of carbide particles into the shallow melt pool. The size range of carbide particles used was between 40-150 μm. Helium gas was used as powder carrier gas as well as the shielding gas during the process. Laser multi-passes were carried out with an overlap pitch of 1 mm to treat a wider surface area. The treated surfaces were reported to have possessed between 15-65% embedded carbide volume fractions with a uniform distribution within the melt. Figure 2.27 shows the microstructure of Ti-6Al-4V embedded with TiC particles. The shape of the TiC angular particles were observed to be preserved with their edges rounding due to surface melting. The surface melting provided the Ti melt with sufficient carbon to allow the formation of TiC dendrites. Surfaces are prone to cracking during processing when large volume fraction of TiC, as high as 60%, is used. Cracks were observed on the TiC particles in the overlapped region of the treated Ti-6Al-4V surface.

However, a crack-free Ti-6Al-4V modified surface was achieved with a WC volume fraction up to 37% [74]. On solidification, the overlap regions are characterised by alloyed Ti-W carbide precipitates. A slightly higher concentration of WC particles was observed in the overlap regions, as these zones experience particle injection twice.

Table 2.10 shows the result of a dry sand rubber wheel (DSRW) wear test conducted on surface treated Ti-6Al-4V. The wear improvement ratios were found to be between 7 and 13, which justifies the presence of the embedded carbide particles in the Ti-6Al-4V

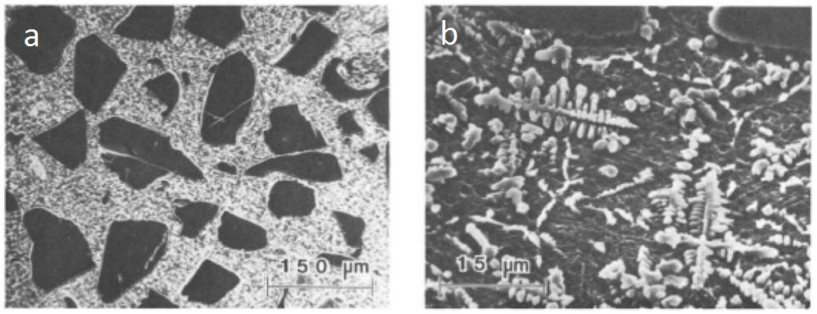

FIGURE 2.27: (a) Ti-6Al-4V injected with TiC particles; (b) TiC dendrites formed during solidification [74].

TABLE 2.10: Dry sand rubber wheel wear results for Ti-6Al-4V alloy with different volume fractions of TiC and WC particles [74]

Alloy	Carbide type	Mean carbide size (μm	Carbide volume (vol.%)	Wear volume (mm^3)	Normalised wear rate
Ti-6Al-4V	WC	125	26	8.2	8
Ti-6Al-4V	WC	125	34	6.3	11
Ti-6Al-4V	TiC	150	45	9.3	7
Ti-6Al-4V	TiC	50	59	5.2	13
Ti-6Al-4V	-	-	-	67	1

surface. The result showed that WC is more effective than TiC in abrasion wear, but due to carbide dissolution and cracks, higher volume content of WC in Ti-6Al-4V was not used. The result shows that abrasion resistance of Ti-6Al-4V surface can be improved by injection of carbides. It can be deduced that a smaller reinforcement size with higher volume fraction in the Ti matrix favours the significant enhancement of the composite layer wear resistance.

In another development, **Folkes** and Shibata [75] conducted laser cladding experiments with a pre-blended mixture of Ti-6Al-4V with various weight percentages of different carbide powders using a 5 kW CO_2 laser on a Ti-6Al-4V substrate. With a constant laser power of 2.5 kW, optimum traverse speed was observed to be 300 mm/min and powder feed rate was found to be between 45-120 g/min for a beam diameter between 3-3.5 mm. The carbide powders included; Cr_3C_2, Mo_2C and WC, and they were selected based on cost, thermodynamic and property considerations. The particle size of Ti-6Al-4V used was <210 μm, Cr_3C_2 and WC had <44 m particle size, while Mo_2C had particle sizes between 80-100 μm. Pre-blended powder mixtures containing 10 and 20 wt% Cr_3C_2 resulted in a β-Ti + TiC clad microstructure. A 10 and 20 wt% Mo_2C resulted into an

(α+β)-Ti + TiC microstructure and β-Ti + TiC structure respectively. Moreover, a 10 and 20 wt% WC resulted in a α-Ti +TiC clad microstructure with the presence of the original WC particles in the pre-blended powder. The Ti phase was not β-stabilised since the W content of the clad did not exceed 22.5 wt%. In all the cases, TiC precipitates were reported apart from the original carbides embedded. It had either a dendritic or feathery morphology depending on the carbide content.

Figure 2.28 shows change in clad hardness with increase in temperature. The WC reinforced clad had the highest hardness and the hardness decreases with increasing temperature. However, amongst other clads, WC reinforced clad maintains high hardness at high temperature (600^{o}C). The researchers suggested that for industrial application of laser surface cladding on Ti alloys, a β-Ti + TiC clad matrix is preferred as the matrix would not be too hard [75].

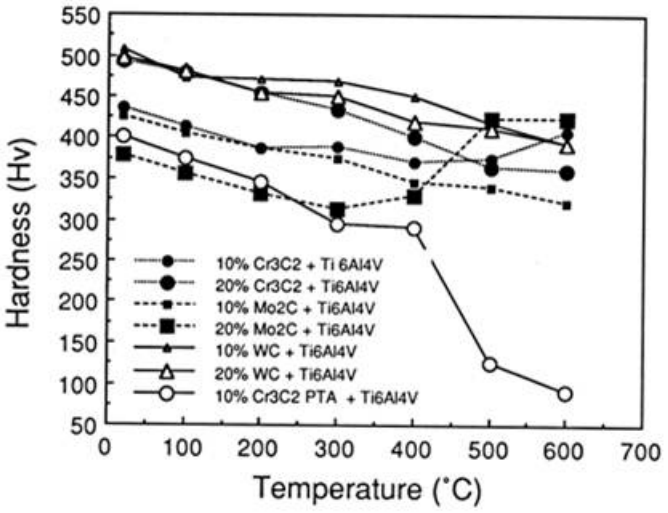

FIGURE 2.28: Change in hardness as temperature increases with Ti-6Al-4V/WC clad showing retained hardness at elevated temperature [75].

Vreeling et al. [76] studied the strengthening of Ti-6Al-4V surface with WC particles by laser melt injection process which was conducted using a 2 kW Nd:YAG laser. The influence of processing parameters was determined on dimensions and microstructure of Ti-6Al-4V laser treated layer. A defocussed laser beam spot size of 3.6 mm was used and spherical WC particles with size 80 μm, were injected into the laser generated melt pool on the Ti-6Al-4V substrate. Optimised parameters reported were 79 W.mm^{-2} power density, 8.3 mm.s^{-1} traverse speed, and 0.125 g.s^{-1} powder feed rate. Maximum track width reported is 1.8 mm, maximum depth of 0.7 mm and WC volume fraction

was 0.25-0.30. It was reported that α-Ti, β-Ti, WC, W_2C, W and TiC were present in the microstructure. Figure 2.29 shows an SEM image of microstructure. A thick TiC reaction layer is observed around the WC particles and it is reported that the thickness of the layer is dependent on the laser processing parameters and the location in the melt pool. Increasing power and slower traverse speed result in a thicker reaction zone formation around WC particles in the melt especially in the top region of composite layer [76].

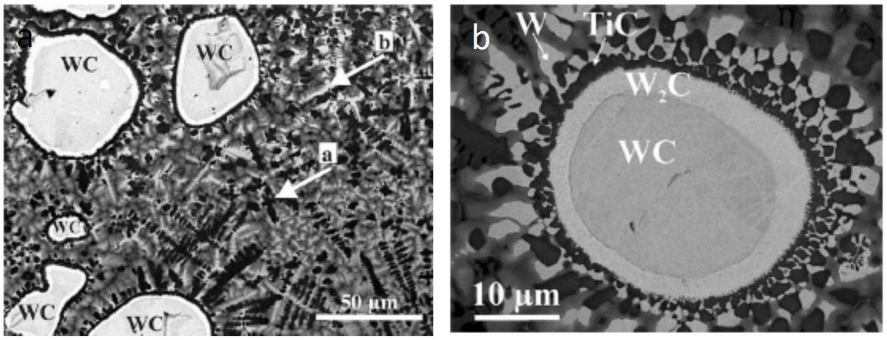

FIGURE 2.29: (a)BSE image showing WC distribution in Ti matrix with dark TiC and W solid solution precipitates;(b)reaction layer around a WC particle [76].

The Ti-6Al-4V/WC surface was subjected to wear using a pin-on-disk setup in an oil bath at room temperature. Table 2.11 shows a significant improvement in the wear performance of the WC embedded surface when compared to untreated Ti-6Al-4V. Specific wear rates of 0.5 x 10^{-6} mm^3/Nm and 269 x 10^{-6} mm^3/Nm were reported for Ti-WC MMC layer and Ti-6Al-4V alloy respectively with a constant applied contact stress of 20 MPa [76].

TABLE 2.11: Specific wear rate of Ti-6Al-4V laser treated layer and pin in pin-on-disk wear test [76]

Sample	Contact stress (MPa)	k_1	k_2	f_a
Ti-6Al-4V	20	189	269	0.21
Ti-6Al-4V remelted	20	40	240	0.18
WC/Ti-6Al-4V layer	20	0.13	0.5	0.11
WC/Ti-6Al-4V layer	100	0.08	0.05	0.12

Where; k_1 = specific wear rate of pin (10^{-6} mm^3/Nm), k_2 = specific wear rate of sample (10^{-6} mm^3/Nm), f_a = average value of friction coefficient

In another study, Zhang et al. [77] conducted laser cladding experiments with different mixtures of a pre-blended Ti and WC powders which have three different atomic percentage compositions of Ti-2WC, Ti-WC and 2Ti-WC. Clad layers were prepared on a CP Ti plates and characterisation of the track appearance and microstructure was carried out. A CO_2 laser was used and an optimum cladding condition was reported as 3 mm beam diameter, 1-1.2 kW laser power, 6-8 mm.s^{-1} traverse speed and an overlap of 60% [77]. Phases identified and reported were α-Ti, (W-Ti)C_{1-x} and Ti_xW_{1-x}, W_2C and W, besides the embedded WC particles. It was reported that decarburisation of WC led to the formation of TiC and the solid solution of W [77]. Dark contrast TiC dendrites and bright contrast herringbone structure of Ti/W solid solutions were observed in the microstructure. The heat affected zone was found to possess a α-Ti martensitic structure (needle like structure).

In another study similar to Vreeling et al. [76], a graded metal matrix composites layer of WC/Ti-6Al-4V was formed by laser melt injection process using a CO_2 laser [78]. The laser beam used was focussed on the Ti-6Al-4V surface to give a spot diameter of 3 mm. Power density of 241-425 W.mm^{-2}, traverse speed 0.2-1 m.min^{-1}, and powder feed rate 60-150 mg.s^{-1} were employed in the study. Monocrystalline WC powder of size range 60-100 μm was used and injected into the melt pool on the surface of Ti-6Al-4V behind the laser beam to reduce WC particle-laser interaction and WC dissolution in the melt pool. It was reported that using monocrystalline WC may reduce the intergranular cracking in WC particles. Also, WC was considered as a desirable reinforcement ceramic for Ti-6Al-4V due to their similar coefficients of thermal expansion values, this is expected to decrease the residual stress in graded metal matrix composite of WC/Ti-6Al-4V [78]. Maximum depth and width reported were 2.3 mm and 0.75 mm respectively. Observed phases reported were TiC, W_2C, (Ti,W)C_{1-x}, W, WC and α-Ti. Figure 2.30 shows the TiC precipitates formed in the Ti melt, these were found to possess either a block or dendritic morphology.

The (Ti, W)C_{1-x} phase was considered as a TiC solid solution in the microstructure as some of the TiC precipitates are rich in W. Two types of reaction layers were identified and reported, these include; a cellular reaction layer and an irregular reaction layer (Figure 2.31). Microhardness data reported for the graded Ti MMC were 540 HV for the top region, 420 HV at the bottom and 365 HV for the Ti-6Al-4V substrate, and it was reported that the change in hardness was gradual from top down into the substrate. The

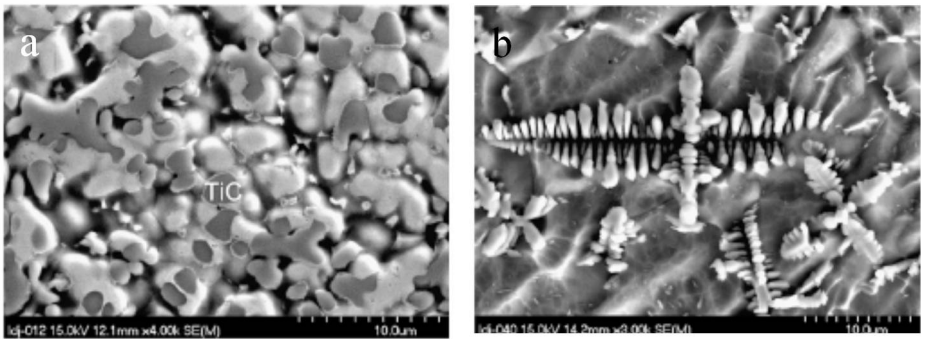

FIGURE 2.30: SEM images showing types of TiC morphology in Ti MMC (a)blocky,(b)dendritic [78].

matrix hardness decreased as process traverse speed was increased which was attributed to a decrease in the formation of reaction products [78].

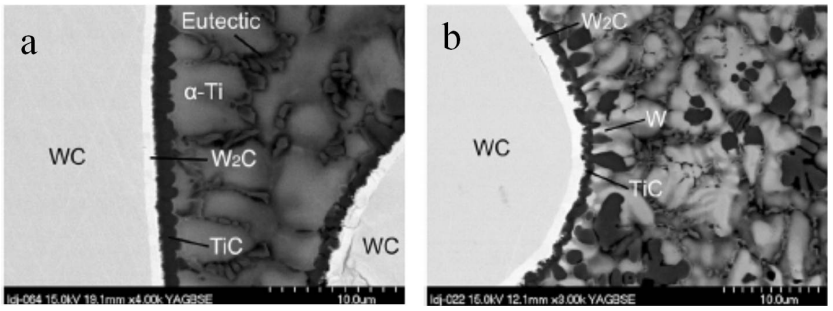

FIGURE 2.31: BSE images showing types of reaction layer around WC particles (a)cellular;(b)irregular [78].

Having considered monocrystalline WC particles as suitable reinforcing particles for Ti-6Al-4V, a further study was conducted to determine the fracture behaviour of the WC/Ti-6Al-4V composite layer produced by laser melt injection process. The composite layer was subjected to tensile loading in a SEM to observe the crack initiation and propagation as fracture occurs while loading. Two modes of crack nucleation were identified and reported, these include WC particle cracking and decohesion of WC/W_2C interface as shown in Figure 2.32 [79]. The crack initiation in the WC particle was reported to have occurred at 0.35% strain, while WC/W_2C decohesion occurred at a strain of 0.44%.

More so, another study was conducted on the microstructure evolution of WC/Ti-6Al-4V composite layer produced via laser melt injection (LMI) and vacuum arc melting (VAM) processes [80]. This was done to determine the effect of cooling conditions

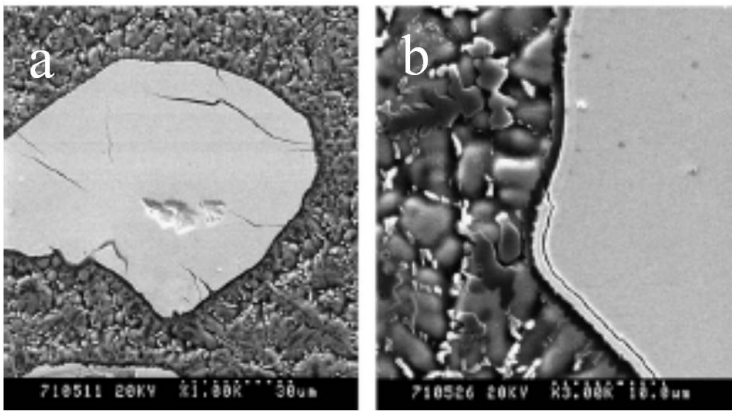

FIGURE 2.32: BSE images showing crack nucleation in WC/Ti-6Al-4V MMC (a)WC cracking;(b)WC/W_2C interface decohesion [79].

on the interfacial reaction between monocrystalline WC and Ti melt. As previously noted that particle/matrix bond and reaction products in the matrix are factors that determine the fracture strength of the MMC [79], thus, it is thought that the interfacial reaction between WC and Ti which is sensitive to cooling rate should be examined. The LMI process for the preparation of WC/Ti-6Al-4V composite layer was conducted as discussed in [78], while the VAM process was carried out on a vacuum arc melting furnace with a current of 180 A. The WC powder was preplaced as a thin layer on Ti-6Al-4V surface with a re-melt Ti-6Al-4V ingot placed on the WC thin layer before an arc was applied. The WC/Ti-6Al-4V composite prepared was allowed to cool in the furnace, after removing the arc source.

A thermodynamic analysis of the possible chemical reactions between liquid Ti and WC was evaluated and reported. Figure 2.33 shows Gibbs free energy changes with respect to temperature for the likely chemical reaction between Ti and WC. It is reported that due to the high affinity of Ti for C, TiC is easily formed, which promotes the decomposition of WC to W_2C. Furthermore, due to the instability of W_2C in liquid Ti, it further decomposes to W. This makes reaction path 1 to be a combination of reaction paths 2 and 3. However, it is shown that the decomposition of W_2C is impossible at temperature above 2364 K. Thus, decomposition of WC to W_2C is likely to occur at high temperatures, while further decomposition of W_2C to W is more feasible to occur as temperature drops to lower values.

The microstructure observation for Ti MMC produced via LMI was similar to the ones presented in Figure 2.31. It is reported that the WC particle surface acted as preferential

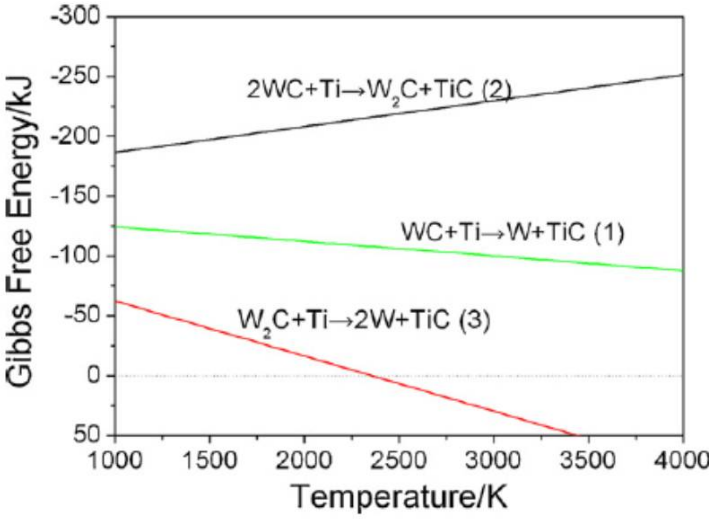

FIGURE 2.33: Free energy change with respect to temperature for reaction between Ti and WC [80].

sites for TiC nucleation, and this made numerous TiC nuclei grow on the surface at high rate similar to the rate of solidification in the melt pool. Thus, the formation of this TiC layer was reported to have prevented the diffusion of W into the Ti melt [80].

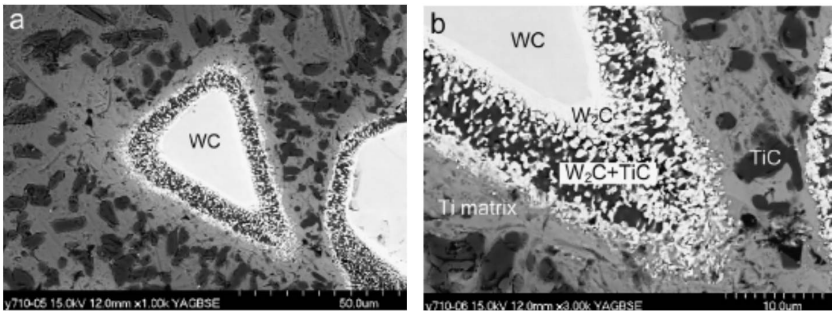

FIGURE 2.34: SEM/BSE images of WC/Ti-6Al-4V composite microstructure obtained from VAM showing intense dissolution of WC due to the absence of the TiC layer [80].

However, the microstructure of the interfacial reaction obtained from VAM was different from that of LMI due to lower cooling rate during the process. Figure 2.34 shows that WC dissolution and interfacial reaction were reported to be intensive; TiC grains were fully grown to have a blocky morphology, no eutectic structure was formed in the matrix and a thick mixture layer of W_2C and TiC was formed around the WC particles. This occurred as a result of having a sustained active melt pool for longer time in VAM than in LMI [80].

In summary, the review of work in the area of laser processing of Ti alloy with carbides showed that the resultant microstructure is dependent on the type of laser used. Phases commonly reported as reaction products after laser processing of Ti alloy with WC are TiC, W and W_2C. These in-situ synthesized products significantly improve the matrix properties. However, the Ti matrix microstructure is either reported as α-Ti [75, 77, 78] or α+β-Ti [76], which may be attributed to the degree of WC dissolution in the Ti melt. **Folkes** and Shibata [75] reports that laser processing of Ti-6Al-4V with Cr_3C_2 using a CO_2 laser results in a β-Ti matrix microstructure, however with WC, α-Ti microstructure is obtained. This α-Ti microstructure is observed to be common to all Ti alloys with WC composite layers processed with a CO_2 laser [77, 78]. Though both W and Cr are beta stabilisers of Ti, the difference in the resulting microstructures can be attributed to the difference in the laser absorptivity of these two carbides. The carbides of Cr possess a higher laser absorption coefficient than that of W, when irradiated by a CO_2 laser (wavelength, 10.6 μm) [81]. This allows higher dissolution of Cr_3C_2 in the Ti melt during processing than with WC. Thus with a higher amount of dissolution, the Ti melt has the tendency to be beta stabilised. It is expected that the laser absorptivity of WC on irradiation with a Nd:YAG laser (wavelength, 1.06 μm) becomes higher. It would be noted that the energy of photons generated in the Nd:YAG laser with wavelength of 1.06 μm is greater than the energy of the photons generated in the CO_2 laser. Thus, the absorption behaviour of the WC when exposed to lower wavelength laser beam can possibly be attributed to the higher energy of the laser photons. With this higher laser absorptivity, WC dissolution increases with higher tendency to stabilise Ti matrix as a beta phase. However, the Ti matrix in a laser melt injection, LMI process remains as α+β-Ti phase when processed with a Nd:YAG laser [76]. In this LMI process, the laser beam-WC particle interaction is intended to be minimised, which reduced the WC dissolution that is capable of full stabilisation of the Ti matrix as a beta phase. Additionally, in another similar process with a CO_2 laser used, a α-Ti matrix microstructure is obtained [78]. It has been noted that a beta stabilised Ti matrix is preferred for any Ti metal matrix composite (MMC), as β-Ti matrix is more ductile than α-Ti [70, 75, 82]. Hence, this current study will examine the dissolution of WC in the Ti melt when processed with a Ytterbium-doped fibre laser (wavelength, 1.07 μm), the concentration of W retained in the Ti melt on solidification and the overall microstructural evolution of the composite formed on cooling. All these are yet to be investigated and are considered important in determining the overall properties

of the composite formed. Moreover, in wear, a higher volume fraction of particulate reinforcement with smaller particle size results in a higher erosion/abrasion resistance [74, 83]. This indicates that WC dissolution in the Ti matrix to reduce the reinforcement size range is beneficial for wear applications of the composite layer.

2.5.2 Laser processing of Ti alloy with borides

Various research work has been conducted on the production of Ti alloys with TiB/TiB_2 reinforcement for surface modification purposes via laser processes. A study of the microstructural evolution of laser clad TiB-Ti composite on Ti-6Al-4V substrate was conducted with three microstructure morphologies identified [84]. A 2-kW Nd:YAG laser was used with a defocused laser beam to get a 2.5 mm spot diameter. The laser power and traverse speed used for the deposition process were 1200 W and 500 mm/min respectively. The Ti powder of particle size range 40-90 μm and TiB_2 powder (10-40 μm particle size) were used, these powders were delivered into the melt pool with 65 vol.% Ti/ 35 vol.% TiB_2 composition using a powder feeder and a cyclone. The deposit microstructure revealed fine needles, plates and coarse needles of TiB precipitates following the deposition as seen in Figure 2.35. The fine TiB needles were observed to possess an aspect ratio of 75, while the TiB plates have an aspect ratio which lies between 3 and 15, and the coarse TiB needles have aspect ratio of 17. It was reported that the TiB whiskers and coarse plates have cores filled with Ti atoms. The Ti atoms filling the TiB cores allows for a good blend of hardness, fracture toughness and wear resistance of the plates themselves [84].

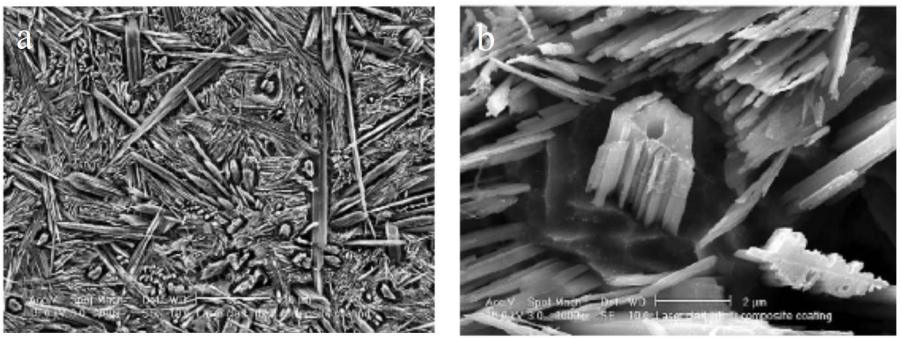

FIGURE 2.35: (a)Microstructure showing TiB fine needles, plates and coarse needles;(b)a TiB coarse needle showing an inner core filled with Ti [84].

In another study, a TiB/Ti-6Al-4V MMC layer was formed on a Ti-6Al-4V substrate by laser cladding of pre-blended TiB_2/Ti powder using a Nd:YAG laser [85]. It was reported that the dissolution of TiB_2 particles can be regarded as a reactive decomposition process. This was observed when high laser power and slower scanning speeds are used in the experiment. Figure 2.36 shows two different microstructures that could be obtained by variation of laser power and scanning speed. Figure 2.36(a) shows the distribution of the primary TiB plates formed through the decomposition of the melted TiB_2 particles achieved by slower cooling due to preheating. The sample is deposited with a laser power of 1000 W, 200 mm/min traverse speed, and a preheating temperature of 300^{o}C. A dendritic microstructure was reported for samples deposited with the same processing variable without preheating. Figure 2.36(b) shows eutectic microstructure with TiB particles distributed in the Ti matrix. The sample is deposited with higher laser power of 1400 W, and same traverse speed of 200 mm/min. This indicates that the TiB/Ti microstructure is sensitive to laser processing conditions as expected.

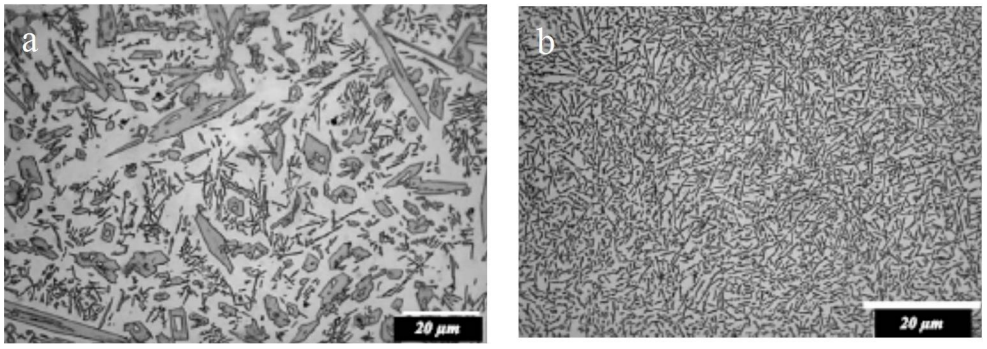

FIGURE 2.36: Optical micrographic view of TiB in Ti alloy matrix (a)primary TiB plates;(b)eutectic TiB particles [72, 85].

The hardness and Young modulus values for TiB needles observed in the microstructure were measured using a nanoindentation technique and reported as 30.7±1.1 GPa and 519±30 GPa respectively. The microhardness of the Ti matrix with the fine, eutectic TiB precipitates was reported as 7.5 GPa (765 HV) for a TiB volume fraction of about 30%. (NB Hardness of Ti-6Al-4V = 1.2 GPa).

The wear performance of the Ti MMC coating was related to the microstructures formed due to the variation of the laser processing variables. An excellent wear performance was observed for the two different types of microstructure with the TiB eutectics having the lowest material loss as illustrated in Figure 2.37. The Ti MMC was reported to

have a relative wear resistance of about 1500 when compared to Ti-6Al-4V substrate, indicative of an outstanding wear performance [85].

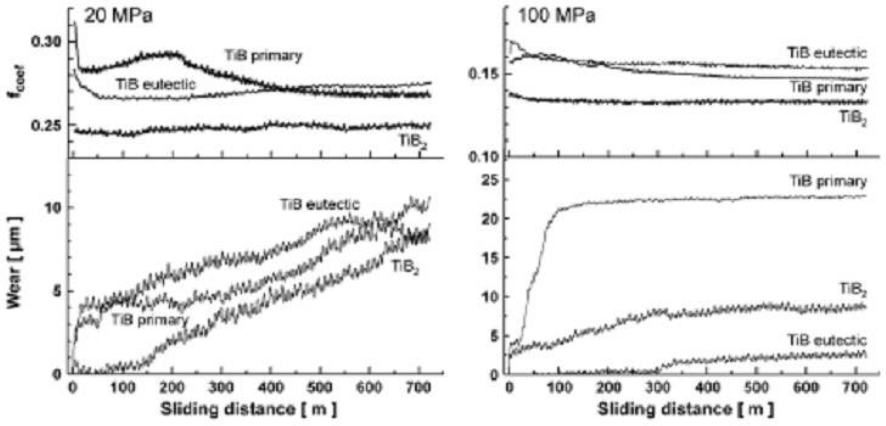

FIGURE 2.37: Sliding wear performance of TiB/TiB_2/Ti-6Al-4V MMC coating with different microstructure [72].

Having considered powder metallurgy routes for production of Ti alloy reinforced with TiB whiskers as time consuming and economically unattractive, a laser engineered net shaping (LENS) process was used to deposit pre-alloyed Ti-6Al-4V and elemental boron powders on a Ti-6Al-4V substrate [13]. The observation of the microstructure showed that TiB precipitates with an acicular (needle-like) morphology were uniformly dispersed in the α/β duplex structure of the Ti matrix. The bright contrast is the α-Ti phase, while the grey constrast is the β-Ti phase. The length of the TiB precipitates ranges from 1-5 μm.

Figure 2.38 shows the microstructures of the as deposited Ti MMC and heat treated specimens. It was reported that coarsening of the TiB precipitates was limited due to low solubility of boron in α/β which indicates that, the composite is thermodynamically stable at elevated temperatures. A comparison with LENS deposited Ti-6Al-4V showed that the microstructure of the Ti-6Al-4V is refined by the presence of boron, which resulted in large α-Ti precipitates instead of Widmanstatten lath-like structure of α-β Ti alloy [13]. In another development, LENS process was also used for the deposition of pre-blended Ti/B powder into a laser generated melt pool on Ti-6Al-4V substrate by Nd:YAG laser to produce nanoscale TiB precipitates in a Ti MMC [86]. Acicular (needle-like) TiB precipitates with length and width ranges of 0.5-5 μm and 30-50 nm respectively, were observed in the microstructure [86]. The nanoscaled TiB precipitates

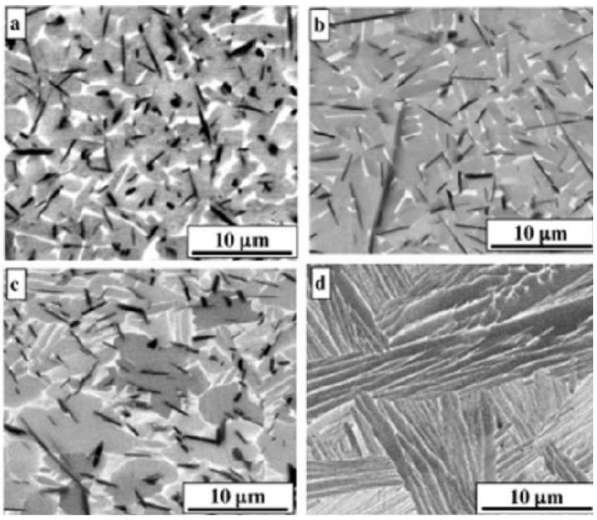

FIGURE 2.38: BSE images of (a)LENS deposited Ti-6Al-4V-TiB composite;(b)Heat treated specimen at 700^{o}C;(c)Heat treated specimen at 1100^{o}C;(d)SEM image of LENS deposited Ti-6Al-4V alloy [13].

were uniformly distributed in the α-Ti solid solution (ss) as observed in a bright field TEM image (Figure 2.39).

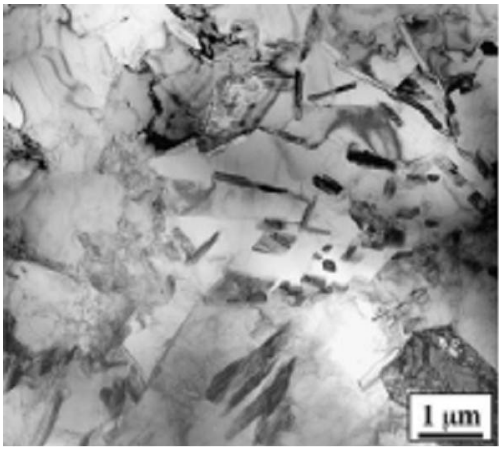

FIGURE 2.39: A bright field TEM image of nanoscaled TiB needles in α-Ti matrix [86].

It was reported that rapid solidification rates (100-1000 K/s) inherent in laser processes are responsible for the fine scale of TiB produced and dispersed in the matrix. It was also stressed that there may be a possibility of having a supersaturation of B in α-Ti, and upon secondary reheating, well refined nanoscaled TiB precipitates are formed in the matrix.

In an attempt to enhance the surface hardness of a Ti/TiB MMC produced via reaction sintering of Ti-Fe-Mo-TiB_2 powder, laser surface hardening was conducted which caused a considerable increase in the surface volume fraction of TiB whiskers using a CO_2 laser system [73]. Figure 2.40 shows that as input laser energy increases the visual observation of microstructure shows increase in TiB whiskers with a corresponding increase in hardness from around 513 HV for untreated Ti MMC to a value of 1055 HV with a TiB volume fraction of ∼67%. Furthermore, the hardness of the untreated Ti MMC was reported to be around 513 HV, however, laser hardening treatment enhanced the hardness, as shown in Figure 2.40.

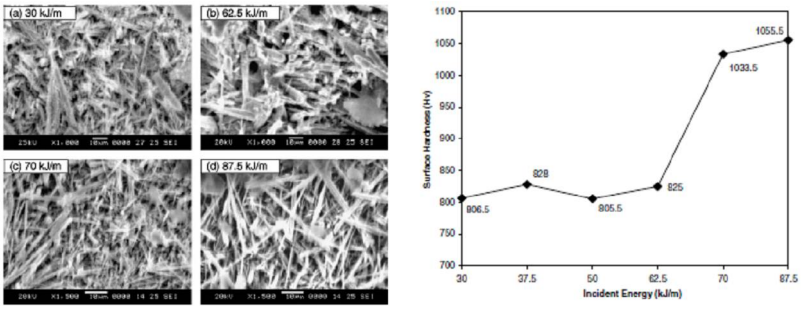

FIGURE 2.40: Increasing surface volume of TiB whiskers as laser energy input increases with increase in corresponding hardness [73].

In attempt to understand the effect of varying processing speed on microstructure and properties, long rod-like TiB precipitates were formed and dispersed in a grey dendritic Ti matrix [87]. This was developed by laser scanning of a preplaced powder mixture of Ti and B on a Ti-6Al-4V substrate using a CO_2 laser. Figure 2.41 shows the TiB precipitates formed as speed changes, which implied that in the study, increasing scanning speed favours the emergence of TiB precipitates. The TiB whiskers were reported to have been formed by accelerated nucleation due to rapid cooling. However, highest hardness and lowest material wear loss was reported for coatings produced using lowest scanning speed [87].

A surface coating of TiB dispersed in a Ti matrix was developed by laser cladding of Ti/2 wt.% B alloy powders (50-100 μm) using a diode laser on a Ti-6Al-4V substrate [88]. Primary, elongated rod-like TiB precipitates were observed in the microstructure with coarsening when higher laser power was applied, as shown in Figure 2.42. With a TiB volume fraction of about 10%, mean hardness of the Ti matrix was reported to lie

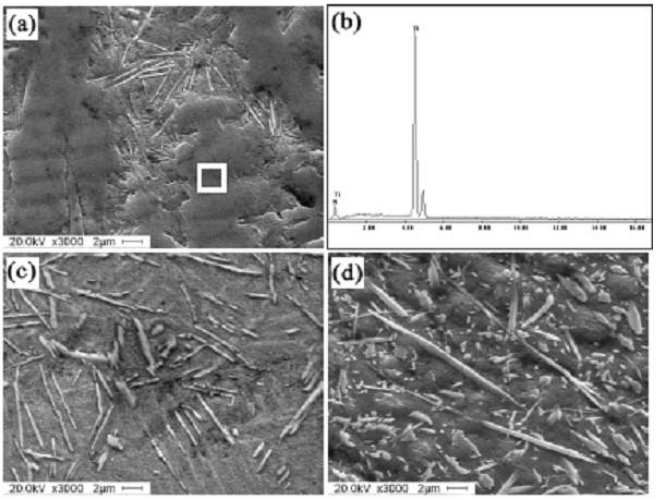

FIGURE 2.41: Micrographs of TiB/Ti coating formed with a traverse speed(a)2 mm/s;(b)Ti matrix EDS result;(c)5 mm/s;(d)8 mm/s [87].

between 290-500 HV measured via the nanoindentation technique, Youngs modulus of the composite were reported to vary between 159-165 GPa.

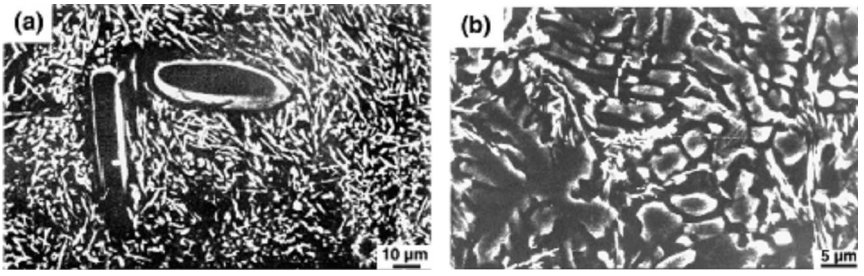

FIGURE 2.42: (a)Primary elongated TiB precipitates in Ti matrix;(b)Coarsened TiB due to applied higher laser power [88].

In a recent study, laser cladding of a preplaced mixture of powders Ti(90 wt%), B_4C(6 wt%) and Al(4 wt%) with 4% polyvinyl alcohol on Ti-6Al-4V substrate was conducted using a CO_2 gas laser. It was aimed to have Ti MMC with a dual reinforcement from in-situ TiB and TiC. Figure 2.43 shows the microstructure observed, where coarse primary cellular dendrites were identified as solid solution of α-Ti, needle shaped whiskers as TiB precipitates, and equiaxed particles as TiC precipitates [103]. A dry, pin-on-disc, sliding wear was conducted as well, and friction coefficient value range of 0.073-0.117 and 0.123-0.437 were observed for the coating and Ti-6Al-4V respectively [89]. This showed an excellent wear performance of the coating with respect to Ti-6Al-4V substrate.

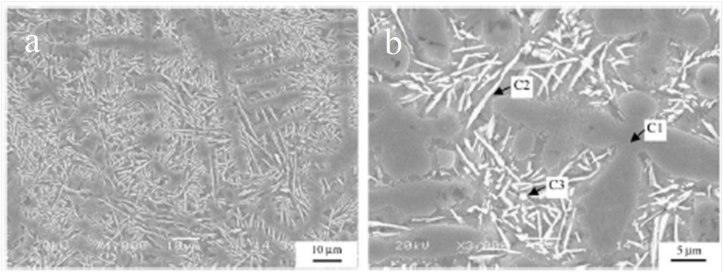

FIGURE 2.43: SEM images of microstructure with the identification of C1:coarse cellular Ti dendrite; C2:needle shaped TiB whisker; and C3:equiaxed TiC precipitates [89].

In summary, the review of work on laser processing of Ti alloys with elemental boron or boride compounds shows that the resultant microstructure is dependent laser processing variables (laser power, traverse speed, powder feed rate amongst others). The most widely reported reaction product from the laser processing is TiB. This reaction product, TiB is the most preferred phase amongst other phases such as TiB_2 and Ti_3B_4, owing to the thermodynamic stability of its microstructure at high temperature [13, 90, 91]. Though TiB is the most desirable, deposit microstructure characterised by TiB, TiB_2 and Ti_3B_4 phases have also been reported [85], which could have resulted from having a high fraction of the boride compound and favourable cooling conditions. Different types of deposit microstructure have been reported such as eutectic TiB, primary TiB plates, and TiB coarsening and dendritic structure with TiB interdendrites [84, 85, 87–89]. Though laser processing is a technique that may produce a non-equilibrium microstructure, some of the studies on deposit microstructure seemed not to match the information that can be obtained from the Ti-B phase diagram. Having a boron concentration less than the eutectic concentration (2.1 wt.% - Figure 2.26) would not have produced a eutectic TiB dominated microstructure with primary TiB plates under the equilibrium condition as reported by [88]. Also, the authors have not considered the influence of substrate dissolution with the melt pool composition on the resulting microstructure on cooling. Moreover, owing to the difference in the boride and the Ti alloy particle sizes, different researchers have employed preplaced deposition of the pre-blended material before laser scanning (two-stage process) [89]. Others have used two powder feeders connected to a cyclone to deliver the powders into the melt pool under low pressure of the carrier gas [84, 85]. However, for commercial deposition purposes, where higher deposition rate is desirable at low manufacturing cost, preplaced deposition and perhaps the use of two powder feeders and cyclone may not be appropriate. Hence,

a new method of delivering a feedstock of multiple compositions into the melt pool, which is commercially viable, needs to be developed.

2.6 Erosive wear testing

The section discusses the theory and mechanics of liquid and solid impacts on solid surfaces with the associated modes of failures. Previous studies on the resistance of composite materials to erosion wear when subjected to plain water and abrasive water jets are as well reviewed. The understanding of this study is essential for the discussion of the erosion performance of the Ti-6Al-4V/Spherotene composites detailed in chapter 6.

2.6.1 Theory and mechanics of liquid impact

Historically, the cavitation damage due to liquid impact on steam turbines motivated researches into the aspect of liquid impact erosion of solid materials [92]. When water is highly pressurised and discharged through a small orifice, a high velocity jet is produced such that if the compressibility of the water and other forms of energy losses are neglected, the pressure head is proportional to the square of the jet velocity as presented by Bernoullis equation (2.4) [83, 93].

$$P_h = \frac{1}{2}\rho_o v_o^2 \tag{2.4}$$

Where, P_h = pressure head, (Pa), ρ_o = density of water (998 kg.m^{-3}) at normal temperature and pressure and v_o = jet velocity at orifice exit.

Leu et al. [94] explained that as the jet exits the orifice with a high velocity, discretisation of the continuous jet into droplet occurs due the aerodynamic interaction of the jet with the surrounding air. The flowing jet is classified into three regions namely: initial, main and final region. The main region of the jet is most effective for material removal, characterised by concentrated packets of accelerated water droplets. Moreover, the atomisation of the water jet into droplet would occur at a critical standoff distance (SODc) of 175 times the orifice exit diameter of the jet approximately [93]. Field [92]

reported that as the water droplets collide with a solid target, they behave in a compressible manner, thus generating a high pressure, generally regarded as water-hammer pressure. This hammer pressure is responsible for most of the damages observed as a result of liquid impact on surfaces. Figure 2.44 shows the initial stage of water droplet impact on a solid target. The high pressure impact, which can be evaluated using equation (2.5), causes the contact area between the impacting droplet and the solid to expand supersonically.

$$P_w = c_s \rho_o v_o \tag{2.5}$$

$$c_s = c_o + k v_o \tag{2.6}$$

Where, P_w = water hammer pressure, (Pa), and c_s = shock velocity in the water droplet, which can be determined by equation (2.6), c_o = the acoustic velocity in water at normal temperature and pressure (1480 $m.s^{-1}$) and k is a constant with a value of 2 for water jet in a velocity range up to 1000 $m.s^{-1}$ [92]..

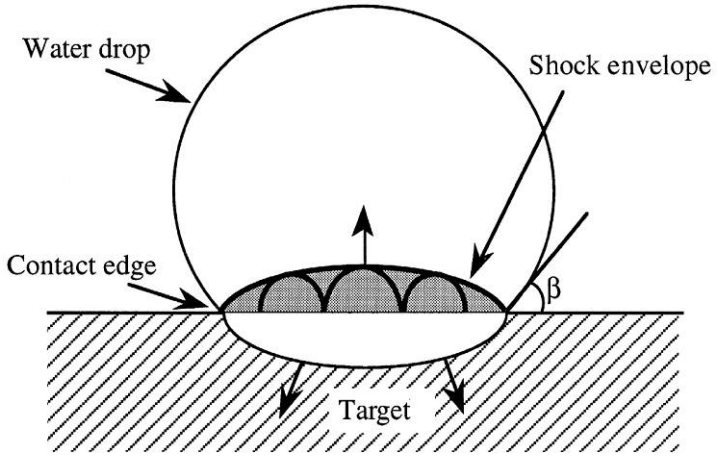

FIGURE 2.44: Initial stage of the impact between a water drop and a solid target with the contact edge moving faster than the shock velocity in the liquid and liquid behind the shock envelope and target are subjected to high pressure [92].

2.6.1.1 Modes of Failure of solid materials under water droplet impacts

Adler [95] reviewed the mode of failure in solids when subjected to water droplets and reported that four primary failure modes may be responsible for damage initiation and subsequent material removal. These modes are:

- Direct deformation

- Stress wave propagation
- Lateral outflow jetting
- Hydraulic penetration

It was noted that the mechanical response of material determines which of the loading conditions of failure modes would predominate the material erosion. Brittle materials are reported to have an elastic-brittle response, and non-brittle materials response in a plastic manner of ductile material.

It is reported that the action of water droplet impacting a brittle material would result in the development of cracks provided the droplet impact exceeds the fracture threshold of the material. The fracture would occur as a result of high tensile stresses which had developed in the neighbourhood of the liquid/solid impact region owing to the stress wave propagation. Thus, direct deformation mode may not be accountable for fracture in brittle materials. The stress wave interaction with micro-surface cracks, asperities and other microstructural features which act as stress raisers would result in fracture initiation and propagation in materials [95]. It is further discussed that locally damaged regions can act as erosion pit nucleation sites and owing to lateral outflow jetting and hydraulic penetration, tunnelling process becomes inevitable. Moreover, in metals, the damage mechanism is due to plastic deformation, as the internal stress induced in the material exceeds its fracture strength.

2.6.1.2 Modes of Failure of solid materials under solid particle impacts

Abrasive particles are injected into the high velocity water jet stream to enhance the erosion of solid materials subjected to jet impacts. Ruff and Wiederhorn [96] reviewed the research works in the area of erosion by solid particle impact and reported that the impact of solid particles on ductile materials result in the formation of impact craters with an observation of the displaced crater material flowing in the direction of the particle incidence until the material fractured at high accumulated strains. It is further reported that the surface deformation experienced by impact of solid particle on ductile materials is dependent on the particle shape morphology, as spherical particles could result a ploughing deformation, while angular abrasive particles could result in cutting

deformation. Karelin et al. [97] gave illustrations in Figure 2.45 to explain the mechanism of material damage and removal.

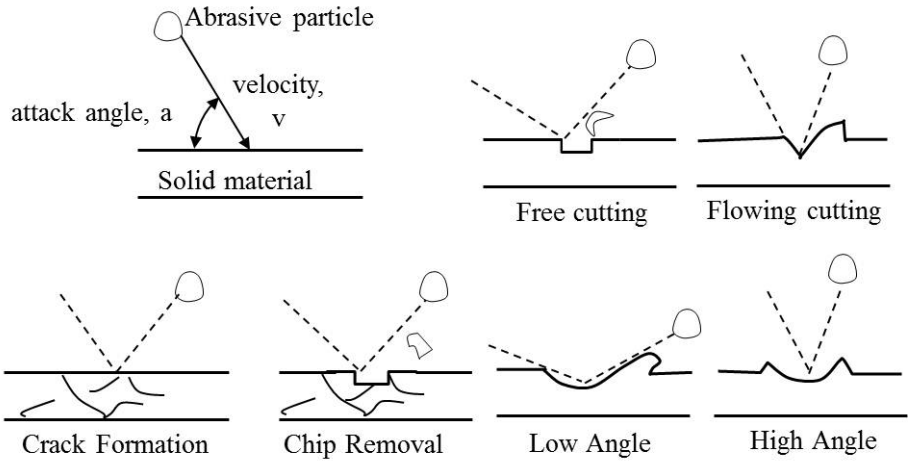

FIGURE 2.45: Mechanism of material removal by solid particle impact [97].

It is evident that erosion by solid particle impact on solid materials is dependent on particle shape and orientation at contact, particle velocity, attack angle,"a", particle material properties, concentration of abrasive particles in a liquid flow, and particle size distribution [96, 97].

In the case of solid particle impact on ceramics, material removal has been described to be a brittle process of chipping which is assumed to have resulted from a plastic deformation process. The fracture morphology in ceramic materials during solid particle impact is dependent on the particle shape morphology (spherical or angular). The impact of spherical particles on ceramics material results in the formation of cone-shaped cracks, also known as Hertzian cracks. These cracks are initiated from the pre-existing flaws which lie outside the area of contact between the particle and the ceramic surface and it is an elastic process. Hertzian cracks are known to form over a wide range of impact loads, and as contact force exceeds a threshold level which is dependent on the hardness of the ceramic material, plastic deformation occurs beneath the impacting particle. The plastic deformation results in the formation of the second set of cracks, also known as radial cracks, which are observed to be normal to the impacted surface. The impact of angular particles on ceramic surface results in the direct formation of radial cracks which would occur when the surface is impacted using high velocity spherical particles. The threshold particle velocity that determines the transition between the hertzian cracks and the

radial crack formation is reported to be dependent on the hardness, fracture toughness and surface structure of the target ceramic material. Angular particle impact results in formation of radial cracks perpendicular to the target surface, which is responsible for strength degradation and lateral cracks parallel to the surface, which is responsible for the erosive wear by chip formation [96]. Figure 2.46 shows the schematic illustration of the material removal by abrasive impact on ductile and brittle materials. The maximum erosion rate is observed at lower angles for ductile material while maximum erosion is observed at 90_o for brittle materials. However, Ruff and Wiederhorn [96] reported in their review that ceramic materials may also experience ductile-to-brittle transitions in their mode of erosion, and this is dependent on the particle size of the abrasives employed. Small abrasive particle size has the tendency to cause a ductile erosion mechanism of the ceramic target while larger size abrasive would result in a brittle fracture mechanism.

Thus, subsurface plastic deformation occurred at the impact site of solid particle/ceramics target, which result in residual stress which developed lateral crack formation and surface chipping.

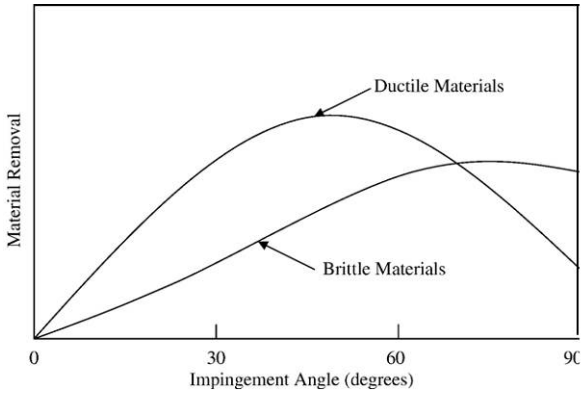

FIGURE 2.46: Schematic representation of material removal on impingement angles for ductile and brittle materials [96, 98].

Therefore, the combination of the effect of both liquid and solid particle impact on composite material can be derived from the integral contribution of impacts on ductile and ceramic materials.

2.6.2 Resistance of composite materials to solid and liquid impact erosion

Previous studies have revealed the potential of particle-reinforced composites as effective abrasion resistant materials. The degradation of material surface by fluids is classified into liquid droplet erosion and cavitation erosion. Both classifications are similar in terms of their erosion mechanism caused by shock associated with liquid jet impingement or collapsing bubbles. The liquid impact erosion is often experienced in steam turbine and aircraft, while cavitation erosion is often experienced in pumps and hydraulic turbines [83, 99]. However, Mann and Arya [99] reported that the damage experienced by materials under the action of liquid jet impact is close to reality, however, many investigations have been made on cavitation/droplet erosion of different materials subjected to water jet impact.

Yarrapareddy and Kovacevic [100] subjected nano-particles reinforced surface NiWC coatings to slurry erosion by exposing their surfaces to high velocity garnet abrasive-waterjet impacts. The Ni based coating was achieved via laser-based direct metal deposition. After erosion test, it is reported that having nano-sized WC particles to reinforce the composite matrix (Ni binder) apart from the micro-sized WC particles strongly improve the erosion resistance of the composite coating. Shipway and Gupta [83] studied the erosion behaviour of sintered and thermally sprayed WC-Co composite as well as Ti-6Al-4V as a control specimen subjected to plain water jet impacts. It was reported that the sintered materials exhibited an incubation period where damage was not experienced, while no incubation period was identified for the thermally sprayed composites and the titanium alloy. Sintered WC-Co with the smallest carbide particles and the highest carbide fraction exhibited the highest erosion resistance and it was concluded that during the incubation period, damage initiation and removal of the Co binder phase occurred which led to further hydraulic penetration and removal of the carbides. Pugsley and Allen [101] investigated the slurry erosion of ultrafine WC-Co sintered composite subjected to silica abrasive-waterjet impacts, and they observed an increased erosion resistance as WC grain size decreases with three times resistant performance when compared to the conventional material. It was also reported that there is a transition from brittle to ductile mode of erosion as grain size reduces and as the average distance between the embedded particles is reduced to retard the preferential erosion of the binder

phase. In a similar work, Wentzel and Allen [102] subjected cemented WC with different binder phases (Co, Ni and Cr) to erosion-corrosion testing by employing a silica-water slurry. Erosion rate was observed to decrease with increasing composite hardness and maximum erosion rate was observed at an impact angle of 75^o. The corrosion resistance of the composite are maintained and dependent on the corrosion behaviour of the binder phase employed. They further identified binder removal followed by subsequent WC grain detachment as the mechanism of erosion.

In another study, Lathabai and Pender [103] evaluated the erosion behaviour of alumina-based composite by subjecting it to silicon carbide abrasive-slurry jet, observed that material removal mechanism is dominated by chipping of lateral cracks caused by impact of erodent particles, grain boundary cracking, grain pull out and plastic deformation caused by repeated sliding and impact of the particles. In a recent study, Castberg et al. [104] investigated the dependence of Co-WC and CoNiCr-WC erosion performance on WC grain size, WC distribution and binder composition by subjecting the materials to silica abrasive water jet impacts. It was reported that 80% reduction in grain size reduced the erosion level to 30-50% in Co-WC composite at a jet angle of 90^o. Reduction of erosion rate was observed for the CoNiCr-WC composite due to the increased binder hardness. Erosion rate was found to reduce by 15-20% when jet angle was reduced from 90^o to 60^o, as a stronger hammering effect is expected at 90^o and it was concluded that lower carbide size and lower impingement velocity changed the erosion behaviour from brittle to a more ductile mode. In another development, Gant and Gee [105] studied the structure-property relationships of WC-Co based composite subjected to silica abrasive liquid jet erosion. The erosion volume loss for the composite was observed to have an inverse log-linear relationship with the composite hardness. Thus erosion decreases with increasing hardness. With abrasive jet at 45^o inclination to the composite surface, erosion behaviour was dominated by fracture, re-embedment of larger WC grains with planar facet, micro-cracking and slips in larger WC grains. Also, preferential binder denudation and subsequent WC pull-out is prominent. With jet at 90^o, greatest degree of fracture and wear is experienced by edge chipping, transgranular fracture, spalling of large grains, and attrition fracture. It was reported that the ductile erosion is dominated by plastic deformation and fracture of the binder and volume loss is proportional to the square root of the average distance between the embedded ceramic particles in the composite. Momber and Kovacevic [106] explained that failure of multiphase brittle

materials subjected to high energy water jet impacts is based on micro-crack growth owing to the applied hydrostatic pressure. It was reported that particle/matrix interfaces are the preferred locations for crack growth and the embedded particles in composite materials acts as crack arresters due to absorption of higher amount of the fracture energy. Thus, the enhanced erosion performance of composite materials is based on this fundamental principle when compared to the erosion of the base material subjected to the same condition of high energy liquid jet.

The extensive studies carried out by different authors on the erosion performance of mostly WC-Co and Ni based composites prepared either by sintering, plasma arc spraying or thermal spraying have demonstrated the benefits of composites for combating liquid impact erosion wear. The review of the works from these authors showed that erosion mechanism experienced by composite subjected to plain high velocity water jet impact ranged from damage initiation, preferential denudation of the binder, and subsequent removal of WC particles due to further hydraulic penetration [83]. Erosion mechanisms of composites subjected to high velocity abrasive water jet impact experienced a great deal of wear by edge chipping of ceramics, attrition fracture, ceramic pull-out, spalling and plastic deformation [102, 103, 105]. The reduction of erosion wear was found to be favoured by small WC grain size, reduced mean free path between embedded ceramics, reinforcement of the composite matrix by nano-sized particles and high hardness of the composite [100, 104, 105]. Furthermore, maximum erosion volume loss in composites was achieved by having the abrasive water jet impinging the composite surface at 90^o [104, 105]. However, laser based deposition processes are capable of producing hard-facing composites directly on engineering components. These clad composites have received limited attention by researchers in the area of their erosion performance characterisation under high energy jet impacts. More so, the characterisation of Ti-6Al-4V/Spherotene composite subjected to high energy PWJ and AWJ impacts is yet to be investigated.

In this study, Ti-6Al-4V/Spherotene composites prepared via laser cladding will be subjected to high velocity plain and abrasive waterjet impacts to determine their erosion wear performance with wrought Ti-6Al-4V as a control specimen. Previous studies have concentrated on the erosion performance of WC composite with Co and Ni as binder, however, the study is carried out to elucidate the potentials of Ti-6Al-4V/Spherotene

composites in combating liquid impact erosion wear. as it would be subjected to when cladded on pipes and collars to be used for mining and oil exploration purposes.

2.7 Summary of the literature

The literature review presented can be consolidated into the below key findings:

- A 60% of titanium production is made for Ti-6Al-4V. It is widely used for different industrial applications from aerospace, automotive, chemical, oil and gas exploration, petrochemical to marine applications amongst others.
- Ti-6Al-4V has a good specific strength, excellent corrosion resistance and is suitable for applications between room temperature and a maximum temperature range of 315-400^{o}C in the presence of air, but it is rarely used for application where wear of any kind is of great concern.
- Different approaches to laser surface engineering have been deployed to improve the surface properties of Ti-6Al-4V. Surface nitriding of the alloy by laser surface melting was found to improve its hardness, wear and erosion resistance properties. Carburisation of the alloy surface by laser surface alloying was observed to improve its surface properties.
- Laser surface alloying which involved refractory powder injection into the laser melt and is otherwise known as laser melt injection (LMI) process has been examined to improve the surface properties of Ti-6Al-4V. Several refractory carbide powders have been used as reinforcement in Ti-6Al-4V with more emphasis on the usage of tungsten carbide and titanium carbide.
- Tungsten carbide is a refractory, metallic carbide. It has an excellent chemical and thermal stability, high hardness, excellent oxidation resistance, low coefficient of thermal expansion, and good wettability. It exists in three phases, WC, WC_{1-x} and W_2C. WC is the most stable phase even at temperature as high as 3049 K before decarburisation of this phase can occur.
- Titanium carbide is also a refractory ceramic carbide which exhibits good resistance to high temperature oxidation, corrosion and wear. The carbide exists as TiC phase over a wide composition range.

- The laser processing of Ti-6Al-4V alloy with various carbides has been shown to yield a common reaction product TiC phase in the melt, as the melt is enriched by C due to surface melting of the carbide particles. The original carbide particles are as well retained in the melt. The retained particles become smaller in size due to surface melting and possess either rounded edges (as in the case of TiC particles) or a reaction layer (as in the case of WC particles). Two different types of reaction layer have been identified and they include: a TiC cellular reaction layer in which TiC layer is formed around the WC particles in the melt, and an irregular reaction layer in which the WC particles have a continuously dissolved edges with TiC formed in the creeks randomly around the particles.

- The injection of WC particles with uniform distribution in laser melt injection processing of Ti-6Al-4V has shown to significantly increase wear resistance when compared to monolithic Ti-6Al-4V. This was confirmed by results from a dry sand rubber wheel wear test and a sliding pin-on-disk wear test. Also, among different carbide particles used in a laser processing of Ti-6Al-4V alloy, WC particles reinforced clads retain high hardness (425 HV) at elevated temperature (600^oC).

- Titanium diboride, TiB_2, is another important refractory material which is used for surface improvement of Ti-6Al-4V. It has a high melting point (3225^oC), low specific weight, high hardness, high strength to density ratio, good wear resistance and excellent thermal and chemical stability.

- Ti-6Al-4V/TiB_2 composites have been found promising to improve the surface properties of Ti-6Al-4V for a diverse range of industrial applications (automotive, aerospace, nuclear, etc). The most preferred phase sought for is TiB phase which resulted from the TiB_2 reaction with the Ti melt. The TiB phase is preferred to be in the form of whiskers reinforcing the Ti matrix as they have good load bearing capacity due to their increased surface area for active reinforcement.

- Laser processing of Ti-6Al-4V with TiB_2 powder particles has been found to be favourable, as it rapidly promotes the formation and growth of TiB whiskers in the Ti melt which is the preferred microstructure. Thus, laser processing promotes TiB whisker formation due to the rapid solidification and cooling characteristics of the process, and also reduces steps involved in solid state reaction fabrication of Ti-6Al-4V/TiB_2 composite.

- The development of TiB whiskers in the Ti alloy matrix after laser processing of Ti-6Al-4V/TiB_2 powders enhances the hardness, elastic and wear properties when compared to Ti-6Al-4V. The variation of the laser processing parameters has revealed that TiB plates or eutectics are either or both formed. TiB eutectic enriched microstructure are said to have the most excellent wear performance.

2.7.1 Research opportunities from literature

Rapid solidification processes such as laser surface engineering of Ti-6Al-4V have been noted to significantly improve the alloy surface properties such as hardness, wear and corrosion resistance. Laser melt injection processing of Ti-6Al-4V with WC particles has been mostly examined, and has shown promising improvement of Ti-6Al-4V composite hardness and wear resistant properties. More so, the formation of TiB whisker to reinforce Ti alloy matrix using laser processing of Ti-6Al-4V/TiB_2 powders have been found promising for improved Ti alloy surface properties. However, the following research opportunities have been identified based on the knowledge gap in the reviewed literature:

- Research on laser cladding of Ti-6Al-4V with WC particles is limited, and laser melt injection processing of this alloy cannot be used to accomplish the regeneration of worn Ti-based engineering components. Thus, laser cladding which is one of the key laser surface engineering techniques needs to be explored for Ti-6Al-4V with WC particles. This would allow the regeneration of worn surfaces, component repair, 3-dimensional component building and functionally graded component fabrication.

- Titanium alloys are known to be costly, but possess excellent properties that make them desirable for various industrial applications (oil exploration, aerospace, automotive, chemical processing, etc). Thus, from the manufacturing point of view, the use of Ti-6Al-4V powder in laser processing with WC powder particles is disadvantageous. Hence, the use of Ti-6Al-4V wire instead will be more economical as utilisation of the costly material feedstock would approach 100%. The laser cladding of Ti-6Al-4V alloy wire with WC particles is yet to be investigated.

- In the microstructural evolution of the laser melt injection processing of Ti-6Al-4V alloy and WC particles, the Ti melt is reported to be enriched with W and C atoms as surface melting of the particles occur resulting in the formation of W and TiC as reaction layer product. The influence of the laser processing parameters on the thickness of reaction layer have been reported, but the influence of laser processing on WC dissolution and how this influence the resulting microstructure is yet to be investigated. This is important as it determines the stabilization of the Ti melt as either α- or β-phase and hence the overall properties of the clad layer.

- Improved hardness and sliding/dry sand abrasion wear resistance of the Ti-6Al-4V/WC composite layer have been reported. However, with the use of Ti-6Al-4V in oil and gas exploration, petrochemical and chemical processing, where erosion/abrasion wear damage is prominent, it would be preferred to study the erosive wear performance of Ti-6Al-4V/WC composite. This is yet to be explored. This performance evaluation is essential as it provides information on resistance of the composite to fluidic media accelerated against its surface and the influence of the embedded WC particles and phases formed in the composite matrix on resistance may be identified.

- The promising nature of laser processing for the formation of TiB whiskers in laser Ti-6Al-4V/TiB_2 composites has been highlighted. It has been observed that the TiB_2 powder material is mostly supplied in micron sizes that make the powder unsuitable as feedstock in laser processing. Additional steps for feeding the stock have been reported such as the use of cyclone before feeding into melt pool or the feedstock used in a preplaced form. Thus, there is need for modification of Ti-6Al-4V/TiB_2 feedstock to eliminate additional steps and also to enhance uniformity in the TiB whisker distribution in the composite. This makes the delivering of the feedstock of multiple compositions to be commercially viable.

- Limited results have been reported on the improved hardness and elastic properties of bulk Ti-6Al-4V/TiB_2/TiB composite produced via laser processing. Those reported were obtained using a nanoindentation technique, but the influence of laser processing parameters on the hardness and elastic properties of the bulk laser clad composite are yet to be reported. These can be compared to values obtained from Ti-6Al-4V/TiB composite produced via solid state reaction processes to display the versatility of laser processing to the composite production.

2.8 Research hypotheses

Having explored the laser processing of Ti-6Al-4V with WC and TiB_2, the following research hypotheses are proposed:

- The use of Ti-6Al-4V in the form of wire and the WC as powder to produce clads may be better than using a pre-blended powder of these materials in laser processing.
- The use of a modified pre-blended feedstock of Ti-6Al-4V and TiB_2 powders which can be coaxially or laterally fed into the melt pool may be better than using a preplaced deposition of pre-mixed powders .

2.9 Research objectives

Having identified the various research opportunities in the literature on laser processing of Ti-6Al-4V alloy with WC and TiB_2 powder particles, the objectives of this research work are set out to address the gaps. Firstly, the research work will focus on laser cladding of Ti-6Al-4V in wire form with Spherotene (WC/W_2C) particles on a Ti-6Al-4V alloy substrate and secondly on the laser cladding of modified Ti-6Al-4V/TiB_2 powder feedstock on a Ti-6Al-4V substrate as well to achieve dense composite deposits which are crack and pore free and well bonded to the substrate. Thus, the following objectives set for this research work are:

- To deposit Ti-6Al-4V wire with Spherotene (WC/W_2C) powder on a Ti-6Al-4V substrate, identify suitable processing parameter ranges and determine the influence of laser processing parameters on the physical characteristics (width and height) of beads and the efficiency of Spherotene deposition (Chapter 4).
- To study the microstructural features of composite beads and determine the influence Spherotene particle dissolution on the composite microstructure formed. Also to characterise the overlap cladding of Ti-6Al-4V/Spherotene composite beads in terms of microstructure and microhardness, and also to demonstrate the suitability of the wire-powder process for the development of 3-D functionally graded structures (Chapter 4).

- To prepare a suitable powder feedstock for one stage laser cladding process by agglomeration of Ti-6Al-4V and TiB_2 powders (Chapter 5).

- To study the microstructural evolution of the Ti-6Al-4V/TiB_2 composite bead produce, assess the formation of ceramic phases with respect to changes in laser processing parameters, substrate dilution and influence on composite microhardness. Also to identify the microstructural changes in multilayer deposition of the Ti-6Al-4V/TiB_2 feedstock and influence on multilayer microhardness (Chapter 5).

- In the case of Ti-6Al-4V/Spherotene, to study the erosion wear performance of the composite clad with different reinforcement fraction when subjected to both plain water jet and abrasive water jet erosion. Also, in the case of Ti-6Al-4V/TiB_2 3-D composite multilayers to investigate their tensile properties at room temperature.

Chapter 3

Experimental Procedures

This chapter describes the experimental arrangement used for the laser cladding and the characterisation techniques used for the feedstock materials and deposits obtained from cladding. It contains particle size analysis of feedstock powders used and their microstructural characterisation, fibre laser deposition setup, bead characteristics measurements, sample preparation for microstructural examination and description of scanning electron microscopy (SEM), energy dispersive X-ray spectroscopy (EDX) and X-ray Diffraction (XRD) techniques used for both powder and deposit characterisation. Procedures for microhardness test, erosion test and tensile test are also reported.

3.1 Materials

The materials involved in this study are 1.2 mm diameter, Ti-6Al-4V wire supplied by VBC Group (Loughborough, UK), Spherotene powder produced by Technogenia Company (France) and supplied by Laser Cladding Technology Limited, Sheffield, UK, Ti-6Al-4V powder supplied by Crucible Research, USA, TiB_2 powder supplied by Sigma Aldrich Chemical Company, UK and rectangular Ti-6Al-4V coupons with dimensions 180 mm x 100 mm x 5 mm. Microstructural and particle size analyses were further conducted on the as-received powders.

3.1.1 Microstructure and Phase analysis

The powders to be employed in this study need to be characterised to identify phases present in the feedstock. Moreover, the Spherotene powder was known to consist of carbides of tungsten, thus it was important to carry out microstructural examination and phase analysis to identify which of the carbide phases are present in the powder. SEM analysis was conducted on the powder samples both in secondary electron (SE) and back scattered electron (BSE) mode to observe the surface morphology of the powder particles. XRD analysis was employed to obtain the phase composition of the powders.

3.1.2 Particle size analysis

The Spherotene powder was supplied with a particle size range between 40-160 μm as stated by the manufacturer, Ti-6Al-4V powder size was quoted as -100+325 mesh by the supplier and TiB_2 powder was said to be <10 μm by the supplier. A Mastersizer S particle size analyser (Malvern Instruments Limited, UK) was employed to determine the powder particle size distribution.

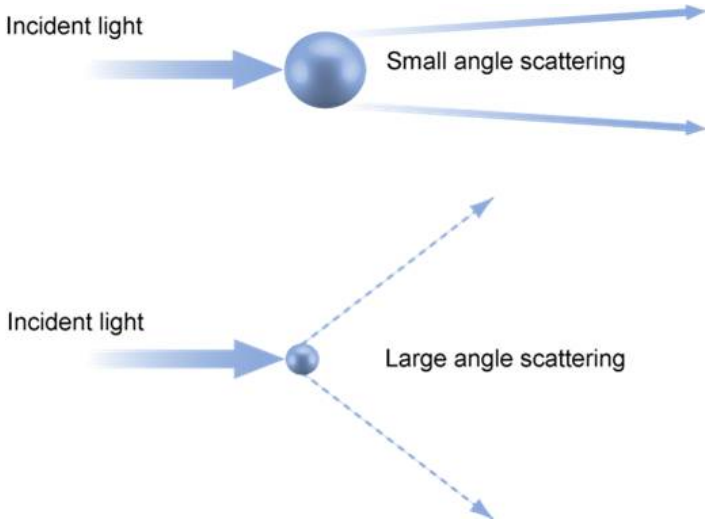

FIGURE 3.1: Particle size measurements by laser light diffraction [107].

The machine works on the principle of laser diffraction to measure the sizes of the particles. As laser light strikes the powder particles suspended in a dispersant, their particle sizes are measured by the angular variation of the scattered laser beam intensity (Figure 3.1). Distilled water was used as the dispersant and the powder was added to the

circulating water under a continuous agitation to maintain a uniform dispersion of the particles in the medium. An obscuration level of the mixture to laser beam exposure was maintained between 20-22 % before the analysis of the particle distribution was made. A monomodal analysis mode with a Standard-Wet presentation was selected since it was expected to be a good model for the size distribution present in the powder based on the information from the supplier. The volume mean diameter of the powder was observed to be ∼138 μm, 108 μm and 10 μm for Spherotene, Ti-6Al-4V and TiB_2 powders respectively.

3.2 Fibre laser deposition setup

Cladding experiments were conducted using a 2-kW, Ytterbium-doped, continuous wave (CW), fibre laser (IPG Photonics). The laser machine operates at a wavelength of 1070 nm, with a beam-optics delivery system (125 mm collimating lens and a 200 mm focusing lens) and a coupled Precitec YC 50 cladding head. The delivered laser beam has a Gaussian profile with a spot circular diameter of ∼1 mm at focus when a 600 μm diameter beam delivery fibre is employed to convey the laser beam to the cladding head. It is commonplace to operate the laser system out of focus, which provides a wider circular spot to accommodate the materials to be fed into the melt pool generated by the laser beam on the substrate. At a defocus distance of 20 mm, a 3.1 mm circular, spot diameter was obtained as measured by PRIMES Focus Monitor. Figure 3.2 shows typical beam profiles and intensities at focus and at 20 mm out-of-focus for the maximum laser power. Appendix A.1 gives information about the calibration of the 2-kW fibre laser which was carried out by Dr. W.J. Suder from Welding Engineering and Laser Processing Centre, Cranfield University, United Kingdom.

For all the cladding experiments, the beam was defocused to give 3.1 mm diameter spot. The laser system was mounted on a 4-axis CNC table to achieve a relative motion of the work-piece with respect to the stationary laser beam. The laser head arrangement is mounted on the z-axis and kept stationary while a traverse movement of the substrate was achieved in the x and y-axes directions.

The Ti-6Al-4V wire was delivered through a side-fed guide nozzle and the Spherotene powder was simultaneously delivered through another side-fed nozzle into the melt pool.

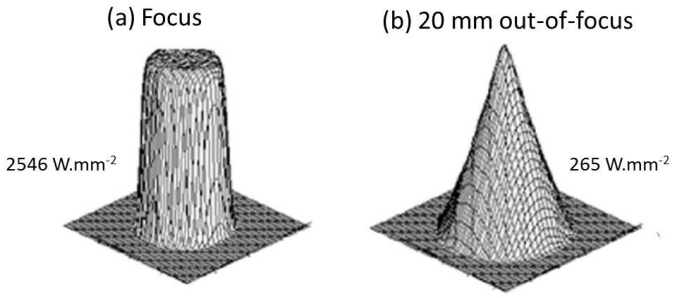

FIGURE 3.2: Typical laser beam profiles and intensities at (a)focus; (b)20 mm out-of-focus [28].

Moreover, the same setup configuration without the guide nozzle for wire delivery was employed for the laser cladding of the pre-blended TiB_2/Ti-6Al-4V powder. Figure 3.3 shows a typical setup of the side fed deposition experiments. The wire was fed into the leading edge of the laser-generated melt pool using a standard wire feeder mechanism (Redman Controls and Electronic Limited, England). The wire feeder has a knob and a digital display for the wire delivery rate control. The wire feeder was calibrated by taking series of measurements of wire length delivered within a certain period of time. A rear feeding nozzle with an exit circular diameter of ∼4 mm was used to deliver the powder during the experiments for the hybrid deposition of Ti-6Al-4V wire and Spherotene powder to generate Ti metal matrix composite (Ti MMC). The powder delivery was achieved by using a Model 1264 powder feeder (Praxair Surface Technologies) which has a powder chamber that was pressurised by argon, Ar, as a carrier gas. The powder feeder was calibrated for different powder feed rates according to changes in the revolutions per minutes (rpm) of the motor speed that spins an edge-perforated disk in the feeder while the powder chamber is pressurised with a constant gas flow rate of 10 L/min. The powder calibration was undertaken by weighing series of powder delivered within a certain period of time.

Prior to deposition experiments, the Ti-6Al-4V substrates were grit-blasted in a Guyson grit blast system using alumina garnet powder to improve laser absorptivity of the plate surface. The surfaces to be exposed to the laser were also degreased using acetone ($(CH_3)_2CO$) to eliminate surface contaminants. The rectangular substrate coupon is then mounted on the work table of the CNC system. In order to avoid atmospheric contamination and also for safety reasons, the deposition work area is isolated from the

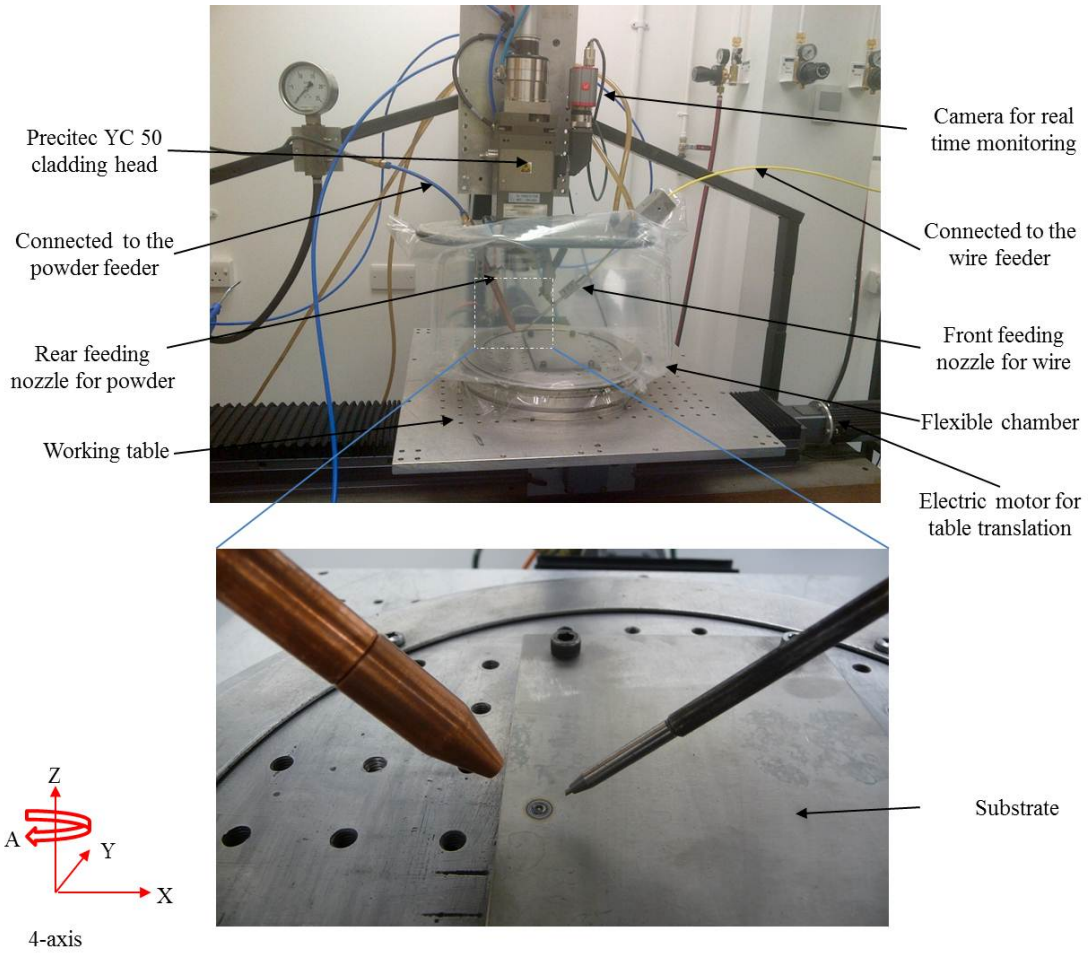

FIGURE 3.3: Side-fed hybrid materials-laser deposition experimental setup.

laboratory room using a flexible plastic chamber. The chamber is purged with an Ar gas at a constant gas flow rate of 30 L/min for about 10 minutes to create an inert isolated environment prior to the deposition to prevent deposit oxidation. The shielding gas was left to purge the chamber continuously throughout the deposition period. The cladding of the pre-blended TiB_2/Ti-6Al-4V powder was carried out using the rear- fed nozzle to deliver the powder into the laser generated melt pool without using the Ti-6Al-4V wire feed stock.

3.2.1 Laser cladding of Ti-6Al-4V wire

The laser cladding experiment of Ti-6Al-4V wire only was carried out using the setup as described in Section 3.2 with only wire delivered into the melt pool. In this experiment, the inter-relationship of the three major processing parameters is examined for the wire

deposition. The processing parameters include; laser power, traverse speed and wire feed rate. The experiment was conducted to determine the following:

- The range of processing parameters required to achieve consistent and stable deposition of the wire. Consistency and stability would be assessed by visual examination of deposition process and beads after deposition. This gives information on the range of each of the process parameters that could interact to give a suitable deposit with no defects such as waviness and dropleting.
- The influence of the processing parameters on bead characteristics and to obtain the optimised processing conditions required to achieve maximum bead height and width. These were investigated by measurements and statistical analysis. Results would help to evaluate the processing time required for either surface coating (maximum bead width) or additive manufacture of structures (maximum bead height).

Moreover, this experiment would give an insight to the processing parameters suitable for the hybrid deposition of both Ti-6Al-4V wire and Spherotene powder to be discussed in Section 3.2.2. After trial depositions, the following ranges of process parameters were selected for the optimisation of the wire deposition process:

- Laser power: 1400 - 1800 W
- Traverse speed: 200 - 400 mm/min
- Wire feed rate: 700 - 800 mm/min

The length of each bead was 80 mm with a pitch of 10 mm from the centre of one bead to another. A steady deposition state was reached after the Ti-6Al-4V substrate has traverse for about 30 mm based on observation. A 1-minute waiting time was allowed before the next bead deposition was made to allow for substrate cooling. An L-18 Taguchi orthogonal, fractional factorial experimental design was employed to obtain single bead characteristics data from the Ti-6Al-4V wire deposits. Eighteen single beads were obtained from this experiment as these are enough to give statistical significance of the influence of the process parameters. Nine different treatment combinations were employed with a single repetition of each treatment. The geometrical characteristics

(clad height and width) were measured using a Talysurf CLI 1000 surface profiler. Measurements were obtained from three different locations along each track. This was done to ascertain the repeatability of measurements of the bead geometrical characteristics as processing parameters change.

3.2.2 Laser cladding of Ti-6Al-4V wire and Spherotene powder

The cladding experiment was carried out as described in Section 3.2. The wire and powder were simultaneously fed into the melt pool as shown in Figure 3.4. This was done to achieve the graded structure of Ti composite matrix with uniform distribution of Spherotene particles (Ti MMC) to enhance hardness, wear resistance, contact deformation resistance thermal properties, and structural stiffness amongst other properties.

The processing parameters interacted were the same as those used in wire deposition experiments and Spherotene powder feed rate in addition to the other parameters. The experiments were performed to establish the following:

- The range of processing parameters required to achieve consistent and stable hybrid deposition of wire and powder.
- The influence of the processing parameters on bead characteristics and to obtain near optimised processing conditions.
- The influence of processing parameters on reinforcement weight fraction in the deposited beads and to determine the optimum processing parameter to achieve the highest reinforcement weight content in bead.

Trial experiments were set out using the following list of processing parameters:

- Laser power: 1200 - 1400 - 1600 - 1800 W
- Traverse speed: 100 - 200 - 300 - 400 mm/min
- Wire feed rate: 500 - 600 - 700 - 800 mm/min
- Powder feed rate: 10 - 20 - 30 - 40 g/min

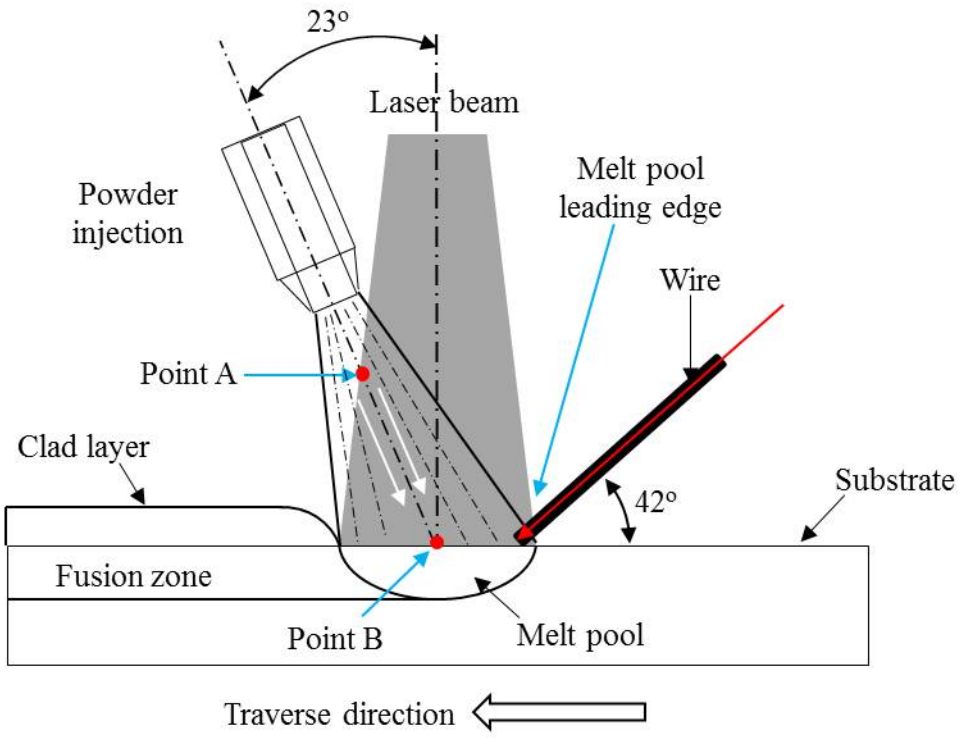

FIGURE 3.4: Schematics of the Ti-6Al-4V wire and Spherotene powder deposition.

Four levels of processing parameters were selected to have a wide range of process factor combinations from which consistent deposition of the hybrid materials can be achieved. An L-16 orthogonal array of the four (4) process factors was generated to give sixteen treatments, as presented in Appendix A.1. The deposition was made according to the serial arrangement of treatment in the table. The process was observed to be unstable for some of the single tracks deposited which resulted in an inconsistent deposition. Inconsistent deposition for some of the treatment combinations was validated after some repeated trials. After the trial deposition, a range of processing parameters that gave consistent deposition was obtained. Other parameter values deselected were prone to give droplet deposition and other deposition defects. These are documented in Chapter 4 of this report. The following processing parameters were selected to optimise the hybrid deposition of the Ti-6Al-4V wire and Spherotene powder:

- Laser power: 1400 - 1800 W
- Traverse speed: 200 - 400 mm/min
- Wire feed rate: 700 - 800 mm/min

- Powder feed rate: 10 - 30 g/min

The length of each bead was 80 mm with a pitch of 10 mm from the centre of one bead to another. There are four process factors with three (3) levels each. An L-27 orthogonal array was generated from these factors. The array was an L-9 type, as shown in Appendix A.2 with three replications. A total number of 27 tracks were deposited on a grit blasted substrate. The experiment was carried out by randomly selecting the treatment combinations. This allows a fair comparison of the deposition process as to whether the process is repeatable. The deposition of the two materials was stable yielding consistent single tracks. Furthermore, all the replicates deposited randomly were found to yield regular deposits which may signify reproducibility with the selected processing parameters. Similarly, measurements of physical characteristics of each Ti-6Al-4V/Spherotene beads were undertaken as reported for Ti-6Al-4V wire only. After the experiments, bead characteristics (bead height and width) were measured and statistical analysis undertaken to achieve the experimental objectives.

3.2.3 Laser cladding of pre-blended TiB_2/Ti-6Al-4V powder

The cladding experiments were conducted using the side fed material delivery system described in Section 3.2. The powder blend was delivered into the melt pool via the rear powder feeding nozzle. The processing parameters varied were laser power and traverse speed, and the objectives of the study were to investigate the influence of cladding parameters on physical characteristics of beads, microstructure, hardness and tensile properties. The following processing parameters were employed:

- Laser power: 1400 1600 1800 W
- Traverse speed: 200 300 400 mm/min
- Powder feed rate: 10 g/min

Also, each length of travel in both forward and backward directions was 80 mm. The depositions were made on a rectangular Ti-6Al-4V substrate with 180 mm x 100 mm x 5 mm dimensions. A steady state was reached at about 30 mm after the deposition has started. Prior to the main experiment, preliminary deposit trials were carried out to

assess the feasibility of the cladding process. Side fed material delivery was attempted, but cladding was not possible with the pre-blended feedstock of Ti-6Al-4V/TiB_2 powder. This led to the deposition trial with a coaxial feeder nozzle and the following processing parameters were used:

- Laser power: 600 800 1000 W
- Traverse speed: 400 500 600 mm/min
- Powder feed rate: 20 g/min (constant)
- Step up height: 0.5 mm (constant)

The TiB_2 powder used was relatively fine, while the coarse Ti-6Al-4V powder was used to serve as a carrier for the fine TiB_2 powder. The preliminary experiment and microstructural analysis of the powder blend documented in Chapter 5, necessitated modification of the feedstock as the TiB_2 powder in the mixture became separated in the powder feeder during cladding experiment. The small scale of the TiB_2 powder size when compared to Ti-6Al-4V powder is attributed to the powder segregation. This resulted in little or no trace of TiB/TiB_2 phase and non-uniform distribution of TiB_2 particles in the microstructure of the deposited beads. Thus, a modified TiB_2/Ti-6Al-4V blend is required before setting out the main experiments to overcome the shortcoming. In order to provide a solution to the shortcoming, it was thought that a means of attaching the fine TiB_2 powder on the coarse Ti-6Al-4V particles is essential and should be provided.

3.2.3.1 TiB_2/Ti-6Al-4V powder mixture preparation prior deposition

The powder pre-blending for Ti-6Al-4V and TiB_2 was carried out to achieve a mixture volume ratio of 9:1 respectively. It was anticipated that about 20% volume fraction of TiB reinforcement in Ti-6Al-4V matrix would be developed provided there is a complete decomposition of TiB_2 particles when subjected to laser processing.

The means of attaching the fine TiB_2 particles on the Ti-6Al-4V particles was experimented by spraying an aerosol of 2.7 volume% poly vinyl alcohol (PVA) solution on a pre-blended mixture of the powder. Having wet the powder with the PVA solution, it was thoroughly mixed to achieve particle agglomeration devoid of big clusters of the mixed powder. The following measurements were taken during the mixing process:

- Weight of TiB_2/Ti-6Al-4V (1:9) powder: 267.2 g
- Weight of PVA solution used : 5.2 g
- Weight of green mixture (powder + PVA): 272.4 g
- Weight of dry mixture: 271.1 g

The ratio of the mixed powder to the PVA solution was about 50:1. The powder mixture produced was fed into the laser generated melt pool using a side feeding system.

3.3 Design of experiment and Statistical analysis

The design of experiments is a systematic way of carrying out experimental work such that a justifiable conclusion can be reached based on the experimental objectives set out prior to the experiments. This gives a unique pattern by which the processing parameters (also called process factors) can be combined such that the influence of each process factor on the output(s) (otherwise called response(s)) can be independently or dependently examined and analysed. It has been previously observed that there is partial or no interaction among the process factors in laser cladding [19, 36], thus a direct influence of the factors on the responses may only be examined and analysed. This characteristic has led to the selection of the Taguchi experimental design for the entire laser cladding experiments in this study.

3.3.1 Taguchi experimental design

Taguchi experimental design is a fractional factorial design with a lean, less expensive and faster approach to experimentation. It gives possible combinations of process factors with a small number of experimental runs to obtain useful observations from the process. The design method is useful and adequate when interactions of the process factors are considered unimportant. It is suitable for processes with multiple process factors each having large range of values (called levels) interacting [108]. A set of orthogonal arrays (OAs) of factor level combinations are presented in tables which can be followed to conduct experiments. It is possible to have repetition of each level combination trials to validate the quality of the responses.

In this study, the laser processing of Ti-6Al-4V with Spherotene and TiB_2 powders, the process factors are either 3 factors with 3 levels or 4 factors with 4 levels. Also, 4 process factors with 3 levels were used in the deposition experiment of Ti-6Al-4V wire and Spherotene powder. For example, Table 3.1 presents an L-9 Taguchi orthogonal combination design for 3 factors with 3 levels combination. A single repetition of each treatment, gives an L-18 OAs design. The columns of the table are assigned to each of the process factors while the numbers in each column represents the levels with 1 for the lowest value and 3 for the highest value of the factor under consideration in the column.

TABLE 3.1: An L-9 orthogonal array with treatment combinations for process factors (A,B,C)

	Process factors		
Trials	A	B	C
T-1	1	1	1
T-2	1	2	2
T-3	1	3	3
T-4	2	1	2
T-5	2	2	3
T-6	2	3	1
T-7	3	1	3
T-8	3	2	1
T-9	3	3	2

Considering a process factor such as laser power with value range 1400-1800 W, and three factor levels can be obtained as 1400, 1600 and 1800 W. Thus, if column A stands for laser power, the numbers in the column A which are 1, 2 and 3 would represent the levels 1400, 1600, 1800 W respectively. Other process factors are assigned to each column as done for laser power. Thus, the table is assigned with process parameter combinations required, where, T-1,.....T-n (with n = 9) are the treatment combinations for the design of the experiments. This particular array was used for the experimental deposition of Ti-6Al-4V wire only and TiB_2/Ti-Al-4V powder blend. An L-16 array was used for the initial trial experiment for Ti-6Al-4V wire and Spherotene powder and an L-27 array was used for the optimisation of the hybrid deposition (Appendices A.3 and A.4).

3.3.2 Statistical analysis

Data obtained from the experiments were analysed using Analysis of Variance (ANOVA) and presented in a tabular form. This analysis allows statistical conclusions to be made on the results obtained from the experiments. From the analysis, the significance of each of the factors on a particular response is made known, and their percentage contributions were determined. Having obtained and conducted ANOVA of the bead characteristics measurements, a full detail of the influence of each process factor is determined on the outputs (bead height, width, and Spherotene weight fraction in beads). A two-way ANOVA was employed for the analysis in this study since there is more than one factor with more than two levels. More information on the elements of ANOVA can be found in the literature [108].

3.4 Bead characteristics measurements

The widths and heights of beads deposited were measured using a Talysurf CLI 1000 surface profiler (Taylor Hobson Precision Limited, UK) in non-contact mode (laser interferometry). Measurements were taken at three positions along each track in the steady state region (within 30 - 60 mm middle section of the bead) to determine mean height and width for each bead.

In order to determine the Spherotene weight fraction in the composite beads deposited, two - 10 mm lengths of the hybrid deposited tracks were cut off using Electrical Discharge Machine (EDM). These samples were measured with a scale having a sensitivity of 0.0001 g. This was done to determine the mean Spherotene weight fraction of the bead. The weight values of the Ti-6Al-4V substrate were calculated from the substrate volume and density value (4420 kg/m^3 see Table 2.2). The weight of the track deposited was obtained by the subtraction of the substrate weight from the weight of the samples. The weight of deposited wire per unit length of track is obtained by weight of wire delivered per minute divided by the traverse speed of the deposition system. Therefore, the weight fraction of Spherotene in the track per unit length is the subtraction of wire weight from the track weight per unit length. The analysis was based on the assumption of having 100% wire deposition efficiency.

Two samples of 10 mm length each were prepared using Wire Electro-Discharge Machining (WEDM) from each single track deposited on substrate. These samples were weighed to an accuracy of ±0.0001 g. The weight values of the substrate were calculated from the substrate volume and density value of Ti-6Al-4V. The weight of the 10 mm track deposited was obtained by the subtraction of the substrate weight from the overall weight of the samples. These two weight values for each track were averaged and taken as the mean weight of track over a length of 10 mm. Thus, the track weight per unit length is the average value divide by ten. Further analysis was undertaken to determine the weight of Ti-6Al-4V wire used during deposition. The weight of deposited wire per unit length of track is obtained by weight of wire delivered per minute divided by the traverse speed of the deposition system. Therefore, the weight of Spherotene in track per unit length, $W_{Spherotene}$, is the subtraction of wire weight from the track weight per unit length and is mathematically expressed in equation (3.1-3.3). The ratio of the Spherotene weight in track to the track weight is the reinforcement weight fraction in track. This analysis is done with an assumption of having 100% consistent deposition of Ti-6Al-4V wire with no consideration of loss.

$$W_{Spherotene} = W_{beadonsubstrate} - W_{Substrate} - W_{Ti-6Al-4Vwiredeposited} \tag{3.1}$$

$$W_{Substrate} = \rho.V_{Substrate}.g \tag{3.2}$$

$$W_{Ti-6Al-4Vwiredeposited} = \frac{\rho.V_{wiredeposited}.g}{V} \tag{3.3}$$

Where; ρ = density of Ti-6Al-4V (kg/m^3), $V_{substrate}$ = volume of the Ti-6Al-4V substrate (m^3), V_{wire} = volumetric flow rate of Ti-6Al-4V wire fed (m^3/s), V = traverse speed of deposition process (m/s), g = acceleration due to gravity (9.81 m/s^2)

3.5 Overlap cladding of Ti-6Al-4V/Spherotene composite

Having successfully completed the analysis of the physical characteristics of the single track beads with optimum process parameters obtained which gives a high Spherotene weight fraction in beads, Ti-6Al-4V/Spherotene overlap area cladding experiments were conducted on the Ti-6Al-4V substrate using the laser cladding setup for wire and powder described in Section 3.2. Table 3.2 gives the 3 sets of optimised laser processing parameters used for the area claddings. These parameters are capable of achieving above 65%

wt Spherotene in the Ti composite matrix based on the analysis made on the single beads.

TABLE 3.2: Laser processing parameter set for overlap deposition

Set	Laser power (W)	Traverse speed (mm/min)	Wire feed rate (mm/min)	Powder feed rate (g/min)	Spherotene fraction (wt.%)
A	1800	300	700	30	76±1
B	1600	200	750	30	74±2
C	1400	400	800	30	68±2

Figure 3.5 shows the deposition strategy used for the overlap area cladding. The deposition of single tracks was overlapped in a discontinuous pattern to give the area cladding. All single tracks have their start and finish ends on the same side with an overlap pitch of 0.6W for successive tracks, where W is the track width and T_1, T_2, T_3, are the single tracks overlapped in succession. Ten single tracks were deposited in this overlap manner for each of the parameter set.

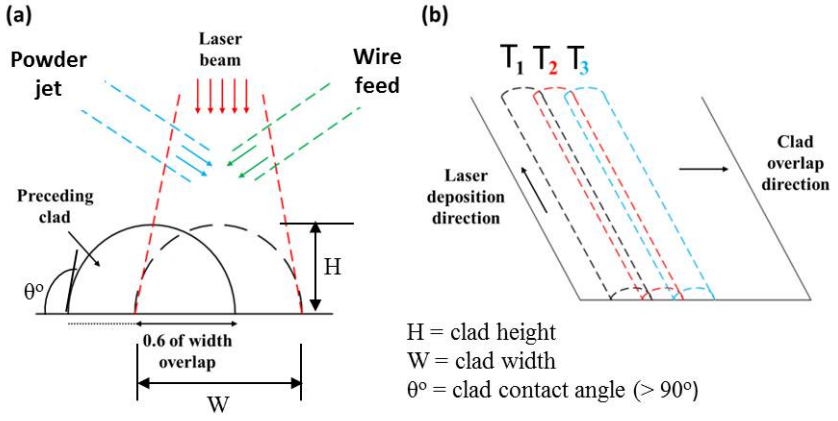

FIGURE 3.5: Deposition strategy for area clad layer.

3.6 Multilayer wall cladding of TiB_2/Ti-6Al-4V composite

Having being able to deposit the powder blend with the deposits containing a significant presence of TiB whiskers and little trace of un-fully melted TiB_2 particles in the composite matrix, multilayer cladding experiment was carried out with the feedstock to build walls. The side fed system was used and a continuous deposition strategy was

adopted as shown in Figure 3.6. At the corners where the traverse direction changes, the susbtrate is momentarily stationary, and more materials are fed in to the melt pool and also, more laser-material interaction is experienced. The walls were built in preparation for tensile test pieces to determine the elastic properties of the laser clad composite. A length of 130 mm was selected and sufficient to obtain the test piece with consideration of the acceleration and deceleration at both ends of the wall.

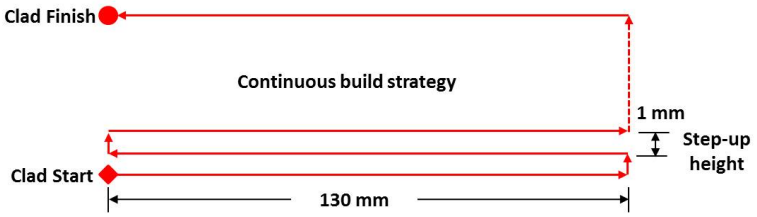

FIGURE 3.6: Continuous build strategy for multilayer wall cladding.

3.7 Microstructural characterisation techniques

The characterisation of the feedstock powders and the deposited beads were conducted using X-ray diffraction (XRD), scanning electron microscopy (SEM) and energy dispersive X-ray spectroscopy (EDX) techniques for phase identification and phase elemental compositions. It is necessary to have an understanding of the principles of these techniques.

X-ray Diffraction (XRD)

This technique is used to reveal crystallographic information about materials. Figure 3.7 shows typical schematics of X-ray diffraction. It has an electromagnetic radiation source which emits X-rays with short wavelength. X-rays are produced by having a high voltage across a cathode (an electron source) and an anode (a target material). As electrons are emitted from the cathode and are accelerated to strike the anode, X-rays are emitted from the target material (anode) [109]. When the X-rays are made to strike a crystalline specimen, the X-ray beam is scattered which is known as diffraction. The scattering of the beam occurs based on the atom arrangement in the crystal of the specimen. The diffracted beam is collected by an X-ray detector and analysed to give crystallographic

information of the sample. A general rule known as Braggs law (equation 3.4) is obeyed in X-ray diffraction [109].

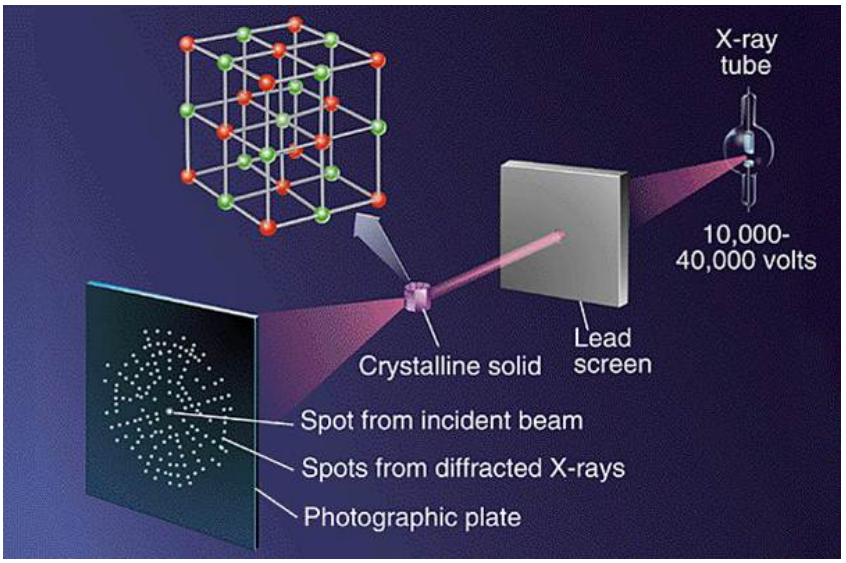

FIGURE 3.7: A schematics of X-ray diffraction [110].

$$n\lambda = 2.d.sin\theta \tag{3.4}$$

Figure 3.8 shows the X-ray diffraction by a crystal which obeys the Braggs law. The X-ray wavelength, λ, is related to the distance, d, between the scattering centres of atom layers P1 and P2. Also, both incident X-ray beam and the diffracted beam are coplanar with angle between them measured as 2θ. Thus, in a powder diffraction method used in material characterisation in this research work, the X-ray wavelength is fixed while the 2θ is varied.

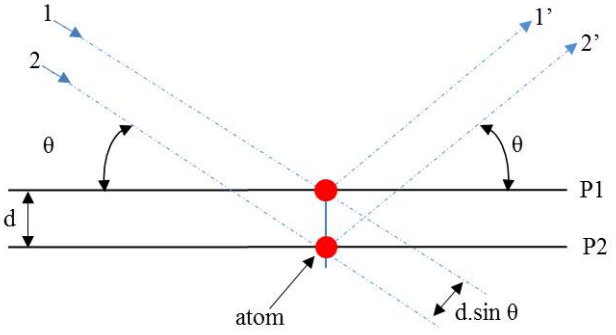

FIGURE 3.8: A typical X-ray diffraction by a crystal.

Scanning Electron Microscopy (SEM) and Energy Dispersive X-Ray (EDX)

Scanning Electron Microscope (SEM) is a versatile tool for microstructural investigation with wide applications in material research, material development, failure analysis, and quality control [111]. SEM has an electron beam source which is a heated tungsten cathode. The electron beam is communicated in a vacuum created by a diffusion or turbomolecular pump and the beam is focussed on to the specimen surface by a magnetic lens arrangements. The focussed electron beam has an accelerating voltage which lies between 1000-50,000 V and a current of 10^{-8}-10^{-7} A. As the primary focussed electron beam strikes the specimen surface, electrons and other radiation is emitted from the near surface. This can be used to form images and for chemical analysis of the microstructural features of the surface. The emitted electrons are received by an electron detector. The received electron signal is amplified such that an image of the surface is displayed on the screen with adjustment made to image brightness and contrast. These emitted signals give information about surface topography, material contrast, crystal orientation contrast, material composition and elemental distribution depending on the depth from which the signal is being emitted. The most common of the signals may include, Secondary Electron (SE), Back Scattered Electron (BSE) and X-ray signals.

- Secondary Electron (SE) signal: This is formed by the electrons on the specimen surface at a depth less than 10 nm, as the primary electron bombardment occurs. It is dependent on the energy of the primary electron and the angle of tilt between the focussed beam and the specimen surface. It gives information about surface topography and material composition among others.
- Back Scattered Electron (BSE) signal: This is formed by elastic scattering events at a depth of $\sim$1 μm below the specimen surface. A wide spectrum of emitted electron energies is obtained which is dependent on the energy of the incident focused electron beam, surface tilt of specimen with the beam, number of electron in outer shell of atoms of the specimen material. Elements with low atomic number releases few back scattered electrons and more energy is lost, resulting in dark contrast; while having a bright contrast in micrograph display on screen. BSE signal yields information about the topography, material contrast and composition.

X-rays are excited by the focused beam at a depth of 0.2-2 μm (Figure **??**) and are diffracted as radiation with a distinct line spectrum. The line spectrum is analysed

by energy dispersive spectrometry with a multichannel analyser in most cases. The analyser separates the line spectrum for different elements which is easy for higher atomic number elements, but elements with atomic number less than 11 cannot be effectively analysed due to background noise and superimposition of wavelengths. However, the quantification of the elemental compositions of specimen may be quite accurate for heavy elements with a relative error of ∼10% [111].

3.8 Sample preparation for microstructural studies and materials testing

The 10 mm length samples were mounted in a conductive resin in preparation for microstructural examination. The mounted samples were ground using wet SiC papers with grit range of P240-P4000, and polished using diamond paste on polishing cloth and paraffin to a 1 μm Ra finish. These samples were examined using scanning electron microscopy (SEM). The top curve surfaces of another 10 mm length of overlapped beads were ground and polished to give a flat surface which is wide enough for X-ray Diffraction experiments.

3.8.1 Scanning Electron Microscopy

A Philips XL 30 Scanning Electron Microscope (SEM) operated at 20 kV was employed to investigate powder morphology and microstructural features in the composite bead deposited. Secondary electron (SE) and back scattered electron (BSE) signals were utilised to form images. Phase identification was analysed based on contrast level of the phases present in the BSE micrographs, while SE images gives information about morphology. Energy Dispersive X-ray (EDX) spectroscopy incorporated with the SEM was used for phase identification and also to make a semi-quantification of the elemental composition of phases.

3.8.2 X-Ray Diffraction

A Siemens D500-1 X-ray diffraction machine was employed to investigate both powder and deposited beads. The machine was set at 40 kV and 25 mA to generate a Cu K(α)

radiation (wavelength, $\lambda = 0.15406$ nm). A 2θ scan range of 30-90^o was used in the study. A step-scan mode with a step size $\Delta\ (2\theta) = 0.05^o$ and 4 s counting time per data point was employed. Phase identification was carried out by matching the diffracted peaks in the experimental scan spectrum with the phase patterns in the International Centre Diffraction Database (ICDD) to identify the corresponding peaks diffracted.

3.8.3 Tensile test piece

Tensile test pieces were obtained from the multilayer wall builds produced as described in Section 3.6. The samples were prepared according to BS EN 10002-1:2001. The surface of the tensile samples was mill-finished to eliminate the surface ripples due to peaks and troughs on as-deposited samples. Figure 3.9 shows the schematic of the test piece samples with dimensions.

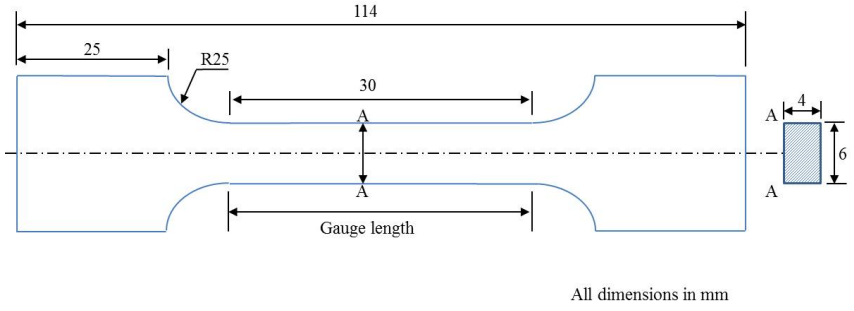

FIGURE 3.9: Schematic of the tensile test piece (BS EN 10002-1:2001).

3.9 Microhardness assessments

Microhardness tests were conducted using a Breuher Microhardness Tester. A load of 300 gf was applied for a loading time of 15 s to create each indent. Indentations were made at a distance of 254 μm apart from the top of the clad cross section down into the substrate with the avoidance of indents on the embedded Spherotene particles. Also, microhardness profiles across the overlap area cladding cross section were obtained to determine the influence of processing on hardness of the composite matrix. Similar tests were conducted with a 127 μm interval indent spacing on TiB_2/Ti-6Al-4V bead cross sections.

3.10 Tensile test setup

Tensile tests were performed using the Instron^{TM} tensile testing machine as shown in Figure 3.10. The samples were mounted and subjected to tensile loading at an extension speed of 1 mm/min. An extensometer was clamped on the 30 mm gauge length of the test piece to measure the elongation of the specimen as the tensile stress increases. The test pieces were loaded until fracture occurs.

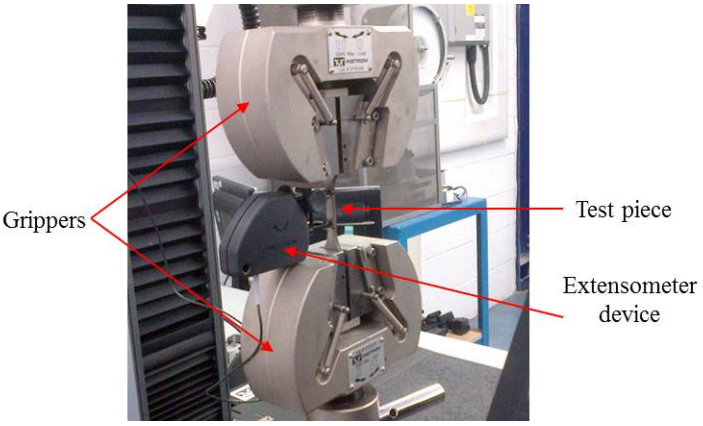

FIGURE 3.10: Tensile test setup.

3.11 Erosion test setup for abrasive and plain waterjet impacts

In order to evaluate the erosion performance of the laser clad Ti-6Al-4V/Spherotene, a method for establishing abrasion/erosion using both plain waterjet (PWJ) and abrasive waterjet (AWJ) impacts was implemented. This approach is good for quick characterisation of composite coatings and can as well be related to slurry pipeline applications. A series of single track treatments were made on the Ti-6Al-4V/Spherotene composites layer surface with various combinations of water jetting parameters. For a comparison purpose, the single-track erosion trials were also conducted on wrought Ti-6Al-4V. An Ormond 5-axis AWJ machining system which is equipped with a KMT Streamline SL-V100D ultra-high pressure intensifier pump was employed for the experimental trials. The cutting head is made up of a Rotec 100 tungsten carbide round-jet focusing tube

(1mm in bore diameter and 76 mm in length). The experimental runs were firstly carried out by subjecting the Ti-6Al-4V/Spherotene composite surfaces to PWJ impacts, as well as wrought Ti-6Al-4V, to identify the most resistive composite layer among others and the erosion rate of composites when compared to a wrought Ti alloy. The best performing Ti-6Al-4V/Spherotene composite during PWJ erosion was selected for the AWJ experimental trials to investigate its erosion performance under AWJ conditions. Australian GMA garnet abrasive mesh 80 with size range of 150-300 μm with 7.5-8 Mohs (1160-1570 kgf.mm^{-2}) was used in the AWJ machining. Due to the lack of prior information on AWJ cutting of Ti-6Al-4V/Spherotene composite, the selection of processing parameters was based on established knowledge on AWJ cutting of Ti-6Al-4V.

TABLE 3.3: Process parameters for PWJ and AWJ erosion test of both Ti-6Al-4V and laser clad Ti-6Al-4V/Spherotene composites

PWJ runs		
Head pressure (MPa)		275, 345
Traverse speed (mm/min)		20, 50, 100
SOD (mm)		3
Impingement angle, (^{o})		90
AWJ runs		
	Set 1	Set 2
Head pressure (MPa)	207	138
Abrasive feed rate (g/s)	0.39	0.39, 0.92
Impingement angle (^{o})	90	90
Standoff distance (mm)	3, 10	3
Traverse speed (mm/min)	50, 100, 200, 500, 1000	50, 100, 200, 500, 1000

Figure 3.11 shows the laser clad Ti-6Al-4V/Spherotene composite on Ti-6Al-4V substrate with illustrations of the AWJ cutting strategy. A series of single tracks were machined from the ground surfaces of Ti-6Al-4V/Spherotene composites using all combinations of process parameters shown in Table 3.3. The length of traverse path was 18 mm; and the spacing between each track was 3 mm.

3.11.1 Determination of erosion rate

All PWJ and AWJ-treated tracks were scanned using a Talysurf CLI1000 profilometer with a laser displacement sensor which has a resolution of 1 μm. Only the centre section of each track (with a length of 6 mm) was used for the profilometry study as sections near the jet start point and jet end point were not uniform in terms of their erosion

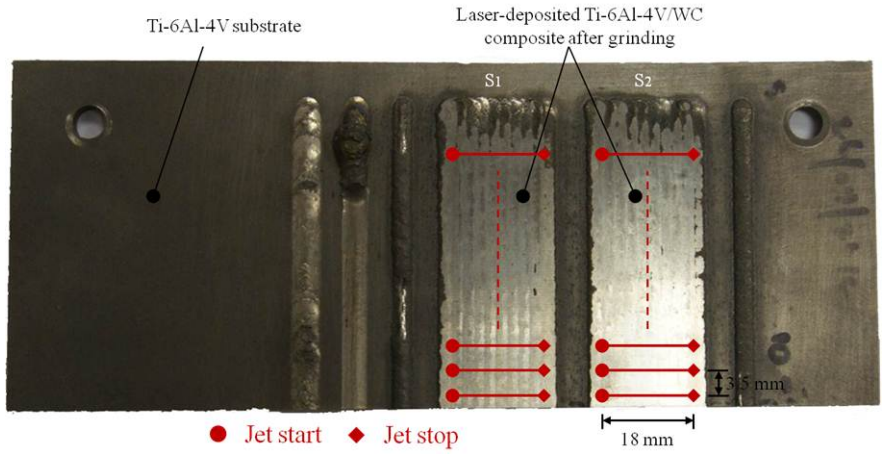

FIGURE 3.11: Ground surfaces of laser-deposited Ti-6Al-4V/Spherotene composite with illustrations of AWJ cutting strategy.

removal depth due to acceleration and deceleration during stage traverse. The mean profile of the cross-section of each track obtained was used to calculate the material volume removal rate. The mean profile was determined by the average of 30 scans (P1 to P30 as shown in Figure 3.12) with a spacing of 200 μm. The surface roughness Ra along the bottom of each track was also measured with a sampling length of 3 mm and a cut-off length of 0.8 μm.

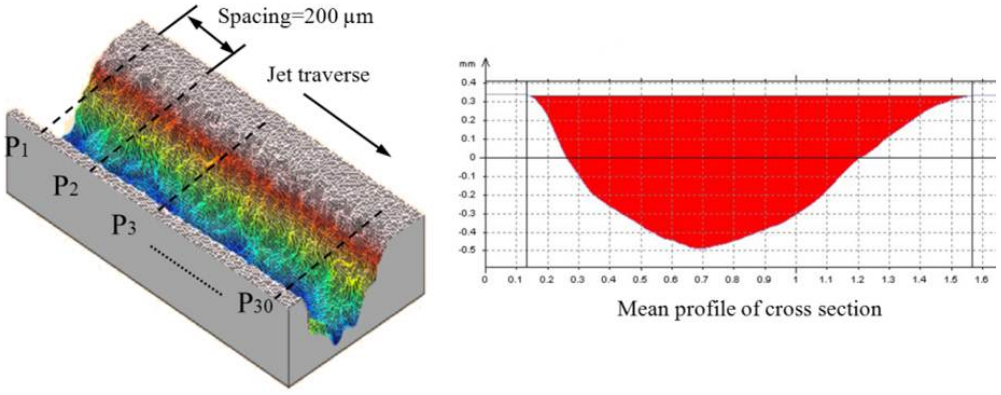

FIGURE 3.12: A schematic of the 3D scan of the AWJ-treated slot obtained by a laser profilometer and the mean profile of its cross-section.

The erosion performance was evaluated by the material volume removal rate (MRR) which can be estimated by the following equation (3.5).

$$MRR = A_c.V_j \tag{3.5}$$

Where; A_c = the area of cross-section of the mean profile, (mm^2) and V_j = the jet traverse speed, (mm/min). The surface roughness of the ground surfaces before water jet treatment was measured to be 3 μm Ra.

Chapter 4

Laser cladding of Ti-6Al-4V/Spherotene composites

This chapter discusses the laser cladding of Ti-6Al-4V/Spherotene in the form of wire/powder deposition. The single bead deposition of the Ti-6Al-4V wire and Ti-6Al-4V wire/-Spherotene powder are discussed based on the effect of the processing parameters on the bead characteristics. The bead characteristics to be investigated are bead height, width, percentage weight of Spherotene in composite bead and melt depth. The processing parameters considered here are laser power, traverse speed, wire feed rate and powder feed rate. These process factors are chosen amongst others to determine their main effects on the deposits characteristics. Other process factors such as laser spot size, gas flow rate, etc, are not varied during the laser process. The characterisation of the powders is discussed in terms of their particle size, particle morphology and phase composition. The microstructure and microhardness of the deposits are examined to determine variations with processing parameters. Furthermore, overlap and multilayer deposition of the hybrid Ti-6Al-4V wire and Spherotene powder with a development of a functionally graded cylinder as a demonstrator are discussed. In summary, an understanding of the influence of the processing parameters on the deposit characteristics, microstructure and microhardness is obtained and presented.

4.1 Bead deposition of Ti-6Al-4V and Ti-6Al-4V/Spherotene composite

This section reports the laser deposition of Ti-6Al-4V and Ti-6Al-4V/Spherotene composite to determine the influence of the processing parameters on bead characteristics. Firstly, the Ti-6Al-4V deposition was made to calibrate the laser deposition system for cladding optimisation. This experiment gives an insight into the range of processing parameters to be employed for the hybrid deposition of the Ti-6Al-4V wire and Spherotene powder.

The Ti-6Al-4V cladding experiment is conducted as discussed in Section 3.2.1 and the hybrid deposition of the Ti-6Al-4V wire and Spherotene powder, as discussed in Section 3.2.2. These experiments are conducted according to a DoE methodology. A Taguchi DoE method, which is a form of fractional factorial design, is chosen, as it yields reliable results with fewer experimental runs compared to full factorial design method. It is important to note that there are limited or no interactions among the process factors in laser cladding [19, 36].

The process factors and levels employed for a consistent Ti-6Al-4V deposition are:

- Laser power: 1400-1600-1800 W
- Traverse speed: 200-300-400 mm/min
- Wire feed rate: 700-750-800 mm/min
- Focal position: 212 mm (20 mm out of beam focus)
- Beam diameter: 3.1 mm

Figure 4.1 shows the Ti-6Al-4V deposits on plate. The deposition is consistent based on the suitable process condition employed.

Having successfully deposited Ti-6Al-4V wire on plate, the laser cladding of Ti-6Al-4V/Spherotene is investigated. The characteristics of the single beads deposited, and the influence of processing parameters on the weight composition of Spherotene in beads is determined and optimised. In this study, two sets of experiments are conducted to achieve a hybrid deposition of the Ti-6Al-4V wire and Spherotene powder with the

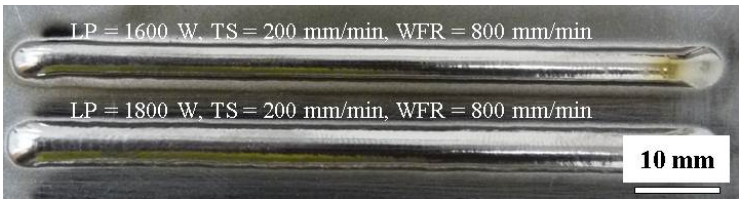

FIGURE 4.1: Ti-6Al-4V bead on plate showing a consistent deposition.

purpose of maximising reinforcement fraction. The first experiment is conducted to determine the processing parameters to achieve a consistent cladding operation. The second experiment seeks to maximise the Spherotene weight fraction in track.

Figure 4.2 shows some of the single tracks obtained from the first experiment. Unstable deposition occurred when there is a transfer of Ti-6Al-4V wire in droplet form into the melt pool. This happens as the wire tip is melted before reaching the leading edge of the melt pool. The globule droplet of the wire tip causes inconsistency during the process.

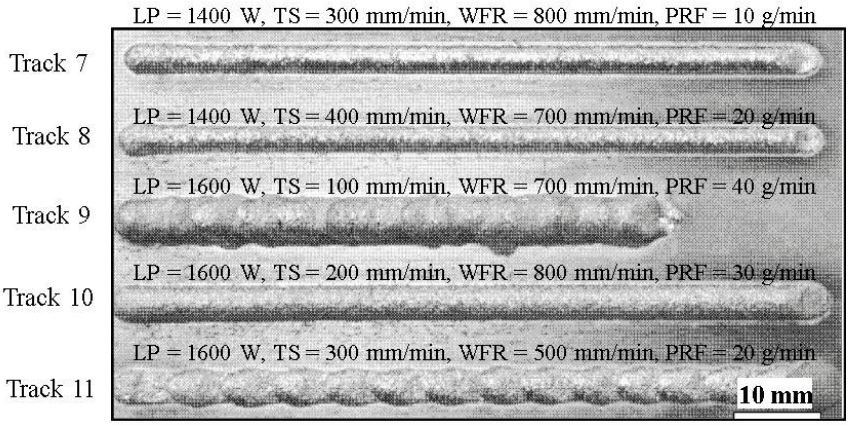

FIGURE 4.2: Single track deposits showing the development of stable processing conditions.

The first experiment shows that wire feed rates between 500-600 mm/min may not be suitable for the deposition process, as inconsistency is prevalent. A traverse speed of 100 mm/min is also found to be unsuitable for a consistent deposit. The study also reveals that a lower laser power (1200 W and below) may be considered less suitable to give a stable deposition. For Ti-6Al-4V deposition, a laser power of 1200 W is not even suitable for consistent deposition of Ti-6Al-4V wire only. Thus, having Spherotene powder stream attenuating the laser beam before arriving at the melt pool, reduces the laser power reaching the substrate.

The second experiment was conducted based on the observations from the first experiment. The effects of the main process factors on track characteristics (height, width) and Spherotene weight fraction in the deposited track are investigated.

The process factors and levels employed for a consistent Ti-6Al-4V/Spherotene deposition are:

- Laser power: 1400-1600-1800 W
- Traverse speed: 200-300-400 mm/min
- Wire feed rate: 700-750-800 mm/min
- Powder feed rate: 10-20-30 g/min

Figure 4.3 shows selected Ti-6Al-4V/Spherotene deposits on plate. The deposition is consistent based on the suitable process condition employed.

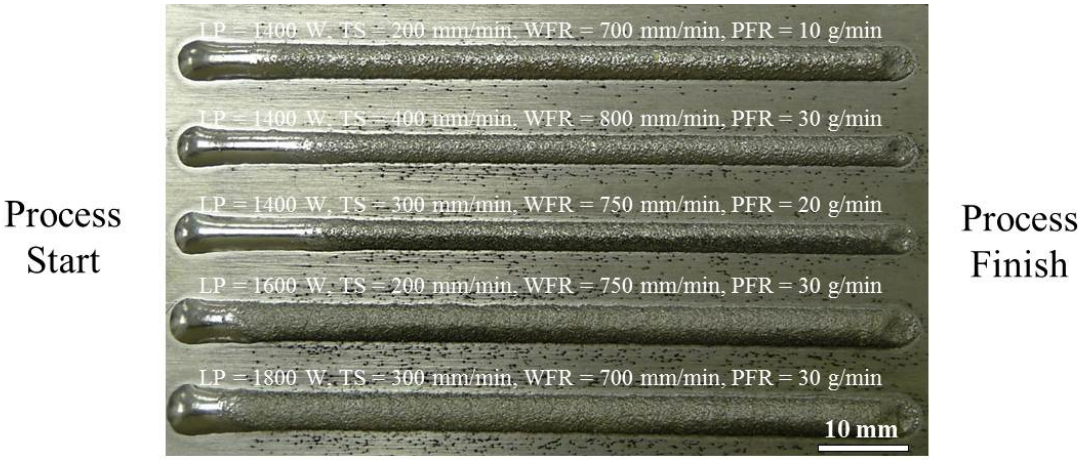

FIGURE 4.3: Ti-6Al-4V/Spherotene beads on plate showing a stable deposition.

A comparison of results can be made of the influence of process factors on bead characteristics for both Ti-6Al-4V and Ti-6Al-4V/Spherotene deposition. This gives an understanding of the effect of the processing parameters on the bead characteristics and deposition rate. The bead characteristics (height and width) allow an estimation of the processing time required for area cladding and additive structure deposition. The mean bead heights and widths values with standard errors obtained from the deposition measurements are presented in Appendices B.1 and B.2.

4.1.1 Effect of the process factors on bead height and width

The influence of the process factors on the deposit height is analysed using ANOVA as shown in Table 4.1.

TABLE 4.1: Analysis of variance for deposit height of (a) Ti-6Al-4V wire; (b) Ti-6Al-4V/Spherotene beads

(a)

Source	DOF	SS	MS	F	S'	P(%)
Laser Power (LP)	2	0.083	0.042	63.914	0.082	7.27
Traverse Speed (TS)	2	1.014	0.507	776.913	1.013	89.71
Wire Feed Rate (WFR)	2	0.024	0.012	18.552	0.023	2.03
Error	11	0.007	0.001	1.000	0.011	0.98
Total	17	1.129	-	-	-	100

(b)

Source	DOF	SS	MS	F	S'	P(%)
Laser Power (LP)	2	0.049	0.024	30.427	0.047	1.07
Traverse Speed (TS)	2	3.494	1.747	2173.390	3.492	78.66
Wire Feed Rate (WFR)	2	0.122	0.061	75.702	0.120	2.07
Powder Feed Rate (PFR)	2	0.761	0.380	473.173	0.759	17.10
Error	18	0.014	0.001	1.000	0.021	0.47
Total	26	4.440	-	-	-	100

The variance ratio, F-value from the tables (Appendix B.3) at a significance level of 0.01 for $F_{.01}$ (2, 11) = 7.2057 and $F_{.01}$ (2, 18) = 6.0129 (99% confidence) for Table 4.1 (*a*) and (*b*) respectively. From the ANOVA tables (Table 4.1), all the process factors have their computed F-values greater than the limiting value obtained from the F-tables for both Ti-6Al-4V and Ti-6Al-4V/Spherotene depositions. Thus, all process parameters are considered statistically significant within the 99% confidence level as factors influencing the deposit height. The traverse speed is the most significant factor influencing the deposit height in both cases.

Figure 4.4 shows the main effects plot of the process factors against the deposit height. The plot shows that a linear and inverse trend exists between traverse speed and height. Combining the ANOVA results and the main effects plots, increasing laser power and traverse speed are capable of reducing the deposit height with traverse speed as most influential. The percentage contribution, P-value column (Table 4.1) s hows that traverse speed contributes 90% and 79% to change in deposit height of Ti-6Al-4V and Ti-6Al-4V/Spherotene deposits respectively. Increasing material delivery rate is observed to

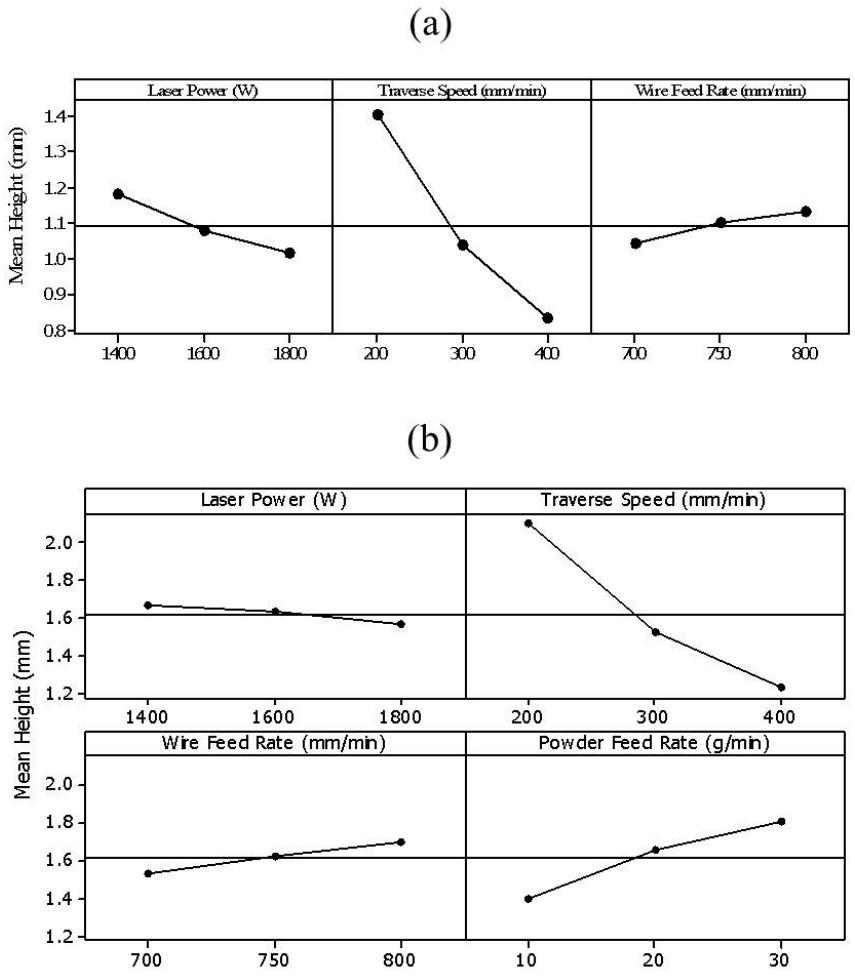

FIGURE 4.4: Main effects plot for deposit height of (a)Ti-6Al-4V wire; (b)Ti-6Al-4V/Spherotene.

increase deposit height with powder feed rate (17.1% contribution) as the most influential for Ti-6Al-4V/Spherotene deposition.

Equation (4.1) and (4.2) give the linear regression models that predict the heights as a function of the process factors for Ti-6Al-4V and Ti-6Al-4V/Spherotene deposits respectively. The positive and negative signs indicate the influence of the factors on the clad heights. The coefficient of determination, R^2, which is the variability in the data as well as measure of degree of fit for Equation (4.1) and (4.2) are 0.97 and 0.96 respectively.

$$Height, H(mm) = 1.95 - 0.000413LP - 0.00287TS + 0.000883WFR \quad (4.1)$$

$$Height, H(mm) = 1.69 - 0.000256LP - 0.00433TS + 0.00164WFR + 0.0203PFR \quad (4.2)$$

Where; LP = Laser Power (W), TS = Traverse Speed (mm/min), WFR = Wire Feed Rate (mm/min), and PFR = Powder Feed Rate (g/min).

Similarly, the influence of process factors on deposit width is analysed as presented for deposit height. Table 4.2 presents the ANOVA result for the influence of the process factors on the deposit width.

TABLE 4.2: Analysis of variance for the deposit width of (a)Ti-6Al-4V wire;(b)Ti-6Al-4V/Spherotene beads

(a)

Source	DOF	SS	MS	F	S'	P(%)
Laser Power (LP)	2	4.197	2.098	315.862	4.184	82.88
Traverse Speed (TS)	2	0.746	0.373	56.172	0.733	14.52
Wire Feed Rate (WFR)	2	0.031	0.016	2.359	0.018	0.36
Error	11	0.073	0.007	1.000	0.013	2.24
Total	17	5.048	-	-	-	100

(b)

Source	DOF	SS	MS	F	S'	P(%)
Laser Power (LP)	2	3.344	1.672	216.634	3.328	67.91
Traverse Speed (TS)	2	0.789	0.394	51.089	0.773	15.77
Wire Feed Rate (WFR)	2	0.208	0.104	13.499	0.193	3.94
Powder Feed Rate (PFR)	2	0.422	0.211	27.315	0.406	8.29
Error	18	0.139	0.008	1.000	0.201	4.09
Total	26	4.901	-	-	-	100

At a significance level of 0.01, $F_{.01}$ (2,11) = 7.2057 and $F_{.01}$ (2,18) = 6.0129 for Table 4.2 (a) and (b) respectively. Within the range of process factor levels used in the experiment, laser power, traverse speed and powder feed rate are statistically significant for both Ti-6Al-4V and Ti-6Al-4V/Spherotene deposit width. Their computed F-values are greater than the limiting value obtained from the F-table. The F-value for wire feed rate was lower than the limiting F-value and is considered statistically insignificant for Ti-6Al-4V deposit width. However, WFR is statistically significant with a lowest P-value contribution of 3.94% for Ti-6Al-4V/Spherotene deposit width. In all, laser power is the most significant factor with the highest percentage contribution. Figure 4.5 shows the dependencies of deposit width on the process factors. A positive linear trend exists between laser power and width, and a negative linear trend for traverse speed and powder feed rate with width.

Combining the ANOVA results and the main effect plots, in both cases, increasing laser power is capable of increasing deposit width, while increasing traverse speed and

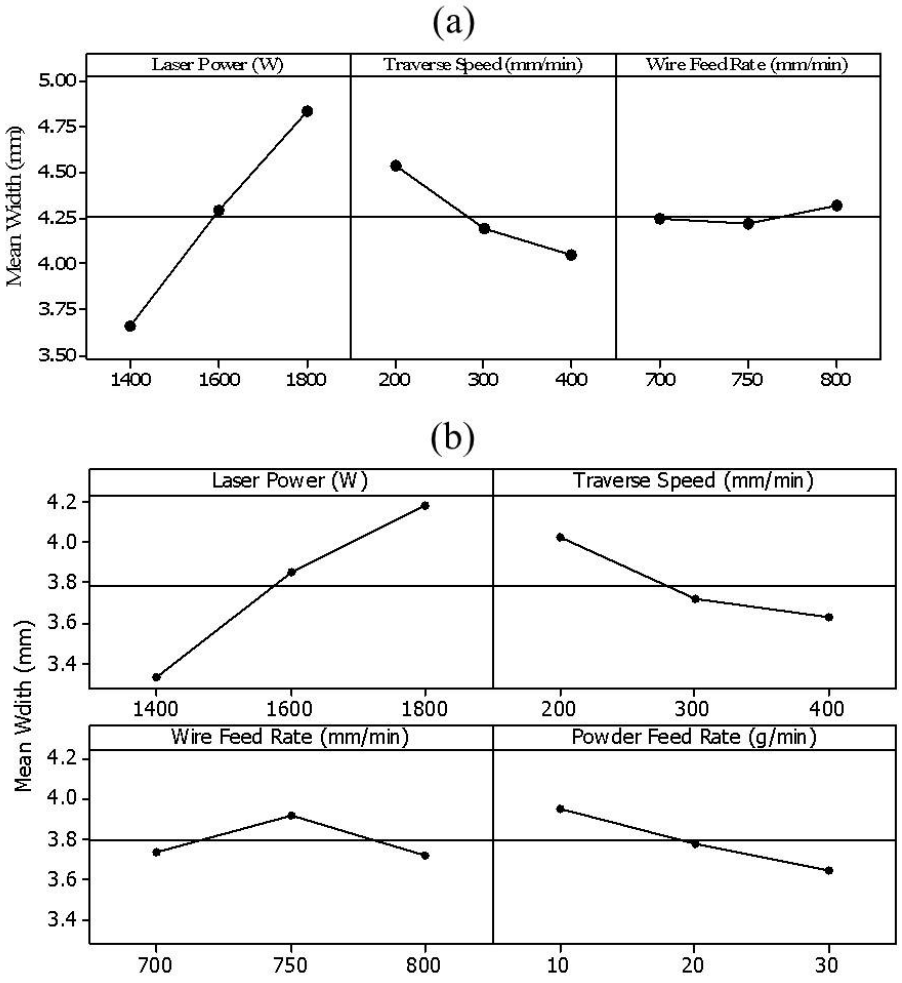

FIGURE 4.5: Main effects plots for deposit width of (a) Ti-6Al-4V wire; (b) Ti-6Al-4V/Spherotene.

powder feed rate decrease deposit width. Wire feed rate has no particular trend and can be considered as an invariant factor. The percentage contribution, P-value, which shows that the influence of laser power to increase deposit width are 83% and 68% for Ti-6Al-4V and Ti-6Al-4V/Spherotene deposits respectively. Traverse speed was the most influential factor contributing to the reduction of the deposit width with P-values of 14.5% and 16% for Ti-6Al-4V and Ti-6Al-4V/Spherotene deposits respectively. Equation (4.3) and (4.4) give the linear regression models that predict the widths as a function of the process factors for Ti-6Al-4V and Ti-6Al-4V/Spherotene deposits respectively. The coefficient of determination, R^2, for Equation (4.3) and (4.4) are 0.97 and 0.90 respectively.

$$Width, W(mm) = 0.00295LP - 0.00243TS + 0.000683WFR - 0.253 \tag{4.3}$$

$$Width, W(mm) = 1.41 + 0.00214LP - 0.002TS - 0.000174WFR - 0.0153PFR \quad (4.4)$$

4.1.2 Effect of process factors on Spherotene weight fraction in composite bead

This section examines the composition of the deposited tracks as described in Section 3.4. The influence of the process factors on the weight fraction of Spherotene in composite bead is studied. The average values of the Spherotene wt.% for the process conditions employed are presented in Appendix B.4. Table 4.3 presents the ANOVA result for the dependence of Spherotene fraction in track on the process factors used in the experimental process.

TABLE 4.3: Analysis of variance for Spherotene (%wt) fraction in composite track

Source	DOF	SS	MS	F	S'	P(%)
Laser Power (LP)	2	68.601	34.300	23.351	65.663	3.79
Traverse Speed (TS)	2	56.554	28.277	19.251	53.616	3.10
Wire Feed Rate (WFR)	2	36.005	18.003	12.256	33.067	1.91
Powder Feed Rate (PFR)	2	1543.147	771.574	525.277	1540.210	88.99
Error	18	26.440	1469.000	1.000	38.191	2.21
Total	26	1730.747	-	-	-	100

At a significance level of 0.01, the F-value for $F_{.01}$ (2,18) = 6.0129 from the F-table. The computed F-values for each factor have a greater value than the limiting value from the table with wire feed rate having the least F-value of 12.256. All the factors are considered significant on the content of Spherotene in the deposited track. The P-value of the factors shows that powder feed rate is the most significant with P-value of 88.99%. Others are significant in this order: laser power (3.8%), traverse speed (3.1%) and wire feed rate (1.9%).

Figure 4.6 shows the main effect plot for the Spherotene content in track. The trend of dependencies between the process factors and the response (Spherotene weight fraction) are examined.

The main effects plot shows as expected that a linear increase in Spherotene fraction in deposited tracks is dependent on increasing laser power and powder feed rate. There is an inverse linear trend between Spherotene fraction and the two other factors (Traverse speed and Wire feed rate). The powder feed rate with the largest gradient is the most

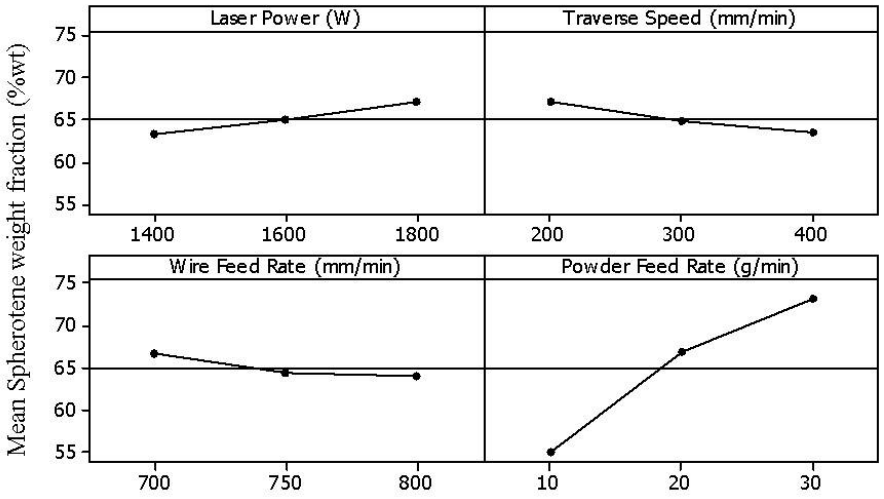

FIGURE 4.6: Main effects plot for Spherotene weight fraction (%wt) in track.

influencing factor that promote increase in fraction of Spherotene in track. This complements 88.99% P-value contribution of PFR obtained from the ANOVA (Table 4.3). Equation (4.5) gives the linear regression model that predicts the Spherotene fraction in wt. % as a function of the process factors for Ti-6Al-4V/Spherotene deposit. The coefficient of determination, R^2, for Equation (4.5) is 0.95.

$$Spherotene, (wt.\%) = 56.2 + 0.00975LP - 0.0174TS - 0.0263WFR + 0.911PFR \quad (4.5)$$

Figure 4.7 shows the Spherotene content in the deposited composite beads in terms of volume fraction which is equivalent of the Spherotene weight fraction (% wt). For all composite beads, the Spherotene weight fraction lies between (49 - 77)% wt with an equivalent volume fraction range of (22 - 49)% vol. Thus, the volume fraction of the Ti-6Al-4V wire deposited to form the composite bead would lie between (55 - 78)% vol.

The Spherotene capture efficiency which is the ratio of the Spherotene weight fraction assimilated into the melt pool to the weight of Spherotene powder exposed to the melt pool lies between (27 - 57)%. Figure 4.8 shows the main effect plot for mean Spherotene capture efficiency. The capture efficiency increases with increasing laser power, decreasing traverse speed (increasing heat input) and decreasing powder feed rate. This indicates that a higher fraction of the powder fed at lower powder feed rate during cladding is caught up in the melt pool than employing higher feed rates.

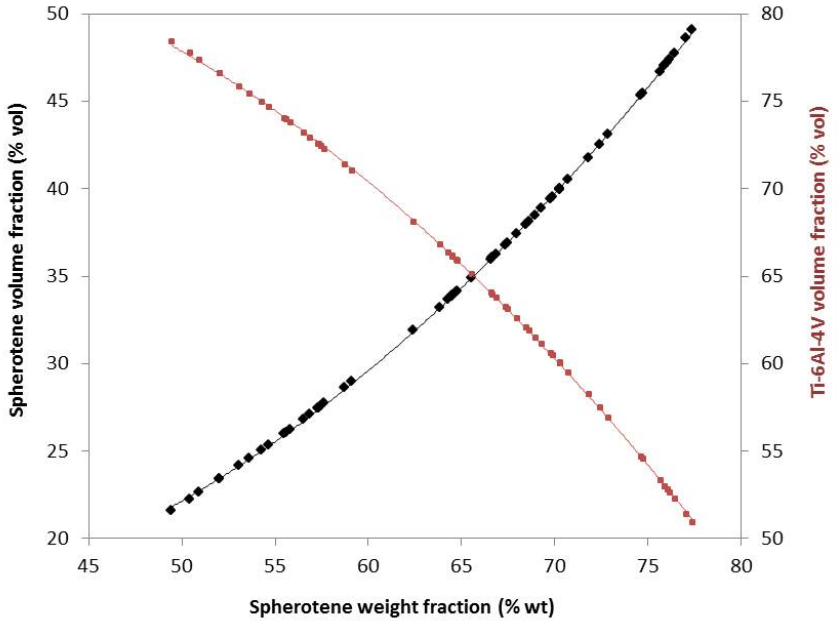

FIGURE 4.7: Variation of the Spherotene content in composite beads in volume fraction (%vol).

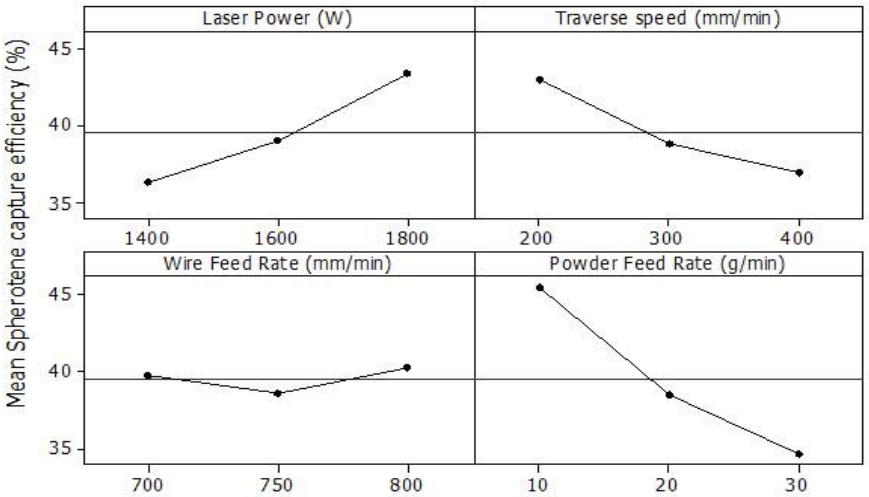

FIGURE 4.8: Main effects plot for Spherotene capture efficiency during the cladding process.

4.2 Energy density requirement for maximum deposit physical characteristics

This section determines the energy density requirement to achieve the maximum key physical characteristics of the deposit such as height, width and percentage composition of Spherotene in Ti-6Al-4V/Spherotene beads. Energy density combines the primary processing parameters which include: the laser power, the traverse speed and the laser beam spot diameter to give a unified value. It is important to note that different values of the primary processing parameters can be computed to achieve the same energy density value whose relation is expressed in equation (4.6). For example, with a laser power of 1800 W applied, a process traverse speed of 200 mm/min, and a circular spot diameter of 3 mm, the average energy density is 229 J.mm^{-2}. Moreover, the same energy density can be obtained when a laser power of 1350 W and a traverse speed of 150 mm/min with a common spot diameter of 3 mm are employed. Specific point energy may be more appropriate to use rather than using energy density which can be obtained using different combination of process parameter values. However, energy density value is often required to describe laser deposits.

$$E = \frac{P_L}{(\pi.D^2/4)}.\frac{D}{V} \tag{4.6}$$

Where; E = energy density (J.mm^{-2}), P_L = laser power (W), D = laser spot diameter (mm) and V = traverse speed (mm/s).

4.2.1 Deposit height

Figure 4.9(a) shows the contour plot of the mean height as laser power and traverse speed interact for Ti-6Al-4V deposit. A clear trend is seen in the plot as laser power and traverse speed decrease, clad height increases. The triangular portion at the bottom left corner shows the highest height bounded by laser power (1400-1550 W) and traverse speed (200-220 mm/min). Figure 4.9(b) shows that the clad with highest height values lie between 1550±10 W laser power and 755±5 mm/min wire feed rate. Figure 4.9(c) shows the contour plot of mean height as energy density and the wire feed rate interact. A definite trend is not observed due to the different unified parameters making up the

energy density. Moreover, data from a full factorial experiment may improve this result. However, a patch is identified in the plot for highest clad.

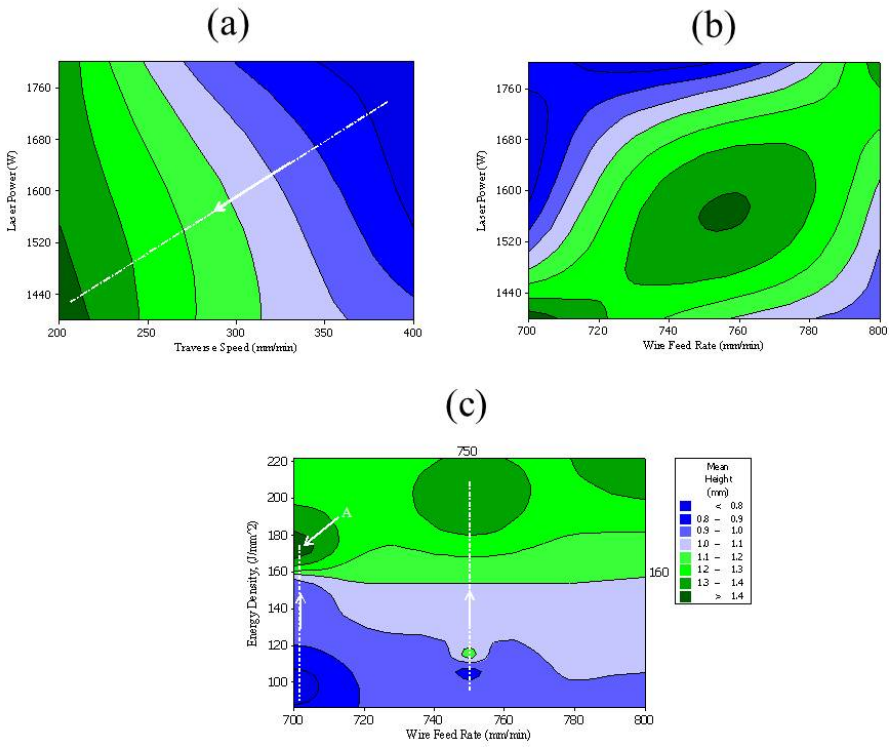

FIGURE 4.9: Contour plots of Ti-6Al-4V deposit height variation for (a)laser power vs traverse speed;(b)laser power vs wire feed rate;(c)energy density vs wire feed rate.

The portion labelled A (Figure 4.9(c)) has the highest values of clad height obtained in the experiment. This implies that energy density required to achieve the maximum clad height (1.4 mm) within the range of process parameters used is 175±5 J.mm^{-2}.

Figure 4.10(a) shows that Ti-6Al-4V/Spherotene deposit height increases as traverse speed decreases at a relatively constant laser power. The maximum height range is bounded by laser power (1550-1760 W) and traverse speed (205±5 mm/min). Figure 4.10(b) shows that the composite bead height increases as both energy density and powder feed rate increase. The maximum height is found to be obtained when the powder feed rate is 29±1 g/min. Figure 4.10(c) shows that the composite bead height increases as energy density increases while the wire feed rate is relatively constant. A maximum height greater than 2.2 mm can be obtained when energy density is 200±10 J.mm^{-2}, and a wire feed rate of 750±5 mm/min is used. Thus, to obtain maximum Ti-6Al-4V deposit height of 1.4±1 mm, the energy density requirement is 175±5 J.mm^{-2}.

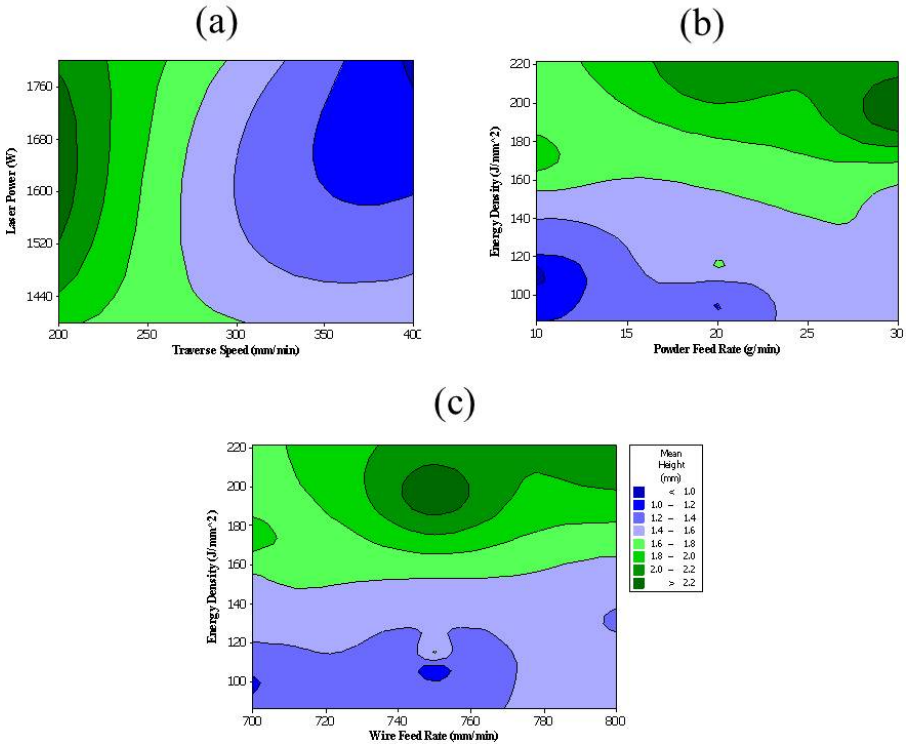

FIGURE 4.10: Contour plots of Ti-6Al-4V/Spherotene deposit height variation for (a) laser power vs traverse speed; (b) energy density vs powder feed rate; (c) energy density vs wire feed rate.

This corresponds to a laser power of 1550±10 W, traverse speed of 210±10 mm/min, 3.1 mm laser beam spot diameter with a wire feed rate of 755±5 mm/min. Also, to achieve a maximum Ti-6Al-4V/Spherotene deposit height of 2±0.2 mm, the required energy density is 200±10 J.mm^{-2}. The corresponding processing parameters are laser power (1650±50 W), traverse speed (205±5 mm/min), wire feed rate (750±5 mm/min) and powder feed rate (30 g/min).

4.2.2 Deposit width

Figure 4.11(a) shows a contour plot of the Ti-6Al-4V deposit width as laser power and traverse speed interact. A good trend is observed as clad width increases with significant increase in laser power and decrease in traverse speed. The maximum value of clad width 5±0.5 mm is bounded by laser power, 1680-1800 W and traverse speed, 200-300 mm/min. The least value of clad width (3.6 mm) is obtained at a traverse speed higher than 300 mm/min and lower laser power not greater than 1420 W. Figure 4.11(b) shows the interrelationship between the traverse speed and wire feed rate. The maximum

clad width is obtained at 210±10 mm/min traverse speed and 790±10 mm/min wire feed rate. The lowest clad width value was observed with a wire feed rate of 760±10 mm/min which is the value range where maximum Ti-6Al-4V deposit height is obtained (Figure 4.9(*b*)). Figure 4.11(*c*) shows the response of the clad width to the energy density. The clad width increases as energy density increases. The plot shows that maximum clad width (5±0.5 mm) is situated at the top right hand corner and requires 210±10 J.mm^{-2} energy density.

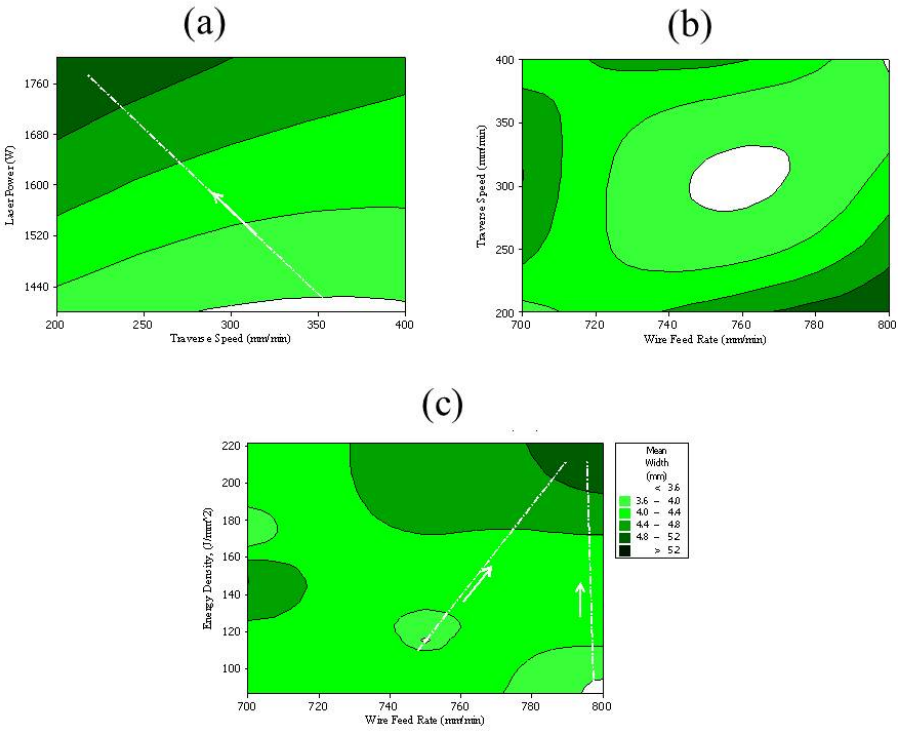

FIGURE 4.11: Contour plots of Ti-6Al-4V deposit width variation for (a) laser power vs traverse speed; (b) traverse speed vs wire feed rate; (c) energy density vs wire feed rate.

Figure 4.12(*a*) shows the two maximum width zones at the top left and right corners of the plot for Ti-6Al-4V/Spherotene deposit as laser power and traverse speed interact. The left corner is bounded laser power of 1700-1800 W and traverse speed of 205±5 mm/min and top right corner is a small region bounded by laser power of 1800 W and traverse speed of 400 mm/min. Figure 4.12(*b*) also shows two maximum width zones relating to energy density and powder feed rate interplay. The first zone is bounded by powder feed rate of 10 g/min and energy density of 110±5 J.mm^{-2}, while the second zone is bounded by powder feed rate of 20±2 g/min and energy density of 215±5 J.mm^{-2}.

However, the latter zone is bigger than the previous. Moreover, the results are not trendy, which makes it a bit difficult to make conclusions; data from a full factorial experiment may improve the results.

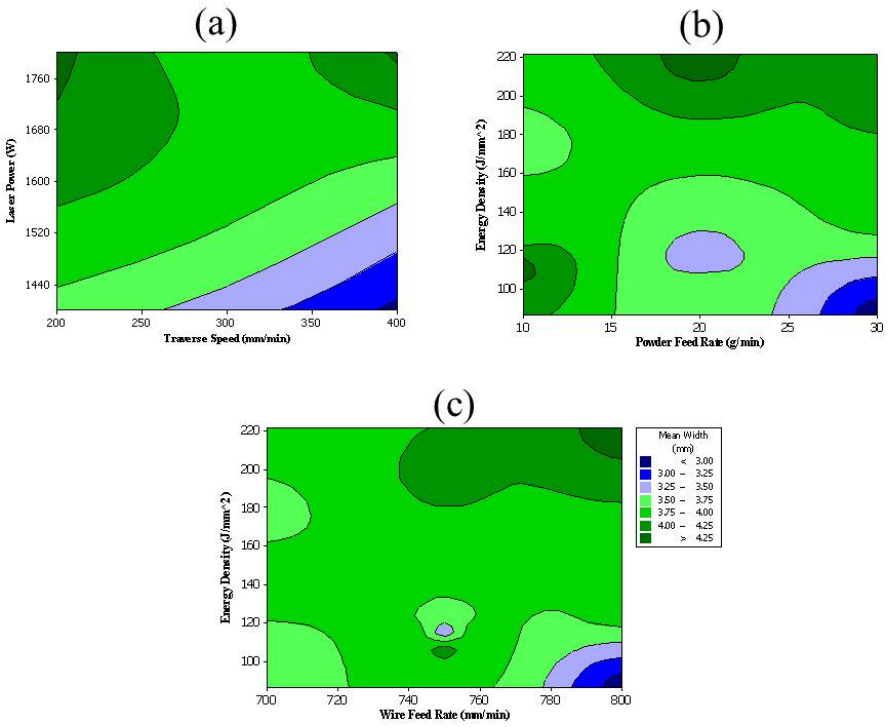

FIGURE 4.12: Contour plots of Ti-6Al-4V/Spherotene deposit width variation for (a) laser power vs traverse speed; (b) energy density vs powder feed rate; (c) energy density vs wire feed rate.

Figure 4.12(c) shows the contour plot of the bead mean width as energy density and wire feed rate change. At the top right hand corner of the plot, maximum width of 4.25±0.2 mm is bounded by energy density 210-220 J.mm^{-2} and wire feed rate of 795±5 mm/min.

Thus, the Ti-6Al-4V deposit maximum width of 5±0.5 mm can be obtained with energy density value of 210±10 J.mm^{-2}. This amounts to the combination of 1800 W laser power, 210±10 mm/min traverse speed, laser beam spot of 3.1 mm, with a wire feed rate of 790±10 mm/min. Also, to obtain maximum Ti-6Al-4V/Spherotene deposit width of 4.25 mm, the energy density requirement is 215±5 J.mm^{-2}. The energy requirement for maximum width of composite bead is similar to that obtained for maximum Ti-6Al-4V deposit width. The corresponding processing parameters are laser power of 1750±50 W, traverse speed 205±5 mm/min, wire feed rate 795±5 mm/min and powder feed rate 20±2 g/min.

4.2.3 Spherotene weight fraction in the composite deposit

Figure 4.13(a) shows that maximum Spherotene content zone occurs at a laser power of 1800 W and traverse speed of 250-300 mm/min as laser power and traverse speed interact. The central region has the greatest percentage of Ti-6Al-4V composition as Spherotene weight fraction falls below 55% wt. The Ti-6Al-4V composition in bead reduces as laser power and traverse speed increase above or decrease below 1550±50 W and 300±40 mm/min respectively. Figure 4.13(b) shows that the Spherotene wt.% in bead increases as the powder feed rate increases, while energy density is relatively constant. The maximum Spherotene content zone lies at energy density of 150±10 J.mm^{-2} and powder feed rate of 29±1 g/min. Figure 4.13(c) shows that the highest Spherotene weight fraction of 75% in a composite bead can be obtained with an energy density of 150±5 J.mm^{-2} and wire feed rate of 700 mm/min.

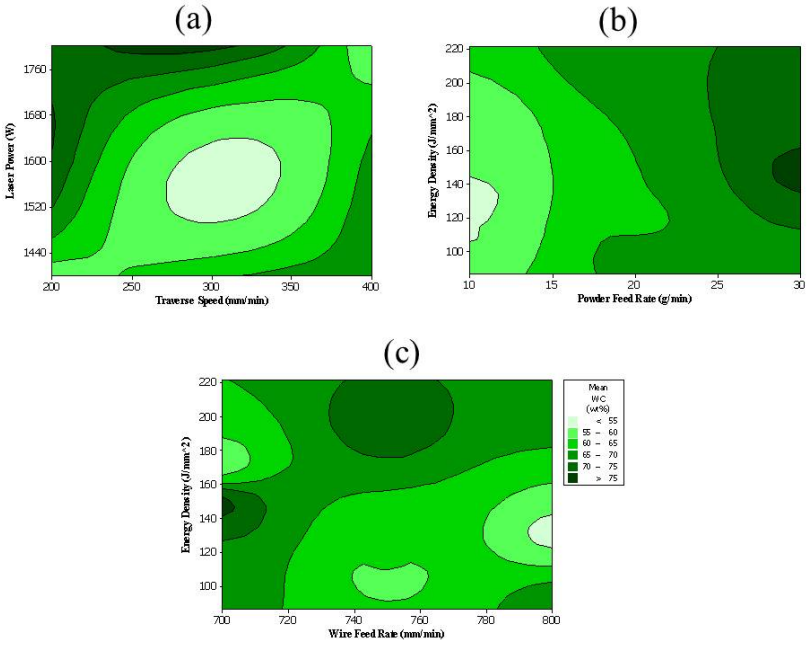

FIGURE 4.13: Contour plots of Spherotene weight fraction in the composite deposit for (a)laser power vs traverse speed;(b)energy density vs powder feed rate;(c)energy density vs wire feed rate.

Hence, to obtain a maximum Spherotene weight fraction of 75% of the bead, the required energy density is 150±10 J.mm^{-2}. The corresponding processing parameters are laser power of 1800 W, traverse speed 275±25 mm/min, wire feed rate 700 mm/min and powder feed rate 30 g/min. Table 4.4 summarises the process parameters required for

maximum physical characteristics of Ti-6Al-4V and composite deposits. It is important to state that beads with maximum height are desirable for building up structures in additive manufacturing, as deposition of components can be achieved within a shorter period of time. However, for area surface cladding on a workpiece, beads with a maximum wider width and low height are desired, which enables each bead to possess a greater contact angle that can eliminate lack of fusion defects of the clad with the substrate.

TABLE 4.4: Optimum process parameters for maximum bead characteristics (a)Ti-6Al-4V; (b)Ti-6Al-4V/Spherotene

(a)

Bead characteristics	Laser power (W)	Traverse speed (mm/min)	Wire feed rate (mm/min)	Energy density (J.mm^{-2})
Max. height (1.4 mm)	1550±10	210±10	755±5	175±5
Max. width (5.2 mm)	1800	210±10	790±10	210±10

(b)

Bead characteristics	Laser power (W)	Traverse speed (mm/min)	Wire feed rate (mm/min)	Powder feed rate (g/min)	Energy density (J.mm^{-2})
Max. height (2.2 mm)	1650±50	205±5	750±5	30	200±10
Max. width (4.3 mm)	1750±50	205±5	795±5	20	215±5
Max. Spherotene fraction (75 wt%)	1800	275±25	700	30	150±10

The predictive models for the Ti-6Al-4V/Spherotene physical characteristics can be presented in a matrix form as show:

$$\begin{pmatrix} H(mm) \\ W(mm) \\ Spherotene(\%wt) \\ Ti-6Al-4V(\%vol) \end{pmatrix} = \begin{pmatrix} 1.69 \\ 1.41 \\ 56.2 \\ 74.2 \end{pmatrix} +$$

$$\begin{pmatrix} (-2.56x10^{-4}) & (-4.33x10^{-3}) & 1.64x10^{-3} & 2.03x10^{-2} \\ 2.14x10^{-3} & (-2x10^{-3}) & (-1.74x10^{-4}) & (-1.53x10^{-2}) \\ 9.75x10^{-3} & (-1.74x10^{-2}) & (-2.63x10^{-2}) & 9.11x10^{-1} \\ (-1.18x10^{-2}) & 1.90x10^{-2} & 2.9x10^{-2} & (-9.03x10^{-1}) \end{pmatrix} \begin{pmatrix} LP(W) \\ TS(mm/min) \\ WFR(mm/min) \\ PFR(g/min) \end{pmatrix}$$

This 4x4 matrix may be executed as a program on an integrated cladding system that controls the laser power, traverse speed of cladding, and rate of feedstock delivery requirements for generation of functionally graded parts or area cladding. The system can further use the output response (bead height, width and material composition) as feedback to the control system.

The percentage contribution of error in all the analysis is low. This error contribution ranges between 0.47-4.09 % which is considered acceptable. A higher error in measurement is noticed in the analysis of the deposit width. This is attributed to the Talysurf profiler exiting scanning range at periphery regions between the clad and the substrate, as illustrated in Figure 4.14. This occurs when the contact angle between the clad and the substrate is about 90^o, however, measurement becomes more accurate when clad contact angle is greater than 100^o.

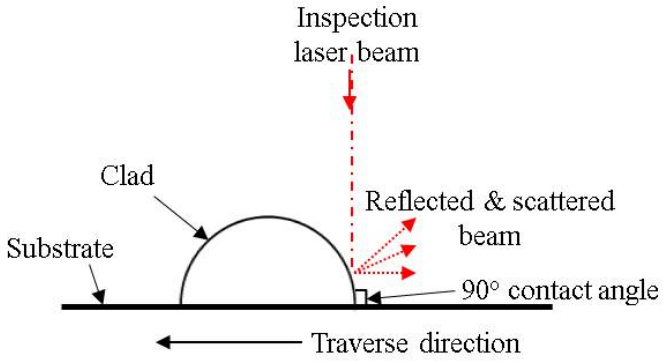

FIGURE 4.14: Schematic of the sharp clad-substrate region where the profiler exits scanning range.

4.3 Successful cladding protocol for Ti-6Al-4V wire/Spherotene powder

The laser cladding process is sensitive to the alignment of the feed material with the melt pool, and the process variables to achieve a stable and consistent deposit. Before

the start of the deposition process, the wire is aligned with the leading edge of the melt pool. The powder feed nozzle is also aligned to deliver the powder into the centre of the melt pool. When the wire becomes aligned with the melt pool centre, it melts before reaching the melt pool. This results in droplet formation on the substrate rather than a consistent deposit as illustrated by a schematic configuration shown in Figure 4.15 This droplet effect can also occur when the process traverse speed is too slow relative to the wire feed rate. Thus, there must be a balance in the relative speeds to achieve a consistent deposition.

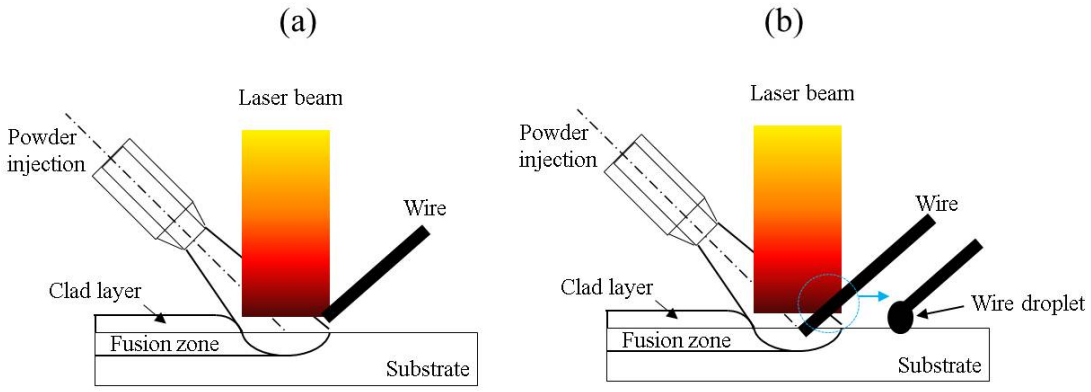

FIGURE 4.15: Feedstock alignment with the laser generated melt pool with Ti-6Al-4V wire positioned at (a)leading edge of the melt pool; (b)centre of the melt pool resulting in droplet formation.

The maximum catchment of Spherotene powder is achieved by having a higher fraction of the powder exposed to the melt pool. This is accomplished by aligning the powder nozzle exit with the centre of the melt pool. Therefore, with proper alignment of materials with the melt pool, good catchment is realised and stable process is achieved. Before the deposition of Ti-6Al-4V wire and Spherotene powder, a stable and consistent process is aimed. The systematic steps to achieve consistency as the process starts are:

- Laser power is first switched on
- Wire feeder is switched on to deliver the Ti-6Al-4V wire only to the leading edge of the melt pool and allow to run consistently for 2-3 sec
- Thereafter, powder feeder is switched on to deliver the Spherotene powder into the melt pool.

FIGURE 4.16: Single tracks deposited with the same parameter combination (a)Deposited with both powder and wire fed at the same time, (b)Deposited with wire firstly fed followed by powder injection.

It is important to follow the order, as this promotes stability in the process at the initial start. Figure 4.16 shows single tracks deposited with the same process parameters. Different visual results are observed when the same process factor combination is used. Figure 4.16(a) shows a deposited track with a rough surface obtained when both the powder and the wire are fed at the same time into the melt pool. The deposition is not stable, as wire droplet occurs during deposition. Figure 4.16(b) shows a deposited track of a better surface quality with wire firstly fed into the melt pool before powder delivery. With a smooth deposition of the wire only at the beginning, the substrate and the wire would have been preheated, and this helps the make the deposition to remain stable even with the injection of the Spherotene powder.

4.4 Characterisation of Spherotene powder and Ti-6Al-4V/Spherotene composite

This section reports the characterisation of Spherotene powders in terms of their particle size, particle morphology, and phase composition. The deposits are characterised using X-Ray Diffraction (XRD) and Scanning Electron Microscope (SEM) with Energy Dispersive X-ray Spectroscopy for phase identification and microstructural features. The microstructural observations of composite are related to the laser processing. Deposit hardness is reported with respect to the processing parameters employed and the changes in the microstructure.

4.4.1 Spherotene, tungsten carbide powder

The particle size analysis of the Spherotene powder and its phase composition are conducted as described in Section 3.1.2 and 3.8.2 respectively. The powder has a size distribution range of 40-160 μm as quoted by the supplier. Figure 4.17 shows the particle size analysis obtained by laser diffractometry. The particle size ranges from 40-270 μm. The cumulative volume curve shows that 10% of the powder has size below 91 μm (d_{10}) and above 186 μm (d_{90}). The d_{50}, mass median diameter size of the supplied powder is 136 μm. This means 50% of the powder has size greater than this value and 50% of the powder has a size less than 136 μm. The volume mean diameter of the powder is 138 μm in the as received condition. Figure 4.18 shows the SEM image of the powder particle surface morphology. The particles are predominantly spherical, with some asymmetric shaped and few satellite particles. Grain boundaries/surface cracks are observed on the powder surface at higher magnification. This is suggested to be due to rapid cooling during powder production. Figure 4.19 shows the Spherotene particle cross section at both low and high magnification. Tangled needles are observed which is consistent with the description of the Spherotene particle microstructure as the powder is produced by a patented cold crucible process [112]. This process is a form of non-conventional gas atomisation. The dark areas in the particle cross section are likely to be WC and the bright areas W_2C due to different mean atomic numbers.

Figure 4.20 shows the XRD pattern of the Spherotene powder obtained with the phases identified and labelled for a scan over a 2θ range of 30-90^o. The peaks in the spectrum are compared with the standard patterns in the International Centre Diffraction Database (ICDD) for varying combinations of tungsten, W and carbon, C. The diffracted peaks match patterns of WC (ICDD no: 01-073-0471) and W_2C (ICDD no: 00-035-0776). The powder pattern with the matching phases can be found in Appendix B.1. The crystallographic information about the phases identified (ICDD files) can be found in Appendices B.2 and B.3.

The phase, W_2C, HCP (101) has the strongest single reflection at $2\theta = 39.6^o$ in the spectrum. This suggests that W_2C could be the dominant phase on the surface layer of the as-received Spherotene powder. However, peaks matching tungsten carbide, WC, HCP, are found at 31.5^o, 35.6^o, 48^o, 64^o, 66^o, 73^o, and 84^o.

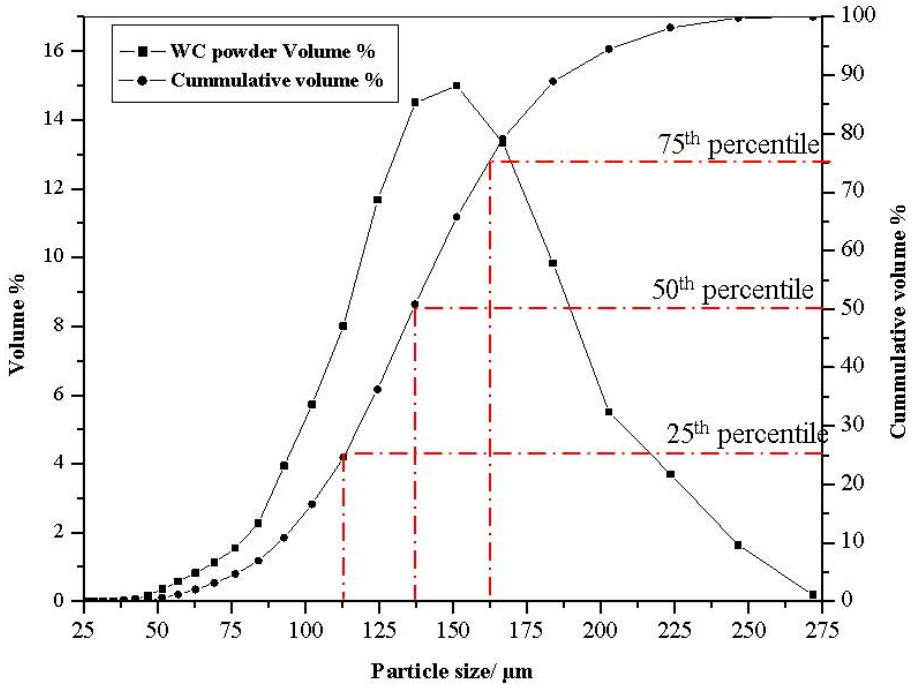

FIGURE 4.17: Particle size distribution of as received Spherotene powder with cumulative volume % curve showing that the 50th percentile as mean size of 136 μm.

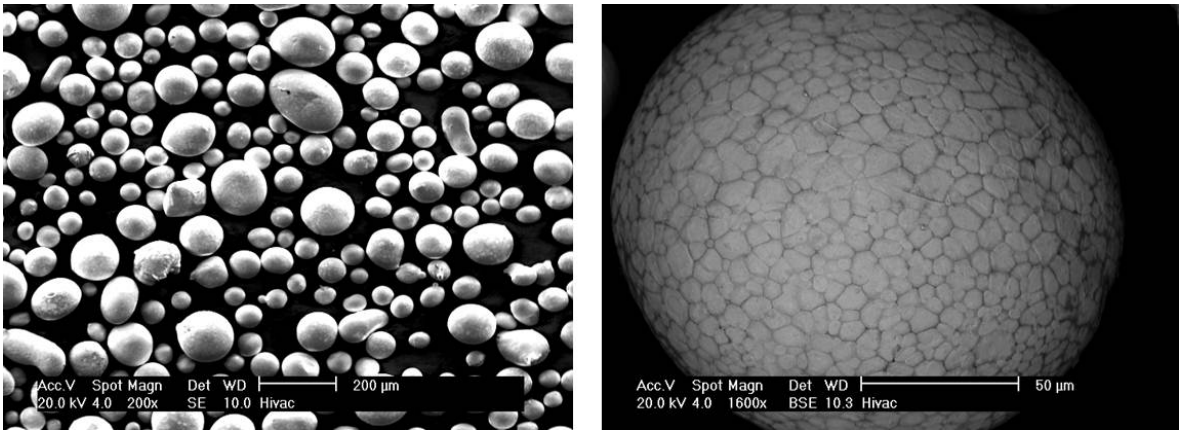

FIGURE 4.18: Spherical surface morphology of Spherotene in the as received condition.

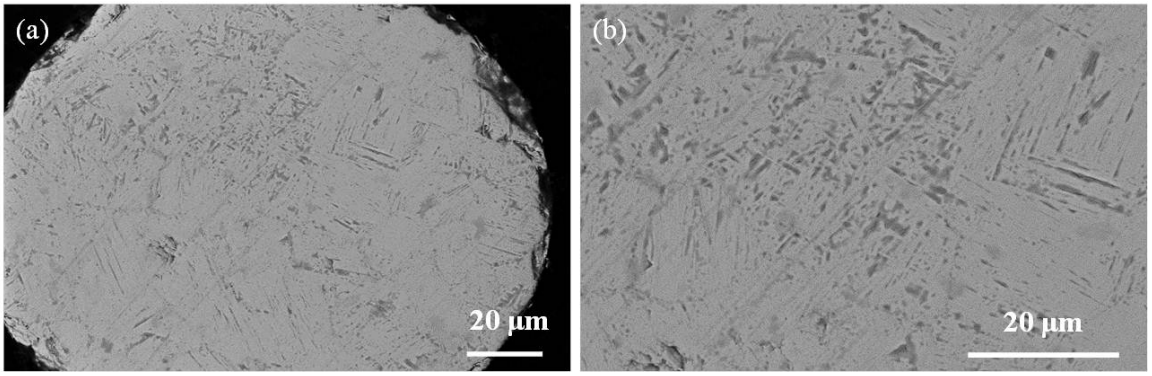

FIGURE 4.19: BSE images of the Spherotene powder cross section showing the tangled needles.

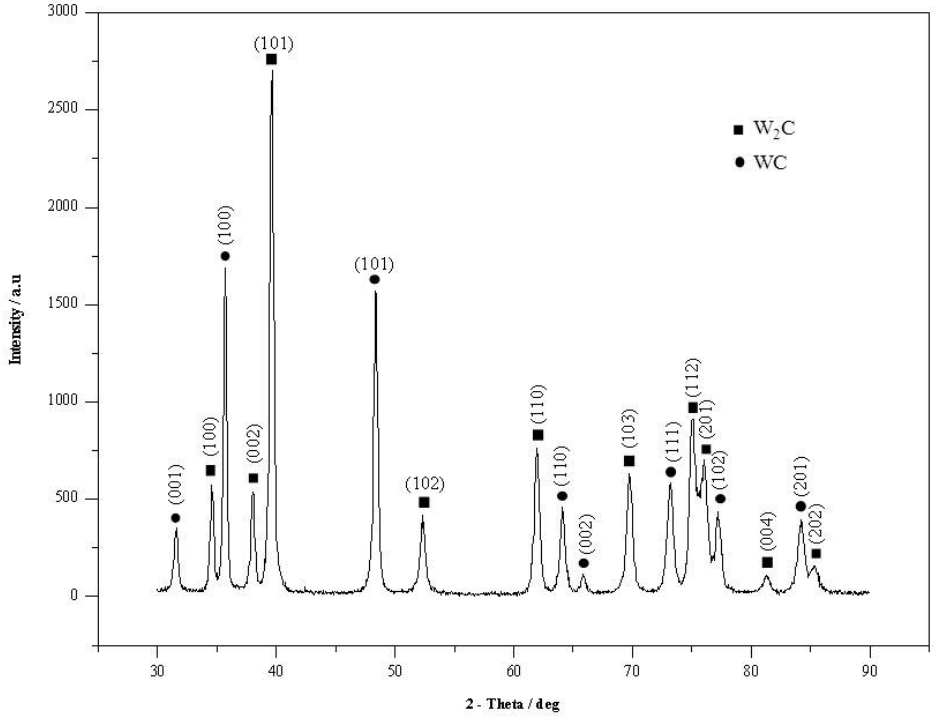

FIGURE 4.20: XRD spectrum for Spherotene with W_2C and WC identified.

The mean density of the Spherotene was measured to be 16.257±0.007 g/cm^3 using AccuPyc 1330, gas pyncometer, to determine the volume ratio of WC to W_2C in the powder. Having the density of WC as 15.7 g/cm^3 [57] and density of W_2C as 17.1 g/cm^3 (Appendix B.3), and using the linear rule of mixture (RoM) (equation 4.7), a 0.6:0.4 volume ratio of WC to W_2C is obtained.

$$\rho_{Spherotene} = \rho_1.x + \rho_2.(1 - x) \tag{4.7}$$

Where, x = volume fraction of WC, ρ_1 = density of WC, ρ_2 = density of W_2C and $\rho_{Spherotene}$ = mean density of Spherotene measured.

4.4.2 Microstructure of Ti-6Al-4V/Spherotene deposits

4.4.2.1 Composite bead characteristics

Figure 4.21 shows micrographs of the bead cross sections prepared as described in Section 3.8. The energy density analysis reported in Section 4.2.1 shows that the composite bead with maximum height of 2±0.2 mm corresponds to Figure 4.21(d). The lowest of the bead cross section is Figure 4.21(i). The composite bead with maximum width of 4 mm corresponds to Figure 4.21(g) and (i). These beads with maximum width are deposited using a high laser power of 1800 W which had a significant influence on bead width.

Based on previous analysis on Spherotene content in Section 4.2.3, the cross section of the bead in Figure 4.21(h) has the highest. The Spherotene/Ti-6Al-4V bead composition weight ratio is determined as 76:24. The micrograph of the bead cross section in Figure 4.21(d) shows an appreciable amount of Spherotene particles retained and the bead composition ratio is 74:26. Its composition is relatively similar to the bead (Figure 4.21(h)) determined to possess the highest amount of Spherotene. All the beads are metallurgically bonded to the Ti-6Al-4V substrate with minimal melt depth with no cracks or delamination observed. The melt depth would be analysed in a later section to determine its size range and the influence of the processing condition on the depth range.

In all the bead cross section, there is a relatively uniform distribution of particles in the composite matrix even when lower laser power (1400 W) is employed. Fewer particles are observed in bead cross sections (Figure 4.21(a), (e), and (i)) owing to a low powder flow rate (10 g/min) employed.

4.4.2.2 Reinforcement distribution and size variation in composite bead

The bead cross section with the maximum reinforcement wt.% is selected for a microstructural examination using the SEM. Figure 4.22 shows that there is a fairly uniform distribution of the powder particles in the melt. Some of the particles are found

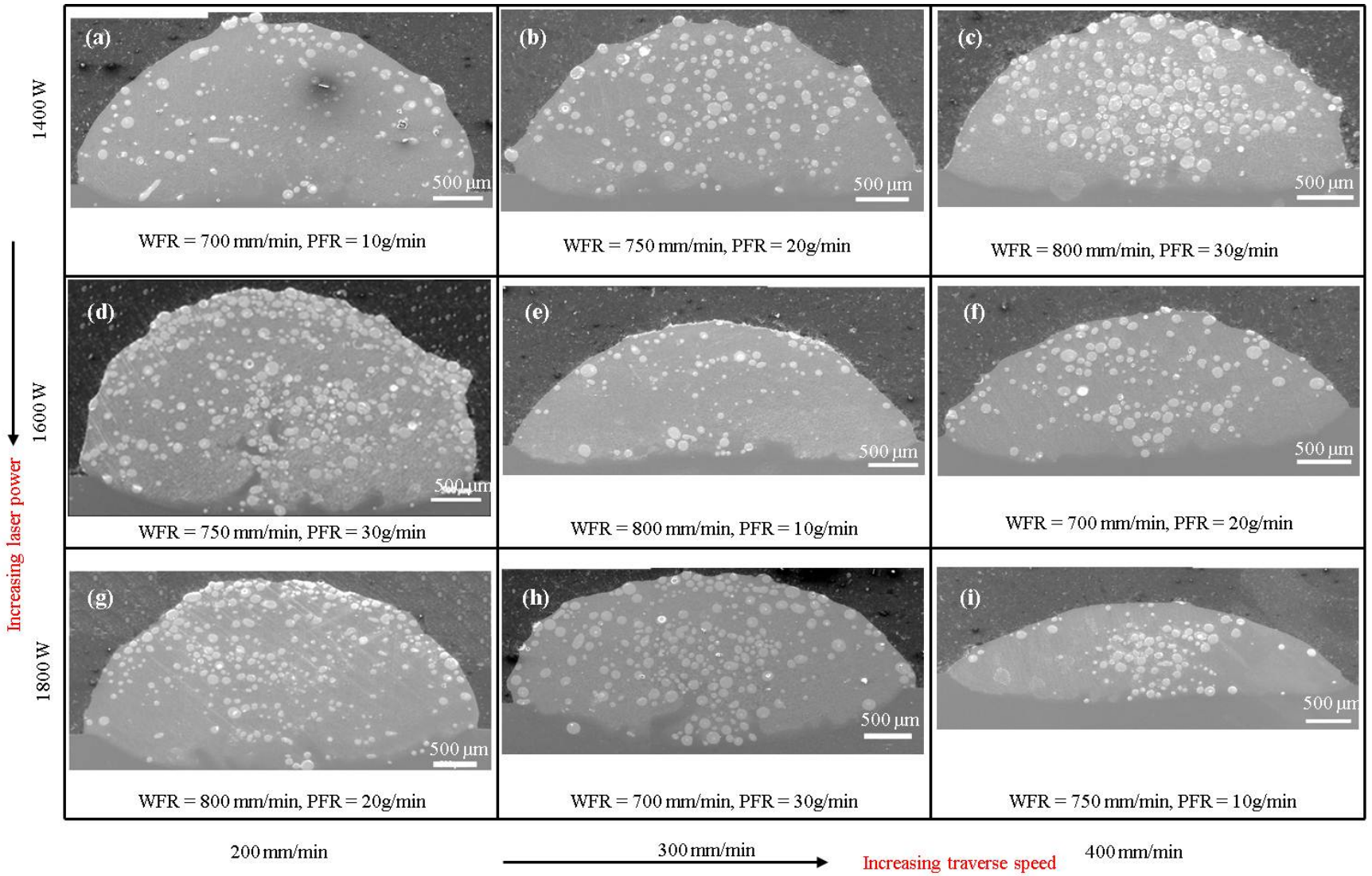

FIGURE 4.21: BSE-SEM micrographs of Ti-6Al-4V/Spherotene composite bead cross sections (White features are Spherotene particles in cross section).

to have pores, but the composite matrix is pore-free.

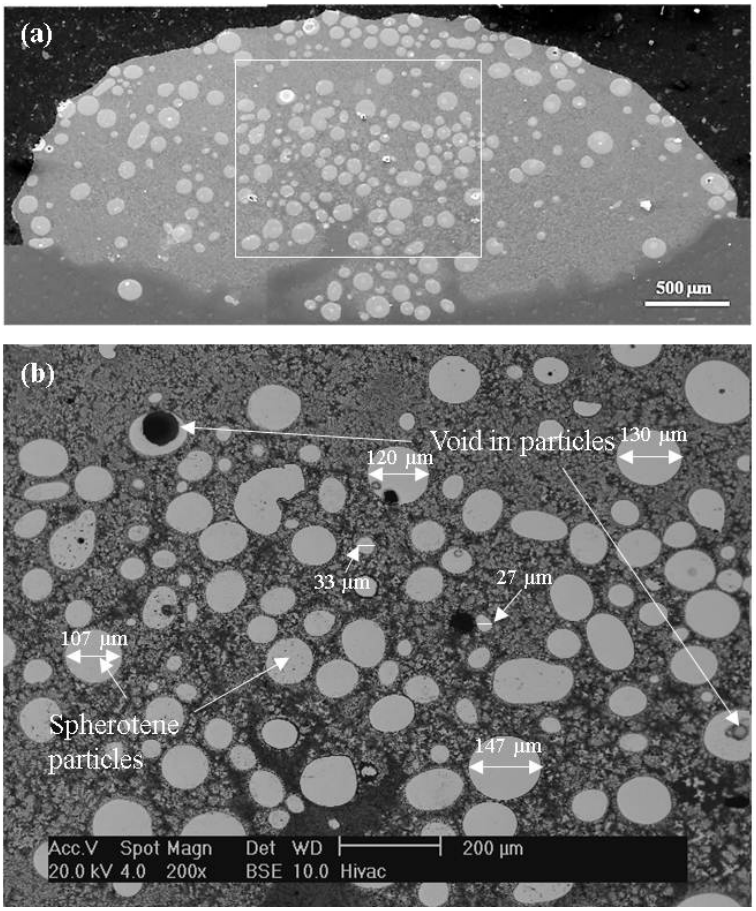

FIGURE 4.22: BSE-SEM image of the Ti-6Al-4V/Spherotene bead (a)Bead deposited with composition 76 wt% reinforcement/24 wt% Ti-6Al-4V (b)magnified box section in (a).

Figure 4.23 shows the particle size distribution of the embedded Spherotene particles in the clad section shown in Figure 4.22 using the ImageJ software. Similar analysis for clad cross sections in Figure 4.21 can be found in Appendix B.4. In reality, it is difficult to measure the particle size in the composite bead using the particle cross sections. Therefore, it is assumed that majority of the spherical particles seen in the micrograph are half-sectioned to assess their sizes. The surface area of the Spherotene particles is measured with an assumption that the each particles have a circular cross section. The diameter of the spherical particle is determined from the surface area measured and plotted against their frequencies in the histogram chart. It is observed that the modal size of the Spherotene particle population in the clad is 80-100 μm. The median diameter size (50%) of the Spherotene particles embedded is 63 μm. The highest Spherotene particle size diameter observed in the clad cross section is 160 μm.

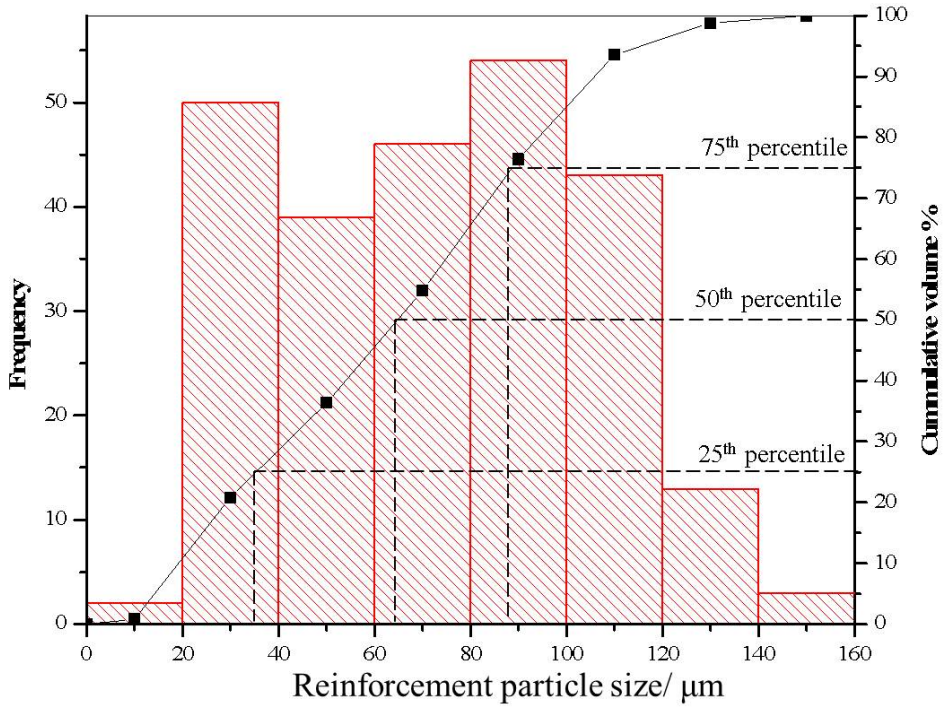

FIGURE 4.23: Particle size distribution of the Spherotene particles embedded in the clad (Figure 4.22).

The highest value of reinforcement particle size diameter in clad is far lower than the largest particle size of 270 μm obtained from laser diffractometry (Figure 4.17). This calls for concern and necessitated the Spherotene particle size to be revisited and evaluated with the imaging software. Figure 4.24 shows particle size distribution of the as-received Spherotene powder using the ImageJ software. The size range of the powder particles measured lies between 40-200 μm. The median size (50%) of the as-received powder particles is 97 μm, based on the imaging analysis. The result obtained from the imaging analysis is in close agreement with the particle size range quoted by the powder supplier.

Comparing the ImageJ analysis of as-received powder and the embedded particles in the clad, the frequency of the Spherotene particles less than 40, 60, and 80 μm sizes is greatly increased after laser processing. The frequency of the sizes less than 40 μm is insignificant in the as-received powder, while after processing, 25% of the retained particles is of size less than 40 μm.

Figure 4.25 shows that the mean particle size of Spherotene has greatly reduced after processing as observed for beads presented in Figure 4.21 (a-i) when compared to the

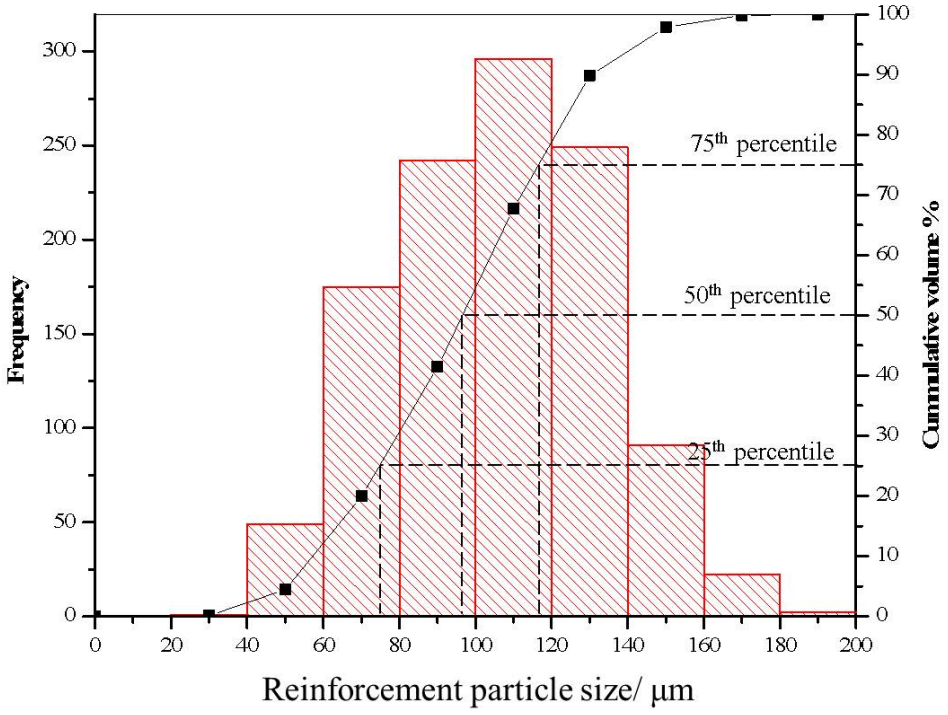

FIGURE 4.24: Particle size distribution of the as-received Spherotene powder using ImageJ (Figure 4.16).

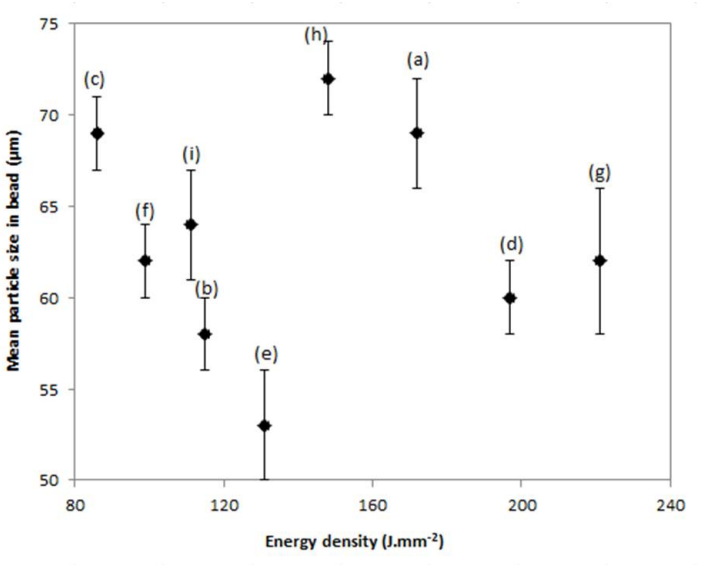

FIGURE 4.25: Variation in the Spherotene particle mean size in beads labelled (a-i) in Figure 4.19.

particle size distribution of the as-received powder. This is expected since the as-received Spherotene particles suffer surface melting during their interaction with the laser beam during processing. This results in a decrease in the observed particle size.

4.4.2.3 Phases present in Ti-6Al-4V/Spherotene composite bead

The XRD spectra of all the beads shown in Figure 4.21 are similar with the same phases identified. Figure 4.26 shows the XRD spectrum obtained for bead characterised to possess the highest weight composition of Spherotene (Figure 4.21(h)). The phase identification is made by comparing the diffraction peaks with the phase patterns in the ICDD database. The matching phases with their pattern file number include:

- W_2C (ICDD No: 00-0356-0776),
- WC (ICDD No: 01-073-0471),
- TiC (ICDD No: 01-073-0472),
- W (ICDD No: 00-004-0806) and
- β -Ti (ICDD No: 00-044-1288)

The spectrum with the matching phase patterns is presented in Appendix B.5. Also the XRD scans for other beads can be found in Appendix B.6. The first two phases (WC and W_2C) mentioned correspond to the phases identified in the Spherotene powder supplied. Thus, the ICDD file for the identified TiC, W and β-Ti are presented in Appendices B.7 - B.9. Broad based peaks are observed and a strong reflection at $2\theta \approx 39^o$ which concides with W_2C and β -Ti phase patterns. The mechanism of phase formation will be discussed in a later subsection.

4.4.2.4 Microstructural features of Ti-6Al-4V/Spherotene beads

Having determined the phases present in the composite beads by XRD, SEM is employed to identify the phases in the slighty etched composite micrograph. Figure 4.27 shows the magnified region around two Spherotene particles in the composite matrix having different reaction zones. Figure 4.27 (a) shows a particle with a uniform reaction layer,

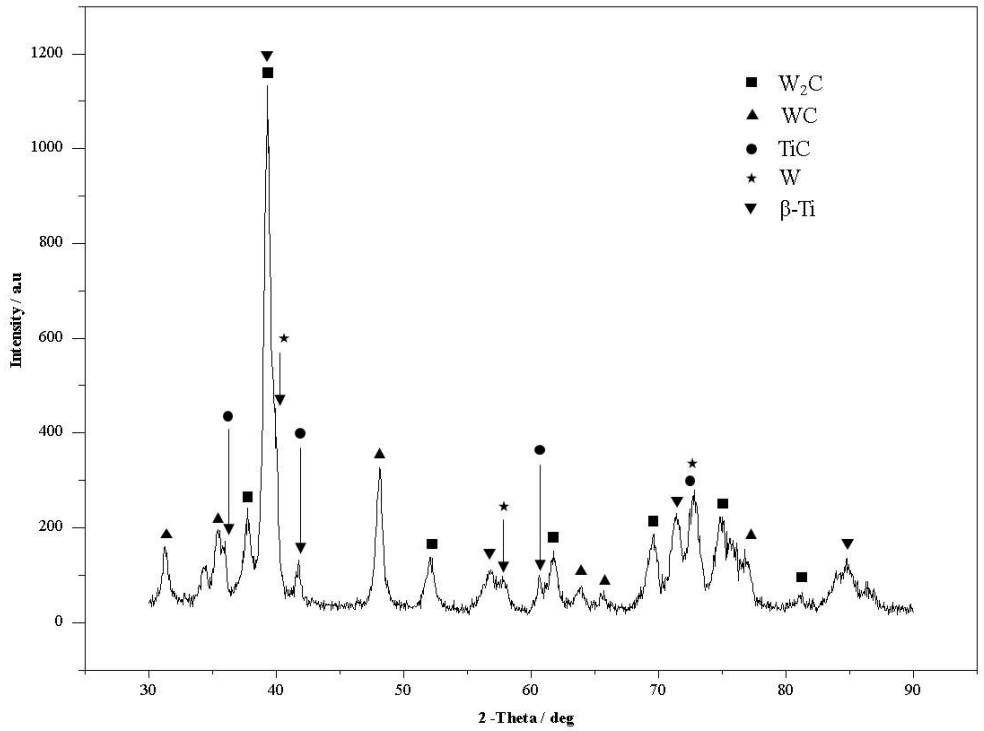

FIGURE 4.26: XRD spectrum for the composite bead with phases identified.

while Figure 4.27(b) shows a mixed reaction layer around the Spherotene particle. The regular reaction layer around the reinforcement particle is observed to be 2±0.2 μm thick. Many of the Spherotene particles found around the bead periphery possess the regular and circular reaction layer. The particles located in the central region of the bead are characterised by the mixed reaction layer. The proportion of the particles possessing either of the reaction layer can be put at 50:50. Based on the mean atomic number, the darkest phase observed in the back scattered electron (BSE) mode is the least dense phase. The phase precipitate with the brightest contrast is the most dense. Thus, TiC phase is identified as the regions with darkest contrast in the micrographs. The TiC precipitates form the reaction layer around the Spherotene particles (Figure 4.27(a)). In Figure 4.27(b), the TiC phase is precipitated and locked in the fragments of the particles which are dissolving into the melt solution. The composite matrix is characterised by a grey contrast identified as the β-Ti phase.

The Spherotene particles have been characterised as a polycrystalliine powder with WC and W_2C phases. Thus, the particles in the melt are expected to retain these phases. White equiaxed dendritic structures with TiC precipitates locked in the tiny pockets of the structure are observed in the composite matrix. These flowery like, white precipitates

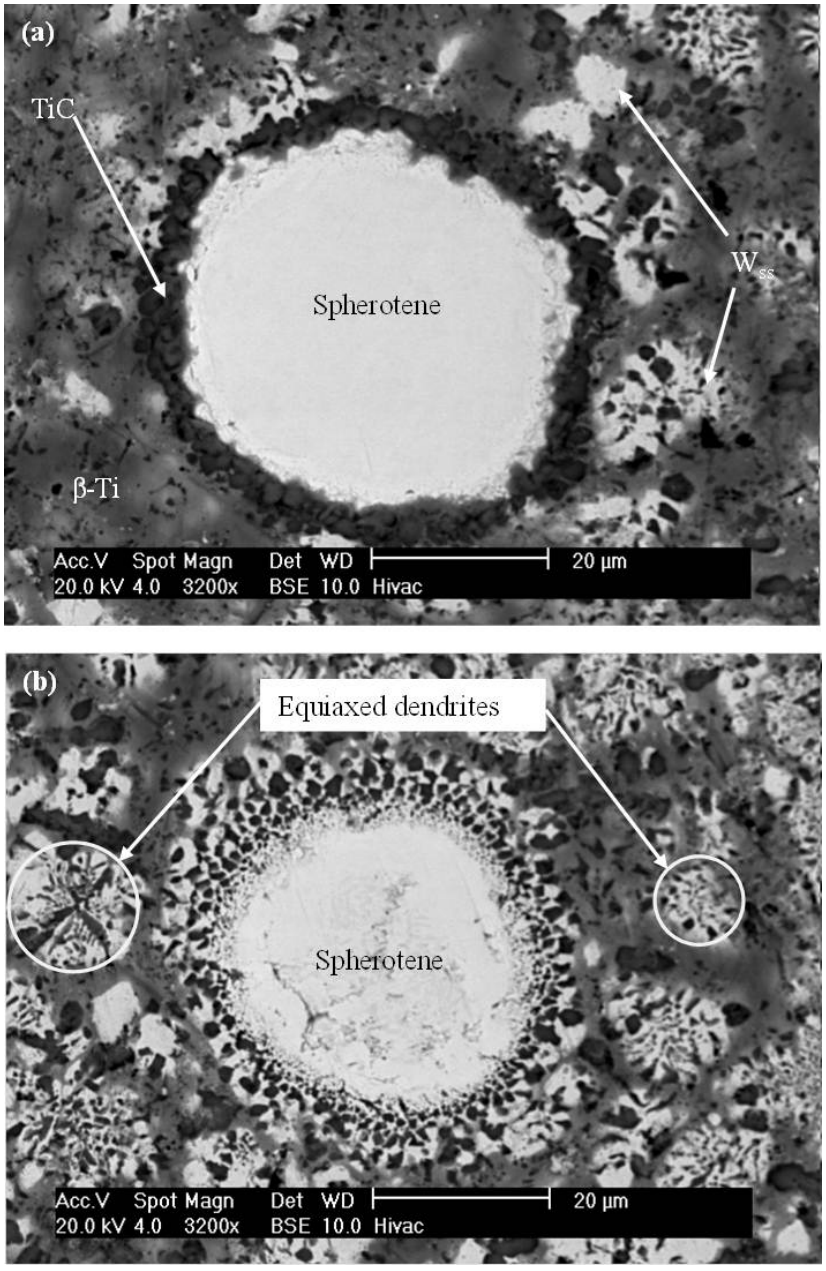

FIGURE 4.27: BSE-SEM images of etched sample with the reaction zone around the Spherotene particles in the matrix showing (a)a regular and circular TiC reaction layer; (b)a mixed reaction layer.

are identified as W solid solution, W_{ss}, according to the XRD result (Figure 4.26). This phase appears to have evolved out of the Ti_{ss} as the melt rapidly cools.

Figure 4.28 shows a magnified view of the composite microstructure at a higher contrast level. A circular casing/layer, brighter than the core part of the Spherotene particle, is observed around the particles. This brighter casing is identified as W_2C, which is expected to be denser than WC. The thickness of the W_2C band observed is 3 ± 0.2 μm and this may increase as WC decarburisation occurs. The flowery, equiaxed dendritic structure is observed to be of the same brightness as the circular W_2C band around the Spherotene particle.

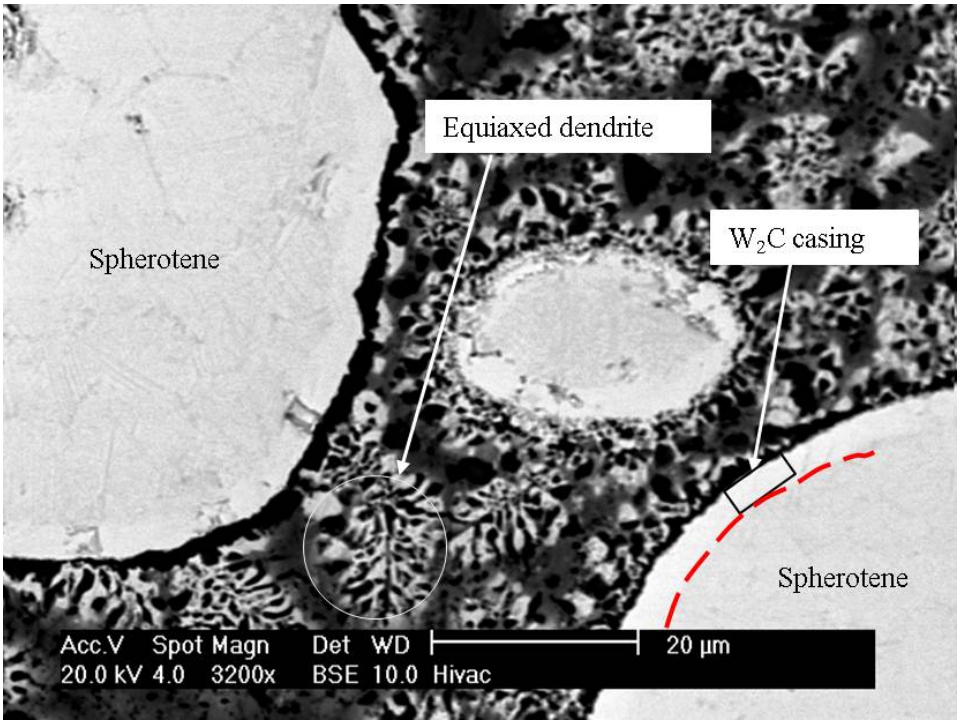

FIGURE 4.28: High contrast BSE-SEM image of etched sample showing the circular bright band of W_2C.

Figure 4.29 shows an EDX linescan across two adjacent particles. The variation of elemental compositions across the line scan complements the phases identified. As the scan passed from the core part of the Spherotene particle A, the scan observed for W is intense with no trace of other elements. As the scan reaches the TiC layer around the particle edge, the intensity of Ti, Al, and V become strong with Ti having the strongest reflection. The intensity of W is negligible in the TiC reaction layer region. As the scan continues into the composite matrix region identified as Ti_{ss} phase, the Ti

intensity drops with an increase in intensities of Al, V and W. As the line scan crosses the continuously dissolved reaction layer around the small particle in the micrograph, there are series of fluctuations of high and low peaks of Ti and W. When the scan line crosses the edge of the Spherotene particle B, the intensity of Ti increase again indicating the TiC precipitate layer. The scanning ends in the particle B and only the intensity of W appears strongly. Figure 4.30 shows an elemental linescan across a Spherotene particle in the matrix at a higher contrast level. An attempted is made towards identifying W_2C and WC phases distinctively using the EDX linescan. The W_2C phase is observed in the micrograph based on the contrast level, but the two phases cannot be differentiated by the EDX linescan.

Figure 4.31 shows W_{ss} precipitates observed as flower-like, equiaxed structure with dark TiC phases locked in between the arms of W precipitates. An elemental area map over the feature shows that the white precipitates are W-rich as indicated by the green colour which traces the white region. The red colour traces region rich in Ti in the area analysed. Ti-rich regions are observed to be areas between the W-rich zones and areas outside the two-phase feature. The distribution of the two-phase feature is observed to be homogenous and are mutually present in regions where TiC precipitates are formed.

Figure 4.32 shows an EDX map used to observe the elemental distribution of vanadium, V in the microstructure after deposition. It is observed that the Spherotene particle edges, the W_{ss} phase and the TiC phases can be distinctly identified from the β -Ti phase. The area map thus confirm the V-rich regions as the background contrast which is the Ti_{ss} phase.

Employing the EDX area quantitative analysis, the W at.% present in the β-Ti phase region is obtained. Figure 4.33 shows a magnified region of the left, central and right sections of the micrograph in Figure 4.22(a). Area elemental compositions of the β-Ti regions in the micrographs are obtained and presented in Table 4.5. The at % values obtained from the area EDX analysis shows that the elemental composition of the Ti, Al, V and W are uniform irrespective of the region in the clad. The standard deviation of the results is less than 1 at. % for all the elements analysed with a standard error value in all cases less than 0.4. The mean atomic value of Ti is 75.4 at.% and that of Al, V and W are 12.6 at.%, 4 at% and 8 at.% respectively. From the area EDX analysis,

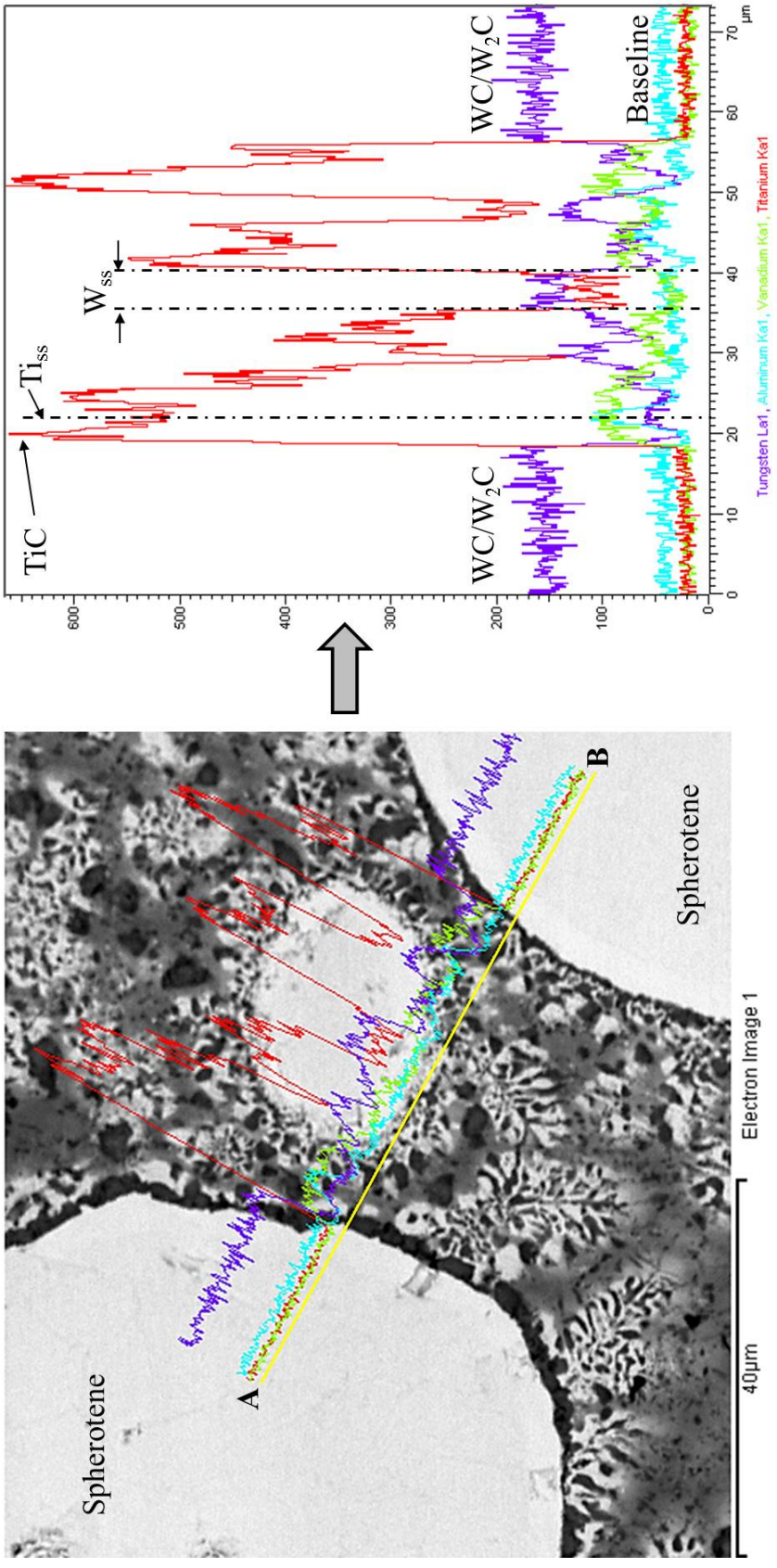

FIGURE 4.29: An EDX linescan across two adjacent Spherotene particles through a particle edge and the composite matrix.

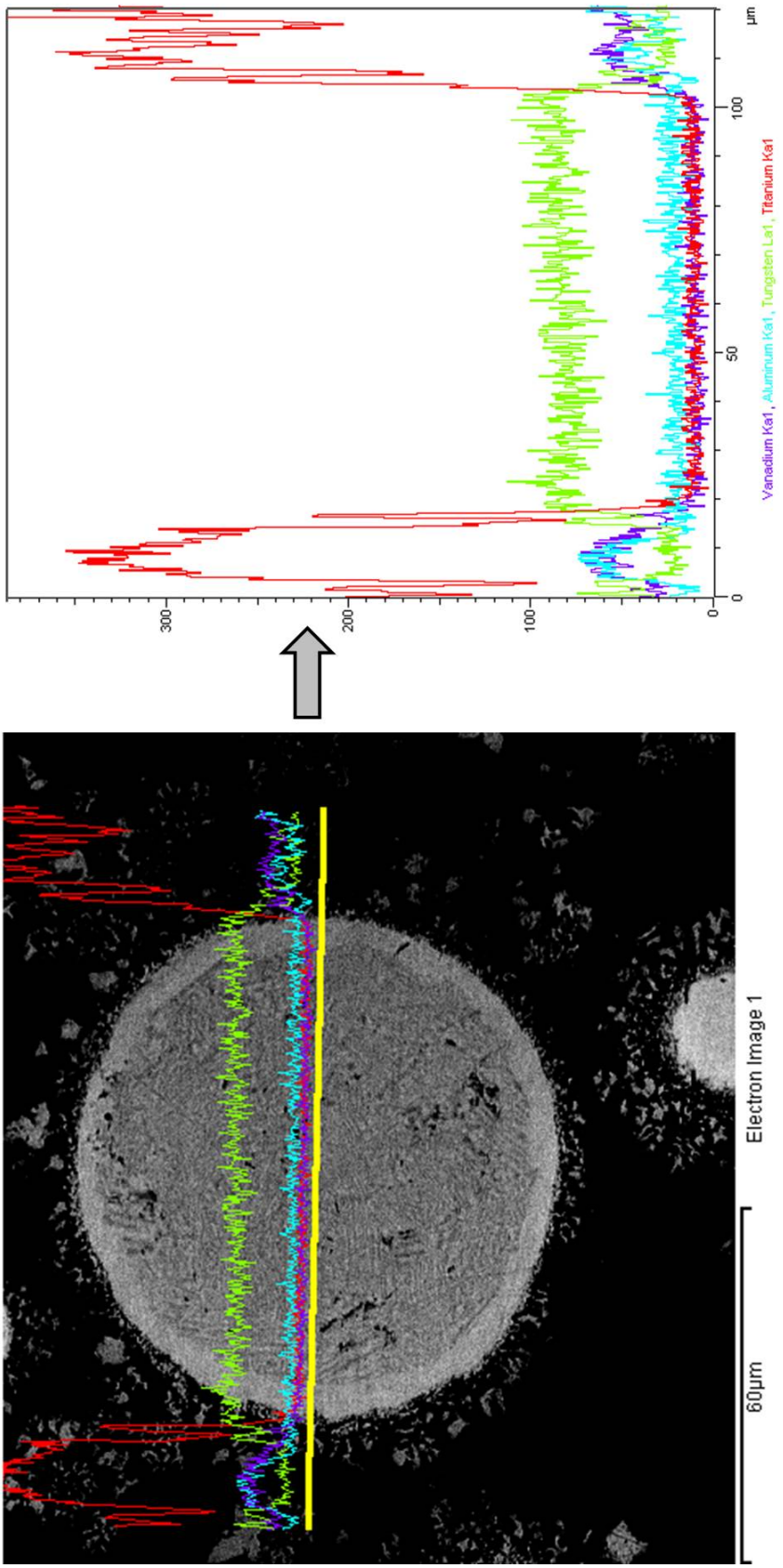

FIGURE 4.30: An EDX linescan across a Spherotene particle with an attempt to identify the elemental composition of the bright casing.

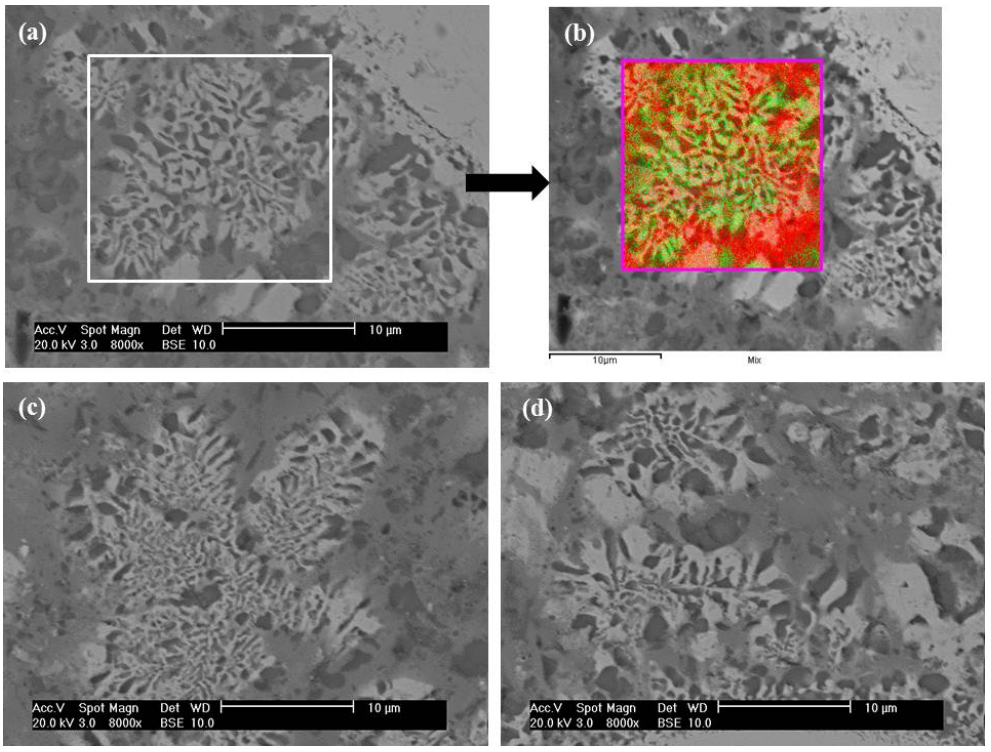

FIGURE 4.31: BSE-SEM images of flower-like equiaxed dendrites formed from β (Ti, W) decomposition, obtained from; (a) right side; (b) elemental map of a section in (a), Red colour Ti; Green W; (c) central region; (d) left side; of the composite.

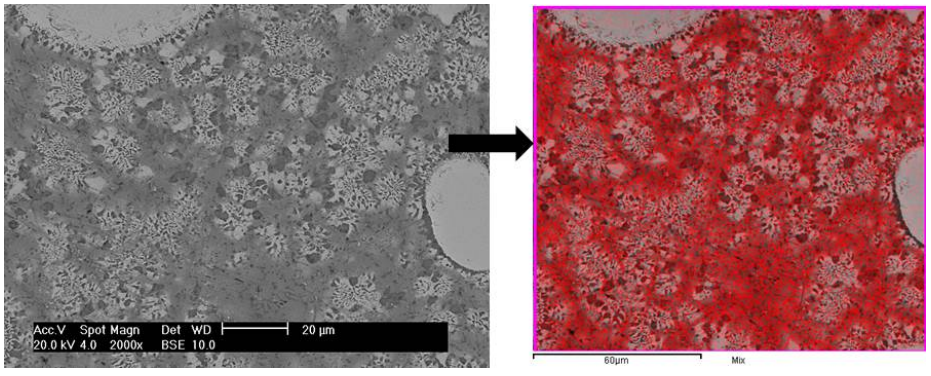

FIGURE 4.32: Elemental distribution of vanadium in the MMC stabilising β -Ti phase(Red colour - Vanadium).

the elemental composition of the β -Ti phase is obtained. The analysis shows that the Ti solid solution possesses less than 10 at.% of tungsten, W.

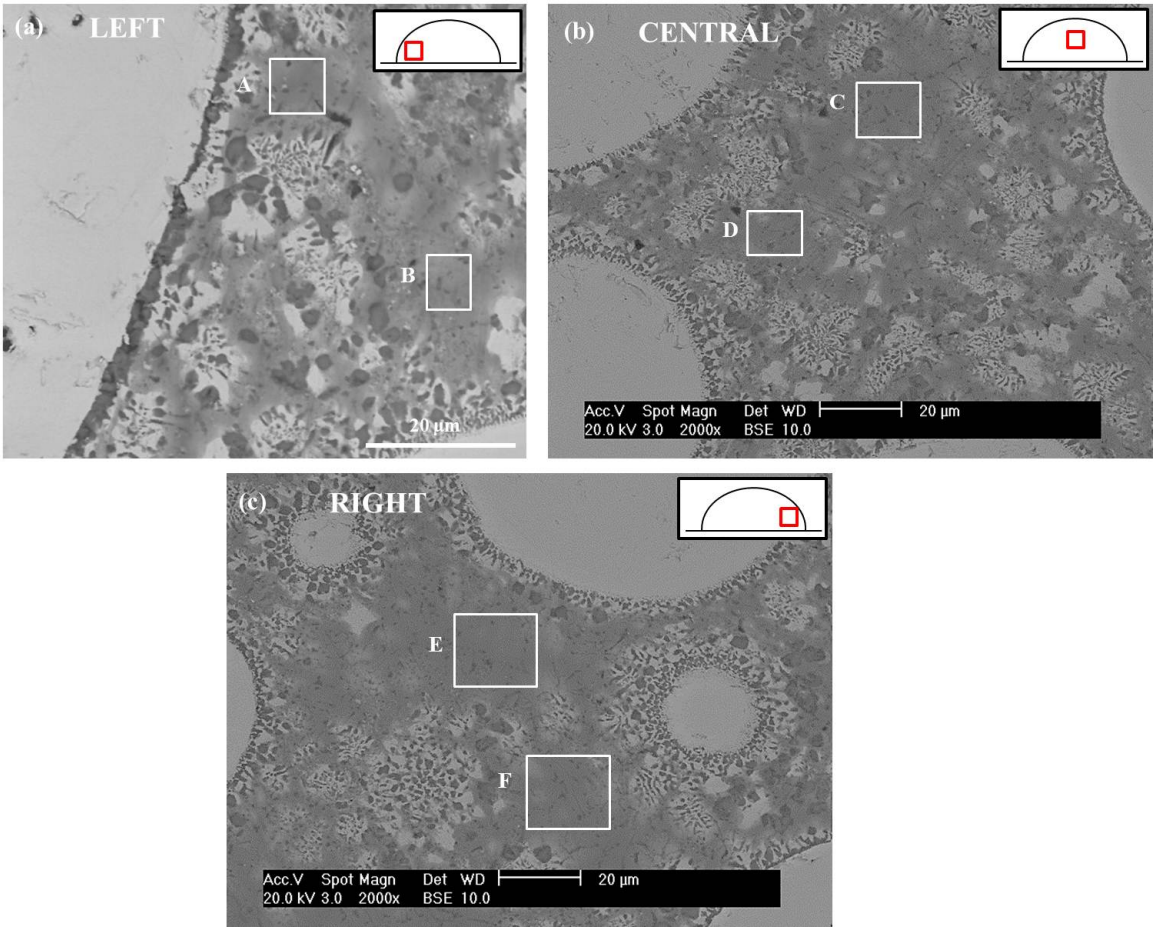

FIGURE 4.33: BSE-SEM micrographs of etched sample showing the composite microstructure with EDX area sections in boxes (a) left; (b) central and (c) right section of Figure 4.22(a).

4.4.3 Effect of the process factors on the W (at.%) in the β -Ti phase

Elemental composition of the β -Ti phase in 6 different locations in the clad cross sections are obtained with their mean values determined. The table of results for the mean values of W (at.%) in the Ti_{ss} can be found in Appendix B.5. Figure 4.34 shows the main effect plot for the influence of the laser power, traverse speed and powder feed rate on the composition of tunsgten, W (at.%) retained in the β -Ti phase before solidification occurs.

TABLE 4.5: Elemental composition (at.%) of boxed sections in Figure 4.33

Clad region		Ti (at.%)	Al (at.%)	V (at.%)	W (at.%)
Left	A	75.12	13.02	4.14	7.71
Left	B	75.47	12.53	3.92	8.08
Central	C	74.02	12.45	4.08	9.45
Central	D	75.13	12.84	3.95	8.09
Right	E	76.41	12.61	4.01	6.97
Right	F	76.21	11.97	3.89	7.94
Mean (at.%)		75.39	12.57	4.00	8.04
Standard Deviation		0.86	0.36	0.10	0.81
Standard Error		0.35	0.15	0.04	0.33

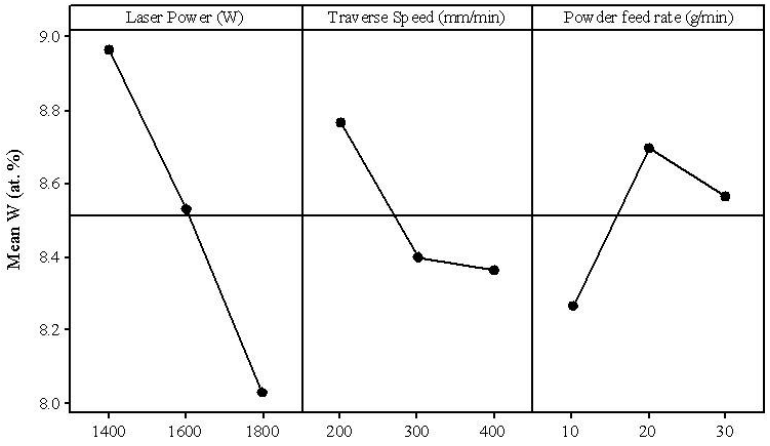

FIGURE 4.34: Main effects plot for W (at.%) in β-Ti phase.

Increasing laser power and traverse speed favour the reduction in the W (at.%) composition in the β-Ti phase of the Ti-6Al-4V/Spherotene composite beads. Increasing powder feed rate favours more retention of the dissolved W in the Ti solid solution. Laser power is the most significant processing variable with a strong, inverse trend observed. A 9 at.% W is retained when 1400 W laser power is employed and decreases to 8 at.% at 1800 W. However, it is noted that the composite bead deposited possessing 76 wt% of Spherotene (Figure 4.21 (h)) has (7.5-8) at.% W retained in its β -Ti phase. This is the lowest amount of W content retention obtained in the laser cladding process for the Ti-6Al-4V wire and Spherotene powder deposits.

4.4.4 Clad/Substrate Interface

Figure 4.35 shows the clad/substrate interface with an appreciable melt pool depth for a proper metallurgical bond between the clad and the substrate. No cracking or

porosity is observed at the interface even in the presence of Spherotene particles around the clad/substrate region. An EDX line scan across from the clad into the substrate confirms a step in elemental variation across the interface.

The melt pool depth and the heat affected zone in the substrate thereafter, were examined using optical microscopy and are discussed in the next subsection.

4.4.4.1 Melt Pool Depth (MPD) and Heat Affected Zone (HAZ)

Figure 4.36 shows the optical image of the clad possessing Spherotene/Ti-6Al-4V (76:24)wt% composition with melt pool depth and the HAZ labelled. The depth of the fusion zone and the HAZ were measured using a Nikkon optical microscope after etching the samples with Krolls reagent. Measurements of the melt depth and HAZ depth into the substrate are presented in a table which can be found in the Appendix B.6.

Figure 4.37 shows the main effect plots for the influence of the laser power and traverse speed on the MPD and HAZ. The effect plot shows that both MPD and HAZ are positively dependent on laser power and inversely dependent on traverse speed. However, increasing laser power significantly increases the MPD with 200 μm and 440 μm when laser power of 1400 W and 1800 W respectively are employed. Increasing traverse speed significantly decreases the HAZ with a 1.8 mm HAZ depth measured when 200 mm/min traverse speed is employed which reduced to 1.2 mm for 400 mm/min.

Figure 4.38 shows the main effect plot of mean MPD against powder feed rate and wire feed rate. It is observed that increasing powder feed rate causes an increase in MPD, while MPD inversely depends on wire feed rate.

4.4.5 Overlap cladding of Ti-6Al-4V/Spherotene composite layer

With the successful cladding of the single beads of Ti-6Al-4V wire and Spherotene to give beads with high volume fraction of reinforcement in the Ti matrix, the near optimum process parameters are identified and presented in Table 3.2. These sets of parameters are used for the overlap cladding with an overlap pitch of 60% as described in Section 3.5. Figure 4.39 shows micrographs of the overlap cross sections. All of them possess a relatively uniform distribution of the reinforcement particles with peak-trough top

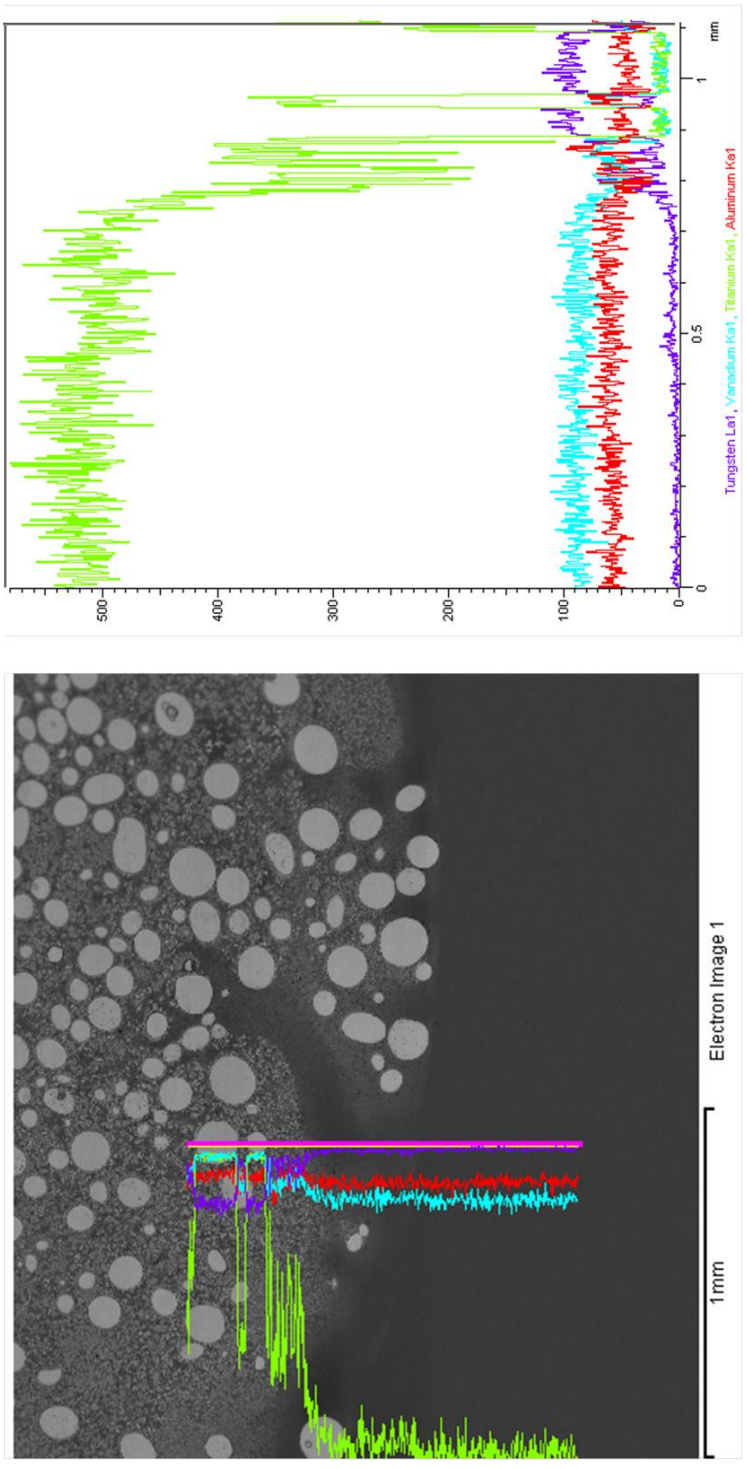

FIGURE 4.35: BSE-SEM image of the clad/substrate interface showing an uninterrupted elemental linescan indicative of a strong metallurigcal bond.

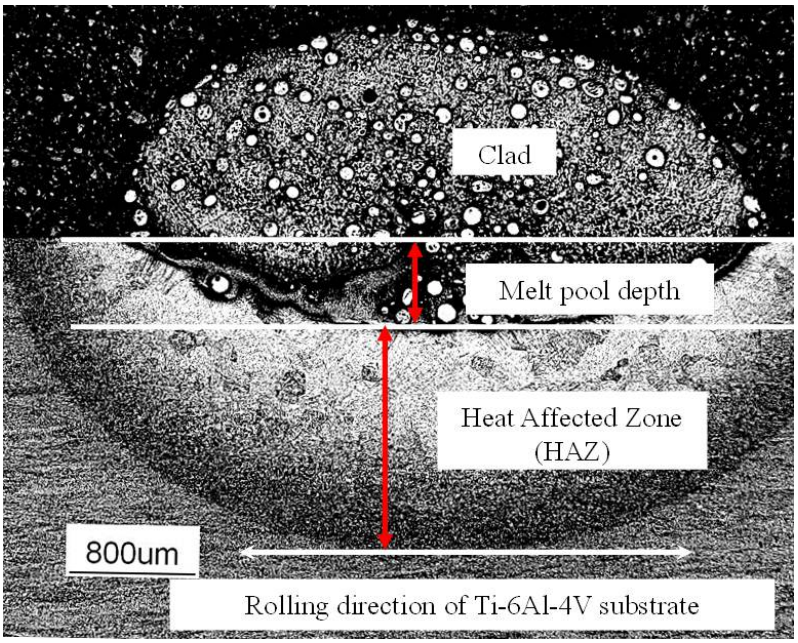

FIGURE 4.36: Optical image of the etched sample characterised by 76 wt% Spherotene/24 wt% Ti-6Al-4V having melt pool depth of 517 μm and HAZ maximum depth of 1.4 mm. Process Parameters: 1800 W, 300 mm/min TS, 700mm/min WFR, 30 g/min PFR.

surface profile. However, the overlap region for the clad layer deposited with 1400 W laser power is less populated with the reinforcement particles. With the 60% overlap pitch, lack of fusion defects are observed at the clad/substrate interfacial region for the clad layers deposited with laser powers of 1400 W and 1600 W, while no inter-run pore is observed for overlap clad deposited using parameter set C. This indicates that 1800 W laser power with the 60% overlap pitch is adequate for the dense coating as inter-run pores and other lack of fusion defects are not observed at the clad substrate interface.

In Figure 4.39 (c), a few cracks are observed to propagate from the top surface of the clad layer to a depth of 0.8±0.2 mm. The cracks emanate from the embedded particles that are close to the top surface of the clad layer. However, the cracks are expected to be eliminated with the peak-trough surface profile by the post deposition surface finish, such as grinding and polishing. The presence of cracks suggests that maximum reinforcement content in the laser clad Ti composite matrix may not exceed 75 wt.%, hence, the coating is susceptible to cracking. For the clad layers deposited with laser powers of 1.4 kW, 1.6 kW, and 1.8 kW, after machining, clad layer thickness of 1 mm, 2.3 mm, and 1.3 mm respectively, are achieved.

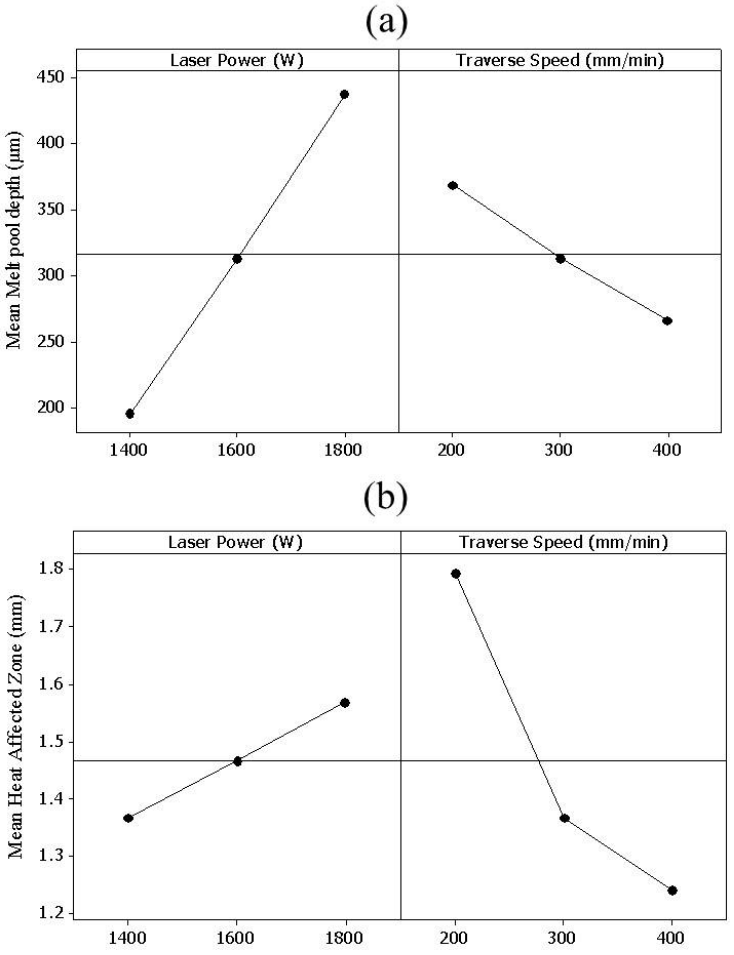

FIGURE 4.37: Main effect plot for (a) melt pool depth (MPD) and (b) heat affected zone (HAZ).

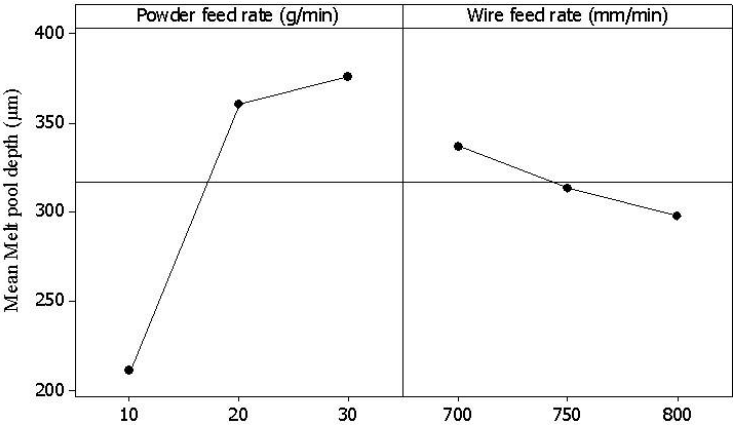

FIGURE 4.38: Influence of material delivery on melt pool depth.

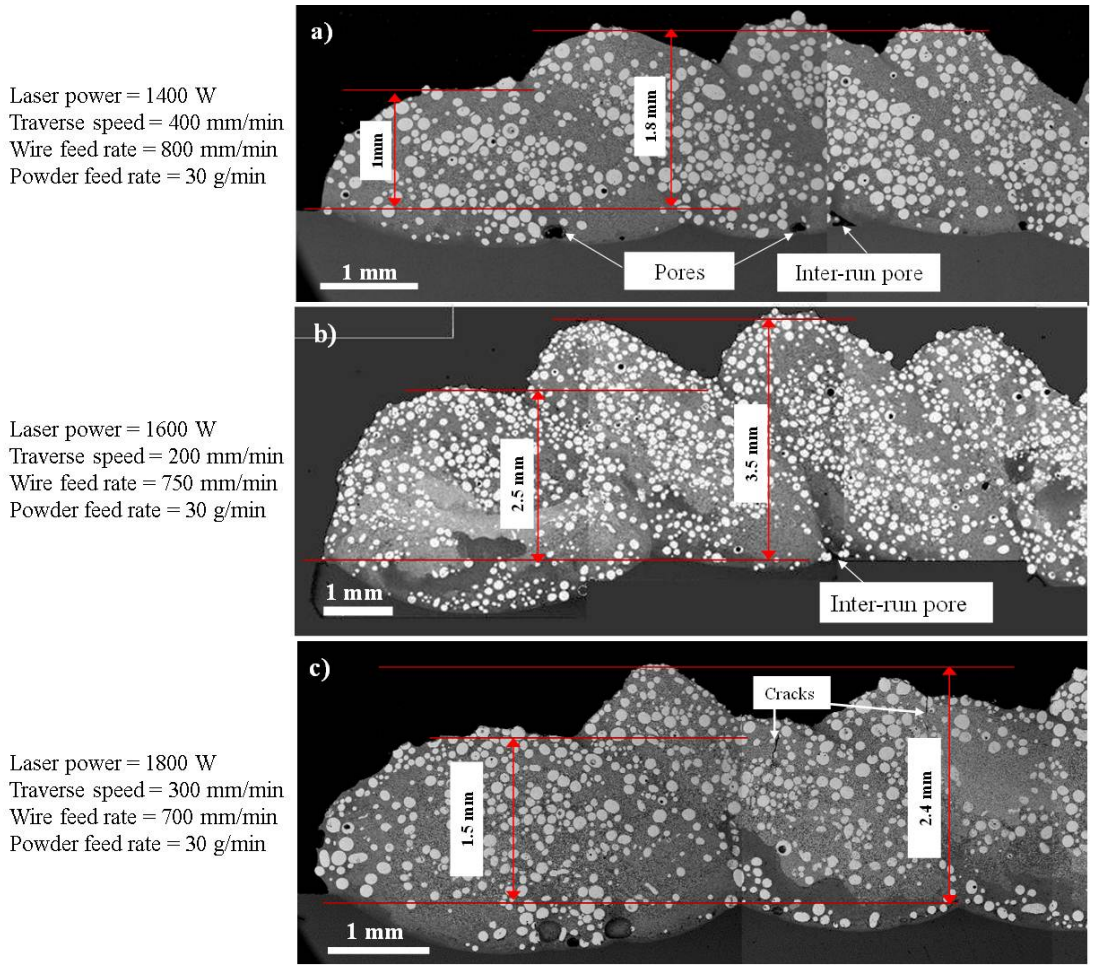

FIGURE 4.39: SEM images of the overlap cross sections deposited with parameter; (a) Set C; (b) Set B; (c) Set A Process parameters as stated in Table 3 2.

4.5 Microhardness of the Ti-6Al-4V/Spherotene composite

Figure 4.40 shows the variation of hardness across the bead cross section measured as described is Section 3.9. The zero position lies on the bead/substrate interface. The single beads subjected to microhardness test are the ones which had over 65 wt % Spherotene content with their cross sections shown in Figure 4.21(c),(d) and(h). The hardness of composite matrix lies between 410-620 $HV_{0.3}$ for all the single beads. The mean hardness of the composite matrix is observed to be 543 $HV_{0.3}$, 507 $HV_{0.3}$, and 455 $HV_{0.3}$ for beads tagged A, B and C respectively. The fusion zones in the melt pool have hardness value range which lies between 420-550 $HV_{0.3}$. The re-crystallised regions of the substrate in the HAZ have hardness value range which lies between 350-370 $HV_{0.3}$.

This is slightly higher than the unaffected region of the substrate with mean hardness of 350±1 $HV_{0.3}$.

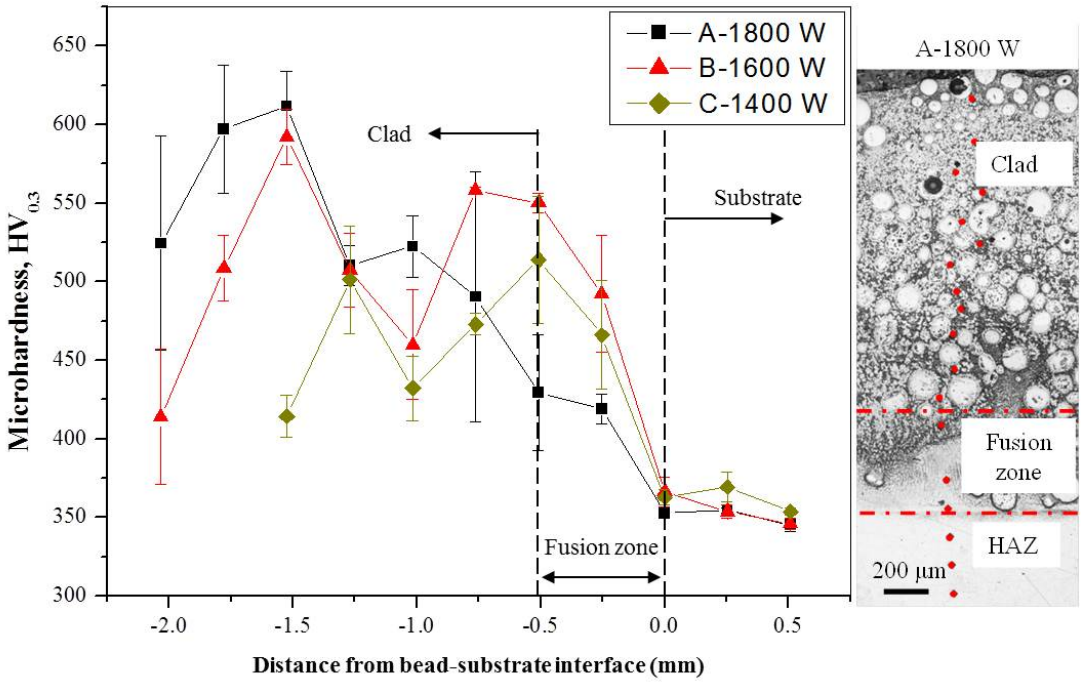

FIGURE 4.40: Microhardness variations across the single beads possessing over 65 wt % Spherotene fraction.

Figure 4.41 shows a hardness indent in region near the embedded Spherotene particle. The hardness value at this point is 652 $HV_{0.3}$. The increased hardness in the near particle region in the clad matrix is due to localised diffusion and microstructure modification around the particles which is associated with TiC precipitates. The ratio of the composite matrix mean hardness to the embedded Spherotene particle hardness is ∼1:5.

Figure 4.42 shows the microhardness variation across the overlap clad layers presented in Figure 4.39. Each hardness point is obtained from the mean of data from three positions at 0.5 mm intervals in the central region of the layer with the avoidance of the embedded particles. The result shows that the clad layer prepared with a laser power of 1800 W exhibits high hardness and the hardness decreases with decrease in laser power. The lowest mean hardness in the clad layers are 670±48 $HV_{0.3}$, 510±16 $HV_{0.3}$, and 470±38 $HV_{0.3}$ for layer deposited with laser power of 1800 W, 1600 W and 1400 W respectively.

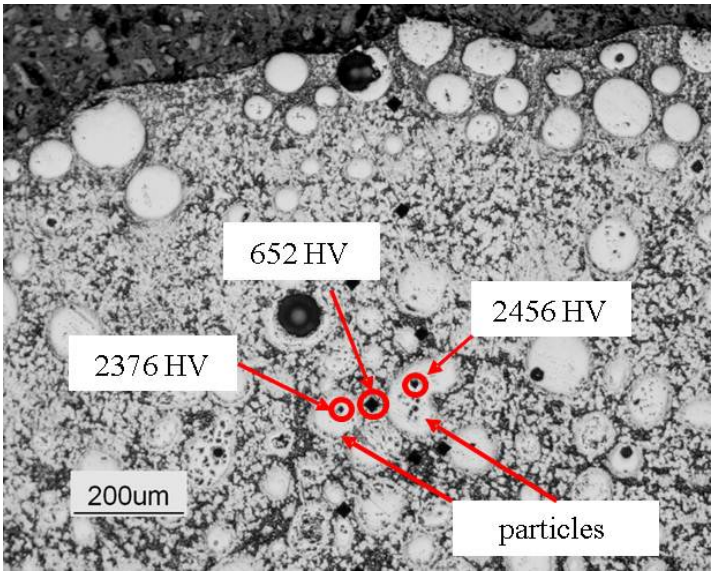

FIGURE 4.41: Increased hardness of the localised region around the embedded Spherotene particles.

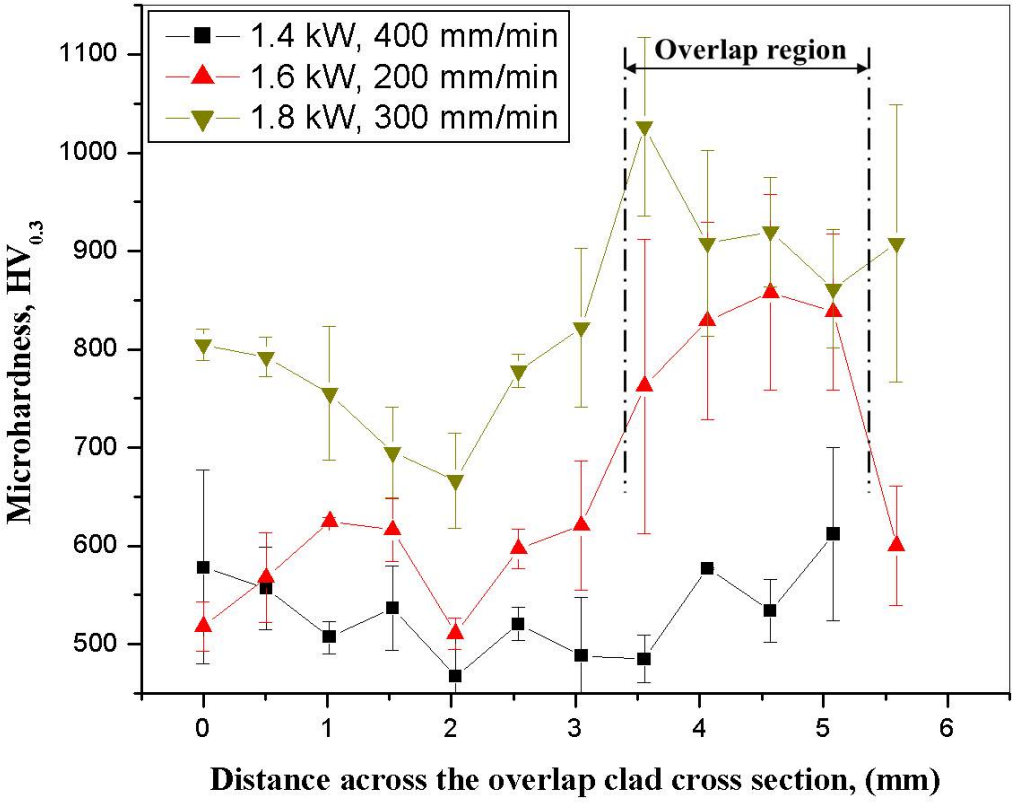

FIGURE 4.42: Microhardness variation across the overlap cross sections in Figure 4.39.

Moreover, the hardness measured in the overlap region is higher with standard errors of 87-99 than in the clad central region for deposits. This is not noticeable in the hardness result obtained for 1400 W deposited clad layer. Mean hardness value as high as 1020±90 $HV_{0.3}$ and 860±99 $HV_{0.3}$ were obtained in the overlap regions of clad layers deposited with laser power of 1800 W and 1600 W respectively.

4.6 3-D cylindrical structure using Ti-6Al-4V wire and Spherotene powder

This section discusses the deposition of a 3-D functionally graded (FG) cylindrical structure to demonstrate the capability of the powder blown and wire fed composite laser cladding process. Having optimised the deposition of Ti-6Al-4V wire and the cladding of the wire with Spherotene powder, the additive fabrication of a component part was attempted to explore the integration of a metal matrix composite (MMC) structure into a metallic structural component. Such integration via additive manufacturing allows functional MMC parts to be built on a selected area of a whole component for thermal management, wear and contact deformation resistance or improved stiffness purposes amongst other. The flexibility of the process allows component manufacture or repair and also eliminate problems associated with joining of functional MMC parts with metallic parts. The capability of the process would as well improve component part/assembly designs [113].

Several attempts were made to have a component with Ti MMC integrated into a Ti-6Al-4V matrix, with an objective of manufacturing the part with consistency and stability of the deposition process. Figure 4.43 shows a 70 mm high, FG cylindrical structure which signifies the success of the trials made. The cylinder is continuously built. The inner diameter (ID) of the cylinder is 66±1 mm, while the outer diameter (OD) is 74±1 mm.

The processing parameters were interacted to achieve a good consistency in the deposition process. After some initial trials, the parameters used to achieve consistency in the process, which is divided into two parts based on section deposited are presented in Table 4.6.

FIGURE 4.43: A functionally graded Ti-6Al-4V/Spherotene cylinder.

TABLE 4.6: Process parameters for each section of the functionally deposited cylinder

Process parameters	Ti-6Al-4V section	Ti-6Al-4V/Spherotene section
Laser power (W)	1000-1600	1400
Traverse speed (deg/min)	323 (200 mm/min)	323 (200mm/min)
Wire feed rate (mm/min)	800	800
Powder feed rate (g/min)	-	10, 20
Step in Z-axis (mm)	1.2	1.4

4.6.1 Ti-6Al-4V section

The deposition of the cylinder is started by the deposition of Ti-6Al-4V wire with a laser power of 1600 W, traverse speed 323 deg/min (200 mm/min linear speed), and 800 mm/min wire feed rate. The parameter values used are obtained from the analysis carried out for maximum bead height in Section 4.2.1. The deposition of a single bead with this parameter gives a bead with 1.4±0.1 mm height (Equation 4.1). Owing to previous layer re-melting which flattens the top surface of the previous bead layer, the step in Z-axis is fixed at 1.2 mm. This indicates that the height of the previous layer is reduced by 0.2±0.025 mm. This is determined based on the several attempts made to achieve a consistent and stable deposition operation. This process parameter is essential to achieve a stable deposition as wire dripping or droplet formation occurred during the trial attempts when there is large discrepancy in the height between the wire tip and the previous layer. The laser power employed as the height increases is ramped down

at defined height stages. This is done in an attempt to keep the thermal mass in the built up relatively constant to maintain the wire tip-previously deposited layer distance. Thus, the laser power is ramped down in a stepwise manner of 100 W reductions each time after an additional 5-layer deposition has been made. This is done as there is a considerable amount of heat in the built which would keep the deposition in a stable condition. A consistent deposition is still achieved even as the laser power is reduced to 1000 W.

4.6.2 Ti-6Al-4V/Spherotene section

The deposition of Ti MMC is integrated into the deposition by ramping up the laser power to 1400 W, as the Spherotene powder is injected into the melt pool. The laser power is maintained at 1400 W throughout the deposition of this section. The height of the composite deposited with this parameter gives 1.8±0.1 mm, but a step in Z-axis of 1.4 mm gives a consistent deposit, which means the composite bead height is decreased by 0.4±0.1 mm due to re-melting. On stopping the powder injection, the laser power is stepped down to 1300 W, as wire deposition alone continues. The laser power is further ramped down until it is 1000 W. Figure 4.44 gives an illustration of stepwise ramping of laser power as the functionally graded cylinder height increases.

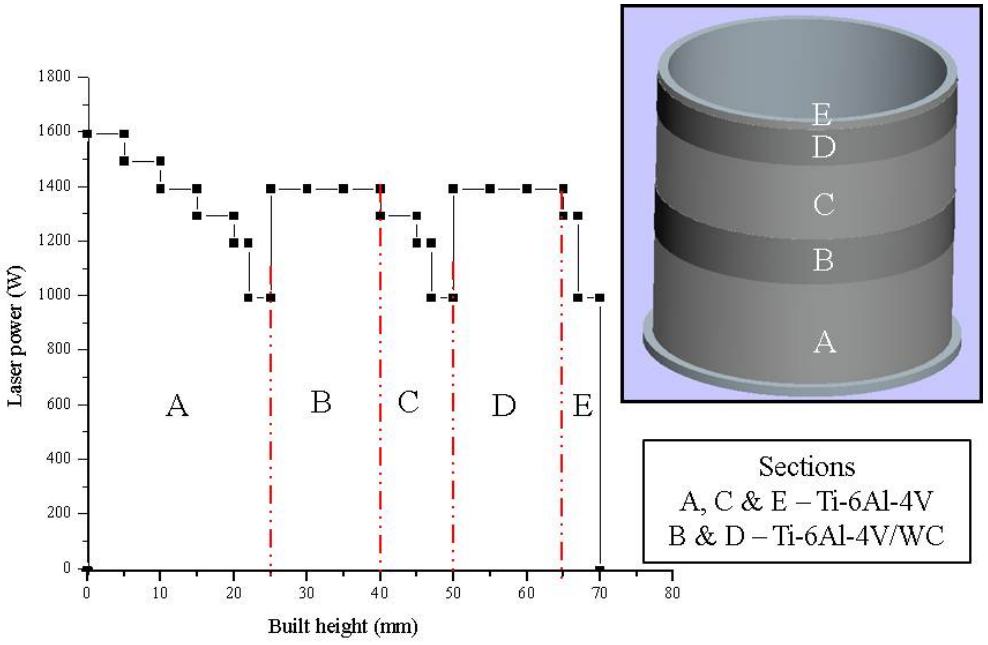

FIGURE 4.44: Schematic illustration for stepwise laser power ramping as built height increases.

The laser power used for the deposition lies between 1000-1600W, unlike area cladding which requires higher power (1800 W) to achieve a better flow of beads on the substrate to limit inter-run porosity. A traverse speed of 200 mm/min is used which is equivalent to 323 deg/min of rotation as the built part rotates about the laser beam axis. Wire feed rate used is 800 mm/min with a Spherotene PFR of 10 and 20 g/min. The increment in Z-axis (step up height) which determines the height for the next layer is to be deposited is important. Based on experimentation, the chosen step up heights compensated for the previous layer re-melting. After deposition, two distinctive boundaries are observed. The bounded regions are the Ti MMC regions that have been developed with the cylinder. This FG cylinder could be used as plain bearing for industrial shafts where higher stiffness and wear may be of great concern. The development of this FG cylinder has demonstrated that functionally graded structures can be incorporated into design of parts by laser cladding. A new design freedom is feasible with this process as it eliminates assembly and joining processes.

4.7 Discussion

In this study, the experimental observations can be explained by evaluating the cladding process as the materials are fed into the melt pool. Hence, this discussion concentrates on melting/molten transfer of Ti-6Al-4V wire and surface melting of Spherotene particles during laser irradiation. The purpose of producing Ti-6Al-4V/Spherotene composite on Ti alloy substrate via laser cladding is to improve its wear/erosion resistance while in service. The enhanced wear resistance of the graded composite structure is dependent on some factors. These factors may include: a uniform distribution of the reinforcement, high fraction of the reinforcement in the composite matrix and composite devoid of cracks and pores and high matrix hardness amongst others [83, 105]. Thus, in this study, in order to produce a composite layer capable of improving wear/erosion resistance, the investigation of the physical characteristics of deposit becomes essential. Moreover, the microstructure and hardness of the laser clad composite are important factors for discussion.

4.7.1 Melting of Ti-6Al-4V wire and dissolution of Spherotene particles

The advantage of feeding the Ti-6Al-4V wire and Spherotene powder independently is to gain control over the resulting composite composition. As the Ti-6Al-4V wire approaches the leading edge of the melt pool, it becomes preheated by the heat radiation from the melt pool and its interaction with the laser beam. The preheating allows the melting temperature of the wire to be attained within a short period of time when irradiated with the laser beam. On reaching the melt pool leading edge as shown in Figure 4.45, the wire is irradiated by the laser beam, and appreciable laser energy is absorbed to raise its temperature to its melting point. This allows the wire tip to melt and flow into the melt pool thus increasing the volume of the pool. The volume of the melt pool is dependent on the wire feed rate (700-800 mm/min) employed in the study. More so, the higher the laser power (1400-1800 W) employed, the less viscous the melt pool solution would be, such that a rigorous liquid convection is envisaged. With a fluidic melt pool achieved, the injection of the Spherotene particles into the pool to form a composite becomes possible.

As the Spherotene powder stream exits the feeder nozzle, the particles experience irradiation as the stream enters into the laser beam zone. The distance travelled by the particles and the time spent under the laser irradiation is dependent on their spatial positions in the divergent powder stream from the nozzle. When the Spherotene particles are irradiated, it is envisaged that the particles will absorb about 82% of the laser energy, since the particles are predominantly characterised as WC [81]. The absorption of the laser energy raises the surface temperature of the particles. The temperature attained by particle entering into the laser beam zone such as in point A (Figure 4.45) before it reaches the melt pool surface at point B is dependent on several factors. These factors include: flight time between point A and B, laser power intensity, particle size, and particle material properties [41, 114].

With the laser system configuration in Figure 4.45, the majority of the Spherotene particles may be irradiated and it is envisaged that each particle surface temperature may be raised to about 3000^{o}C [41]. Provided the attained temperature is greater than the melting temperature of WC (2870^{o}C) for a sufficient time, thus the particle surface may begin to melt. However, due to the short laser-material interaction time before

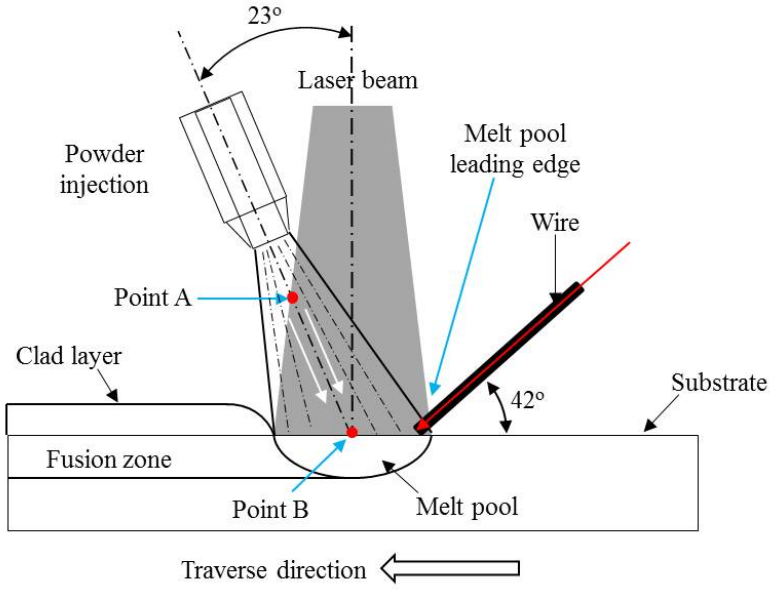

FIGURE 4.45: Schematic of the laser beam-materials interaction process with wire delivered to the leading edge of the melt pool and powder delivered across the melt pool surface.

particles reach the melt pool and higher melting point of Spherotene, the majority of the particles may only experience preheating rather than having a fully molten surface layer on them. Also, there is a possibility that some particles would not be irradiated or melt before entering the melt pool. Thus, these particles will only experience dissolution into the melt pool.

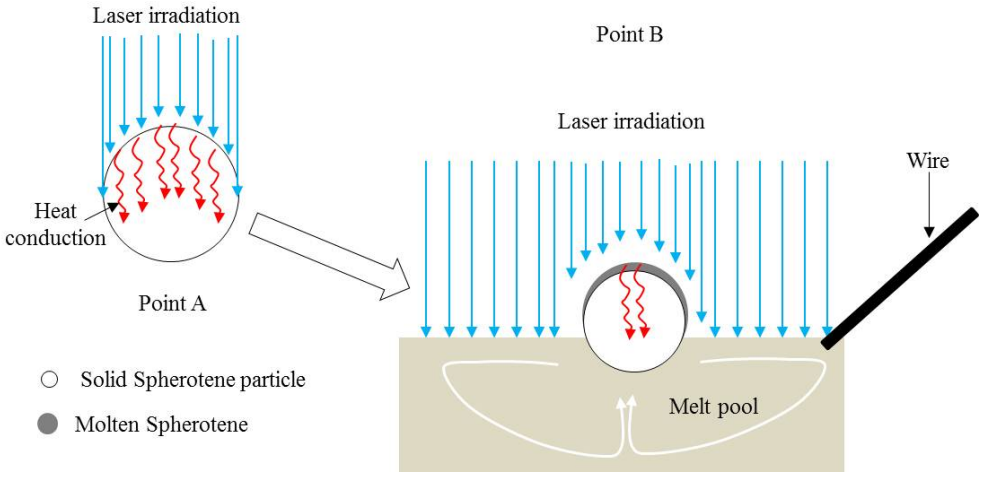

FIGURE 4.46: Schematic of the Spherotene particle melting before entering into the melt pool.

Figure 4.46 shows the schematic of the molten layer around the particle on reaching

point B. Owing to high thermal conductivity of WC (84 W/m/K), it is anticipated that the thickness of the molten layer on the Spherotene particle in the irradiated region may rapidly increase as heat is conducted into the bulk part of the particle. Hence, some of the particles irradiated by the laser beam may approach the melt pool surface with a thin molten layer on their irradiated region.

As the particles plunge into the Ti molten pool, a Ti liquid with an equivalent weight to that of the particles is displaced and each particle would begin to dissolve into the molten liquid as illustrated in Figure 4.47. Thus, owing to the flow convection in the melt pool, W and C solutes in the near particle surface regions are redistributed to uniformly enrich the melt pool with W and C. Hence, the dissolution of the Spherotene particles and diffusion of W and C are possibly enhanced by the extent of melt convection, temperature and time. The dissolution of the particles may continue before solidification occurs, provided there is a rapid diffusion of the W and C solutes farther away from the near particle surfaces, as a state of equilibrium at the particle/liquid interface must be maintained.

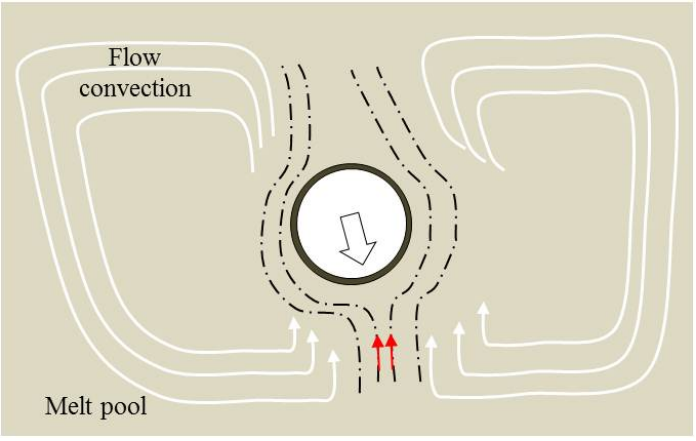

FIGURE 4.47: Schematic of the Spherotene dissolution in the melt pool.

The particle size reduction can thus be attributed to the dissolution of the particles and diffusion of the W and C solutes into the Ti melt. Figure 4.23 shows the analysis of the reinforcement size in one of the composite samples using imaging software. The sample is characterised by 76 wt% Spherotene/ 24 wt% Ti-6Al-4V (Figure 4.21h). The reinforcement size in the composite sample is measured to range between 10-160 μm, while the as-received powder has a particle size range of 20-200 μm (Figure 4.24). Comparing the cumulative frequency curve of the reinforcement sizes in the composite sample to that

of the as-received Spherotene particles, a 46% reinforcement size reduction is evaluated at 25th percentile position, while a 25% size reduction is obtained at 75th percentile position. This indicates that particles with smaller sizes are significantly affected by the dissolution mechanism in the melt pool. Moreover, it is clearly shown in Figure 4.23 as the frequency of reinforcement size, ranging from 20-40 μm becomes more apparent after processing. This size range is insignificant in the as-received Spherotene powder. The rapid dissolution of the smaller particles is encouraged by their higher surface area to volume ratios [115, 116]. In addition, Zeng et al. [117] observed that effective absorption of laser energy decreases with increasing particle size. Hence, smaller Spherotene particles readily absorb the laser energy such that their surface temperature is rapidly raised above its melting point. This allows a significant proportion of the solid particle, if not the whole, to melt and difusse into the Ti-rich molten pool. Though, particle surface melting occurs during irradiation, having the main reinforcement size reduced is quite beneficial to the overall performance of the composite. Previous works have shown that the wear/erosion resistance of particle reinforced composites is improved when the size of the reinforcement is reduced [74, 83, 101, 104, 118]. Therefore, owing to the particle dissolution which results to reinforcement size reduction, a significant enhancement of the erosion resistance of the Ti-6Al-4V/Spherotene composite is envisaged. More so, a uniform distribution of the Spherotene particles is observed in the bead cross section as shown in Figure 4.22. The homogenous distribution of the reinforcement particles is attributed to the stirring effects caused by the Maragoni flow convection in the melt pool [38, 119]. The flow convection had assisted the particles to be transported to different location in the melt pool before solidification occurs to freeze them in position upon solidification.

4.7.2 Composite microstructure on cooling

In this study, all composite samples possess similar phases. These phases include: WC, W_2, W, TiC and β-Ti. This indicates that irrespective of the laser parameters employed, the phases present in the composite formed are the same. A 0.6:0.4 volume ratio of WC to W_2 characterises the Spherotene powder in its as-received form as shown in Figure 4.20. The laser irradiation of the Spherotene particles during processing results in surface melting and dissolution/diffusion of W and C solutes in the molten Ti pool as disscussed in Section 4.7.1. This enriches the Ti melt with W and C, thus encourages the formation

of W and TiC as reaction products on rapid cooling and solidification. However, the rapid heating, cooling and solidification characteristics of laser processing favour the formation of metastable and non-equilibrium phases [19]. In light of this, phases formed, apart from the WC and W_2C present in the Spherotene particles, are considered as solid solutions. However, the study of the microstructure formed on cooling can be explained in two ways. These are: the study of the reinforcement-matrix interface and the study of the matrix microstructure.

4.7.2.1 Reinforcement-matrix interface

Considering the reinforcement particle interface with the Ti matrix, Figure 4.48 shows a schematic of the two types of reaction layer observed around the reinforcement particles in the composite on cooling. A mixed reaction layer is mostly observed around particles located in the central region of the composite bead cross section. This mixed layer is characterised by simultaneous precipitation of the TiC and W/W_2C solid solutions in an alternating manner. This observation is attributed to further dissolution of the particles apart from the surface melting that occurred before the particles plunged into the Ti melt. The centrally located particles experience more intense heating which encourages their rapid dissolution into the melt.

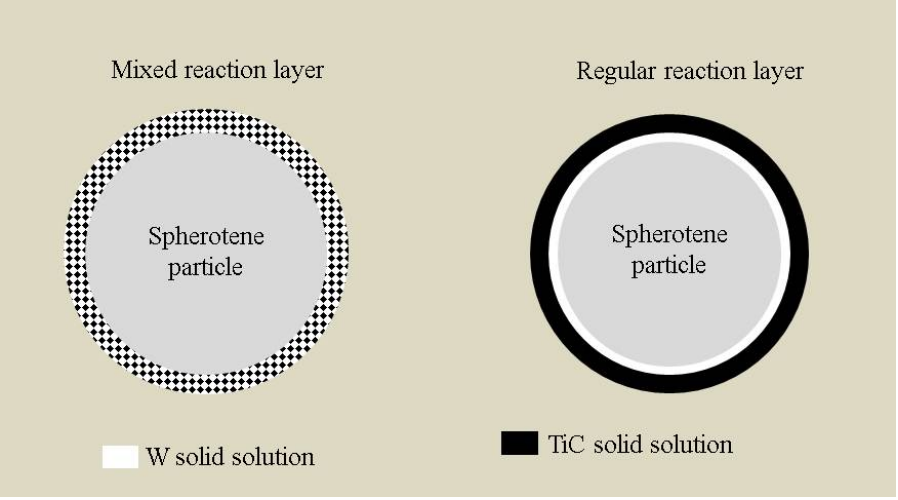

FIGURE 4.48: A schematic of the reaction layers around the main reinforcement particles in the composite.

As the particles further dissolve into the melt, TiC solid solution is formed which is immiscible with W solid solution. And the W solid solution nucleates on the Spherotene

particle to form a net-like structure around the particle with TiC precipitates in the net pockets. This mixed layer is similar to the reaction layer formed around WC particles in a Ti-6Al-4V/WC composite prepared via vacuum arc melting process [80]. However, two circular layers are observed around particles mostly located at the regions farther away from the centre to the periphery. As the molten layer around the particles are stripped off as they plunge into the melt, there remains a thin molten layer around the particles which is rich in both W and C solutes. Since the particles are not experiencing intense heating that can result in a further dissolution of the particles in a rapid manner, the C solute locally reacts with the Ti melt to form the TiC layer. As C depletion to the interface between the molten layer and the Ti melt occurs, the molten layer is reduced to W/W_2C solid solution. This serves as an intermediate layer between the reinforcement and the TiC layer.

4.7.2.2 Matrix microstructure

In order to explain the matrix microstructure, there is a need for the determination of the overall composition of the melt pool. This is evaluated by determining the amount of the particle dissolution, volume of substrate dilution and the volume of Ti-6Al-4V wire deposited. For the purpose of this analysis, sample deposited with the highest Spherotene composition is chosen. The volume fraction of the Spherotene that dissolved is estimated using equation (4.8). It is assumed that 90% of the Spherotene particles present in the composite would have experienced a minimum of 18.5% size reduction owing to surface melting. This amounts to 45.8 vol.% Spherotene dissolution in the Ti melt during processing.

$$Volume fraction of dissolved Spherotene = 1 - \left(\frac{d_{90}}{D_{90}}\right)^3 \tag{4.8}$$

Where;d_{90} = reinforcement particle size in composite at 90th position (106 μm) (Figure 4.23), and D_{90} = as-received Spherotene particle size at 90th position (130 μm) (Figure 4.24).

The analysis of the composite sample to determine the overall melt pool composition is presented in Table 4.7.

TABLE 4.7: Analysis of the composite sample to evaluate the overall melt pool composition

Mass of deposited Ti-6Al-4V (g)	1.167 x 10^{-2}
Mass of deposited Spherotene (g)	4 x 10^{-2}
Volume of deposited Spherotene (cm^3), (density = 16.257 g/cm^3)	2.46 x 10^{-3}
Volume of dissolved Spherotene (cm^3) (Dissolution fraction = 0.458)	1.13 x 10^{-3}
Mass of dissolved Spherotene (g)	1.83 x 10^{-2}
Dissolved Ti-6Al-4V substrate, cm^3 (g)	1.655 x 10^{-3} (7.315 x 10^{-3})
Total mass of Ti-6Al-4V (g)	1.898 x 10^{-2}
Mass of Ti (90% Ti-6Al-4V) (g)	1.709 x 10^{-2}
Mass of W in dissolved Spherotene (g) (95.5 wt% Spherotene)	1.75 x 10^{-2}
Mass of C in dissolved Spherotene (g) (4.5 wt% Spherotene)	8.0 x 10^{-4}

With Spherotene composition of 60 vol.% WC and 40 vol.% W_2C, the equivalent mass ratio of WC to W_2C is 0.44:0.56. This results in an equivalent composition of 95.5 wt.% W/4.5 wt.% C, knowing that the molar mass of WC is 195.85 g with 93.87 wt.% W/6.13 wt.% C; and the molar mass of W_2C is 379.69 g with 96.84 wt.% W/3.16 wt.% C. Hence, from Table 4.7, the probable overall composition of the molten part of the melt pool is 48.3 wt.% Ti / 49.4 wt.% W / 2.3 wt.% C. Figure 4.49 shows the plot of the overall melt pool composition on the liquidus projection of the Ti-W-C ternary phase diagram, neglecting Al and V content. This probable composition lies in the lower region of the phase diagram, and the temperature of the melt pool composition is suggested to be between 2200-2300^oC. Based on the ternary phase diagram, the solidification of the liquid melt pool is likely to follow eutectic reaction path, e_5, (equation 4.9) as the melt temperature decreases to 1646^oC [65].

$$L = \beta(Ti, W) + (Ti, W)C_{1-x}(1646.5^oC, eutectic, e_5) \tag{4.9}$$

However, owing to a higher reactivity of Ti with C and low solubility of C in solid Ti (about 0.28 wt.%) [120, 121], the weight ratio of Ti to C which is 95.5 wt%Ti / 4.5 wt.% C is plotted on the binary Ti-C phase diagram as shown in Figure 4.50. As the melt pool solution cools down to about 2270±20^oC, point A is reached on the liquidus line, and primary TiC begins to form in the molten solution as schematically shown in Figure 4.51. These primary TiC precipitates are evident in the composite microstructure

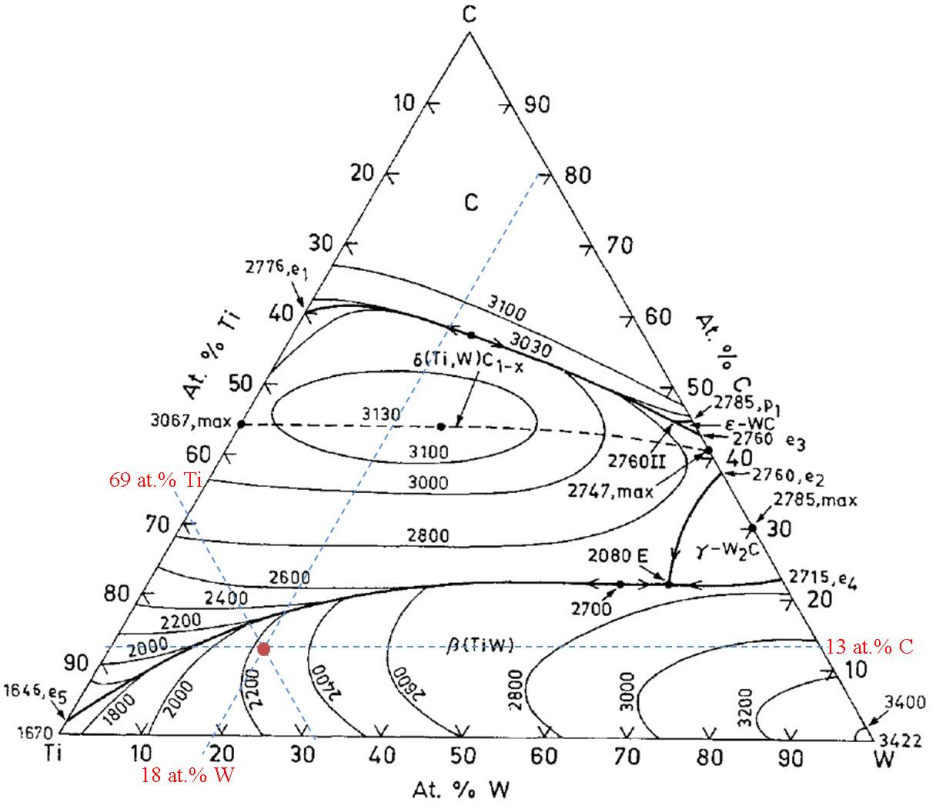

FIGURE 4.49: A plot of the probable overall melt pool composition on the liquidus projection of the Ti-W-C ternary phase diagram.

with either near circular or blocky morphology. As the melt pool temperature decreases further, the primary TiC begins to grow, and the melt pool composition begins to vary along the liquidus line from point A to the eutectic point CE.

It is noteworthy that W has a higher solubility in β-Ti at higher temperature since both have some similar crystallographic features such as BCC structure [65]. This allows W to remain in the melt pool solution while primary TiC crystallizes out of the pool solution. As the melt pool solution approaches the eutectic composition, near-complete depletion of C is envisaged which makes the solution to be more of Ti-W solution.

As the melt pool temperature drops to the eutectic temperature (1646.5^{o}C), the liquid phase transforms into two solid solution phases as expressed in equation (4.10) . Hence, eutectic TiC is formed, as it is evident in the composite microstructure as elongated and fine precipitates illustrated in Figure 4.51. Meanwhile, at eutectic point, W still remain in the Ti, and the concentration of Ti is as well reduced owing to TiC formation. Using, inverse lever rule, the solid composition is 41 wt.% TiC/59 wt.% β-Ti. Moreover, at

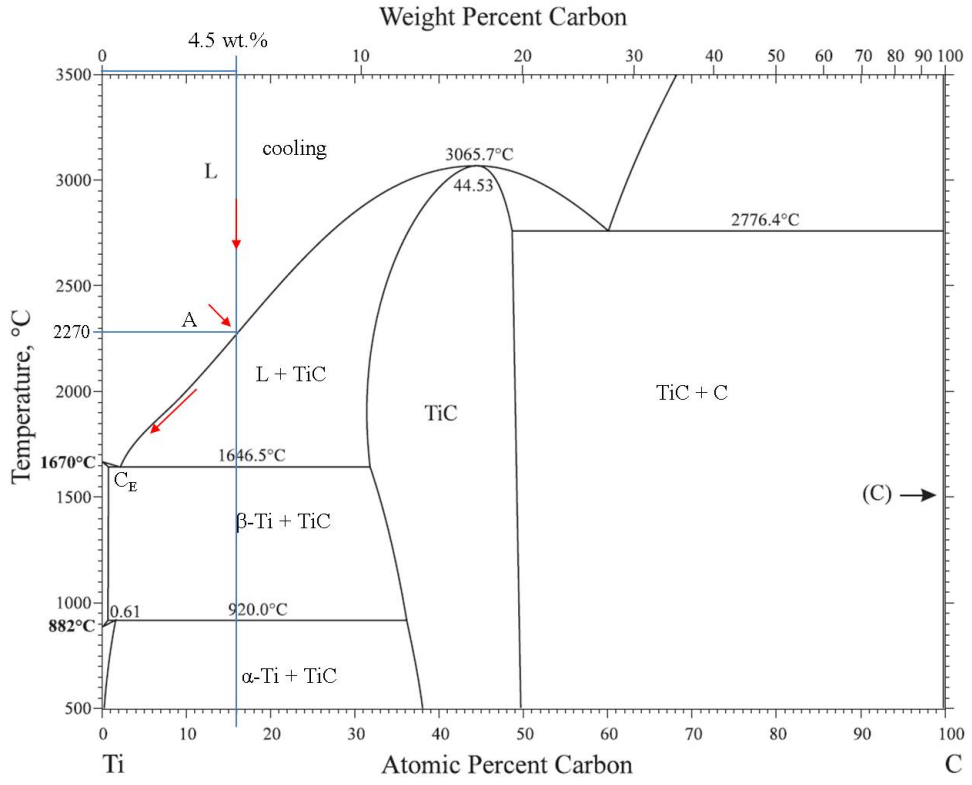

FIGURE 4.50: A plot of the Ti-C melt pool composition (4.5 wt.% C/ 95.5 wt.% Ti) on the Ti-C phase diagram.

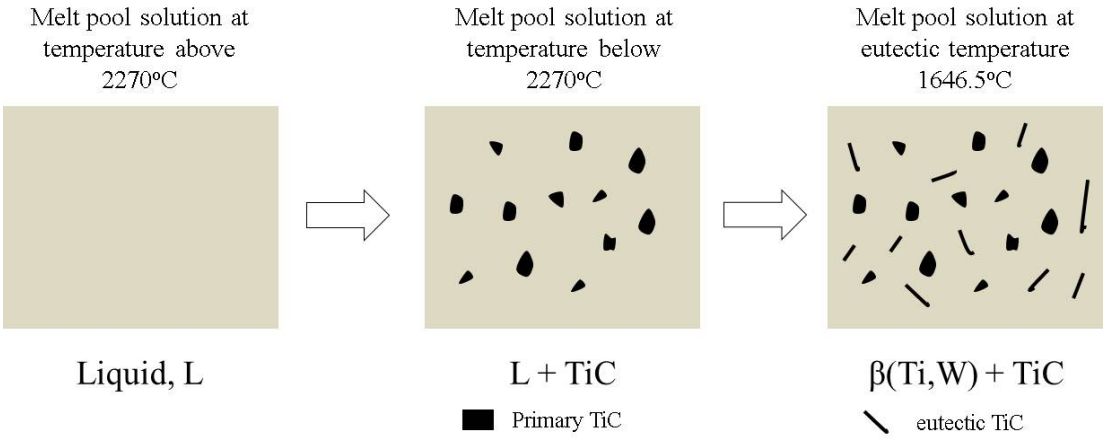

FIGURE 4.51: A schematic of the melt pool composition at temperature below 2150^{o}C with the formation of primary TiC precipitates.

the eutectic temperature, the Ti-W solution solidifes to form a continuous isomorphous BCC solid solution, β(Ti,W).

$$L = \beta(Ti, W) + TiC(1646.5^oC, eutectic) \tag{4.10}$$

Hence the composition of the β(Ti,W) solid solution becomes 62.4 wt.% W / 37.6 wt.% Ti which is plotted on the Ti-W binary phase diagram as shown in Figure 4.52.

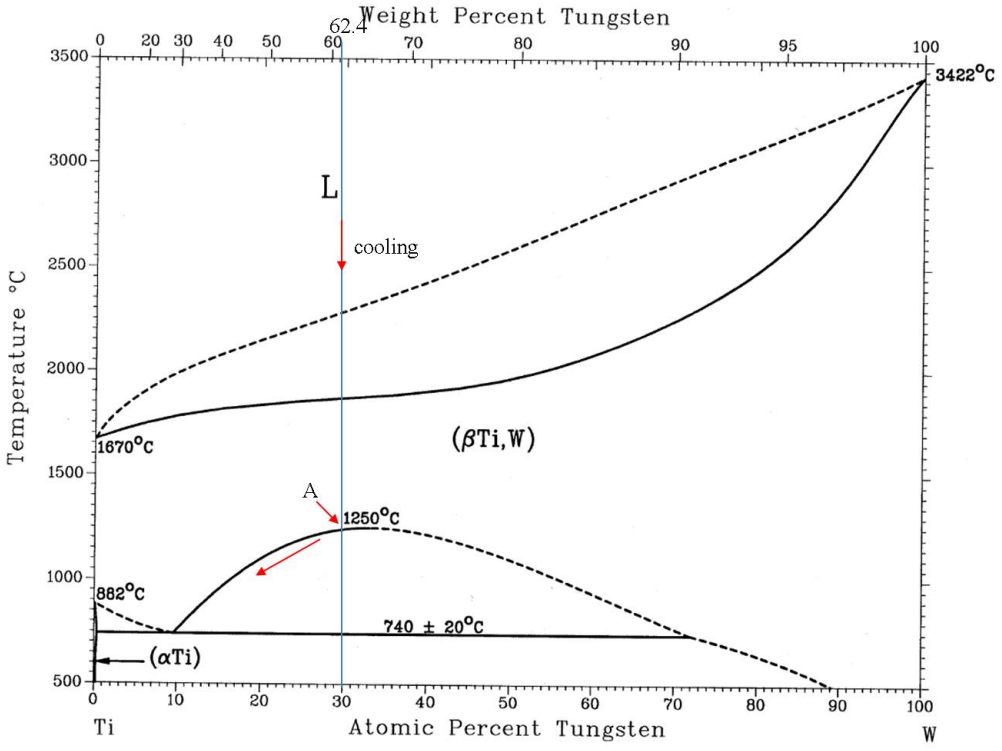

FIGURE 4.52: A plot of the β(Ti,W) solid solution of 62.4 wt% W/ 37.6 wt% Ti on the Ti-W phase diagram.

As the β(Ti,W) solid solution cools down to 1250^{o}C, a monotectoid decomposition occurs and it is expected that the solution transforms to α-Ti and W solid solutions. However, in this study, owing to rapid cooling typical of laser processing, the Ti solution remains beta stabilised as W solute is retained in the Ti . Hence, the solid solution transforms to β -Ti and W solid solutions and primary W solid solution begins to nucleate at temperature 1250^{o}C. The primary W precipitates are evident in the composite microstructure with a blocky morphology in the near region where TiC precipitates are present. As temperature decreases to about 740$\pm$20^{o}C, eutectic W precipitates emerges in the Ti solid solution as illustrated in Figure 4.53. The eutectic W precipitates are observed to

have a leaf-like equiaxed structure with TiC interdendrites. Hence, assuming solidification follows phase diagram, the expected structure is a small fraction of primary TiC, primary W, eutectic TiC and W in a β(Ti,W) matrix.

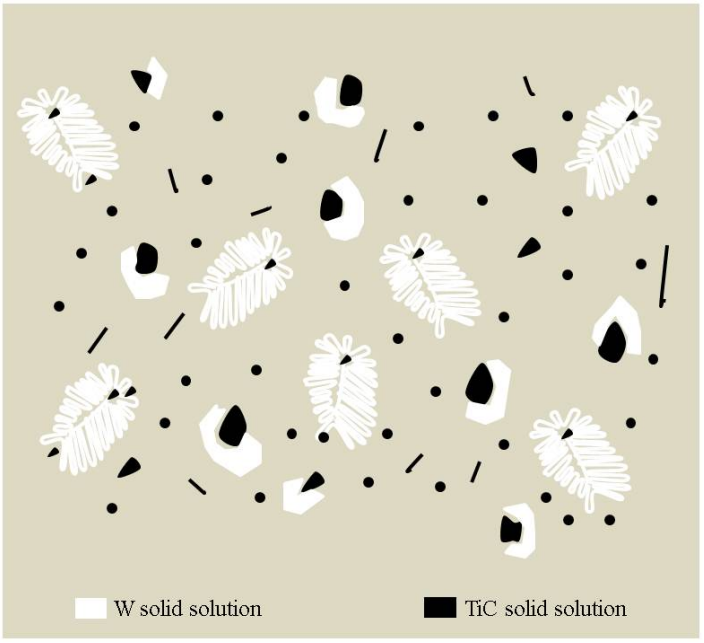

FIGURE 4.53: Schematic of the composite matrix with equiaxed W solid solution precipitates emerging from the β(Ti,W) solid solution.

In the study, the atomic percent composition of W in the Ti solid solution is measured using EDX to range between 7.5-9%. This W composition range is sufficient to favour the stabilisation of the Ti solid solution as a beta phase [75], as solubility of W in α-Ti is 0.3 at.% maximum [65]. However, it would be noted that the neglected vanadium content in the analysis can as well contribute to the beta stabilisation of the Ti matrix. The effect of the aluminium as an alpha Ti stabiliser is not dominating as the matrix is beta stabilised. This suggests that irrespective of the laser processing parameters employed, the W content in the binder phase may not exceed 10 at.%. Hence with 7.5-9 at.% W in Ti corresponding to 22-25 wt.% W, the probably overall melt pool solid solution composition on solidification is 19 wt.% TiC/ (26-29) wt.% W /(52-55)wt.% β -Ti. Having the Ti matrix β-stabilised is beneficial since it is more ductile when compared to the α-Ti phase [70, 82]. It is aniticipated that the ductile β -Ti matrix would prevent brittle failure of the composite with ceramic solid solution phases uniformly dispersed in it.

4.7.3 Composite deposit characteristics

The characteristics of the deposits can be best explained by the heat input (ratio of laser power to traverse speed) and deposited material per unit length (ratio of WFR or PFR to traverse speed). Figure 4.4 shows that the composite deposit height is inversely dependent on traverse speed which is the most influencing processing variable. Material delivery rate, most especially powder feed rate PFR, has a positive influence on deposit height. Table 4.1(b) gives the percentage contribution of traverse speed and PFR as 79% and 17% respectively. This shows the significance of these two parameters to the deposit height in the wire/powder cladding process. Increasing material delivery rate or decreasing traverse speed (Increasing delivered material per unit length) is expected to increase material volume available in the melt pool to promote an increased deposit height [37, 122].

Figure 4.5 shows that the deposit width increases with increasing laser power, LP, which is the most significant variable. Increasing traverse speed and PFR result in a decreased deposit width [29, 122]. Increasing laser power allows for the substrate melting beyond the laser beam size as the temperature of the melt pool edges increases above the melting point. However, as traverse speed increases, the melt pool convection is more promoted than heat conduction [123]. This is due to shorter interaction time, which reduces the rate of heat conduction to the melt pool periphery capable of widening the pool. The increased flow of powder into the melt pool increases laser beam attenuation and energy absorption by the reinforcement particles. This prevents the widening of the melt pool, thus resulting in a narrower deposit width. The increasing heat input per unit length is majorly responsible for the increasing clad width

Figure 4.6 shows as expected that the increasing Spherotene content is dependent on the increasing PFR. Increasing laser power slightly increases the Spherotene content, while an increasing traverse speed slightly decrease the Spherotene content. In all the characteristics, wire feed rate is less significant as a processing variable. This indicates that the influence of the change in Ti-6Al-4V volume delivered into the melt pool is low on achieving increased Spherotene content. Once a consistent deposition of the wire feedstock is achieved, the injection and assimilation of the Spherotene reinforcement into the melt pool is promoted by having a less viscous pool which is promoted by increasing

laser power [124]. Thus, increasing both heat input and powder delivered per unit length encourage increase in Spherotene content.

Table 4.4 shows the summary of the processing parameters with their equivalent energy density requirement to achieve maximum deposit physical characteristics. The energy density required to achieve a maximum Spherotene content (76% wt) in the Ti composite matrix is 148 J.mm^{-2} which falls within the range obtained 140-160 J.mm^{-2}. This energy density range is the lowest obtained among all other physical characteristics (deposit width and height). In both Ti-6Al-4V wire and the composite cladding, energy requirement to achieve a maximum deposit width is always greater than that of deposit height. This is expected as higher energy is required to increase the melt region on the substrate beyond the laser beam diameter. This higher energy may be achieved by increasing the laser power or decreasing the traverse speed of the cladding process. Also, to achieve a higher reinforcement content, the ratio of the wire volume to the powder volume delivered needs to be reduced.

4.7.4 Deposition stability

Figure 4.16 shows that the injection of both powder and wire into the melt pool at the same time may result in an unstable deposition. The unstable deposition is attributed to a strong attenuation of the laser beam as powder flows across the melt pool surface. The blown Spherotene powder absorbs a large amount of the laser energy. This results in a less energy at the melt pool available to melt the wire. The wire then struggles to melt and get deposited. The melt pool is more viscous and solidifies quicker. A blob is formed at the wire tip which would stay longer in the melt zone until the energy available is enough to cause melting as illustrated in Figure 4.54 [125].

With the delivery of wire into the melt pool edge before powder injection, the process starts with full laser energy available in the melt pool region. This makes the wire deposition adopt a stable condition. Thus, as the powder is injected into the less viscous and voluminous melt pool, deposition remains consistent because there is heat input already into the track region and it has started with good stability. Also, the temperature of the wire tip close to the melt pool would have been raised close to the melting point of Ti-6Al-4V. This would aid its molten transfer into the pool.

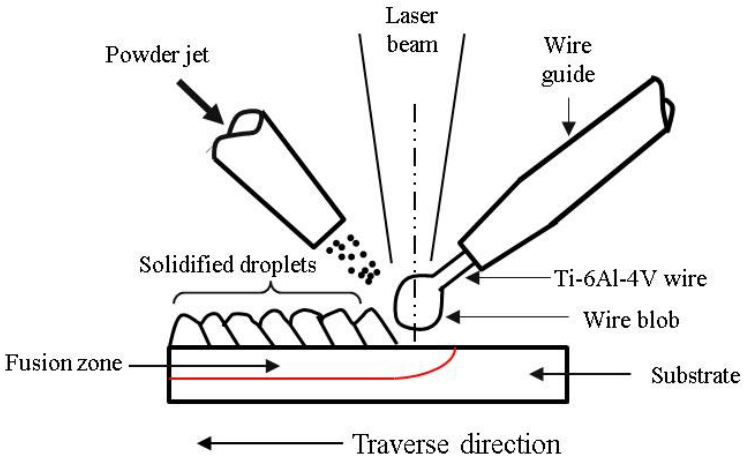

FIGURE 4.54: Schematic illustration for the formation of wire blob and instability in the deposition.

4.7.5 Melt pool and Heat affected zone depth

In Figure 4.37, laser power and traverse speed are the two most significant factors that influence the depth of melt pool and the maximum depth of substrate recrystallisation (HAZ) [30, 37]. These two process factors dictates the heat convection in the melt pool and the heat conduction into the substrate which recrystallises the substrate material in the near region around the melt pool [123]. The effect plot shows that both MPD and HAZ are positively dependent on laser power and inversely dependent on traverse speed which complements other works [29–31]. Laser power significance indicates that the thermo-capillary flow and heat convection in the melt pool increase with increasing laser energy. This causes the substrate solid region nearby the melt pool region to further melt thus increasing the melt pool width and depth. The extension of the liquid/solid interface region into the substrate is aided by the convective melt pool solution. This is in agreement with the explanation for the increase in the melt pool size by Mazumder [123] and Shah et al. [124]. Increasing traverse speed significantly decreases the HAZ. This indicates that most of the heat energy is retained in the pool for convection while less thermal energy is conducted away into the substrate as traverse speed increases [126]. More so, as the powder feed rate increases, it can be suggested that the impinging energy of the flow jet from the powder feeder nozzle increases. This may have caused an increase in depth of the active melt pool resulting in increasing MPD [30]. Another explanation for the deeper MPD as powder feed rate increases may have been that there is an

increase in the amount of heat energy retained in the melt pool during cladding. Since, ceramic particles have relatively high laser absorptivity, and with increasing amount of the particles assimilated into the melt pool, the heat content of the melt pool is expected to be higher. Thus, this causes the region at the molten liquid/solid substrate interface to go into the melt pool solution, resulting in an increase in the melt pool depth.

4.7.6 Microhardness of Ti-6Al-4V/Spherotene

The clad composite matrix hardness is enhanced by the uniform distribution of the TiC and W solid solution precipitates in the β-Ti solid solution. In Figure 4.40, the reduction of the hardness in the fusion zone may be attributed to dilution of the clad region content with substrate material. The localised metallurgical change due to rapid heating and cooling is responsible for increased hardness over that of the measured Ti-6Al-4V substrate which is similar in values found in the literature (349 HV - Table 2.3) [127]. Thus, the ratio of the composite matrix mean hardness to the embedded Spherotene particle hardness is ∼1:5. This makes the matrix tougher and with good wetting of the Spherotene particles in the matrix, good wear resistance is anticipated. The variation of the hardness value at each level as denoted by the error bars is attributed to the anisotropic nature of the composite matrix. Also, there is a possibility of having unseen Spherotene particles situated beneath the composite matrix locations where hardness data were obtained which might resulted in high hardness value. Localised diffusion in the nearby region around embedded Spherotene particles may have contributed to the hardness variation. This observation is attributed to the Spherotene particles densely populating the overlap regions of the clad layer deposited with 1600 W and 1800 W laser power, as observed in the SEM images of the cross sections (Figure 4.39). However, the overlap regions in the 1400 W deposited clad layer was less populated by Spherotene particles, which made the hardness values of the overlap region to be less different from the middle region of each single beads forming the clad layer. Having higher hardness values in the overlap regions, the surface of the composite layer would possess a functionally properties grading feature, such that there would be a periodic variation of hardness across the composite layer. It would be noted that the hardness values obtained for the composite layer processed with laser power of 1400 W, is lower than the other layers, these lower values can be attributed to the results obtained in Figure 4.34 which shows that β-Ti phase is more stable as W at% content increases which is

promoted when lower laser power is used for processing. Thus, the composite matrix is ductile as it is rich in the β-Ti stabilised phase, which resulted into lower hardness value.

4.8 Conclusions

The successful hybrid laser cladding of Ti-6Al-4V wire and Spherotene powder for area cladding and functional graded structure has been reported using a fibre laser. The independent feeding of the materials into the melt pool helps to control the composite composition. A crack- and pore-free clad containing as high as 76±1 wt.% reinforcement in the Ti matrix is achieved via the process with an energy density of 150±10 J.mm^{-2}. The reinforcement dissolution upon laser irradiation seemed to be more significant for small size particles. The resulting microstructure showed that the composite is characterised by WC, W_2C, W, TiC and β-Ti solid solutions. Two types of reinforcement interface are identified which are a mixed and a regular/circular reaction layers. TiC precipitates are in blocky, near circular and fine eutectic morphologies, while the W solid solution precipitates are either blocky or equiaxed. TiC and W solid solutions are uniformly distributed in the composite matrix. A 7.5-9 at% W is retained in the Ti solution on solidification. This helps to stabilise the Ti as a beta phase, which is considered desirable for the composite to retain its ductility. Increasing laser power is observed to decrease the concentration of W retained in the Ti, as cooling rate is lowered to favour the nucleation of W solid solution. The uniform dispersion of the TiC and W solid solutions in the β-Ti matrix phase has significantly improved its hardness which ranged between 410-620 $HV_{0.3}$. A ratio of composite matrix hardness to the embedded reinforcement particles is obtained to be 1:5. It is envisaged that the composite formed will possess good wear and contact deformation properties. To demonstrate the design freedom capability of additive manufacturing process, a functionally graded 3-D cylinder was built. This showed that component manufacture and repairs with selective application of functionally graded material is possible with cladding process, which may not have been achievable via traditional manufacturing route.

Chapter 5

Laser cladding of Ti-6Al-4V/TiB_2 composites

This chapter examines the characteristics of the feedstock powders, and the laser cladding of pre-blended Ti-6Al-4V/TiB_2 powder. The characterisation of the powders is discussed in terms of their particle size, particle morphology and their phase composition for Ti-6Al-4V and TiB_2 blended powders. The physical characteristics, microstructural observations, reinforcement distribution and hardness of the deposits are reported with respect to the influence of key processing variables. Ti-6Al-4V/TiB_2 composite walls are subjected to tensile tests to determine its elastic properties and mode of failure under external tensile load. Fractured surfaces are examined using SEM to study the mode and mechanism of composite failure.

5.1 Ti-6Al-4V powder

The powder used here, Ti-6Al-4V was supplied by Crucible Research, USA. The particle size analysis, obtained by laser diffractometry, revealed that the particle size ranges from 30-300 μm, as shown in Figure 5.1 The cumulative volume curve revealed that 10% of the powder is below 56 μm (d_{10}) and above 171 μm (d_{90}). The d_{50}, median diameter size of the supplied powder is 100 μm. The volume mean diameter of the powder is 108 μm in the as received condition. Figure 5.2 shows the SEM image of the powder particle

morphology. The particles are predominantly near spherical, with some asymmetric shaped and satellite particles, typical of powder produced by gas atomisation.

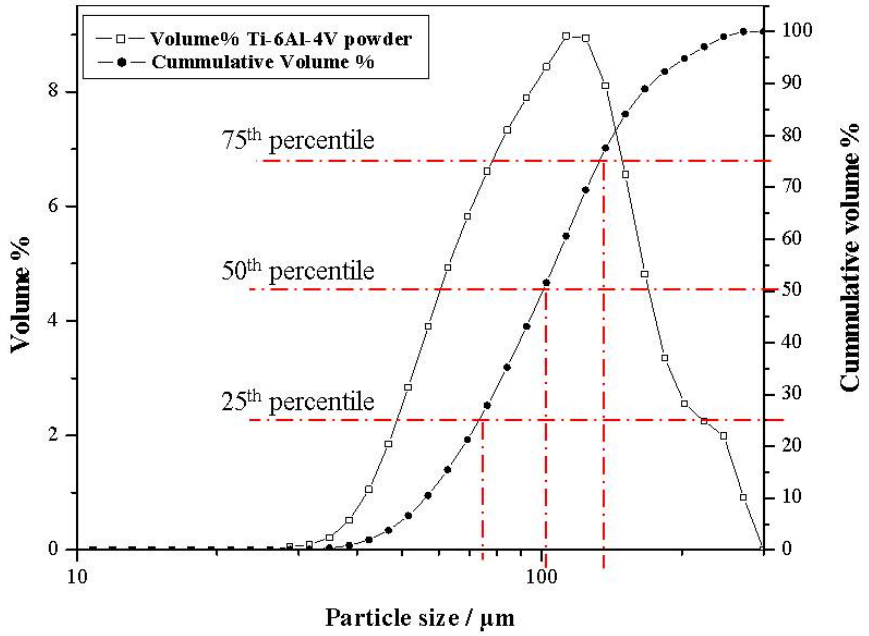

FIGURE 5.1: Ti-6Al-4V particle size with mean distribution size of 108 μm.

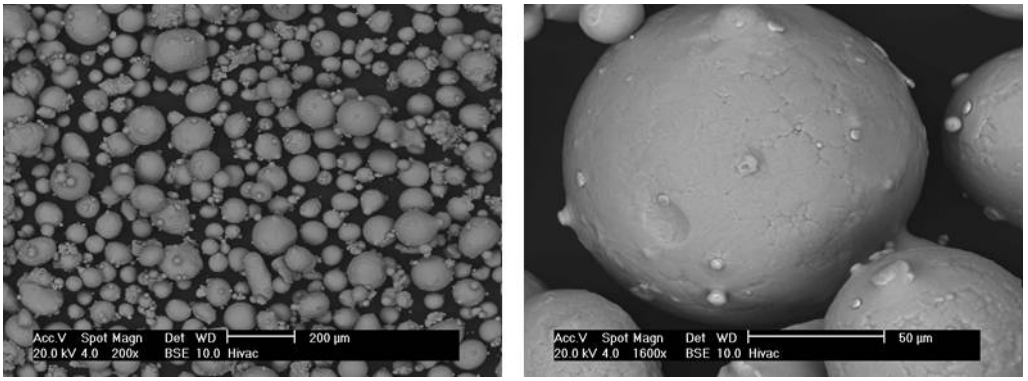

FIGURE 5.2: Ti-6Al-4V powder showing near spherical morphology typical of gas atomised powders.

Figure 5.3 shows the XRD pattern of the as received powder. The peaks in the spectrum are found to match the pattern of α-Ti (HCP) phase with ICDD no: 00-044-1294. The powder pattern with the matching α-Ti phase can be found in the Appendix C.1. The crystallographic information about the phase present is given in Appendix C.2. Ti-6Al-4V is known as an $\alpha - \beta$ Ti alloy [47], however, only α-Ti phase was observed in the

XRD scan with an intense reflection at $2\theta \approx 40.5^o$ which corresponds to α-Ti (101); and no presence of β-Ti phase found in the spectrum of the as-received powder whose reflections were expected to have occurred at positions denoted by dotted lines in Figure 5.3.

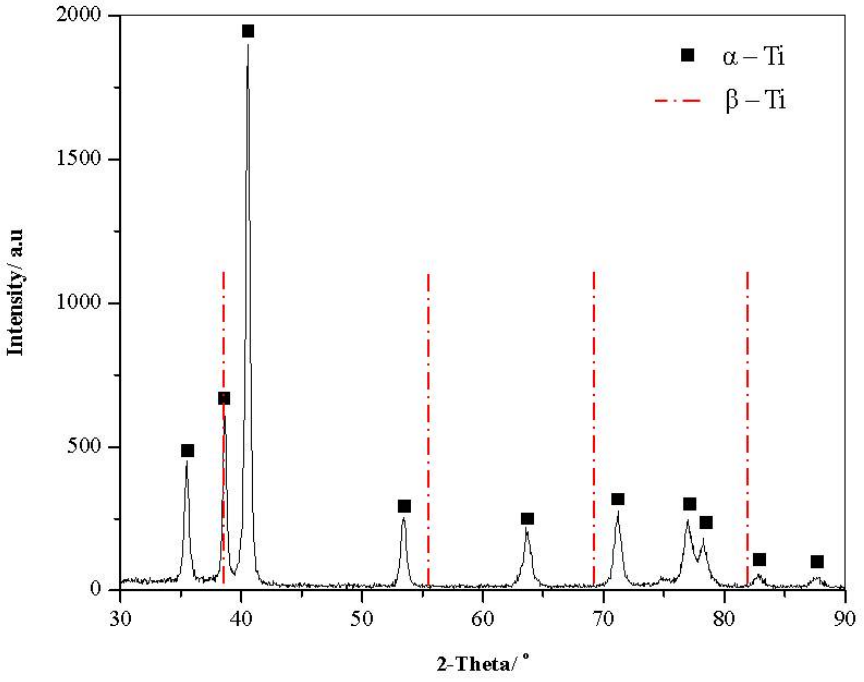

FIGURE 5.3: XRD pattern of Ti-6Al-4V powder with only α-Ti phase identified.

5.2 Titanium diboride powder

The TiB_2 powder was supplied by Sigma Aldrich Chemical Company, UK. The powder particle size was quoted as <10 μm by the supplier. The particle size analysis, obtained by laser diffractometry, revealed that the actual particle size ranges from 150 μm, as shown in Figure 5.4. The cumulative volume curve revealed that 10% of the powder is below 5 μm (d_{10}) and above 17 μm (d_{90}). The d_{50}, median diameter size of the supplied powder is 9 μm. The volume mean diameter of the powder is 10 μm in the as received condition while the surface area mean diameter is 8 μm. Figure 5.5 shows the SEM image of the powder particle morphology. The particles are not only angular,

but possess plate morphology, which suggests that the powder was possibly produced by comminution of larger TiB_2 particles to powder.

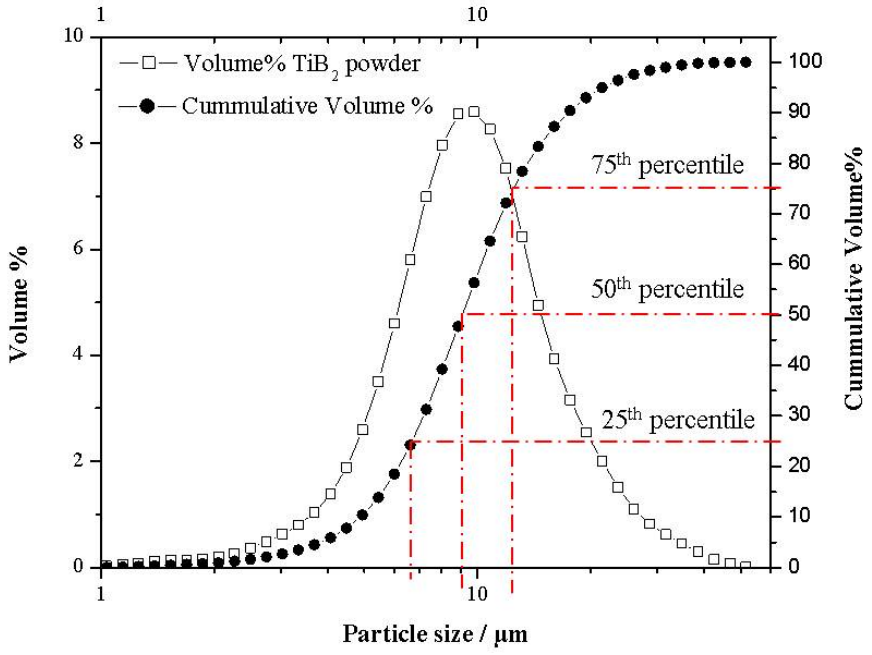

FIGURE 5.4: TiB_2 particle size analysis with mean particle size of 10 μm.

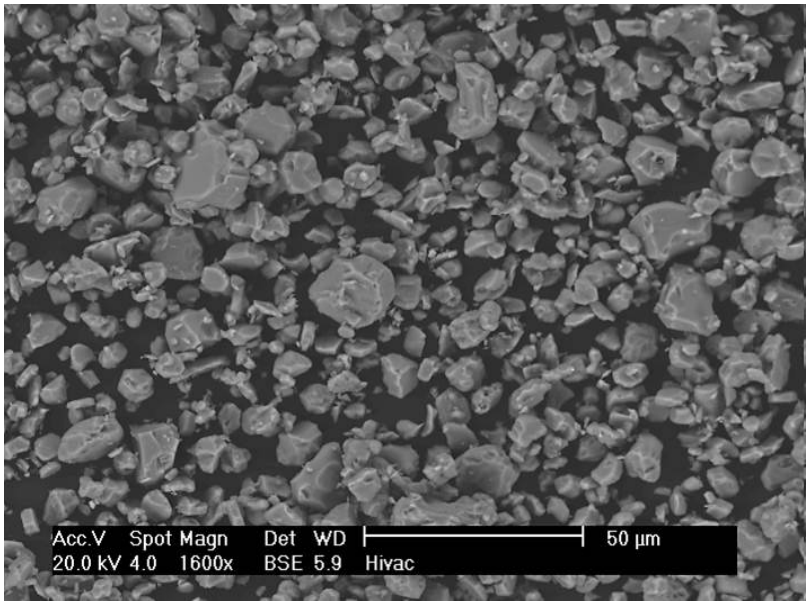

FIGURE 5.5: TiB_2 powder showing angular and plate morphology.

The XRD scan made over 2θ range of 30-90^o shows that the powder is made up of the TiB_2 phase as shown in Figure 5.6. The peaks are found to match the pattern of TiB_2

phase with ICDD no: 01-085-2083. The strongest reflection of the TiB_2, HCP (101) is observed at $2\theta = 44.5^o$. The spectrum with the matching pattern of TiB_2 is provided in Appendix C.3, and the crystallographic information about the matched TiB_2 pattern can be found in Appendix C.4.

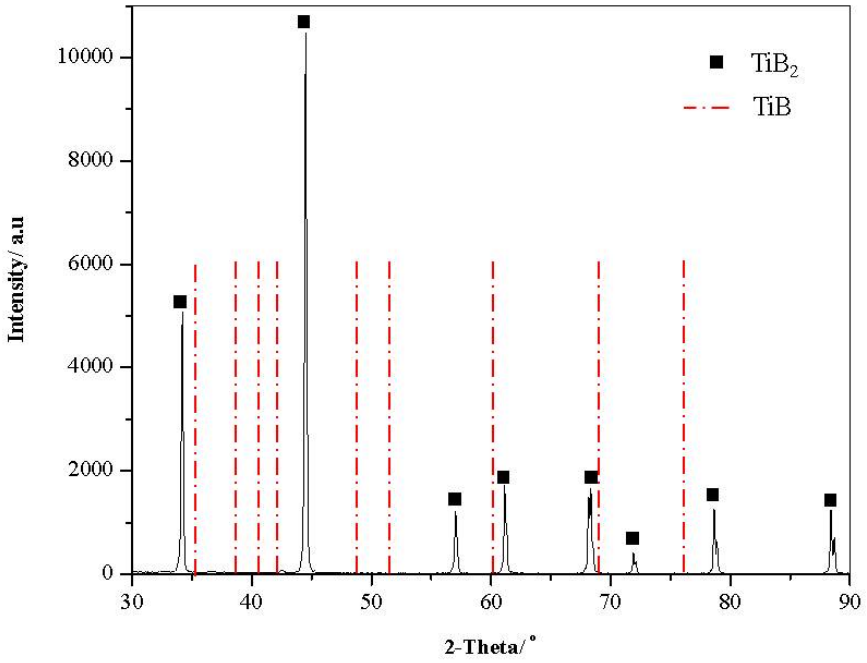

FIGURE 5.6: Powder XRD pattern with TiB_2 phase identified, lines for TiB do not match any peak.

5.3 TiB_2/Ti-6Al-4V powder blend

A blend of the TiB_2 and Ti-6Al-4V with a weight ratio of 1:6 was mixed using a powder mixer for 1.5 hours. The powder size analysis was also made which showed a bimodal curve as presented Figure 5.7. The powder analysis reflects the ratio of the two powders pre-blended. The low peak representing TiB_2 has a 1.5 peak volume% and the high peak representing Ti-6Al-4V has a 9 peak volume%. The volume ratio is similar to the weight ratio of 1:6 pre-blended, since the densities of the two powders are relatively similar (4420 kg/m^3, Ti-6Al-4V and 4520 kg/m^3, TiB_2). This also confirms a uniform blend of the two powders under the mixing conditions, as a small quantity used for the powder size analysis was a representative sample of the blend.

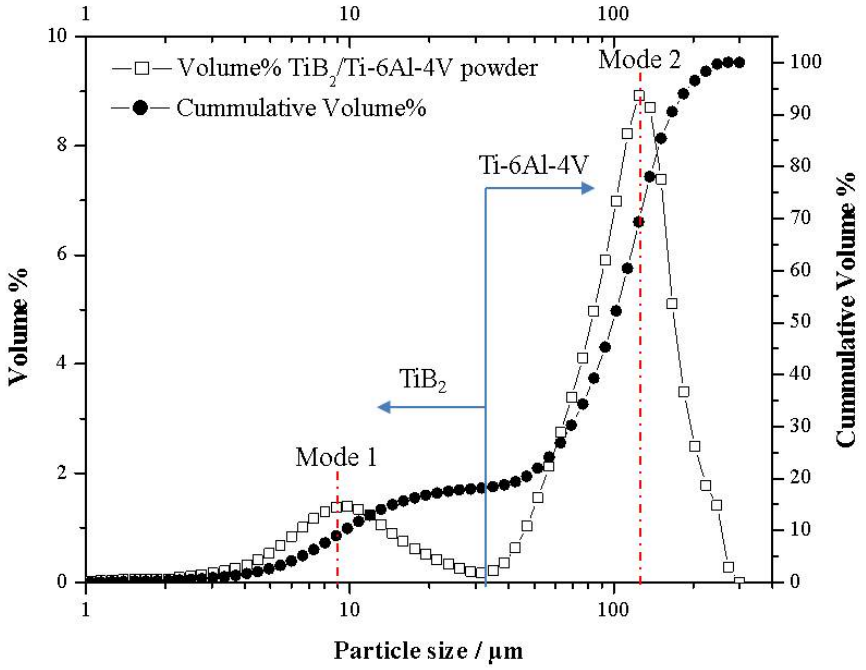

FIGURE 5.7: TiB_2/Ti-6Al-4V particle size analysis showing the bimodal curve.

5.4 Preliminary cladding trials

Cladding trials were conducted for the pre-blended TiB_2/Ti-6Al-4V powders to assess the feasibility of making deposits with the pre-blended powder. The use of the side fed material system (Figure 3.3) for the Ti-6Al-4V/TiB_2 blend proved impossible to develop a steady and evenly distributed feed. This blend did not consistently feed into the laser generated melt pool. This resulted in poor, irregular and inconsistent deposits. Thus, a coaxial feeding system was employed to address this problem. The following processing parameters were used:

- Laser power: 600 800 1000 W
- Traverse speed: 400 500 600 mm/min
- Powder feed rate: 20 g/min (constant)
- Focal position: 192 mm (at beam focus)
- Beam diameter: 1 mm

- Step up height: 0.5 mm (constant)

During this trial with the coaxial feeding nozzle, consistent powder flow was observed which made deposition possible. Each wall was made by ten layers of single beads with varying parameter combinations which can be found in Appendix C.1.

5.4.1 Characterisation of the Ti-6Al-4V/TiB$_2$ trial deposits

Figure 5.8 shows the optical micrographs of the Ti-6Al-4V/TiB$_2$ walls obtained from the trial experiment. Though deposition was possible, clads are of a poor quality. The deposits are characterised by poor interlayer bonding between individual layers, poor bonding at the clad/substrate interface, delamination from substrate and poor side wall surface finish.

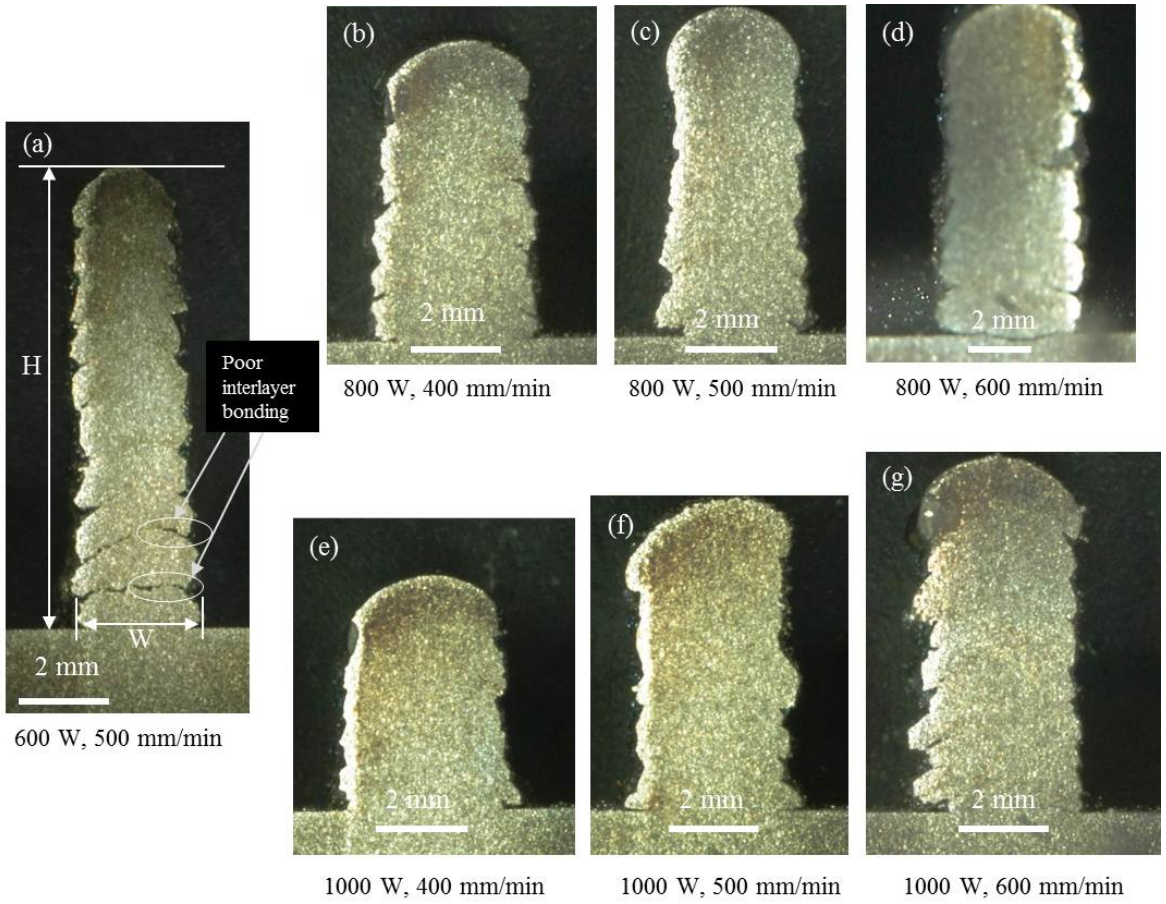

FIGURE 5.8: Optical micrographs of the Ti-6Al-4V/TiB$_2$ trial deposits showing improvement of the interlayer bonding as laser power increases and wall height increases as traverse speed increases.

Microstructural observations were undertaken on the polished cross section using SEM. All clads were characterised by non-uniform distribution of the TiB_2 particles, partially melted Ti-6Al-4V particles and pores. The TiB_2 powder was observed to leave the powder jet as it separates from the powder stream flowing to the melt pool. Figure 5.9 shows the SEM/BSE images of the laser clad deposited with laser power of 1000 W and traverse speed of 500 mm/min. In the SEM examination of the clad, the partially melted Ti-6Al-4V and clusters of TiB_2 particles are mostly present at the clad periphery. In Figure 5.9(*d*), partially dissolved edges of TiB_2 particles can be observed. The edges of the angular TiB_2 particles begin to grow out into the composite matrix as two contrast levels are observed.

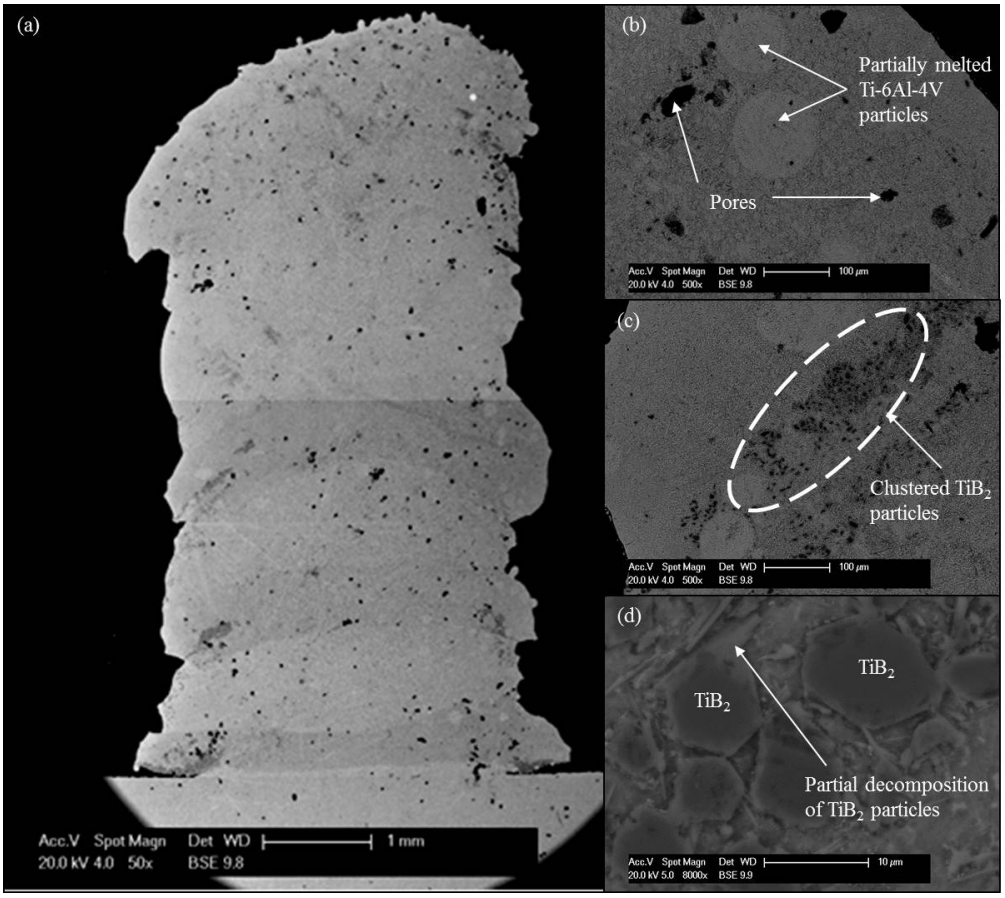

FIGURE 5.9: BSE images of the Ti-6Al-4V/TiB_2 trial clad deposited with laser power of 1000 W, traverse speed of 500mm/min and 20 g/min powder feed rate showing partially melted Ti-6Al-4V and TiB_2 particle clusters.

The observations suggest that the laser power may not be sufficient to completely melt the Ti-6Al-4V powders and incorporate the TiB_2 particles. Pores are observed in the micrograph due to incomplete melting and gas entrapment. The issue of material feeding

method and the pre-blended feedstock significantly affect the distribution of the TiB_2 particles in the deposits. Thus, there is a need for improvement of the feedstock or feeding process to make it suitable for the available powder feeding system to deliver it consistently during the cladding process.

5.4.2 Modified feedstock TiB_2 particle satellites on Ti-6Al-4V powder particles

Having reported the microstructure of the trial deposits, a modification of the pre-blended Ti-6Al-4V/TiB_2 powder feedstock was required. The feedstock modification made was to attach the TiB_2 particles to the Ti-6Al-4V particle feedstock which has been described in Section 3.2.3.1. Figure 5.10 shows the pre-blended powder with a 1:9 mass ratio of TiB_2 to Ti-6Al-4V mixed with a 2.7 volume% PVA solution as binder, then dried. The fine TiB_2 particles are found to adhere to the surface of the spherical Ti-6Al-4V powder particles under the influence of the adhesive. It was anticipated that this modification would resolve the issue of having an uneven distribution of TiB_2 particles in the powder stream flowing into the melt pool. It was also expected that there would be more uniform distribution of TiB_2 particles in the melt pool. Thus, with the proper selection of laser processing parameters, especially energy density, more uniform and complete dissolution of TiB_2 is to be expected.

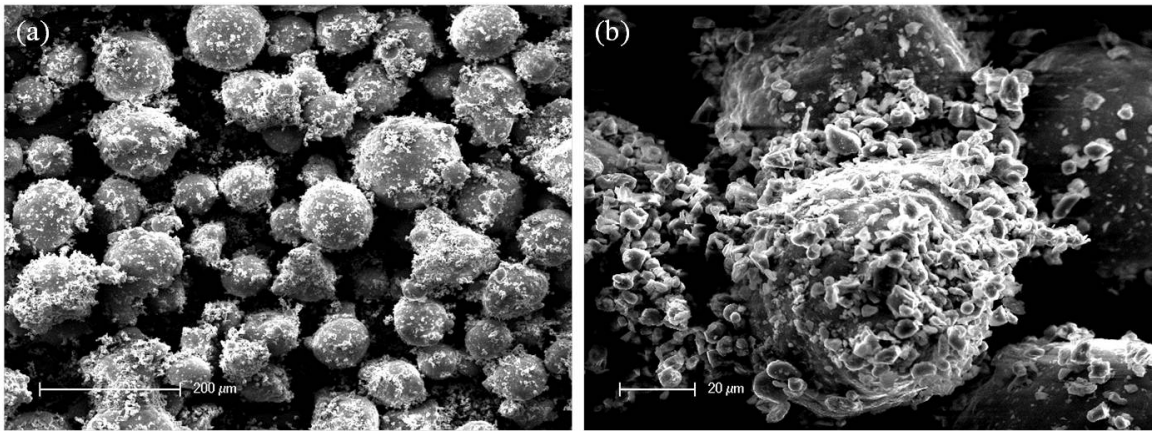

FIGURE 5.10: SE-SEM image of the Ti-6Al-4V particles with TiB_2 particle satellites (a) low magnification (b) high magnification.

Figure 5.11 shows the XRD spectrum of the modified feedstock shown in Figure 5.10. The experimental scan was conducted over a 2θ range of 10-90^o. Two phases are identified in the spectrum. These are α-Ti and TiB_2 phases. The diffraction peaks of these phases are similar to the ones discussed in Section 5.1 and 5.2. A small peak was found at 2θ position of 20^o which is suggested to indicate the presence of PVA in the powder as Yang and Wu [128] reported that PVA exhibits a semi-crystalline structure whose diffracted peaks can be found at low 2θ positions of 20^o and 40^o.

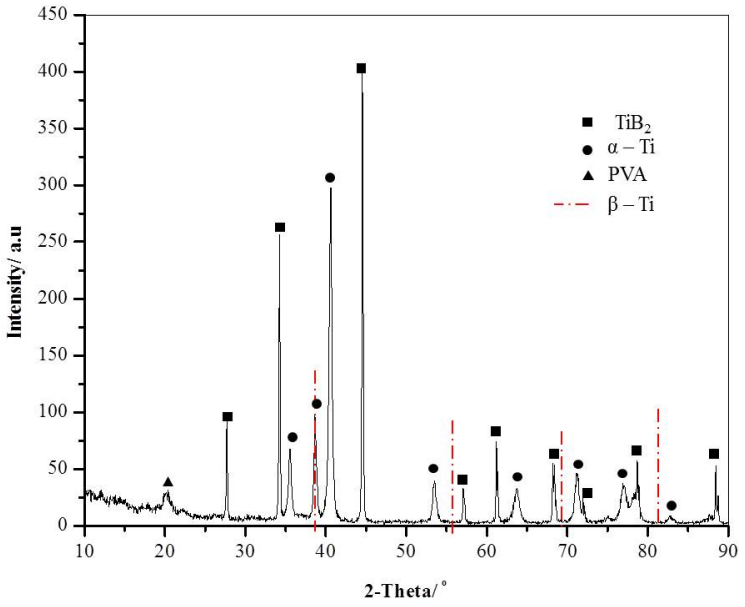

FIGURE 5.11: XRD spectrum for the modified feedstock TiB_2/Ti-6Al-4V pre-blend powder.

5.5 Cladding of the modified TiB_2/Ti-6Al-4V feedstock

This section discusses the laser cladding characteristics of the pre-blended and modified powder. The influence of the processing parameters on the geometrical characteristics of deposits are investigated.

5.5.1 Physical characteristics of laser clad TiB_2/Ti-6Al-4V feedstock

The cladding process was conducted using a side-fed material delivery system (Section 3.2.3) as the powder flow was observed to be consistent. The modification made to the feedstock had facilitated the delivery of the powder into the laser generated melt pool

using a side fed configuration. Single beads were deposited using a constant powder feed rate of 10±1 g/min. Based on the analysis of the outcome from the preliminary experiment discussed in Section 5.4, a laser power less than 1000 W was not adequate enough for cladding the pre-blended powder. In this experimental work, a laser power range of 1400 - 1800 W was used. The process factors with levels considered are as follows:

- Laser power: 1400 1600 1800 W
- Traverse speed: 200 300 400 mm/min
- Powder feed rate: 10 g/min (constant)
- Focal position: 212 mm (20 mm out of beam focus)
- Beam diameter: 3.1 mm

The deposition length of each track was 80 mm and the pitch between track centres was 10 mm. An L - 9 orthogonal array was designed for the experiment which takes into account the variable process factors (laser power and traverse speed) at three levels. This is a fractional factorial experimental design aimed at limiting the number of experimental runs while obtaining reliable results. The table for the process factor combination used can be found in Appendix C.2.

The objective of the section is to determine the main effect of the process factors on the bead height, width, melt pool depth and understanding the resulting microstructure

The width and height of each single track were measured using Talysurf CLI 1000 profiler, and measurements were taken at three different locations along each track. The measurements can be found in Appendix C.3.

5.5.2 Effect of process factors on TiB_2/Ti-6Al-4V deposit height and width

Figure 5.12 shows the main effect of the process factors on TiB_2/Ti-6Al-4V bead height. The bead height was found to be strongly dependent on traverse speed, similar to that observed in Section 4.1.1. An inverse relationship was observed between the mean height

and traverse speed with the highest mean bead height of 1.15 mm when the process speed was 200 mm/min and 0.6 mm height for 400 mm/min process speed.

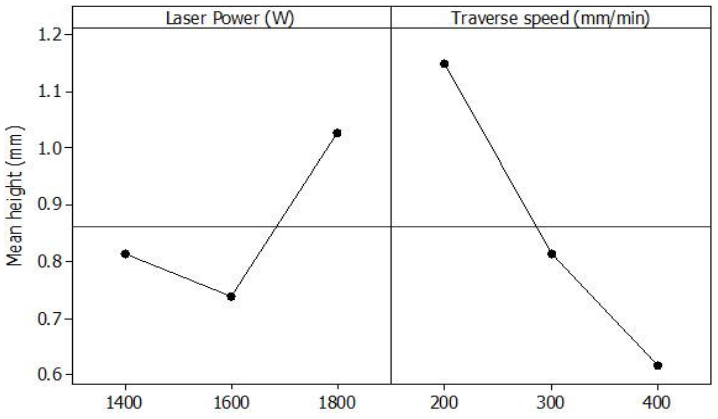

FIGURE 5.12: Main effect plot for mean height for deposited TiB_2/Ti-6Al-4V powder showing positive dependence of bead height on laser power and inverse dependence on traverse speed.

Considering the effect of laser power between the lowest and highest level on the bead height, a positive relationship was observed between laser power and bead height. The mean height observed at laser power of 1800 W was 1.05 mm while at 1400 W, mean height was 0.8 mm.

Figure 5.13 shows the main effect of the process parameters on the TiB_2/Ti-6Al-4V bead width. As expected, a strong and positive relationship was observed between laser power and bead width. The lowest laser power used (1400 W) resulted in a mean bead width of 3.9 mm and the highest laser power used in the experiment (1800 W) yielded mean bead width of 4.7 mm. The bead width was also observed to be inversely dependent on the traverse speed. Mean bead widths of 4.8 mm and 4.1 mm were measured when 200 mm/min and 400 mm/min traverse speeds were employed respectively.

Figure 5.14(a) shows a contour plot which combines the effect of laser power and traverse speed on the deposit height. The arrow in the figure indicates the direction of increasing height as laser power increases and traverse speed decreases. Within the process levels used in the experimental design, the processing parameters that would give the maximum bead height were determined by parameters associated with the top left side of the graph. The maximum height of the bead was greater than 1.4 mm. From the contour plots, the traverse speed required to deposit beads with a maximum height ranged between 200-230 mm/min and laser power required ranged between 1760-1800 W. Based on the

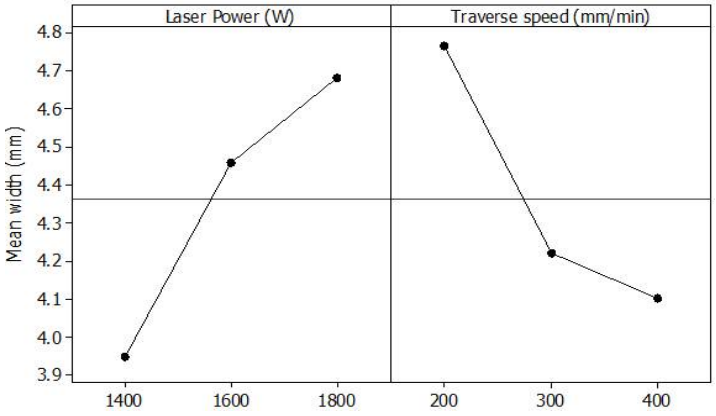

FIGURE 5.13: Main effect plot for mean width for deposited TiB_2/Ti-6Al-4V powder.

experimental work, a maximum bead height of 1.7 mm was achieved when laser power of 1800 W and traverse speed of 200 mm/min were employed (Appendix C.3), and the energy density required is 222 J.mm^{-2} using equation 4.6.

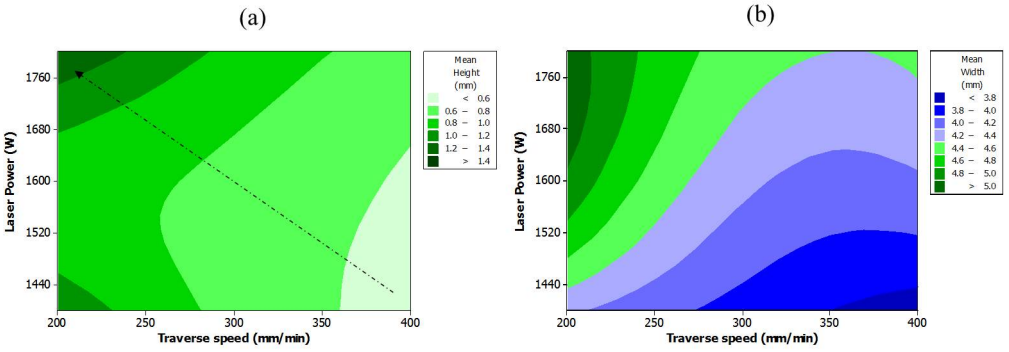

FIGURE 5.14: Combined effect of laser power and traverse speed on TiB_2/Ti-6Al-4V deposit (a) height; (b) width.

Figure 5.14(b) shows a contour plot which combines the influence of both laser power and traverse speed on the deposit width. The plot shows that the width increases from the bottom right hand corner to the top left hand corner, as the traverse speed decreases and laser power employed increases. The maximum bead width can be obtained using process parameters which are in the range of 1650-1800 W and 200-210 mm/min for laser power and traverse speed respectively. The maximum bead width observed was 5.4 mm (Appendix C.3), obtained for bead deposited with laser power of 1800 W and traverse speed of 200 mm/min. This has a similar energy density requirement as obtained for deposit height. This process parameter value falls within the value range for maximum deposit width to be obtained.

The minimum bead width obtained from the experiment was 3.95 mm (Appendix C.3) and the corresponding process parameters value used were 1400 W laser power and 400 mm/min traverse speed. This results in a corresponding energy density value of 86 J.mm^{-2}, with a beam diameter of 3.1 mm. This can be plotted in the bottom right hand corner of the contour plot. Thus, the contour plot is a useful tool to predict the physical characteristics of the beads obtained within the process parameter levels used in the laser cladding experiment. The main effect plot (Figure 5.13) and the contour plot (Figure 5.14(b)) are complementary.

5.5.3 Effect of process factors on bead substrate dilution

Figure 5.15 shows the schematic of bead on plate showing the region of the substrate which melts to dilute the bead composition. The analysis to determine the dilution percentage of the substrate with the bead content is conducted for the lowest and the highest laser power levels employed. The dilution percentage is calculated using Equation (5.1) [10]. Table 5.1 presents the results obtained as dilution varies with traverse speed.

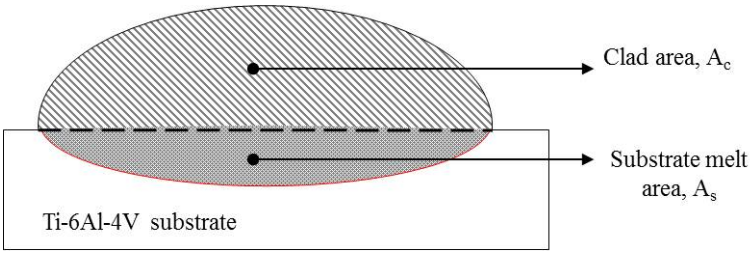

FIGURE 5.15: Schematic of bead on plate showing the region of the substrate which dilutes the clad composition.

$$Dilution(\%) = 100(\frac{A_s}{A_s + A_c}) \tag{5.1}$$

The result shows that bead-substrate dilution % increases significantly as traverse speed increases. A substantial reduction in dilution is also observed at higher laser power (1800 W) and higher traverse speed (400 mm/min) when compared to the lowest laser power level (1400 W). It may have been more appropriate to determine the change in the remelting area or the penetration depth (ratio of A_s to A_c) rather than the study

TABLE 5.1: Substrate dilution percentage showing a significant increase in dilution with increasing traverse speed

Laser power	1400 W	1800W
Traverse speed	Bead - substrate dilution	
200 mm/min	14%	15%
300 mm/min	24%	21%
400 mm/min	33%	23%

of dilution. Since, the rate at which the clad area increases with decreasing traverse speed is greater than the increase in the melted substrate area, the dilution percentage, calculated using equation (5.1), will decrease with decreasing traverse speed.

5.6 Microstructure of TiB$_2$/Ti-6Al-4V composite beads

5.6.1 Composite bead cross section characteristics

Figure 5.16 shows the TiB$_2$/Ti-6Al-4V composite bead cross sections, which have been polished and examined using SEM. All the composite beads are observed to be metallurgically bonded to the Ti-6Al-4V substrate with an appreciable substrate melt depth of 230-360 μm. Based on the process parameters employed in this study, no cracks or delamination are observed in samples deposited. A few pores are observed on some of the clad cross sections near the clad-substrate interface. A few partially melted Ti-6Al-4V particles can be observed in the micrographs in Figure 5.16. These are seen as dark features which are mostly observed in the clad periphery regions. Based on visual observation, the presence of the partially melted Ti-6Al-4V particles was found to decrease with increasing traverse speed for beads deposited with laser power of 1400 W and partially for 1600 W and not for 1800 W.

5.6.2 Phases present in TiB$_2$/Ti-6Al-4V composite beads

Having observed that the beads deposited with high traverse speeds (400 mm/min and above) possess fewer partially melted particles, overlapping tracks corresponding to the single beads shown in Figure 5.16 (c), (f) and (i) were prepared for XRD examination. Figure 5.17 shows XRD patterns for the beads deposited using laser power of 1400 W, 1600 W and 1800 W with a constant traverse speed of 400 mm/min and a constant

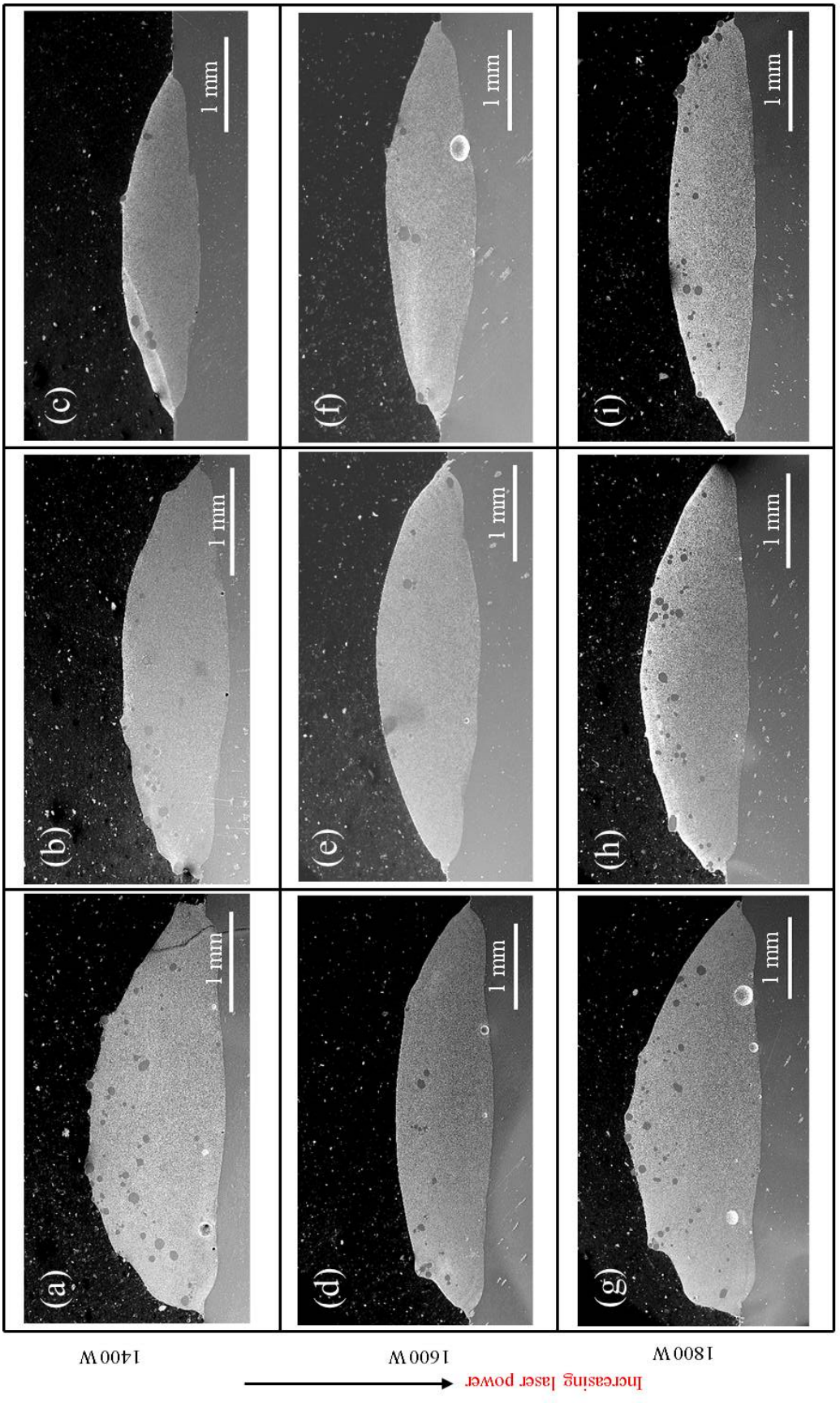

FIGURE 5.16: SE-SEM images of the TiB_2/Ti-6Al-4V bead cross sections. All deposited with 10 g/min powder flow rate.(Dark features are unmelted Ti-6Al-4V).

powder feed rate of 10 g/min. The patterns were similar and the same phases were identified with the exception of the bead deposited with laser power of 1400 W which had a trace of TiB_2 phase remaining from the primary feedstock. The phases were identified by comparing the diffraction peaks in each spectrum with the phase patterns in the ICDD database.

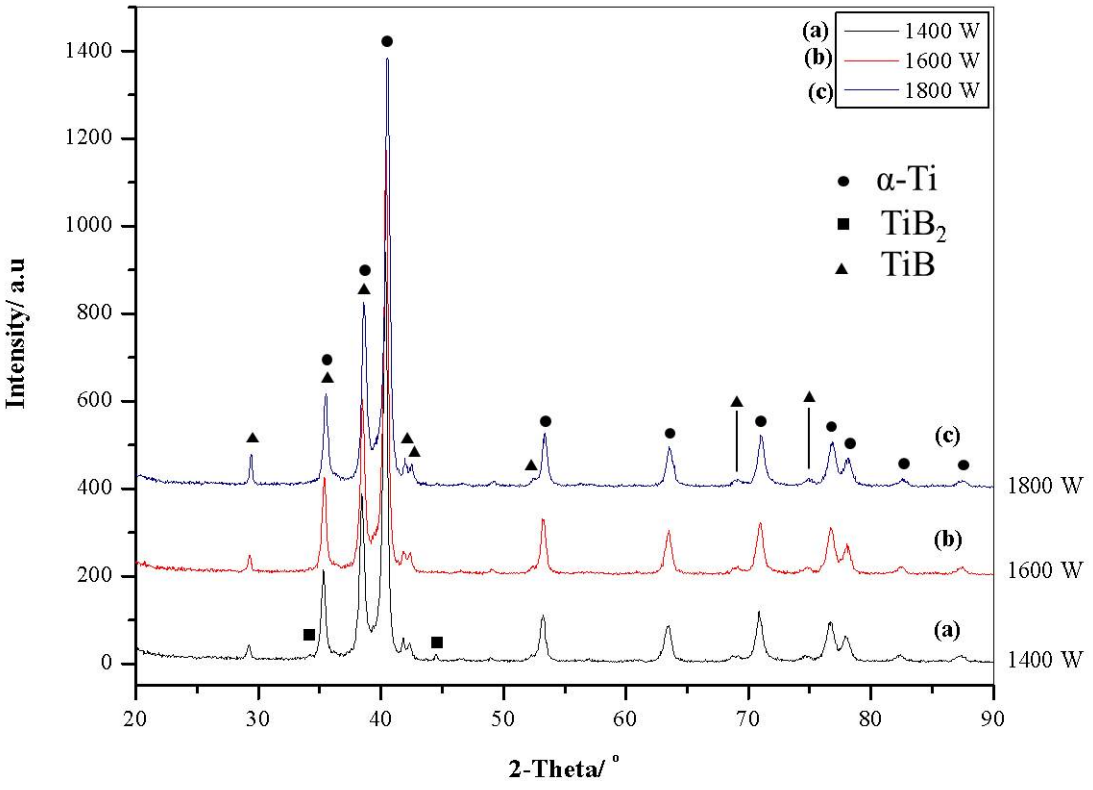

FIGURE 5.17: XRD spectra for TiB_2/Ti-6Al-4V clad layer deposited using a range of laser powers, a traverse speed of 400 mm/min, and a powder feed rate of 10 g/min showing the disappearance of TiB_2 phase as laser power increases.

The matching phases with their pattern file number include:

- α-Ti (ICDD no: 00-044-1294),
- TiB_2 (ICDD no: 01-085-2083), and
- TiB (ICDD no:01-073-2148)

The spectra with the matching phase patterns are presented in Appendix C.5. The first two phases mentioned correspond to the phases identified in the primary feedstock as discussed in Section 5.4.2. Thus, the ICDD file for the identified TiB is presented in Appendix C.6.

5.6.3 Microstructural features of the TiB_2/Ti-6Al-4V composite

Figure 5.18 shows the cross sections of beads slightly etched with Krolls reagent whose phases are presented in Section 5.6.2. In the cross sections, the observed pores are located along the fusion line. Partially melted Ti-6Al-4V particles are seen mostly near the top of the bead cross section down towards the middle section of the sample. A clear fusion line is also observed with the expectation of a good metallurgical bond between the bead and the substrate. The contact angle between the clad and the substrate is observed to be greater than 100^o in all cases. An angle of 150 ± 2^o was measured for bead cross section in Figure 5.18(a). This indicates that all the beads presented are suitable for multipass overlap cladding which would result in no inter-run porosity with the proper selection of overlap pitch. Moreover, the micrographs confirm that bead-substrate dilution is reduced as laser power increases to complement result presented in Section 5.5.3.

Figure 5.19 shows magnified images of the box section of the bead cross sections of Figure 5.18 showing a Ti rich primary phase (dark contrast) and a eutectic like region of needles and matrix in between the dendrites. The dendritic Ti-rich phase is more apparent in Figure 5.19(b) than in (d) or (f). The TiB reinforcements, which are commonly seen as white needles in the micrograph, are randomly oriented. The TiB needles are of varying lengths and a very narrow width. In Figure 5.19(d), the longest TiB needle observed in the micrograph of bead deposited with a laser power of 1600 W is 30 μm, while 40 μm is measured in Figure 5.19(f) for bead deposited with 1800 W laser power. This may indicate that the length of the in-situ synthesized TiB reinforcement is positively dependent on the laser power employed to process the feedstock.

In Figure 5.19(f), the TiB precipitates are well distributed in the Ti phase, while eutectic TiB reinforcements which are oriented in the same direction is prevalent in the Ti-rich interdendritic region in Figure 5.19(b). This is a good indication of a strong mixing activity which must have taken place when higher laser power is employed for the cladding process. The higher magnification SEM images (secondary electron) of Figure 5.20 show the presence of what could be partially dissolved TiB_2 particles and micro pores throughout the bead cross sections irrespective of the laser power used. In the XRD scan, low intensity peaks of TiB_2 phase are identified for the bead processed

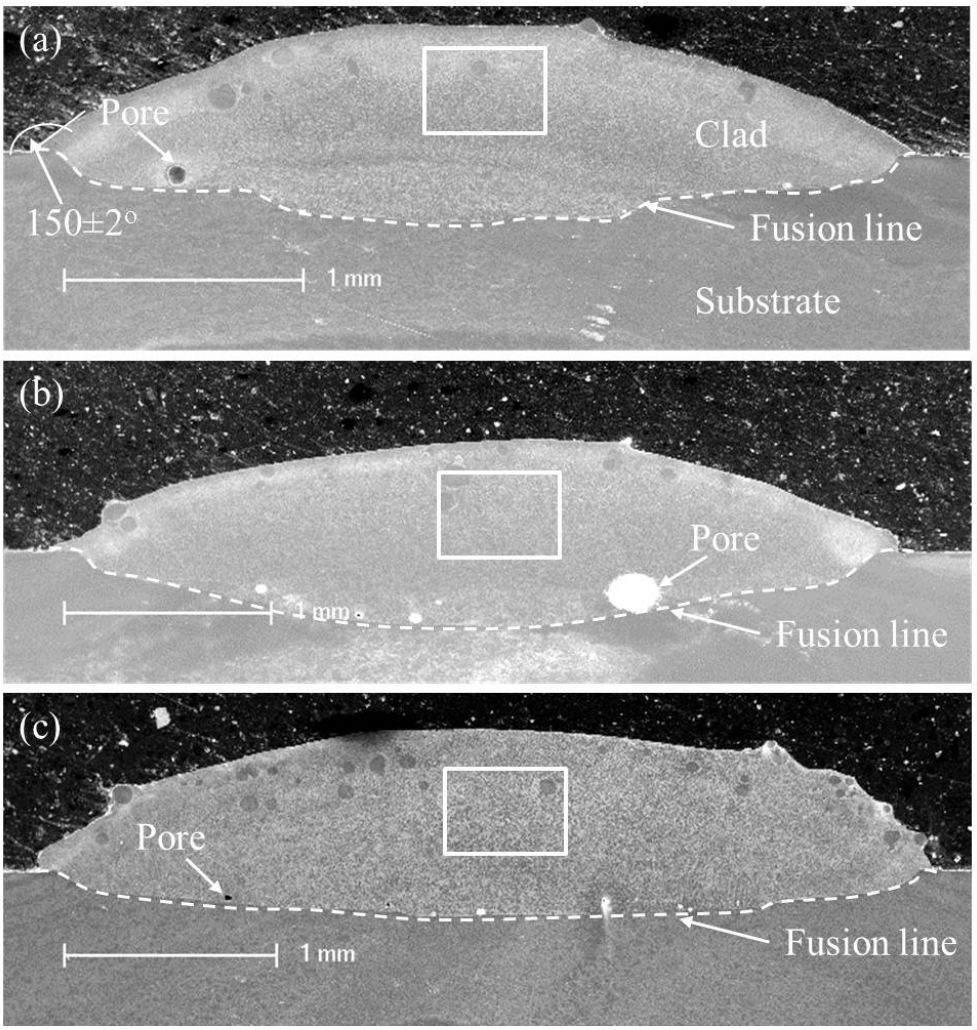

FIGURE 5.18: SE-SEM image of the cross section of single beads showing partially melted Ti-6Al-4V particles around the clad periphery and pores close to the fusion line. Process parameters: Traverse speed = 400 mm/min, Powder feed rate = 10 g/min; Laser power = (a) 1400 W (b) 1600 W and (c) 1800W.

at 1400 W. This may suggest that the presence of partially dissolved TiB_2 particles decreases with increasing laser power. However, there remains a remnant of the unreacted particles when processed with a high laser power such as 1800 W, as seen in Figure 5.20(c). In Figure 5.20(d), the dark grey TiB_2 particle is observed to have a light grey edge with growth of TiB needles around the edge. This indicates that as TiB_2 particles are dissolving into the Ti melt, its boron atoms react with Ti to form TiB reinforcements on cooling.

Micro pores with white halo edges, which are either circular or elliptical in cross section, are observed in the micrographs. In Figure 5.20(d), a near circular micro pore is measured to have a 1 μm diameter size.

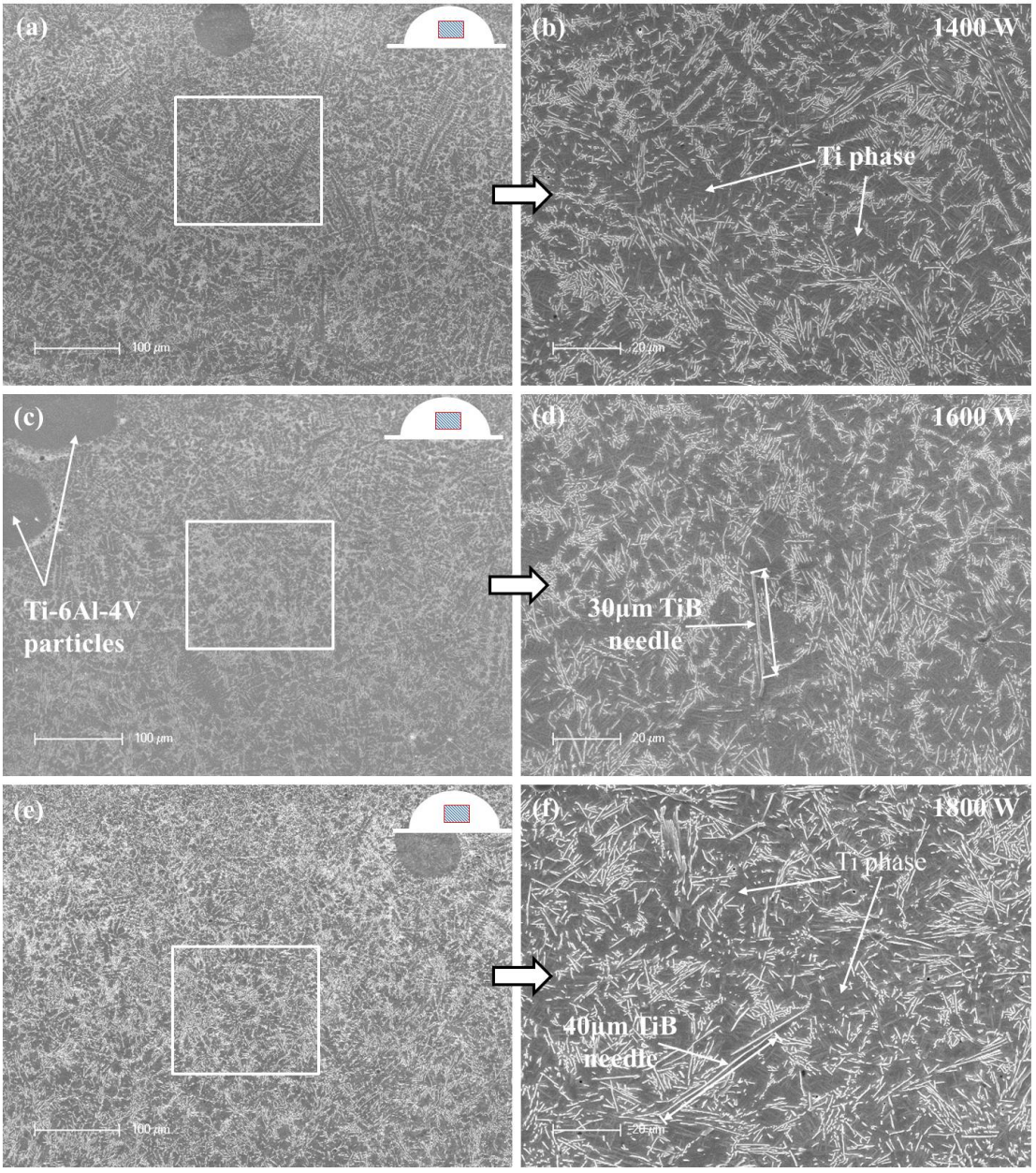

FIGURE 5.19: SE-SEM images of etched samples with the middle section of bead cross sections showing a uniform and random distribution of TiB reinforcement in (a)&(b) higher magnification of box in Figure 5.18(a), (c)&(d) higher magnification of box in Figure 5.18(b) and (e)&(f) higher magnification of box in Figure 5.18(c).

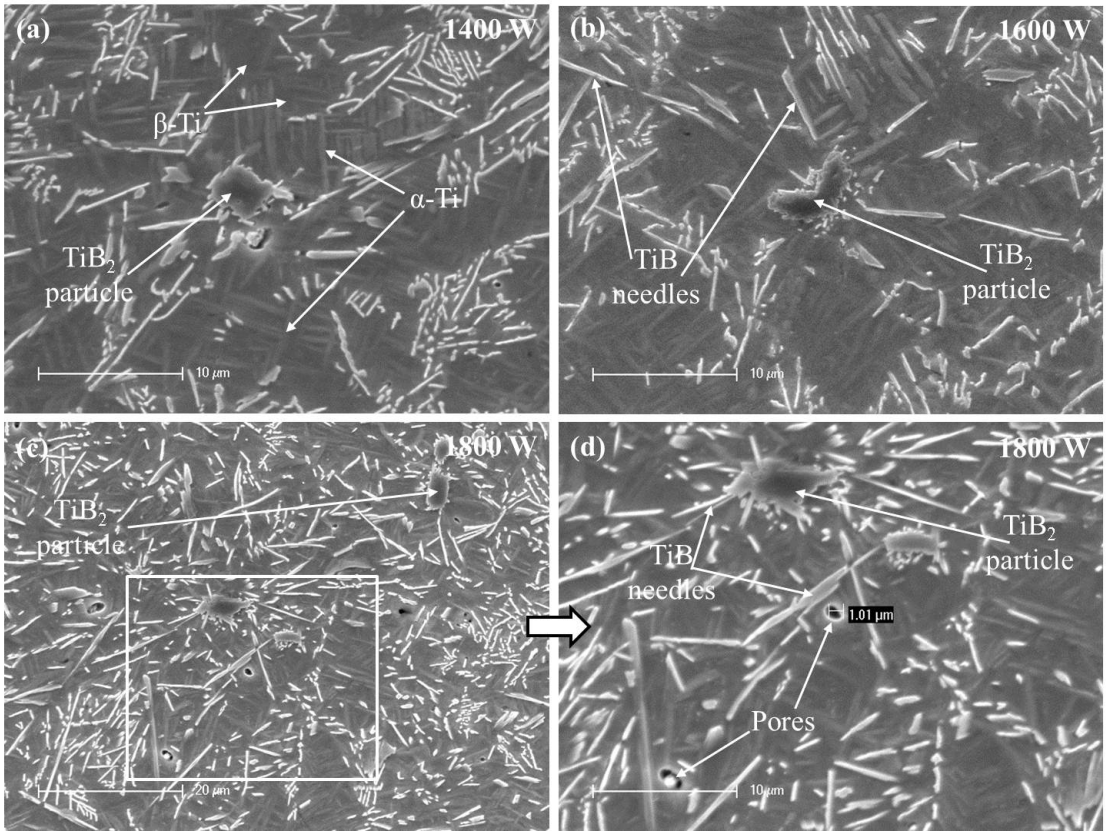

FIGURE 5.20: SE-SEM images of etched samples showing the presence of TiB_2 particles and pores in all bead cross sections.

Figure 5.21 shows the micrograph of the top region of the TiB_2/Ti-6Al-4V composite beads. Partially dissolved Ti-6Al-4V and TiB_2 particles are mostly observed in the region. The cross section of the embedded Ti-6Al-4V is characterised by what could be acicular or martensitic α-Ti structure. In Figure 5.21(b), radial growth of TiB needles is observed to cluster around the partially melted Ti-6Al-4V particle. These TiB precipitates grow from the Ti-6Al-4V particle surface. The TiB clusters had resulted from the TiB_2 powder attached onto the Ti-6Al-4V particles. The TiB_2 particles attached to the Ti-6Al-4V particle have been preserved even after it has been blown through the powder feeding system. Upon laser irradiation, the TiB_2 particles dissolved making region around the Ti-6Al-4V particle boron-rich and reacting with Ti melt to form TiB clusters as observed.

Figure 5.22 shows the micrographs of the clad/substrate region of the composite beads. A clear clad/substrate interface is observed at the fusion boundary. Large pores with a variety of morphologies in cross section are observed in the micrographs which are

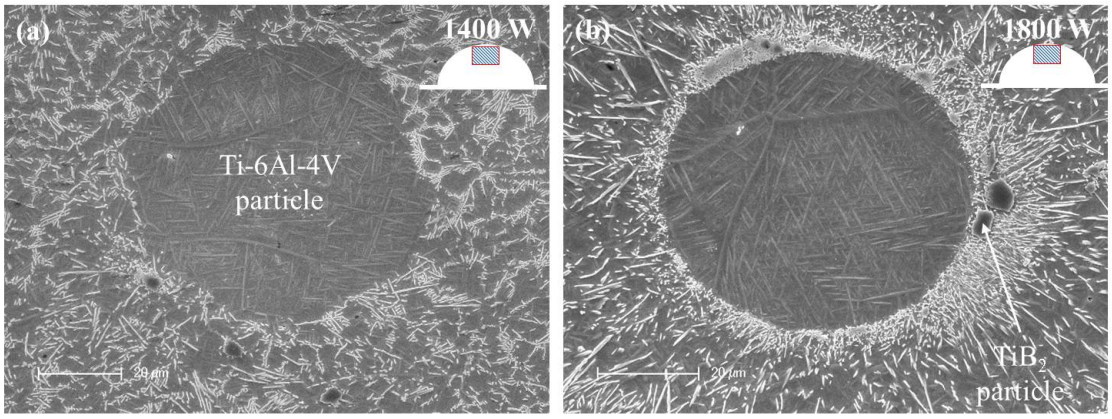

FIGURE 5.21: SE-SEM images of etched samples with the top region of the composite bead showing partially dissolved Ti-6Al-4V and TiB_2 particles with TiB precipitate clusters.

located close to the clad/substrate interface. In Figure 5.22(a), a hemispherical recess is observed with a near circular edge. This pore is not a through hole and the recess indicates a Ti-6Al-4V pull-out. However, in Figure 5.22(b) and (c), the observed pores are deep which is suggested to be associated with incomplete fill or gas entrapment.

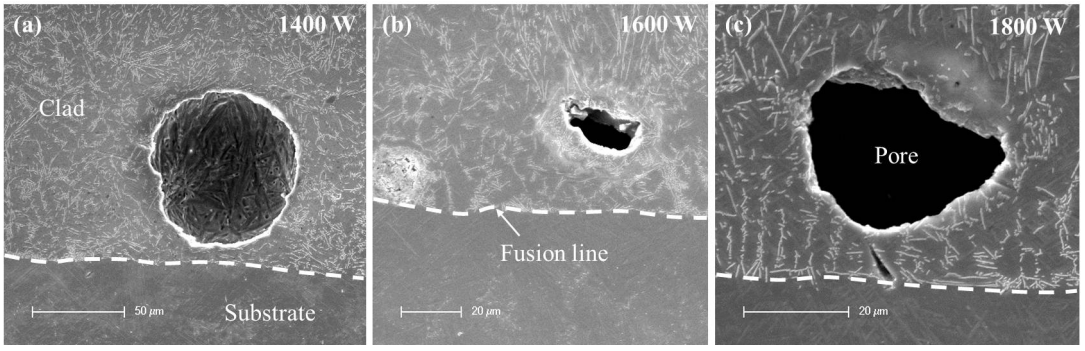

FIGURE 5.22: SE-SEM images of etched samples with the clad/substrate regions of the composite showing large pores and a clear fusion boundary line at the clad/substrate interface.

The SEM images (secondary electron) of these lightly etched TiB_2/Ti-6Al-4V composite samples show that the majority of the TiB_2 particles dissolve in the melt. The dissolution of TiB_2 results in the formation of TiB precipitates in the form of needles on cooling. Depending on the process parameters employed, a Ti-rich dendritic or a eutectic-like TiB dispersed in Ti matrix structure is formed. The TiB reinforcements are uniformly and randomly distributed in a Ti matrix characterized as α-Ti phase. Increasing laser power is observed to produce TiB reinforcement with a longer length. Though partially

dissolved TiB_2 and Ti-6Al-4V particles are evident in all samples, XRD results show that by employing a higher laser power, partially dissolved particles may be reduced. A clear clad/substrate interface, a few large pores at the fusion line and micro pores are observed in the micrographs. The adherence of the TiB_2 powder onto the surface of the Ti-6Al-4V particles was sufficient to survive powder feeding. This promotes a uniform distribution of the reinforcing element (TiB_2 particles/TiB whiskers) in the melt pool when compared to the microstructure of the preliminary cladding experiment discussed in Section 5.4.1.

5.7 Microhardness of the TiB_2/Ti-6Al-4V composite beads

Figure 5.23 shows the variation of hardness across the bead cross sections shown in Figure 5.16. The Vickers hardness test was conducted using a load of 300 gf and a loading time of 15 s with indent spacing of 127 μm from the clad top region down into the substrate. At each level of indent, three hardness values were obtained along lines 254 μm apart. The zero position on each graph is on the fusion boundary between the clad and the substrate. Results show that the top region of the beads had a higher mean hardness value which ranged between 490-590 $HV_{0.3}$ when compared to the central region of the beads which had relatively uniform hardness values. The high hardness in the top region is directly attributed to the presence of partially dissolved TiB_2 particles observed in the clad periphery. Though the hardness of this top region is not as high as the TiB_2 (3650 HV - Table 2.8), the existence of these partially dissolved TiB_2 particles influences the hardness values obtained in this top region of the beads. It is also observed that hardness value at the top region decreases with increasing laser power. A mean hardness of 590$\pm$49 $HV_{0.3}$ is observed when 1400 W laser power is employed, while 490$\pm$14 $HV_{0.3}$ for 1800 W at a common traverse speed of 200 mm/min. The hardness results also show that a homogenous TiB_2/Ti-6Al-4V composite is formed when processing is conducted at higher traverse speeds (400 mm/min). The hardness across all beads deposited using 400 mm/min traverse speed ranges from 440-480 $HV_{0.3}$ with a standard error less than 15. The consistency in hardness values of the beads deposited at 400 mm/min is attributed to the reduced presence of partially dissolved particles in the beads. There is a drop in hardness values when the indents are made in the heat affected zone (HAZ) below the fusion line. The substrate hardness is consistent with the value quoted for Ti-6Al-4V

(349 HV - Table 2.3). A hardness enhancement of 30% is achieved with the 10 wt. % TiB_2 reinforcement in Ti-6Al-4V.

5.8 Multilayer cladding of TiB_2/Ti-6Al-4V powder

Figure 5.24 shows the multilayer wall built using a continuous build strategy as described in Section 3.6 with the TiB_2/Ti-6Al-4V feedstock. The traverse speed and powder feed rate for the wall was kept constant throughout the deposition process at 200, 400 or 600 mm/min and 10 g/min respectively.

Table 5.2 shows the process parameters employed for building the composite walls. A laser power of 1800 W is employed at the initial start of the wall building while the speed is kept constant throughout. This allows for metallurgical bonding to develop between the first bead and the substrate. After the 4th layer, the laser power is reduced to 1600 W to avoid the flattening of the previous layer. A multilayer of single laser pass is made to ensure that wall built is sufficiently high to cut out tensile test piece with dimensions shown in Figure 3.9. In Figure 5.24, there is height discrepancy at both ends which is associated with the acceleration and deceleration of the CNC table. The discrepancy is attributed to re-melting of the previous layer which becomes prominent at the ends. The control of laser power during deposition is expected to eliminate this shortcoming. The walls are cut off the Ti-6Al-4V substrate, and milled to a flat thin wall of 4 mm width. Tensile tests specimens are cut out of the flat thin walls using WireEDM.

TABLE 5.2: Process parameters employed for wall building

Layers	Laser power (W)	Traverse speed (mm/min)	Step height in Z (mm)
1st - 4th	1800	200	1
5th - 7th	1600	400	0.6
8th - nth	1500	600	0.4

5.8.1 TiB_2/Ti-6Al-4V composite wall in cross section

Figure 5.25 shows the etched optical micrographs of the multilayer walls with the individual layer bands clearly seen. The difference in the number of layers required to achieve the same height is accounted for by different step height in z-axis employed during cladding (Table 5.2). The individual layers are metallurgically bonded to one

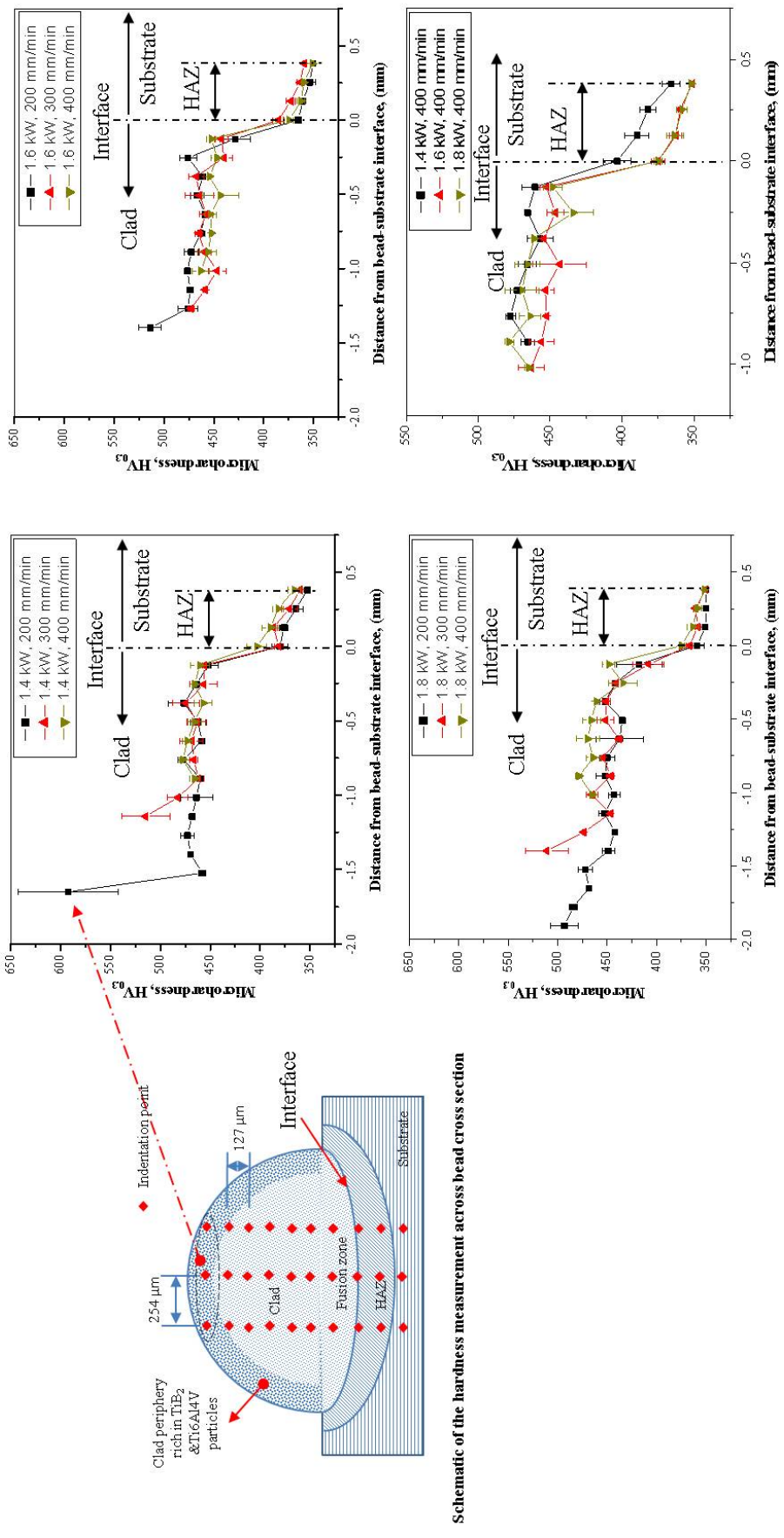

FIGURE 5.23: Microhardness variation across the single beads of TiB_2/Ti-6Al-4V composite.

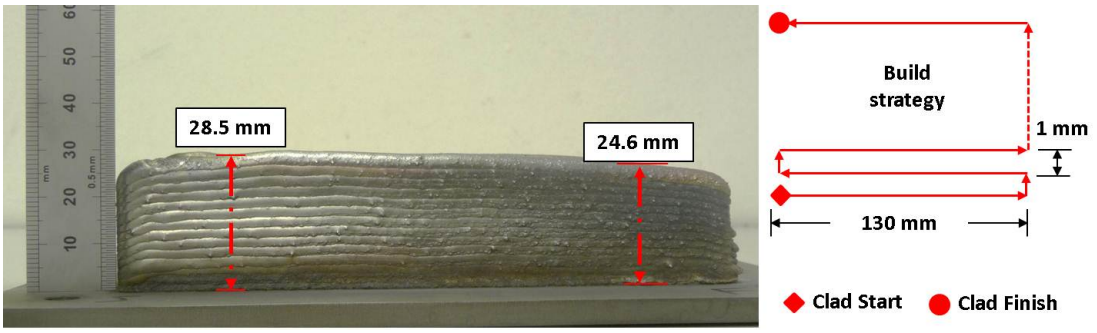

FIGURE 5.24: Multilayer wall built from side-fed TiB_2/Ti-6Al-4V feedstock using a traverse speed of 200 mm/min.

another. However, pores are observed predominantly in the interlayer band regions in all the deposited walls. No crack or delamination is observed in all the multilayer walls deposited based on the process parameters employed. As expected, the width of the deposited walls decreases with increasing traverse speed.

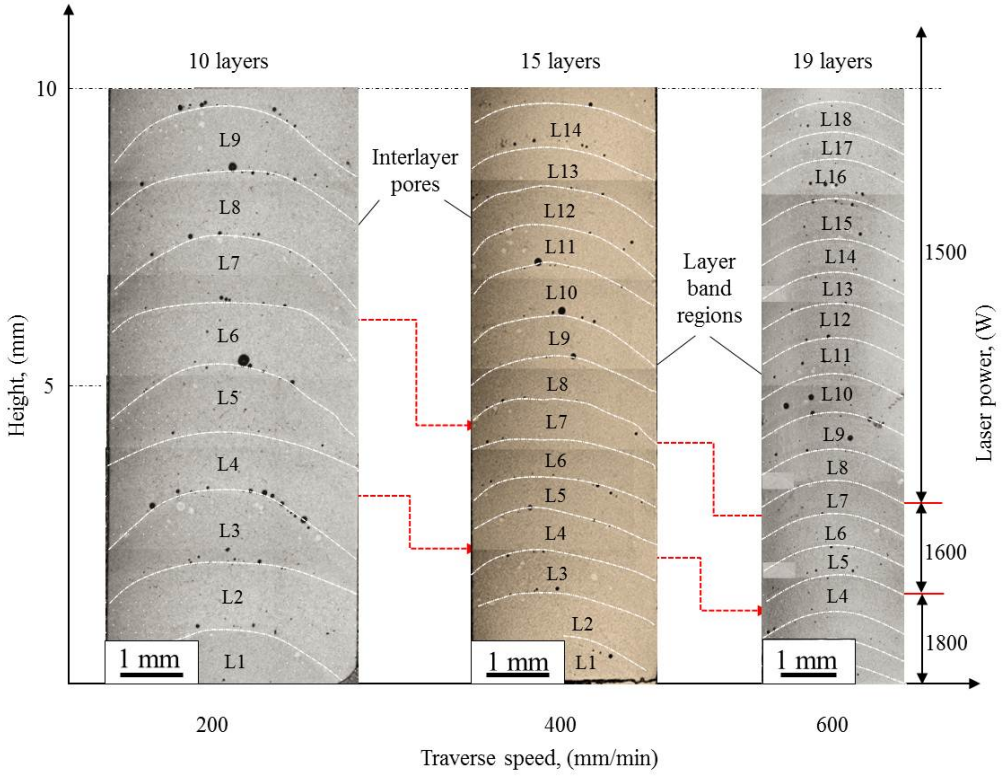

FIGURE 5.25: Etched optical micrographs of multilayer walls built with clearly observed individual layer bands which are marked by white dashed lines.

5.8.2 Microstructure of the interlayer region of the multilayer wall

Figure 5.26 shows the etched optical micrographs of an interlayer region of a TiB_2/Ti-6Al-4V composite wall. The interlayer region is situated between the second and the third layer of wall deposited with a constant traverse speed of 200 mm/min. A common laser power of 1800 W is employed to deposit both the second and the third layer. Thus, the top region of the second layer has experienced reheating and remelts for the third layer to be metallurgically bonded to it. The re-melting of the second layer results in the observed layer bands. Pores and partially melted Ti-6Al-4V particles are observed in the interlayer band regions. These are also previously observed in the single bead characterisation reported in Section 5.6.3.

At higher magnification, the microstructure of interlayer region is characterised by both primary and eutectic TiB precipitates dispersed in the α-Ti matrix as shown in Figure 5.26(b). Regions farther away from the layer band are characterised by predominantly eutectic TiB needles uniformly and randomly distributed in the Ti matrix as shown in Figure 5.26(a) and (c). Hence, the TiB_2/Ti-6Al-4V composite walls are made up of eutectic TiB uniformly dispersed in a Ti matrix with thin interlayer bands possessing both primary and eutectic TiB precipitates owing to re-melting and re-solidification of the surface of the previous layer.

5.8.3 Microhardness of TiB_2/Ti-6Al-4V composite wall

Figure 5.27 shows the microhardness profile along the centre line of the TiB_2/Ti-6Al-4V composite wall in cross section. The Vickers hardness test was conducted using a load of 300gf and a loading time of 15 s with indent spacing of 0.5 mm from the first clad layer to the ninth layer. The mean hardness of the central region of each layer and the interlayer regions are 461±4 HV and 440±5 HV respectively. The hardness of the interlayer region is lower than the central region of each layer. This can be attributed to the microstructural change that occurred in the region as a result of re-melting and re-solidification. The overall wall hardness is 451±4 HV. The hardness values measured falls within the limits of 440-480 HV measured in the central region of single beads as shown in Figure 5.23.

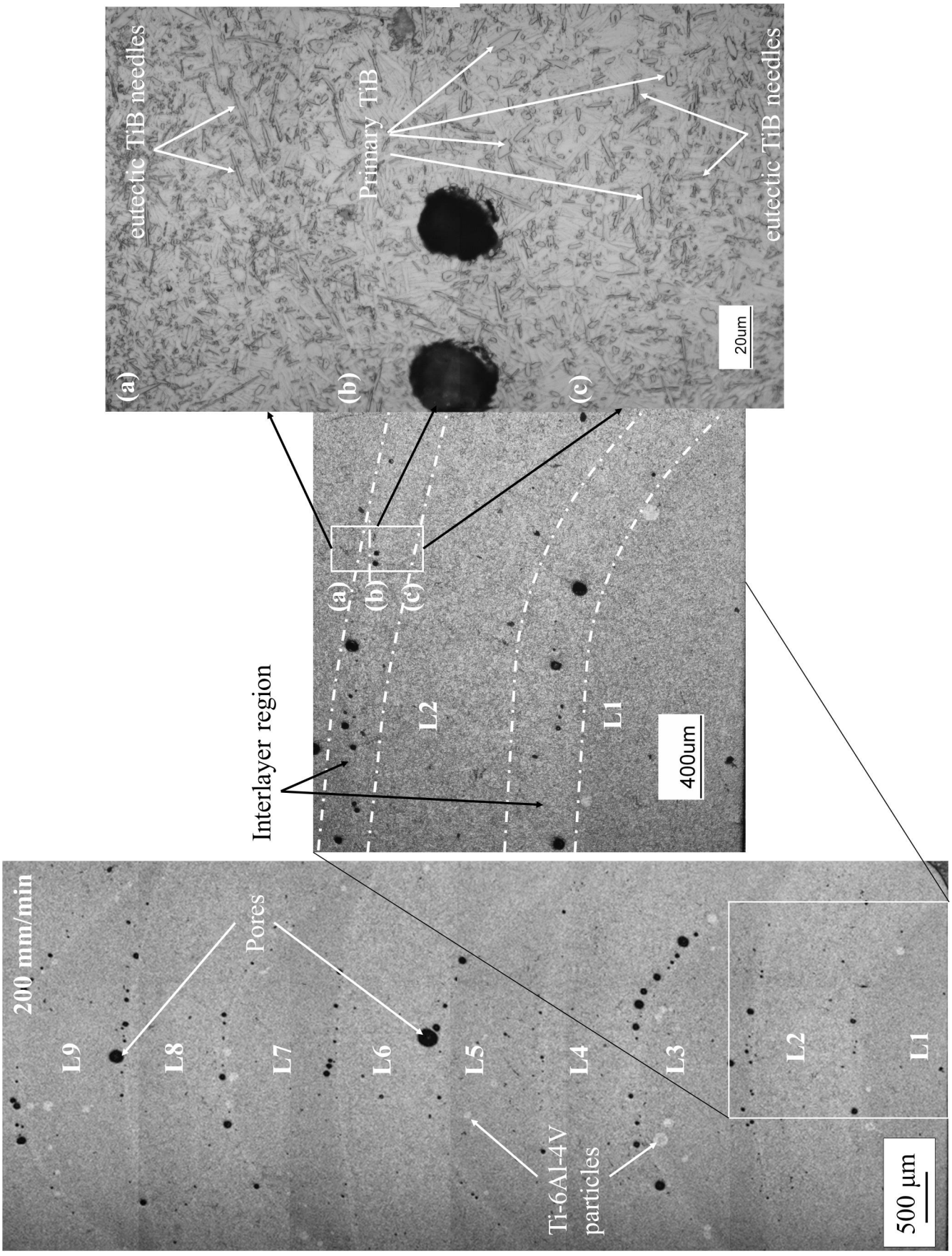

FIGURE 5.26: Etched optical micrograph of the composite wall built at 200 mm/min traverse speed showing the interlayer microstructure with predominantly primary TiB precipitates.

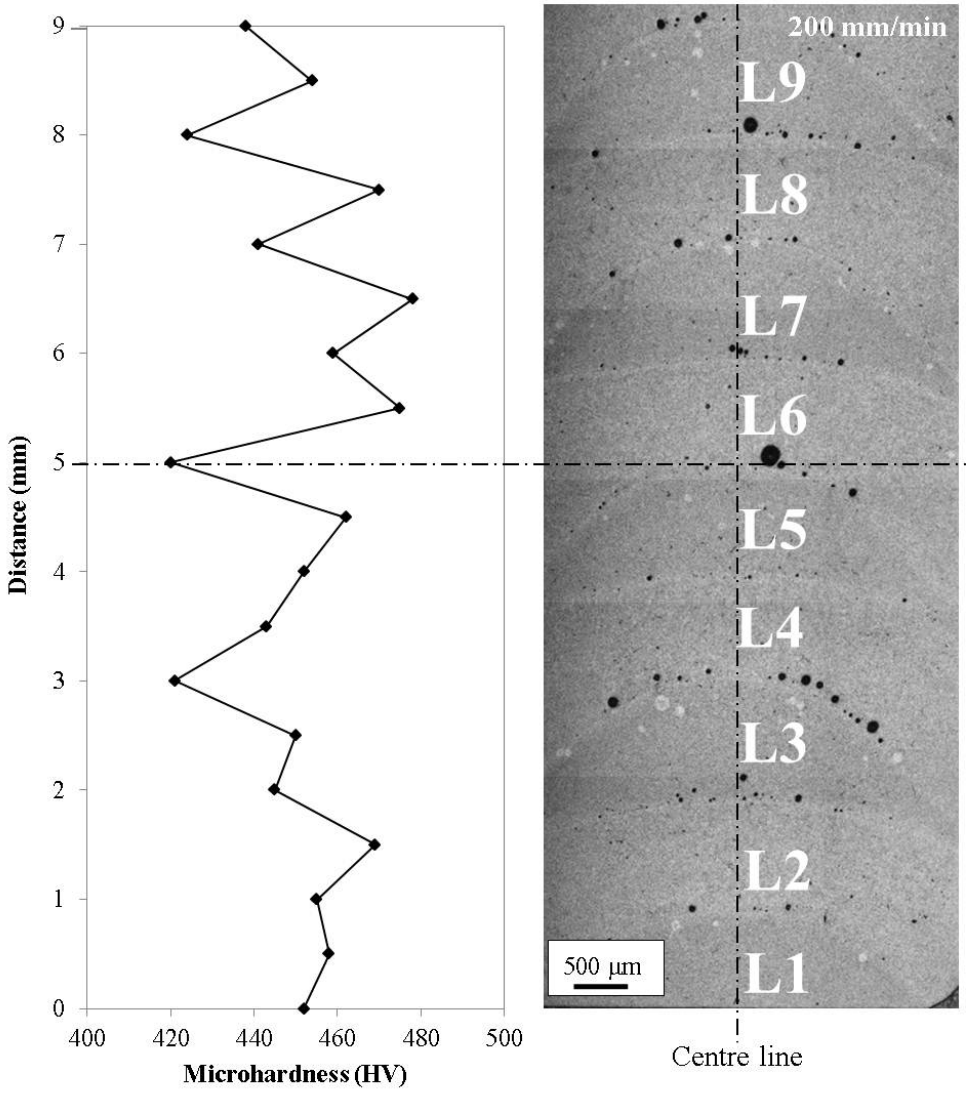

FIGURE 5.27: Microhardness profile along the centre line of the TiB_2/Ti-6Al-4V composite wall built at 200 mm/min traverse speed.

5.9 Tensile properties of the laser clad Ti-6Al-4V/TiB_2 composite

This section details the results obtained from the tensile test conducted on the Ti-6Al-4V/TiB_2 composite specimens. As, the integrity of the composite for structural applications would be based on its elastic properties, thus this section discusses the tensile test conducted on samples and the results obtained in terms of their tensile strength, elongation and modulus of elasticity. The SEM fractograph of the fractured test piece surfaces are analysed and discussed. This allows the performance of components built

in this way to be tested.

5.9.1 Tensile properties

Figure 5.28 shows the TiB_2/Ti-6Al-4V composite test specimens. These specimens are prepared by building walls as discussed in Section 5.8. Samples with dimensions reported in Section 3.8.3 are cut using WireEDM. The test is conducted according to BS EN 10002-1:2001 with the test setup described in Section 3.10.

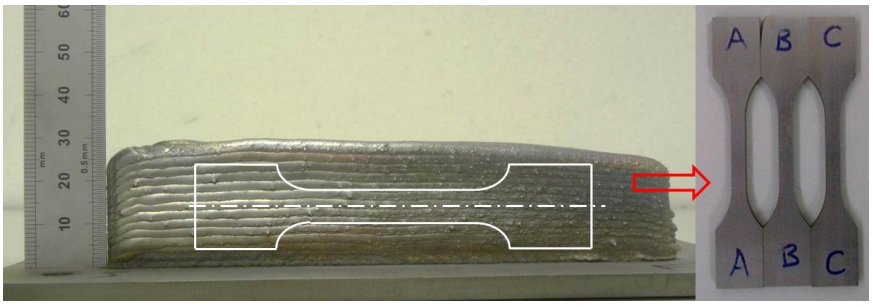

FIGURE 5.28: Tensile test specimens from the Ti-6Al-4V/TiB_2 composite wall built. Specimens A, B and C are built at a traverse speed of 200 mm/min and a powder feed rate of 10 g/min

Three samples labelled A, B and C are prepared from walls built with a common traverse speed of 200 mm/min and a powder feed rate of 10 g/min. These three samples are subjected to tensile pull at the rate of 1 mm/min to ensure the repeatability of their tensile properties. The specimens are loaded at room temperature until fracture occurred and the extensiometer was used to record strain in the samples before failure. Owing to a rapid failure of composite materials, the elongation of the samples is effectively measured over a strain of 0.3-0.4%, and thereafter, the extensiometer is dismounted.

Figure 5.29 shows the stress-strain curve for the three samples. Samples A, B and C have an elastic modulus of 142 GPa, 148 GPa and 135 GPa respectively. These values are evaluated in the region where reliable elongation data is available via the extensiometer. It should be noted that the maximum tensile strength before failure of the samples A, B and C are 905 MPa, 984 MPa and 523 MPa respectively. The maximum tensile strength exhibited by samples A and B are relatively close while that of sample C is lower. Figure 5.30 shows the fractured tensile test specimens. Samples A and B fractured within the gauge length which made the tensile results obtained for these samples valid. However,

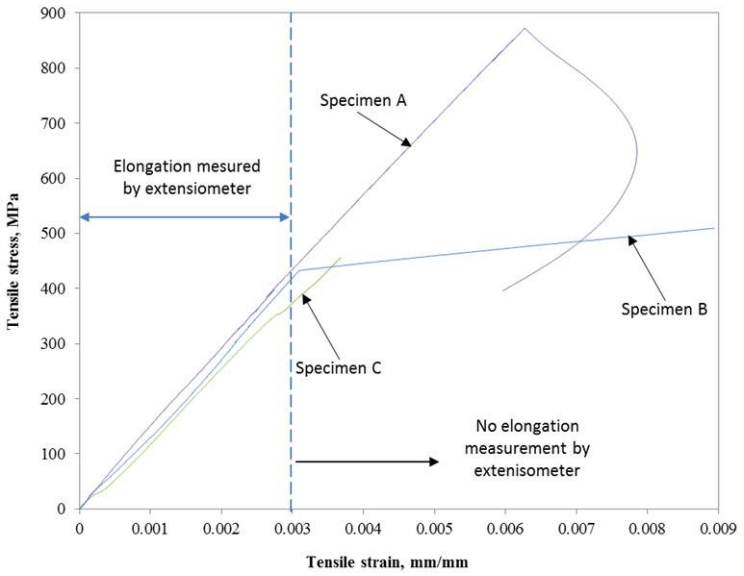

FIGURE 5.29: Tensile stress-strain curve for the laser clad TiB_2/Ti-6Al-4V composite specimens A, B and C built at a common traverse speed of 200 mm/min and a powder feed rate of 10 g/min.

sample C failed at the beginning of the transition radius region, and its result may not be considered as a true representation of the composite properties. Hence, the tensile result obtained from the sample A and B shows that the mean elastic modulus for the laser clad TiB_2/Ti-6Al-4V composite is evaluated as 145 GPa and the mean ultimate strength is 945 MPa. Furthermore, the fractured surfaces would be examined in order to understand the behaviour of the composite under the influence of an external load.

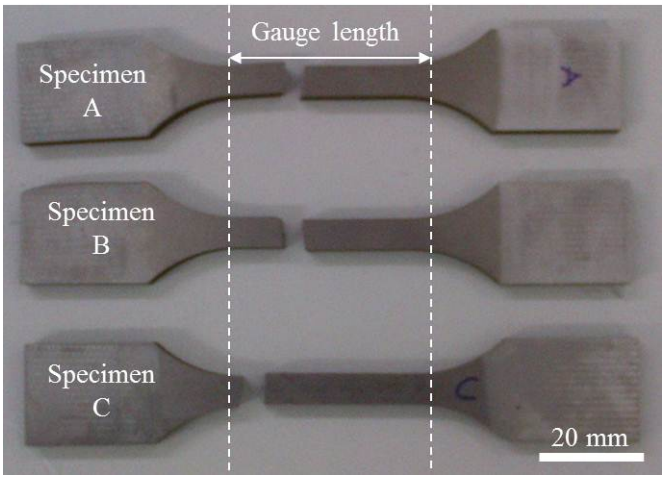

FIGURE 5.30: Fractured composite tensile test pieces.

5.9.2 Fractographs of TiB$_2$/Ti-6Al-4V Composites

Figure 5.31 shows the SEM images of the fracture surfaces of the Ti-6Al-4V/TiB$_2$ tensile specimens. Figure 5.31(a) and (b) are the mating fracture surfaces of sample A with identical features in the white boxes. Figure 5.31(c) and (d) are the fracture surfaces for sample B and C respectively. The surfaces exhibit a brittle fracture as there is no sign of visible plastic deformation and the fracture surfaces are normal to the direction of the tensile loads. Sites of partially melted Ti-6Al-4V particles are observed on the fractured surfaces. The partially melted Ti-6Al-4V particles or their pull-out regions are observed to be arranged along the same line and in a repetitive pattern of regular interval. This particle arrangement is attributed to the presence of partially melted Ti-6Al-4V particles which are mostly arranged at the clad periphery as discussed in Section 5.6.3. This resulted in the repetitive particle arrangement observed in the micrographs. Cleavage features are observed on the fracture surface as cracks are initiated and propagated across the fracture plane.

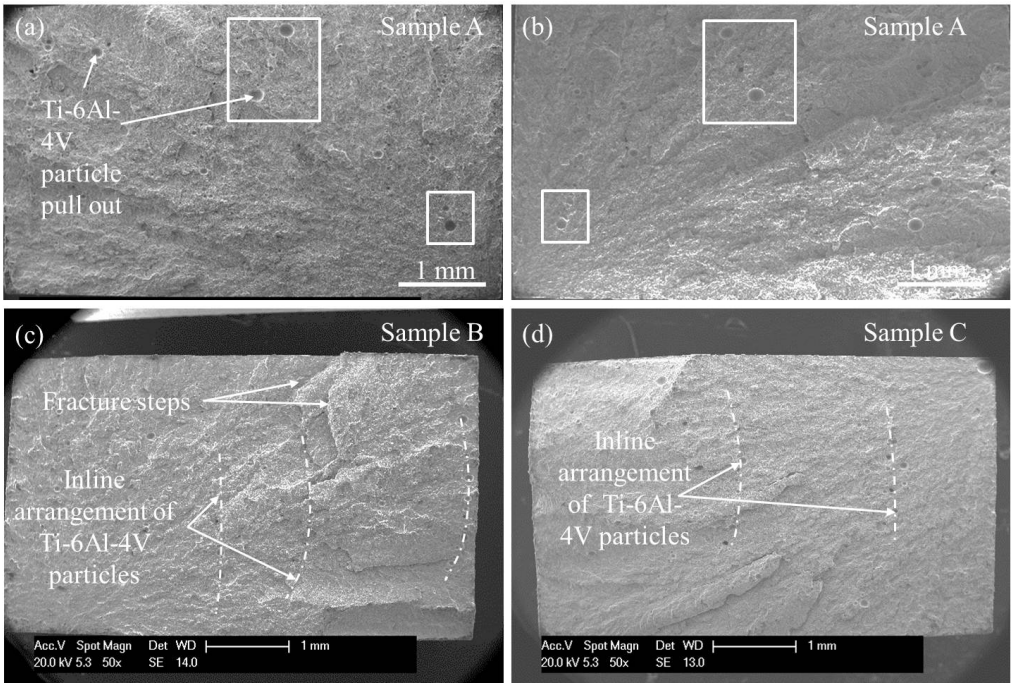

FIGURE 5.31: SE images of the fractured tensile test piece surfaces of the laser clad TiB$_2$/Ti-6Al-4V composite.

Figure 5.32 shows the microscopic features of the fracture surface of specimen A (Figure 5.31a). Micro cracks are suggested to have developed at the particle-matrix interface,

as the localised stress exceeds the interfacial strength between the composite matrix and the Ti-6Al-4V particles. The micro cracks are interlinked by fracture paths as clearly observed in Figure 5.32(a) and (b). The microscopic features of the fracture surfaces show that the TiB needle reinforcements grow radially from the boron source. Radial arrangements of TiB reinforcements are observed which have grown from TiB_2 particles. The reinforcements must have grown out in all directions around each TiB_2 particle until they are all interlinked in the composite matrix forming a tight network. Upon the subjection of the composite to tensile load, cracks are envisaged to have nucleated from the points where the reinforcements had grown. As the crack initiates at this microscopic level, the crack propagation has the tendency to follow the directions of TiB reinforcements which are normal to the tensile load. The fracture paths which followed the radial directions of the TiB reinforcements are observed in Figure 5.32(c) and (d). Owing to the tight network of randomly oriented TiB reinforcements, the fracture paths, which follow the TiB growth directions, are intercepted by another set of radial TiB reinforcements. This causes steps to be formed on the fracture surface instead of having an entirely flat fracture surface. It can be suggested that having a radial growth of the TiB reinforcements which are interwoven to form a tight TiB network is preferred. An excellent load transfer among the TiB reinforcements is envisaged in the composite matrix.

Figure 5.33 shows the fractured surface profile of the TiB_2/Ti-6Al-4V composite subjected to tensile test. TiB reinforcements are randomly oriented in the α-Ti matrix with sub-surface cracks observed below the fractured surface in the micrographs. The cracks propagate along the interface between the TiB reinforcement and the composite matrix as shown in Figure 5.33(a). A crack is also seen to cut across the TiB needle as well, which may be attributed to an effective load transfer from Ti matrix to the TiB reinforcement. More so, cracks are seen to develop in the composite matrix as it is subjected to tensile load.

5.10 Discussion

In this study, the experimental observations can be explained by considering the cladding process as a series of events. The first event occurs during the period of laser irradiation as the composite TiB_2/Ti-6Al-4V particles exit the powder nozzle into the melt pool.

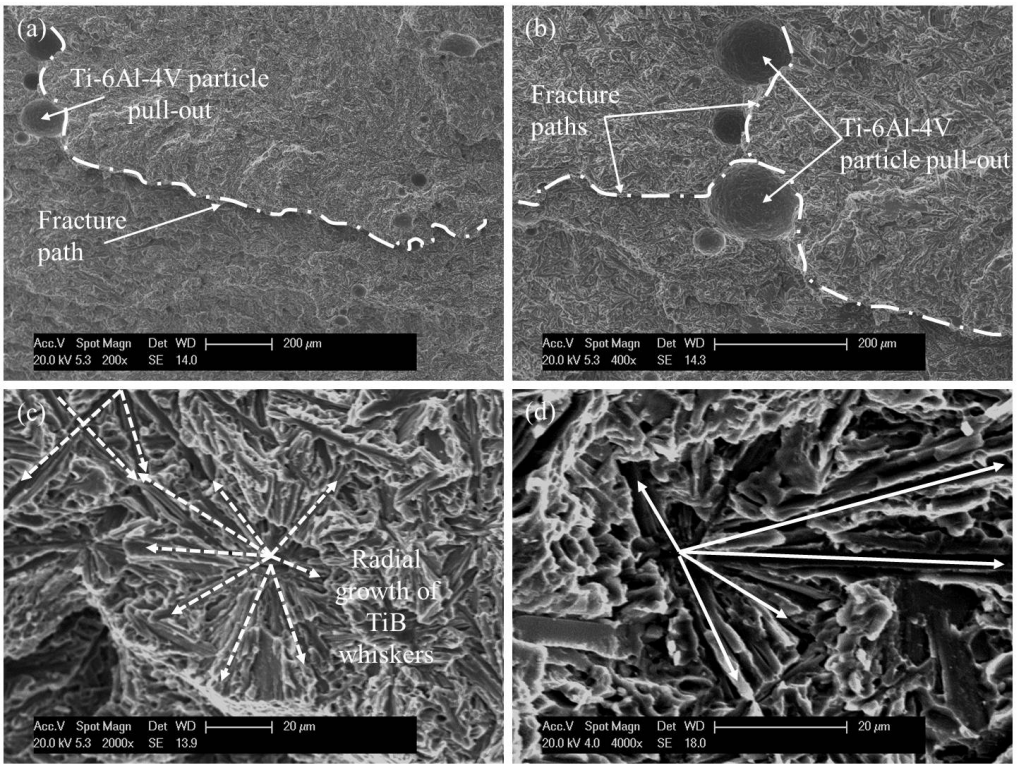

FIGURE 5.32: SEM images of the microscopic features of the TiB_2/Ti-6Al-4V fracture surface of specimen A (Figure 5.31*a*).

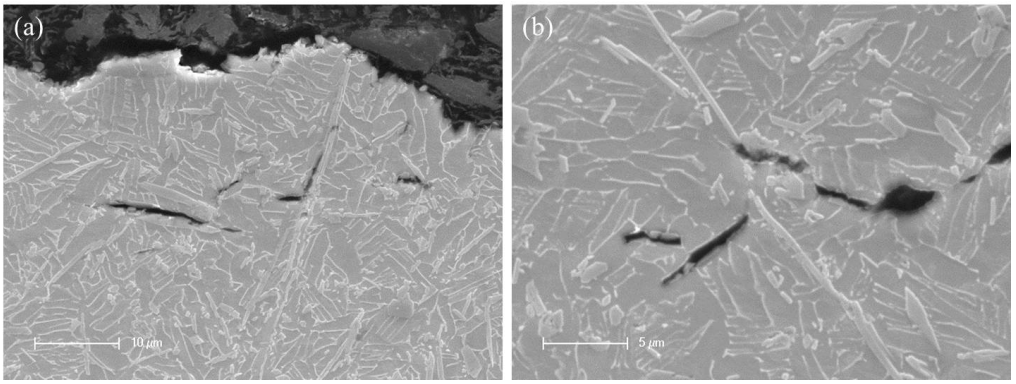

FIGURE 5.33: SE micrographs of the fractured surface profile of the TiB_2/Ti-6Al-4V composite specimen A (Figure 5.31*a*).

The second event is the formation of the microstructure as the melt pool solidifies and cools in solid state. Hence, the discussion on observations focuses on melting and dissolution of the feedstock and microstructure formation on cooling. The influence of the process parameters on microstructural observations and bead physical characteristics with microhardness is also discussed.

5.10.1 Dissolution/melting of Ti-6Al-4V and TiB_2 particles

It is evident that the trajectory of powder particles through the laser beam before reaching the melt pool results in energy attenuation [129]. The attenuated energy is either absorbed or reflected by the particles upon irradiation with the laser beam. The energy absorptivity of the particle is dependent on the laser wavelength, nature of particle material and particle surface geometry amongst others [81]. Non-oxide ceramic materials have the ability to absorb (78-82)% and Ti, 77% of the laser energy, when irradiated with a 1.06 μm wavelength, laser beam [81]. This operating wavelength is similar to that of the fibre laser (1.07 μm) used in this experimental study. Hence, the TiB_2/Ti-6Al-4V feedstock absorbs a reasonably high proportion of the laser energy, as the particles travel through the laser beam into the melt pool.

Figure 5.34 shows a schematic diagram of the laser beam-particle interaction as the particle approaches the melt pool. As the feedstock exits the powder nozzle, a particle at the central region of the powder stream enters the laser beam zone at point A.

As this particle travels through the beam, laser energy is absorbed at a skin layer of the order of 10 nm [81]. As heat is generated within the particle structure, the particle temperature begins to rise. Figure 5.35 shows the schematic of process that occurs as the TiB_2/Ti-6Al-4V particle travels through the laser beam from point A to point B. As heat is generated on the surface layer of the particle exposed to the laser beam, heat is rapidly conducted away into the particle solid structure. Owing to TiB_2's higher absorptivity, the particles attached onto the Ti-6Al-4V surface assist in more laser energy absorption and heat is conducted through to the Ti-6Al-4V particle. The rapid heat conduction encourages the maintenance of a uniform temperature within the particles. As a TiB_2/Ti-6Al-4V particle enters the laser beam at point A and begins to approach the melt pool, the temperature of the particle system increases simultaneously.

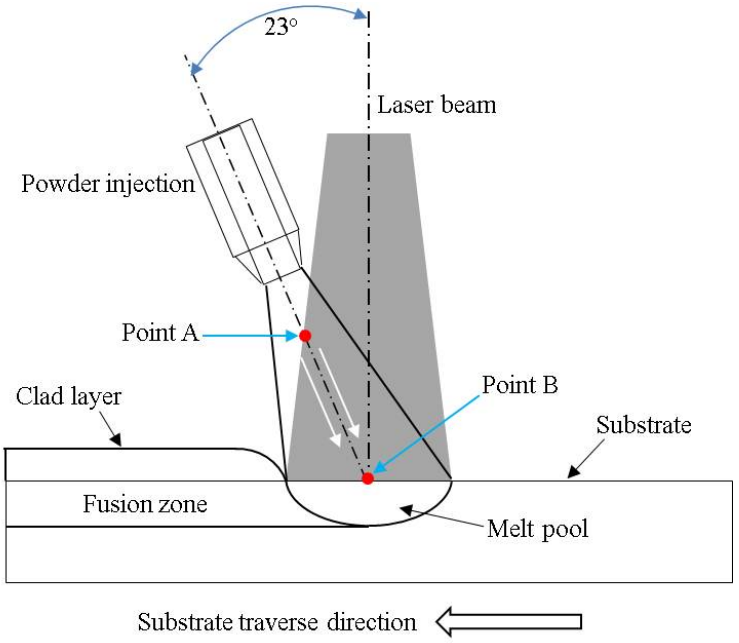

FIGURE 5.34: Schematic of the laser beam-particle interaction before particle reaches the melt pool.

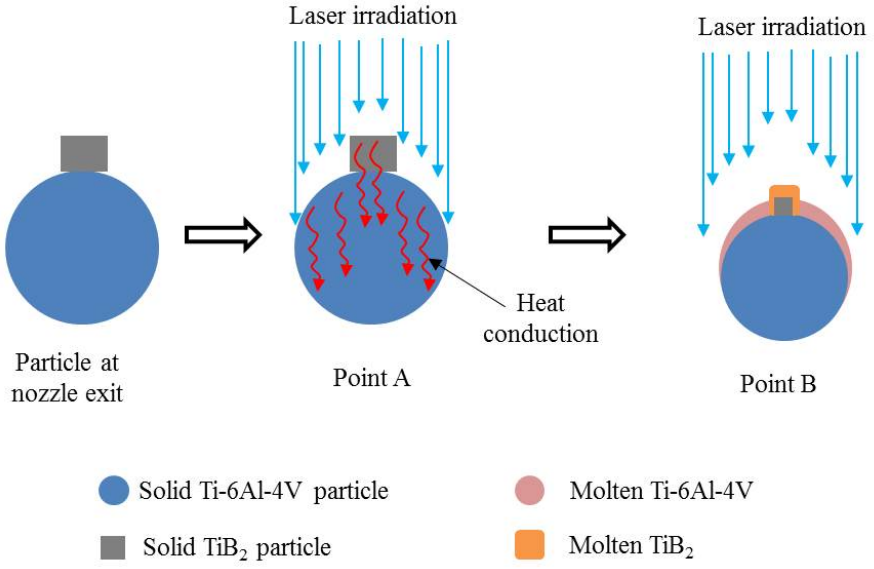

FIGURE 5.35: Schematic of the process occurring as the TiB_2/Ti-6Al-4V particle travel through laser beam.

The temperature attained by the particle is dependent on the distance travelled from point A to point B before entering into the melt pool, the particle speed, laser power density, radiated particle area and particle material properties [41, 114]. Equation (5.2) gives an expression of particle temperature, T, subjected to laser irradiation.

$$T = T_o + \frac{I_{(x,y)}\eta A_p d}{m_p c_p v_p} \tag{5.2}$$

Where, T_o = initial temperature of the particle, $I_{(x,y)}$ = laser power density, η = laser absorptivity of the particle material, A_p = the effective particle area irradiated, d = distance travelled by the particle in the laser beam, m_p = mass of the particle, c_p = specific heat capacity of the particle material, and v_p = the projected particle speed.

Thus, the smaller the angle between the central axes of the laser beam and the powder stream, the longer the distance travelled by the particles in the laser beam. This encourages uniform particle temperature distribution over the melt pool [114]. The particle velocity is dependent on the carrier gas flow rate and the nozzle exit diameter [46]. Hence, in this study, with a 4 mm exit nozzle diameter, and a 10 L/min carrier gas flow rate, the particle speed is estimated to be about 1 m/s. With this speed and owing to the attached TiB_2 particles, the temperature of the particle system may reach a maximum of 3000^oC before entering the melt pool at point B [41]. However, as the temperature of the particle system increases beyond 1650 ± 10^oC, the Ti-6Al-4V particles begin to melt. As the Ti-6Al-4V surface becomes molten, the TiB_2 particle on its surface enters the Ti liquid. With an increasing negative surface tension-temperature gradient and lower viscosity of the molten Ti, the TiB_2 particle begins to sink into the Ti melt. As the TiB_2 particle sinks, the liquid Ti wets the particle surface and this causes the particle to begin to dissolve in the Ti melt. Thus, each particle approaching the melt pool in form of droplet is independently enriched with elemental boron. However, the dissolution of the TiB_2 continues in the melt pool provided it is not yet completed before the particle system reaches the melt pool as schematically shown in Figure 5.36. As the particle system enters the melt pool, the energy absorbed by the particle is transferred into the melt pool [129, 130]. It is assumed that the temperature of the melt pool may approach 3000^oC [41]. Thus, according to the Ti-B phase diagram, as the TiB_2 dissolves in the Ti melt at this temperature, it maintains a state of equilibrium at its solid/liquid interface with boron concentration of 55 at.%.

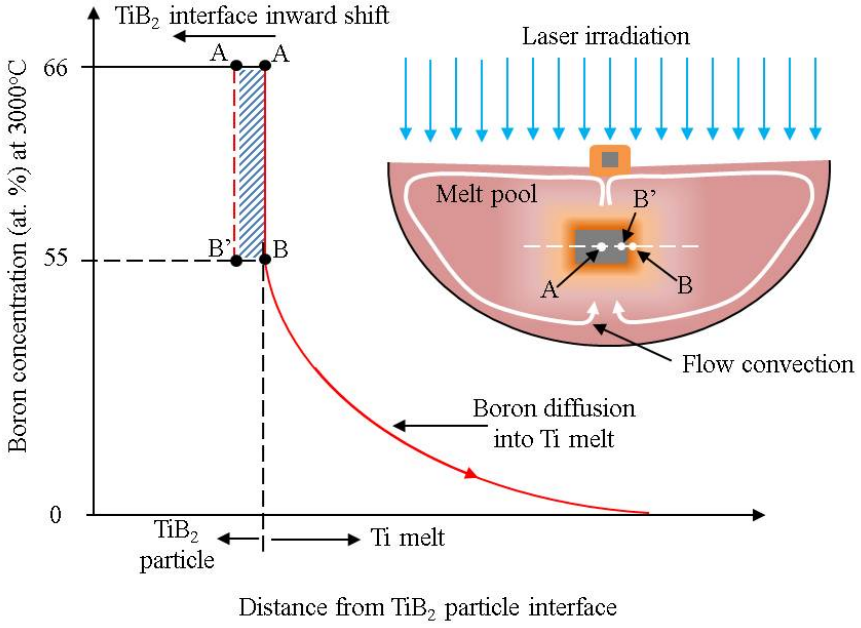

FIGURE 5.36: Schematic of TiB_2 dissolution in the Ti melt showing boron diffusion with 55 at.% B maintained at the solid/liquid interface.

It can be suggested that the rate of boron diffusion, possibly enhanced by convection, into the Ti melt governs the dissolution of TiB_2, which is dependent on temperature and time. As boron solute diffuses farther away from the TiB_2 interface and are redistributed in the melt pool, owing to the flow convection, the boron concentration at the interface begins to fall below 55 at.%. Thus, in order to keep up with the state of equilibrium at the solid/liquid interface, the TiB_2 particle further dissolves to maintain the required boron concentration. This causes the particle size to be smaller as the distance from the centre of the particle, A, to the interface at B, reduce to AB'. It is envisaged that the dissolution will continue. However, as the temperature decreases from 3000^oC over a period of time, the boron concentration required to maintain a state of equilibrium at the TiB_2/melt interface also decreases. Therefore, the dissolution is dependent on temperature, time and extent of melt convection.

The entry of TiB_2/Ti-6Al-4V particles into the melt pool at its periphery may result in reduced laser-particle interaction before entering the pool, since the particle may not have travelled through the laser beam. This results in reduced particle dissolution at the periphery. However, the TiB_2 particles attached on the Ti-6Al-4V particle surface start to dissolve on reaching the melt pool. These particles prevent the wetting of Ti-6Al-4V particle with the liquid Ti in the melt pool. The TiB_2 particles absorb heat from the melt

pool, but do not conduct enough heat to completely melt the Ti-6Al-4V particle. Rather, the TiB_2 particles locally dissolve into the melt, as boron diffuses farther away from the TiB_2 particle interface. Thus, the partially melted Ti-6Al-4V particle surface serves as a suitable site for TiB to nucleate and grow. This explains the reason for clustered TiB whiskers observed around partially melted Ti-6Al-4V particles as shown in Figure 5.21. These are predominantly observed at the bead periphery as the particles are conveyed to the region by the Maragoni flow convection before solidification occurs [38]. However, in order to study the reason for partially melted Ti-6Al-4V particles, Ti-6Al-4V powder only can be deposited. The partially melted Ti-6Al-4V may be attributed to particles which have settled on the melt pool surface and sank below the pool surface owing to gravity.

5.10.2 Microstructure formation on cooling

The microstructure of the laser clad composites is dependent on the melt pool chemistry and cooling rate (temperature gradient and solidification velocity). The dissolution of the feedstock delivered into the melt pool with a corresponding homogenisation of the chemical constituents determines the formation of the resultant reaction products. Thus, in order to explain the final microstructure of the composite, there is a need to consider the overall composition of the melt pool.

In this study, the feedstock comprises of 10 wt.% TiB2 powder and 90 wt.% Ti-6Al-4V powder. With an assumption that these absolute proportions were steadily delivered into the melt pool are fully dissolved and considering the effect of substrate dilution, the likely overall melt pool composition is computed. The bead deposited with a laser power of 1800 W, 400 mm/min traverse speed and 10 g/min powder feed rate, is chosen for the purpose of analysis. The substrate dilution effect on the overall melt pool composition is 23% as presented in Table 5.1. The clad cross sectional area, A_c, is measured as 2.198 mm^2 and the substrate melt area, A_s, is 0.656 mm^2.

The density of Ti-6Al-4V and TiB_2 powders was measured, using helium pycnometer, as 4.439±0.003 g/cm^3 and 4.441±0.003 g/cm^3 respectively. The density of wrought Ti-6Al-4V substrate was taken as 4.42 g/cm^3. The analysis shows that the likely overall melt pool composition is 7.71 wt.% TiB_2/92.29 wt.% Ti-6Al-4V. Since a 90 wt.% Ti is

present in Ti-6Al-4V and TiB_2 comprises 68.88 wt.% Ti and 31.12 wt.% B, the likely overall melt pool composition is 2.6 wt.% B/97.4 wt.% Ti as summarised in Table 5.3.

TABLE 5.3: Analysis of the bead to determine the probable overall melt pool elemental composition

Element	Clad	Substrate	Total	wt.%
Volume (cm^3)	2.198 x 10^{-3}	6.56 x 10^{-4}	-	-
Mass (g)	9.756 x 10^{-3}	2.9 x 10^{-3}	-	-
Ti-6Al-4V (g)	8.78 x 10^{-3}	2.9 x 10^{-3}	1.168 x 10^{-2}	92.29
TiB_2 (g)	9.76 x 10^{-4}	-	9.76 x 10^{-4}	7.71
Ti (g)	88.4		97.36 wt.% Ti	
B (g)	2.4		2.64 wt.% B	

The analysis shows that the probable melt composition is close to the eutectic. Figure 5.37 shows the estimated melt pool composition on the Ti-B phase diagram with Al and V content neglected. On rapid cooling, typical of laser processing, as the temperature of the melt pool liquid decreases to about 1570^{o}C, point A, located on the liquidus line, is reached. At this position, the primary TiB phase is expected to start nucleating from the liquid solution according to equation (5.3). As TiB nucleates and freezes in the melt, the composition and temperature of the liquid melt moves along the liquidus line from point A to point C_E, the eutectic point.

$$L = L + TiB(1570^oC, 2.6wt\%B) \tag{5.3}$$

$$L = \beta - Ti + TiB(1540 \pm 10^oC, eutectic) \tag{5.4}$$

On further cooling to 1540^{o}C (eutectic temperature, point B), the precipitation of the eutectic TiB prevails in the solidified Ti matrix as the liquid freezes and transforms into the two phases, according to equation (5.4).

Hence, assuming solidification follows the phase diagram, the expected structure is a small fraction of primary TiB in a (β-Ti + TiB) eutectic matrix. As temperature decreases further to beta transus temperature (884$\pm$2^{o}C) at position C, β-Ti is transformed to α-Ti. The precipitation of Ti_3B_4 and TiB_2 would not have been possible due to the rapid cooling and low solubility of boron in Ti [131, 132]. This explains the reason for the presence of the eutectic TiB reinforcement only in the microstructure, apart from the presence of partially dissolved particles. The primary TiB may not have been observed

as there is not enough time for its precipitation in a non-equilibrium laser processing technique [85], hence eutectic TiB precipitates prevail in the specimens produced.

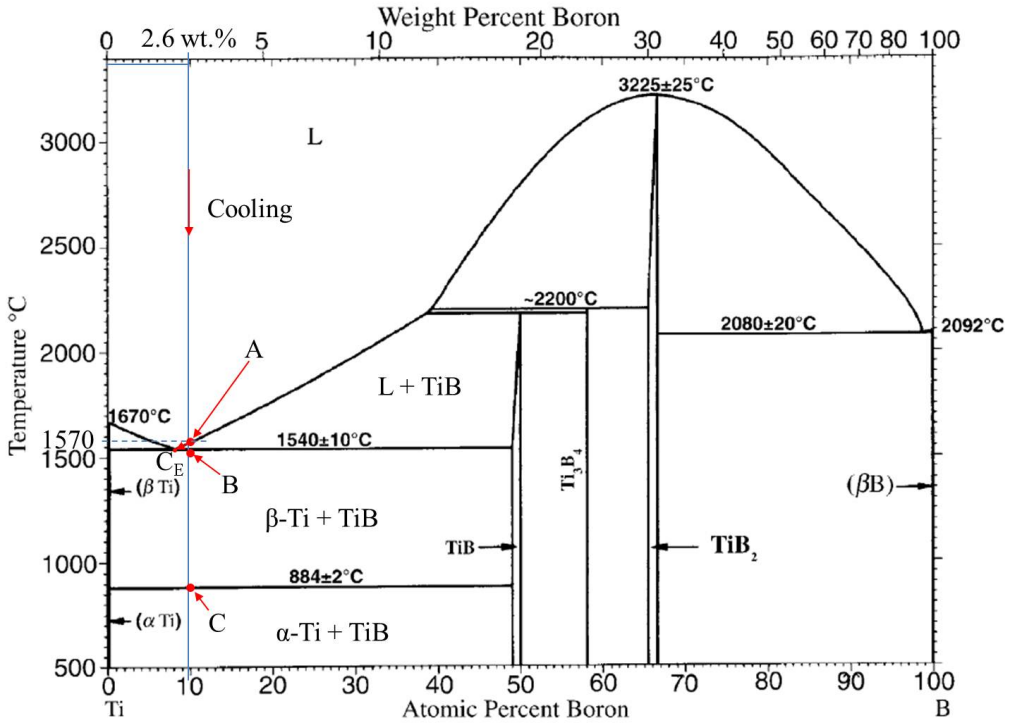

FIGURE 5.37: A plot showing estimated melt pool composition (2.6 wt.% B) on the Ti-B phase diagram.

It is noteworthy that TiB nucleation to complete formation occurs within a short temperature range. The TiB nucleation starts at 1570^{o}C (point A) and complete formation of precipitates is expected to occur on the eutectic line at 1540±10^{o}C (point B) [133]. Hence, the temperature difference is 30±10^{o}C, and the rate of heat dissipation, determines the time taken for the temperature to drop from point A to B.

However, with increased dilution of the melt pool by the substrate material, the boron concentration is further reduced in the overall composition. Such as 1400 W laser power deposited sample having 33% dilution (Table 5.1), it is suggested that its melt pool composition may lie on the eutectic point or in the hypoeutectic region. This suggestion seems to be valid, as its microstructure is characterised by Ti-rich dendrites with fine eutectic in interdendritic regions (Figure 5.19(b)). In theory, having the overall melt pool composition on the eutectic point, the liquid solution cools rapidly to the eutectic temperature and transforms into the two solid phases (β-Ti and TiB) as illustrated in Figure 5.38 [133]. Thus, it may be suggested that the microstructure on cooling for melt

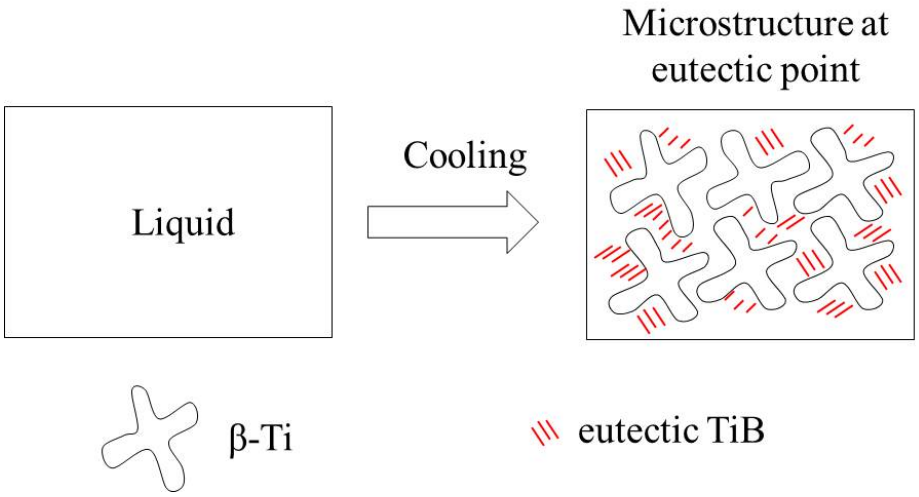

FIGURE 5.38: Schematic of microstructure on cooling of a melt pool with eutectic composition as the liquid transforms to β-Ti and eutectic TiB.

pool, whose boron concentration is less than or equal to that of the eutectic point (2.1 wt.% B), would be characterised by Ti-rich dendrites and eutectic TiB interdendrites. The presence of boron in the Ti melt acts as an α-stabiliser which caused the beta transus temperature to be raised by about 60^{o}C [131, 134] when compared to that of Ti-6Al-4V (999±15) [49].

The microstructure of the multilayer wall is characterised by eutectic TiB plates/needles uniformly and randomly dispersed the α-Ti matrix within each layer. Owing to reheating, the interlayer regions of the wall are characterised by a mixture of primary and eutectic TiB precipitates dispersed in the Ti matrix as shown in Figure 5.26. These observations can be explained by the melt pool composition and the thermal history experienced during the wall deposition. Since, the effect of dilution with substrate is limited in each layer making the wall apart from the first layer, the likely overall melt pool composition is expected to be 10 wt.% TiB/ 90 wt.% Ti-6Al-4V. This composition corresponds to 3.5 wt.% B concentration in 96.5 wt.% Ti liquid solution, assuming all the feedstock delivered into the melt pool is fully molten. This melt pool composition lies in the hypereutectic region when plotted on the Ti-B phase diagram. Thus, on cooling to the liquidus line, primary TiB may likely form in the liquid, provided the cooling rate is less rapid. However, eutectic TiB precipitates are predominantly observed in the central region of each individual layer, indicative of rapid cooling. Owing to the partial remelting of the previous layer, the interlayer band is formed between the layers.

The preheating of the previous layer helps to reduce cooling rate, thus allowing the nucleation of the primary phase before the remaining molten liquid transforms into the eutectic phases [38, 135, 136]. Hence, plate-like primary TiB precipitates are formed in the interlayer regions before the molten liquid is transformed into eutectic TiB precipitates and α-Ti phase, as the region slowly cools to the eutectic temperature (1540^{o}C). Figure 5.39 shows a schematic of the composite wall microstructure with the eutectic structure sandwiched with a thin interlayer structure characterised by a mixture of primary and eutectic TiB. The liquid composition and temperature variation, as the melt pool composition moves along the liquidus line from point A to C_E, determine the characteristics of the microstructure formed on cooling. Since the melt pool composition is in the hypereutectic region, it is highly possible for primary TiB to be formed on slower cooling as composition changes from point A to C_E. This is observed in the interlayer region. However, with the same melt pool composition on rapid cooling, eutectic TiB dominates the microstructure as observed in the regions farther away from the interlayer into each deposited layer.

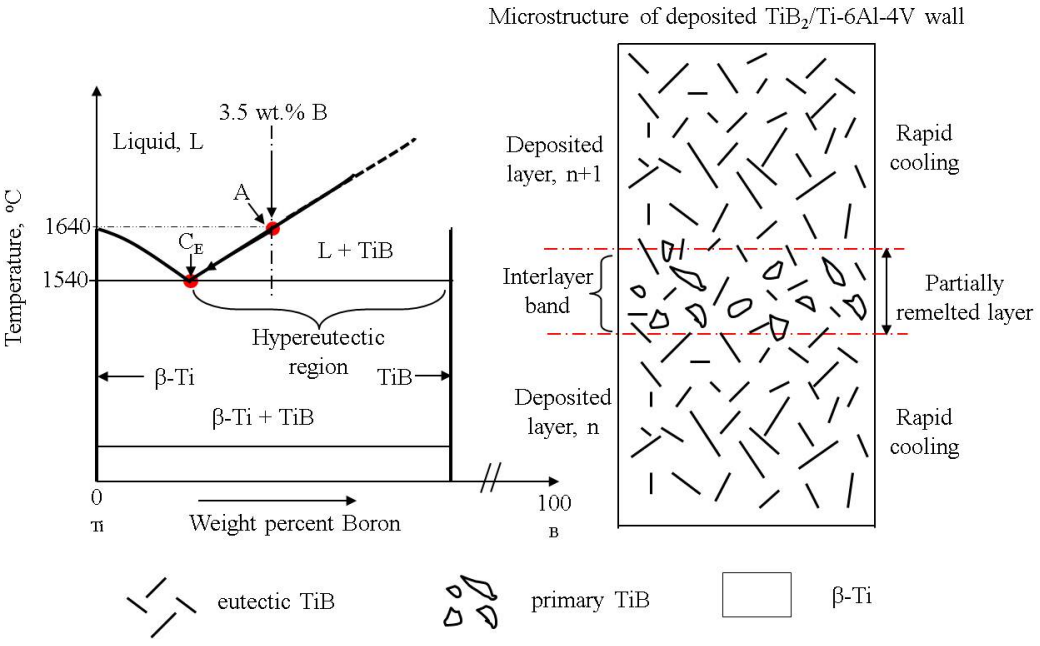

FIGURE 5.39: A schematic of the TiB_2/Ti-6Al-4V composite wall showing the microstructure of the interlayer and the deposited layers with the melt pool composition of 3.5 wt% B in the hypereutectic region.

5.10.3 Process parameter effects

Figure 5.12 shows that traverse speed strongly influences the reduction of deposit height. This is directly attributed to the expected decrease in volume of feedstock delivered per unit length and catchment into the melt pool with increasing traverse speed. Moreover, the melt pool size decreases with increasing traverse speed, due to a corresponding shorter laser-substrate interaction time. However, increasing laser power promotes the increase of melt pool size which corresponds to an increase in deposit width as shown in Figure 5.13 [17, 126]. The effect of process traverse speed on substrate dilution is significant as shown in Table 5.1. Increasing traverse speed causes the dilution of the bead composition with the substrate to increase. This is attributed to a reduction of the material delivered per unit length to form bead. Thus, the process approaches a welding process with no filler material. This made the substrate to be exposed to more laser energy, which promotes its melting to dilute the overall melt pool composition [30]. The reduced presence of partially melted particles observed in Figure 5.16 is attributed to the reduced volume of the feedstock delivered per unit length as traverse speed increases. This encourages a complete dissolution of the partially molten particles delivered into the melt pool irradiated by the laser beam. Thus, a completely molten feedstock in melt pool may be realised when higher heat input per unit length (higher laser power and lower traverse speed) and lower powder feed rate are employed independently or simultaneously.

In Figure 5.17, XRD results establish that all samples possess α-Ti and TiB phases, with minor peaks of TiB_2 phase observed for deposit prepared with lower laser power (1400 W). Both α-Ti and TiB_2 are the same as the starting phases in the pre-blended feedstock as shown in Figure 5.11. In all the composites, the majority of the TiB_2 particles, attached onto the Ti-6Al-4V particles, are dissolved during laser irradiation. The dissolution of the TiB_2 makes the Ti melt to be boron-rich, thus, encouraging the formation of TiB phase upon rapid cooling and solidification [86, 87]. Though, the intensity of TiB peak at 2θ value of 29^o increases with increasing laser power, it cannot be fully established that the volume of the in-situ synthesized TiB in the composite increases as processing laser power increases. As determined from the relative intensity peak height ratios of α-Ti ($2\theta = 40^o$):TiB ($2\theta = 29^o$), ratios of 22.8, 20.1 and 12.4 are obtained

for the employed laser power of 1400 W, 1600 W and 1800 W respectively. These ratios may suggest that the in-situ synthesized TiB increases as laser power employed increases.

Moreover, the influence of laser power becomes evident on the microstructure of the deposit shown in Figure 5.19. In all, TiB precipitates are uniformly distributed in the dark α-Ti composite matrix. During laser irradiation, the dissolved feedstock is diluted with the molten substrate with an even distribution of elements in the melt pool by the flow convection [124, 137]. With a lower laser power (1400W) at 400 mm/min traverse speed, the dilution increases, resulting in a lower boron concentration in the overall melt pool composition. The lowered boron concentration promotes the formation of eutectic TiB clusters in the interdendritic regions of the primary Ti-rich phase on cooling. This is more evident in the microstructure of deposit prepared using a laser power of 1400 W (Figure 5.19(b)) when compared to other deposits with a higher laser power. Hence, it will be logical to conclude that increased dilution of the melt pool by the substrate lowers boron concentration, and on cooling, the volume fraction of TiB reinforcement synthesized is reduced. This complements the XRD results, which show a higher relative intensity peak height ratio of α-Ti:TiB for deposits prepared using 1400 W when compared to those of 1800 W. It is desirable to uniformly disperse the TiB reinforcement in the Ti matrix without clustering to maximize the interfacial area between the reinforcement and the matrix. Thus, keeping the overall melt pool boron concentration above 2.1 wt.% (eutectic point concentration) will encourage uniform TiB distribution, with no clustering in the Ti interdendritic region on solidification. Moreover, the length of some of the TiB reinforcements observed to be longer as laser power employed increases is attributed to lower cooling rate.

With a higher heat input, which is a ratio of laser power and traverse speed, employed [38], the melt pool experiences a vigorous Maragoni flow. The increased flow convection promotes a wider melt pool size, as the higher temperature liquid flows to the melt pool periphery causing further dissolution [123, 124, 138]. With a larger melt pool, temperature gradient and solidification are reduced [126], hence cooling rate is lowered. Thus, slower cooling is achieved by increasing laser power encourages the growth of longer TiB reinforcement before the melt pool solidifies.

5.10.4 Composite hardness

The high hardness values reported for the top regions of composite single beads is directly attributed to the partially dissolved reinforcement particles mostly present at the bead periphery. These remnant particles are transported by the flow characteristics of the melt pool. The composite bead microstructure is more homogeneous as processing traverse speed increases. This effect is observed in all the hardness profiles for the composite bead processed with the traverse speed of 400 mm/min (Figure 5.23). The hardness values are relatively consistent from the top region through to the fusion depth with hardness value of 460±20 $HV_{0.3}$. Effectively, the presence of the partially dissolved TiB_2 particles becomes less apparent, as material delivered per unit length into the melt pool decreases and laser power increases (heat input increases). This promotes a uniform microstructure in the samples.

In the case of the composite multilayer wall, the mean hardness of the central region of each layer is consistent with those measured for single beads. However, the wall interlayer hardness is lower (440±5 HV) than the central layer hardness (461±4 HV), which is attributed to the microstructural change due to re-melting in the region. The interlayer region is characterised by a coarsened TiB precipitates distributed in the Ti matrix as well as the finer scale solidified TiB.

Generally, a hardness enhancement of 30% is achieved with 12-15 wt% TiB reinforcement in Ti-6Al-4V. This enhancement is significant which makes laser processing of the TiB_2/Ti-6Al-4V feedstock to be potentially useful for surface engineering of Ti alloys against wear, corrosion and surface contact deformation. The composite will be good for structural applications where strength to weight ratio is of great significance.

5.10.5 Elastic properties of TiB_2/Ti-6Al-4V composite

The tensile result obtained from the sample A and B showed that the mean elastic modulus for the laser clad TiB_2/Ti-6Al-4V composite may be evaluated as 145 GPa. This is an increase of 27% over the elastic modulus of Ti-6Al-4V (Table 2.3) and the composite ultimate strength is 945 MPa. These values are similar to result presented for 20%TiB/Ti-6Al-4V composite with randomly oriented TiB whiskers produced using a

powder metallurgy route [139]. The composite was reported to possess a Youngs modulus of 153 GPa when compared to 109 GPa for unreinforced Ti-6Al-4V and the ductility of the composite was 0.1% [139]. Comparing the laser clad composite, previously characterised by 12-15 wt% TiB in Ti-6Al-4V, to the 20%TiB/Ti-6Al-4V composite prepared via powder metallurgy, the elastic modulus of the laser clad composite is suggested to be slightly lower owing to the difference in the reinforcement fraction in the composite matrix and the composite characteristics.

The examination of the fractured surfaces shows the influence of inclusions such as the partially melted Ti-6Al-4V and TiB_2 particles on crack initiation and propagation in the composite. Fracture surfaces are known to be created by the absorption of strain energy to initiate crack which propagate to give two separate new surfaces [140]. Hence, the presence of partially melted Ti-6Al-4V particles, which cause internal discontinuities in the composite microstructure, allows localised stress to be developed at the interface between the particles and the composite matrix owing to differential strain experienced by the composite matrix and the Ti-6Al-4V particles. It is envisaged that micro cracks will develop at the particle-matrix interface, as the localised stress exceeds the interfacial strength between the composite matrix and the Ti-6Al-4V particles. The micro cracks are then interlinked by fracture paths as clearly observed in Figure 5.32 (a) and (b). At higher magnification, the TiB reinforcements are observed in the fractured surfaces to grow radially from the TiB_2 source, and these have grown into a tight network. This network of TiB reinforcement is envisaged to improve the isotropy of the composite, as the matrix is reinforced in all directions. However, the boron-rich region from which the TiB grew is suggested to have acted as a stress raiser in the composite. As the composite is subjected to tensile load, cracks are suggested to have nucleated at the boron rich region and the cracks propagate in the growth direction of TiB reinforcements, normal to the direction of the applied load. These fracture paths which followed the radial directions of the TiB whiskers are observed in Figure 5.32(c) and (d). The fracture steps observed in the micrographs have been reported as one of the characteristics of a brittle fracture [140, 141].

It can be suggested that the composite matrix with randomly oriented TiB reinforcement network would possess isotropic properties with the absence of the partially melted Ti-6Al-4V particles [139]. Figure 5.40 shows a schematic illustration of TiB reinforcement orientation in the composite matrix with respect to the external loading. The orientation

plane of the reinforcement to direction of tensile loading is significant, as the TiB are more effective as reinforcing fibres when the growth direction of reinforcement are in the same axial plane with the tensile load, such that there is angle of 0^o between the direction of whisker growth and load. Ma et al. [90] reported an appreciable improvement in the mechanical properties of TiB whisker reinforced Ti-1100 alloy at 923K with the reinforcements oriented almost parallel to the load direction.

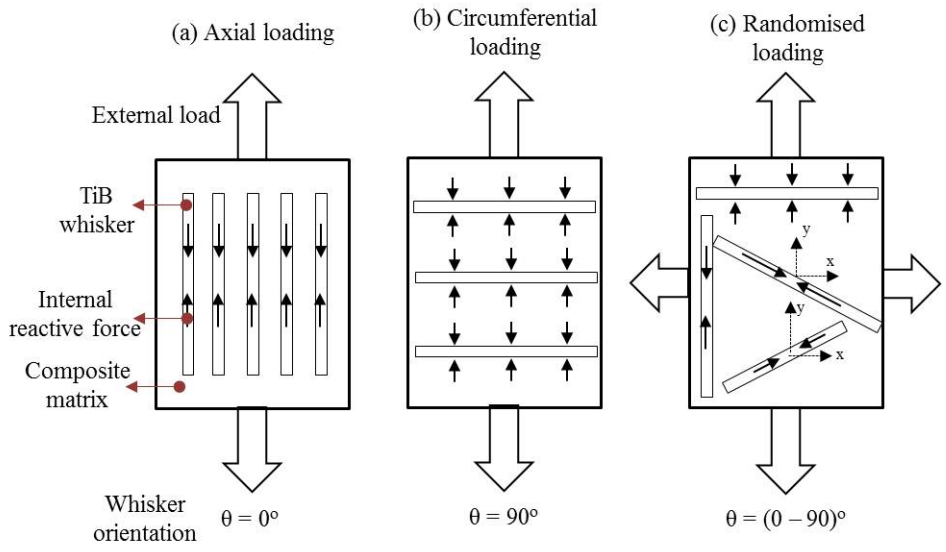

FIGURE 5.40: Schematic of TiB whisker orientation with respect to (a) axial loading; (b) circumferential loading and (c) randomised loading.

As the angle between the orientation plane of the TiB whisker growth direction and the load tends to 90^o, the load transfer effectiveness of the TiB whiskers is reduced. This makes the composite vulnerable to failure as preferred fracture paths propagate through the reinforcement-matrix interface. However, real applications require engineering components which possess isotropic mechanical properties. Therefore, having the reinforcements randomly oriented is desirable to improve the composite properties in all directions as shown in Figure 5.40 (c). The mechanism of load transfer can thus be evaluated as the summation of the components of the internal resistance of each whisker in the direction of external load.

Figure 5.41 shows a schematic of TiB whiskers subjected the circumferential and axial loading with an assumption that the whiskers are hollow as previously observed by Kooi et al. [84] and a strong metallurgical bonding exists at the interface between the composite matrix and the whiskers. Having a whisker subjected to a circumferential load

experiences twice the stress such as a whisker would have experienced when subjected to an axial load. This is suggested to have been responsible for the fracture paths that followed the TiB whisker growth directions when the whiskers are normal to the axis of the external load (Figure 5.32(c) and (d)).

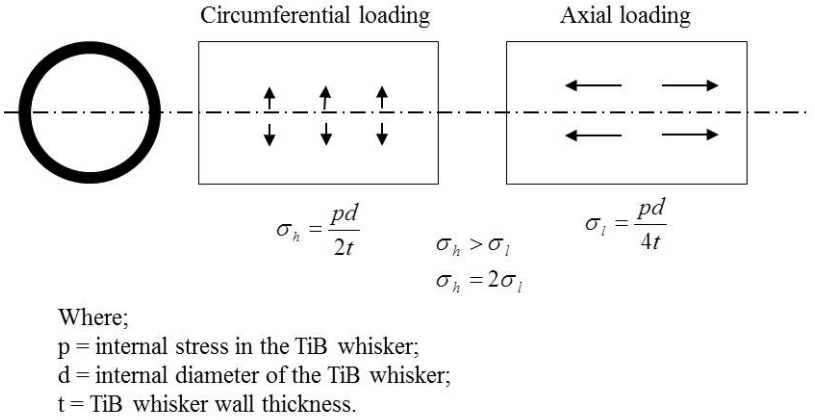

FIGURE 5.41: Schematic of the TiB whisker as a hollow cylinder subjected to circumferential and axial loading.

Gorsse and Miracle [139] reported that having clusters of TiB precipitates would result in a premature crack initiation and propagation through the composite produced via powder metallurgy. However, in this study, the modification of the feedstock before laser processing has helped to overcome the shortcomings of powder metallurgy route for production of TiB whisker reinforced composite. The average elastic modulus of TiB whiskers, estimated using the Halpin-Tsai equations, has been reported as 482 GPa [139], and using rule of mixture (RoM) to predict the elastic modulus of the laser clad composite should result in 185 GPa for 12 vol% TiB/88 vol% Ti-6Al-4V composite (14 wt% TiB/86 wt% Ti). However, the experimental value is 145 GPa which is lower than the estimated value by 20% due to the presence of the partially melted Ti-6Al-4V particles in the composite. Hence, process optimisation to eliminate the presence of partially melted particles in the microstructure with the fine TiB whiskers by further increasing heat input applied per unit length is necessary to further improve the composite mechanical properties.

Thus, the Ti-6Al-4V particle/matrix interfaces and the boron-rich region have been observed as sites of crack nucleation. Cracks are observed to propagate by interconnection

of the cracks at the interfaces between the Ti-6Al-4V particles and the composite matrix. The TiB whiskers in a form of tight network has been found promising, as fracture paths are intercepted which resulted in formation of fracture facets steps instead of a flat fracture surface. The tight network of TiB whiskers in the composite matrix is anticipated to promote isotropy of the composite properties. The load transfer effectiveness of the TiB whiskers is high when the growth orientation is in the same axial plane with the applied load. However, as the growth orientation becomes perpendicular to the loading axis, the load transfer effectiveness becomes low and composite becomes more susceptible to fracture.

5.11 Conclusions

Laser processing of pre-blended TiB_2/Ti-6Al-4V feedstock has been successfully carried out and reported. The agglomeration of TiB_2 particles on Ti-6Al-4V powder promotes steady delivery and uniform distribution of reinforcing phase in the melt pool. Higher heat input per unit length (higher laser power and lower traverse speed) and lower material delivered per unit length are observed to favour complete dissolution of the feedstock delivered into the melt pool. The Maragoni flow convection is responsible for partially dissolved remnant particles transported to deposit periphery. XRD identified TiB and α-Ti as dominant phases in all deposit and TiB_2 was as well identified in sample produced using lower laser power. SEM confirms the formation of TiB precipitates as eutectic needle-like features in a Ti-rich primary phase microstructures. The composite matrix is characterised by α-Ti phase which is promoted owing to the presence of boron. Lower dilution of the melt pool composition with the Ti-6Al-4V substrate reduces the chance of the formation of dendritic Ti microstructure with TiB reinforcement clusters in the interdendritic region. An eutectic microstructure is most desirable and is promoted when the boron concentration in the overall melt pool composition exceeds 2.1 wt.% (eutectic concentration). The formation of an equilibrium-like microstructure is observed at the interlayer region of the multilayer walls deposited. This is attributed to preheating of the previously deposited layer which reduces cooling rate such that the region is characterised by a mixture of both primary and eutectic TiB in Ti matrix. However, the primary TiB has a little significant reinforcement effect. In all, a significant hardness improvement of about 30% is observed in the composites with a TiB reinforcement

fraction of 12-15 wt.%. More so, employing higher laser power slows cooling and longer TiB precipitates are formed which are uniformly distributed to maximize the area of interface between the TiB reinforcement and the Ti matrix.

The formation of TiB reinforcements in Ti matrix when TiB_2/Ti-6Al-4V is laser processed has contributed to the improvement of Ti-6Al-4V mechanical properties. An elastic modulus of 145 GPa is observed for composite characterised by 12-15 wt% TiB in Ti-6Al-4V, which is a 27% increment when compared to monolithic Ti-6Al-4V. Radial growth of TiB reinforcements observed in the composite matrix is encouraging as the composite may possess isotropic properties. Though the fracture surface showed brittle characteristics, typical of composites, the formation of a tight network of TiB reinforcements as they grow radially in the composite is advantageous. This helps to intercept the propagation of cracks in the composite when subjected to tensile load. However, process optimisation is required to improve the quality of the laser clad composite such that partially melted Ti-6Al-4V particles are eliminated.

Chapter 6

Performance Characterisation

In this chapter, the performance of the laser clad composites are reported. Erosion tests are carried out on the Ti-6Al-4V/Spherotene composite by subjecting it to both plain water and abrasive water jet impacts. The erosion rates of the composite are reported and compared to those of bulk Ti-6Al-4V subjected to the same test conditions. Microstructural examination is conducted on eroded composite surface to study the mechanism of failure under water jet impacts.

6.1 Erosion performance of composite layers under plain water and abrasive water jets

The erosion tests were conducted on the Ti-6Al-4V/Spherotene composite coatings prepared on Ti-6Al-4V substrates using the optimised process parameters required to obtain high reinforcement fraction, as presented in Section 4.4.5. Table 6.1 details the laser processs conditions to produced the clad layers and their Spherotene contents. The composite layers were ground to flat surfaces and subjected to plain water and abrasive water jet (PWJ and AWJ) impacts as described in Section 3.11. The erosion rate under PWJ and AWJ impacts and the microstructural features of the eroded surfaces are reported.

TABLE 6.1: Clad layer characteristics subjected to waterjetting

Set	Laser power (W)	Traverse speed (mm/min)	Wire feed rate (mm/min)	Powder feed rate (g/min)	Spherotene fraction (wt.%)
A	1800	300	700	30	76±1
B	1600	200	750	30	74±2
C	1400	400	800	30	68±2

6.1.1 Erosion performance of Ti-6Al-4V/Spherotene composites under PWJ impacts

Figure 6.1(a) and (b) show the erosion rate of Ti-6Al-4V and Ti-6Al-4V/Spherotene composites subjected to PWJ impacts at pressures of 275 MPa and 345 MPa. The erosion rate is measured as jet traverse speed changes from 20-100 mm/min. Slower traverse speed indicates longer exposure time for jet-material surface interaction. It can be seen that for all materials, the erosion rate increases with the decreasing traverse speed of the jet. As the jet traverse speed increases (the exposure time decreases), the differences between the erosion rates of Ti-6Al-4V and composite layers become insignificant at a lower pressure. It is evident that the composite prepared using laser process parameter set A - a laser power of 1800 W, 300 mm/min traverse speed, 700 mm/min wire feed rate, and 30 g/min powder feed rate (Table 6.1) exhibits the best erosion resistance as the erosion rate is minimised for both pressures and all traverse speeds. Also, it can be seen that the differences in erosion rates of the Ti-6Al-4V and the composite decrease as the traverse speed increases.

Figure 6.1(c) and (d) show the ratio of erosion rate of Ti-6Al-4V to the composites at different PWJ conditions. The erosion rate of Ti-6Al-4V and Ti-6Al-4V/Spherotene composites prepared using process parameter set A-C (Table 6.1) are represented as E_O , E_A, E_B, and E_C respectively. As seen, the composite processed using parameter set A gave the maximum ratio of 13 and 11.6 at the jet pressure of 275 MPa and 345 MPa, respectively at a typical jet traverse speed of 20 mm/min. Thus, the ratio of the erosion rate for the composite layer is sensitive to the fraction of reinforcement in the composite.

Figure 6.2 compares the mean profiles of the PWJ eroded cross-sections on the bulk Ti-6Al-4V and the composites. The response of these materials under PWJ impacts can be clearly observed. Although material loss from the composites is much less than that from Ti-6Al-4V, there is a noticeable material removal from all composites. It

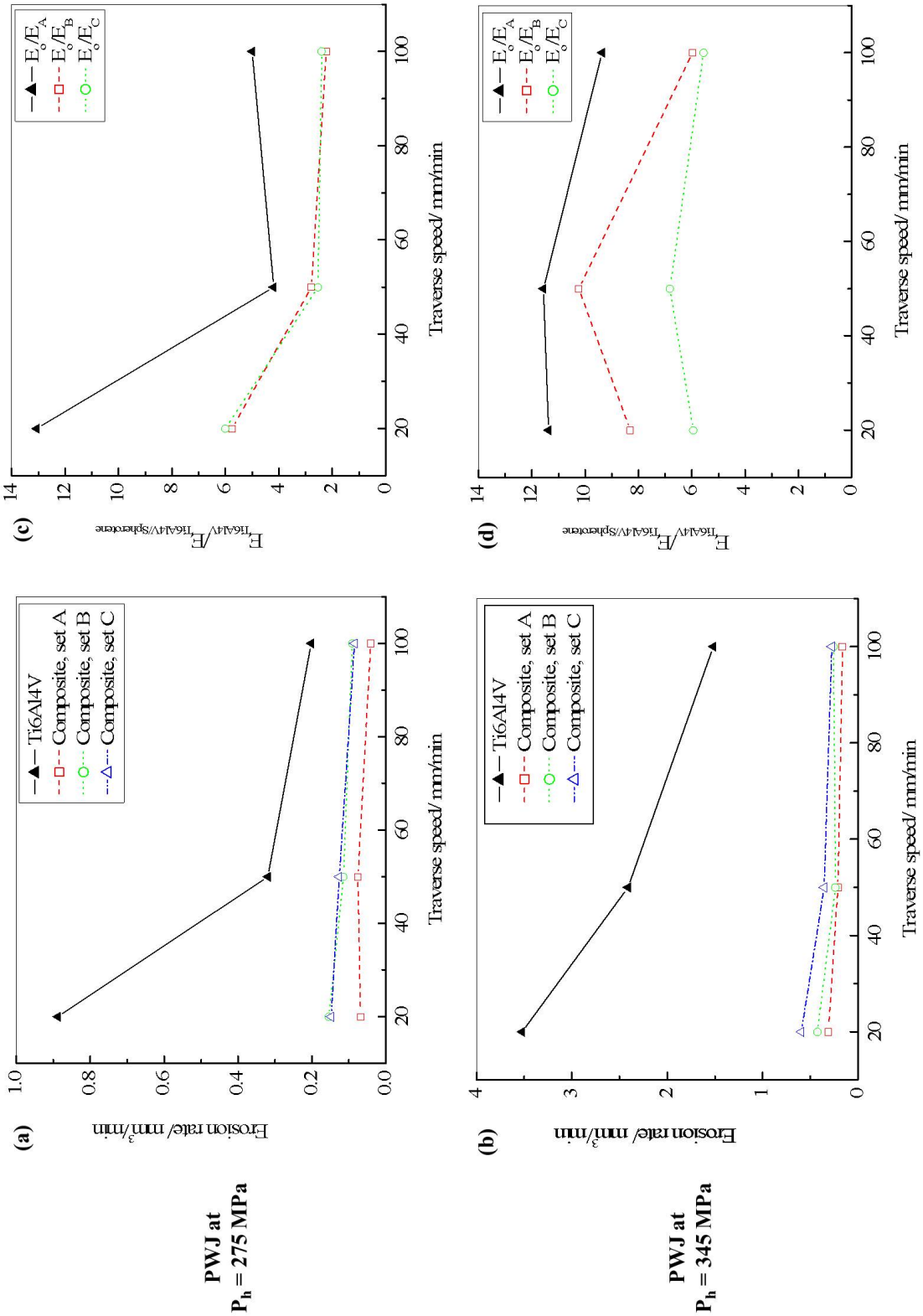

FIGURE 6.1: Erosion rate of Ti-6Al-4V and laser clad Ti-6Al-4V/Spherotene composites subjected to PWJ impacts at SOD=3 mm at pressures (a) 275 MPa; (b) 345 MPa, and erosion rate ratio of Ti-6Al-4V to composite at pressures (c) 275 MPa; and (d) 345 MPa.

should also be noted that the erosion depths on the Ti-6Al-4V within the waterjetting conditions are $\leq$300 μm. However, the erosion depths on the composite are not more than 50 μm. It is expected that plain water jet with head pressure greater than 345 MPa is required to achieve a through cutting of a bulk Ti-6Al-4V with thickness higher than 300 μm. Also, there would be a consequential increase in material loss from the composite should it be exposed to jets of higher head pressure .

Figure 6.3 shows the micrographs of the PWJ impact damage on the composite surface prepared with process parameter set A. At lower pressure (275 MPa), the erosion mechanism is characterised by erosion pits and tunnelling on both the embedded Spherotene particle surfaces and the composite matrix. The interfacial layer between the particles and the composite matrix is significantly eroded with formation of channels around the Spherotene particle (Figure 6.3(a) and (b)). However, at higher pressure (345 MPa), the erosion became more aggressive as the eroded surface is characterised by particle surface fracture, cracks in the interfacial region between particle and matrix, deep cavities and pits. The particles are exposed to erosion as the interfacial layer, which is characterised by TiC and W solid solutions, around them are eroded away. It is anticipated that at a higher pressure or higher exposure time of the impinging jet on the composite surface, Spherotene pull-out from the matrix is inevitable.

6.1.2 Erosion performance of Ti-6Al-4V/Spherotene composite under AWJ impacts

After the PWJ erosion experiments, the Ti-6Al-4V/Spherotene composite prepared using the process parameter set A (Table 6.1) has been considered as the most robust erosion-resistant materials under PWJ impingement. Thus, AWJ erosion trials are carried out on this composite as well as Ti-6Al-4V in order to investigate its potential as erosion resistant coating to be subjected to slurry and abrasive environmental conditions. Figure 6.4(a) compares the erosion rates of Ti-6Al-4V and the composite under AWJ impingement at different pressures. More prominent differences in erosion rates of the two materials are observed at the higher pressure. The normalised erosion rate, which is the ratio of erosion rate of Ti-6Al-4V to that of the Ti-6Al-4V/Spherotene composite, is shown in Figure 6.4(b). The maximum ratio is $\sim$8, resulting from AWJ machining at pressure of 207 MPa and traverse speed of 200 mm/min. Both Figure 6.4

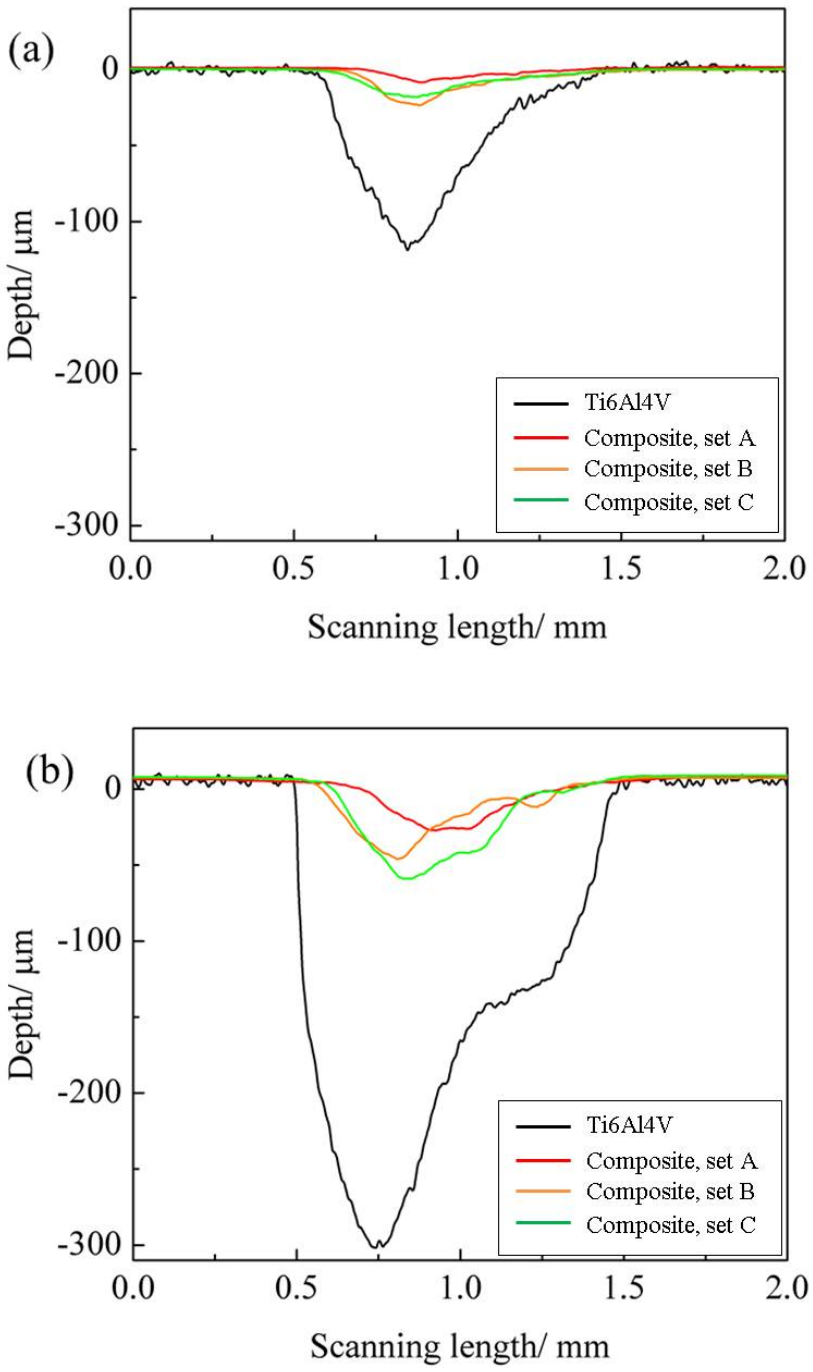

FIGURE 6.2: Comparison of the mean kerf profiles on Ti6Al4V and Ti6Al4V/Spherotene composites resulting from PWJ impacts at SOD = 3 mm, V_j = 20 mm/min, and (a) P_h = 275 MPa; and (b) P_h = 345 MPa.

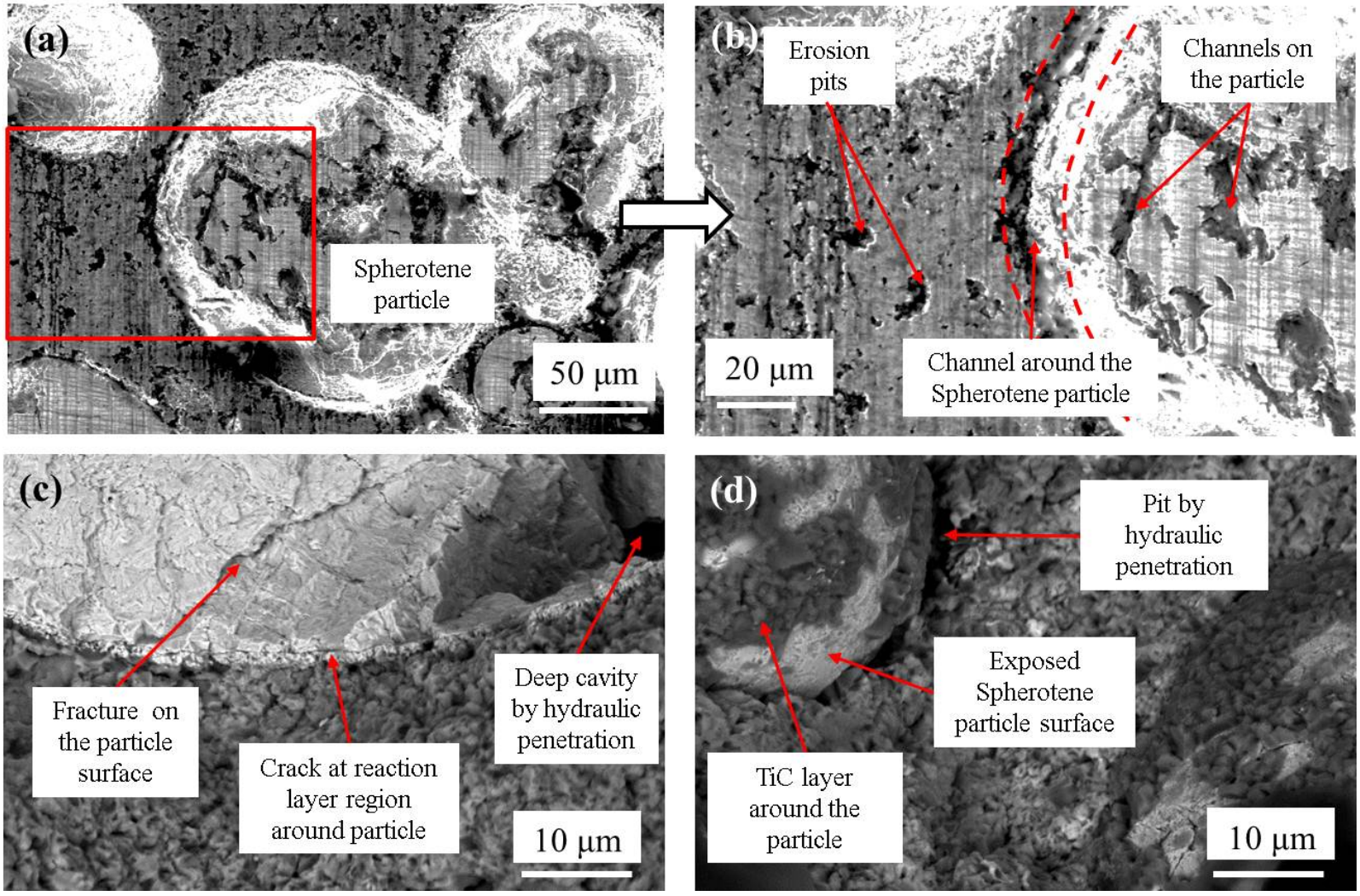

FIGURE 6.3: Micrographs of PWJ impact damage on Ti-6Al-4V/Spherotene composite (set A) with (a) and (b) SE images obtained from surface treated with 275MPa pressure, 100 mm/min traverse speed; (c) and (d) BSE images, 345 MPa pressure, 100 mm/min traverse speed.

(*a*) and (*b*) suggest that the composite performance under abrasive erosion is influenced by the machining parameter due to the diverse responses of the composite and virgin Ti-6Al-4V under AWJ impingement.

Figure 6.4(*c*) shows the erosion rate of Ti-6Al-4V and the composite under AWJ impacts at different standoff distances, while the normalised erosion rate is shown in Figure 6.4(*d*). Again, the graphs suggest that there is an optimal jet traverse speed (i.e. 200 mm/min) which results in the most significant difference in erosion rate between the composite and Ti-6Al-4V. Figure 6.4(*d*) indicates that a lower standoff distance lead to a higher normalised erosion rate. Figure 6.4(*e*) compares the erosion rate of Ti-6Al-4V and the composite during AWJ exposure using different abrasive flow rates. Similarly, the erosion rate of Ti-6Al-4V reached a maximum value at the traverse speed of 100 mm/min and 0.92 g/s AFR, resulting in the highest normalised erosion rate (Figure 6.4(*f*)). The lower abrasive flow rate (0.39 g/s) generally lead to greater differences in erosion rate between the two investigated materials.

It should be noted that the erosion rate of the composite coating was less influenced by the investigated AWJ parameters than that of the Ti-6Al-4V. Hence, a high normalised erosion rate is observed to be associated with high erosion rates of the virgin Ti-6Al-4V.

Figure 6.5 shows the micrographs of the damage associated with the AWJ on the Ti-6Al-4V/Spherotene composite possessing the highest reinforcement fraction of 76 wt%. The erosion mechanism of the composite surface is characterised by lateral cracks on the reinforcement particles, reinforcement pull-out, and ploughing of the composite matrix. Upon impact by the AWJ, fractures/cracks are observed on the particles as shown in Figure 6.5(*a*) and (*b*). This indicates a brittle response of the reinforcement when impacts by the abrasive garnets. Large craters are also observed which depict the locations of embedded reinforcement before pull-out occurred. Small craters are observed on the eroded surface of the composite matrix with crater material displaced as a result of the ploughing effect by the action of the AWJ. This indicates that, though the Ti matrix is reinforced by in-situ synthesized TiC and W solid solutions, the composite matrix still possesses its ductile characteristics. This allows plastic deformation and ploughing of the composite matrix to be evident in the micrograph.

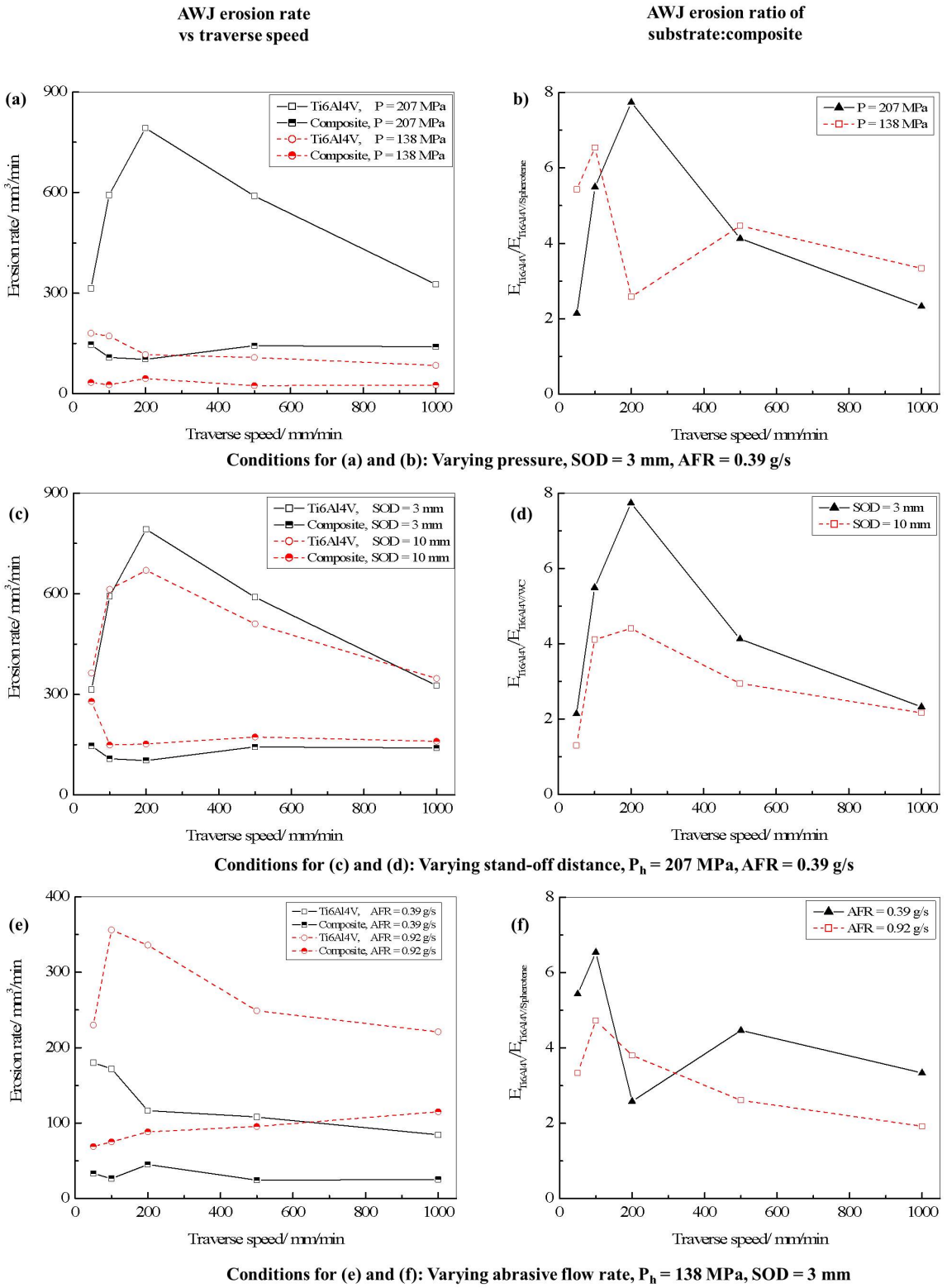

FIGURE 6.4: Erosion rates and ratios of Ti-6Al-4V and Ti-6Al-4V/Spherotene composite for varying pressure head, standoff distance, and abrasive feed rate.

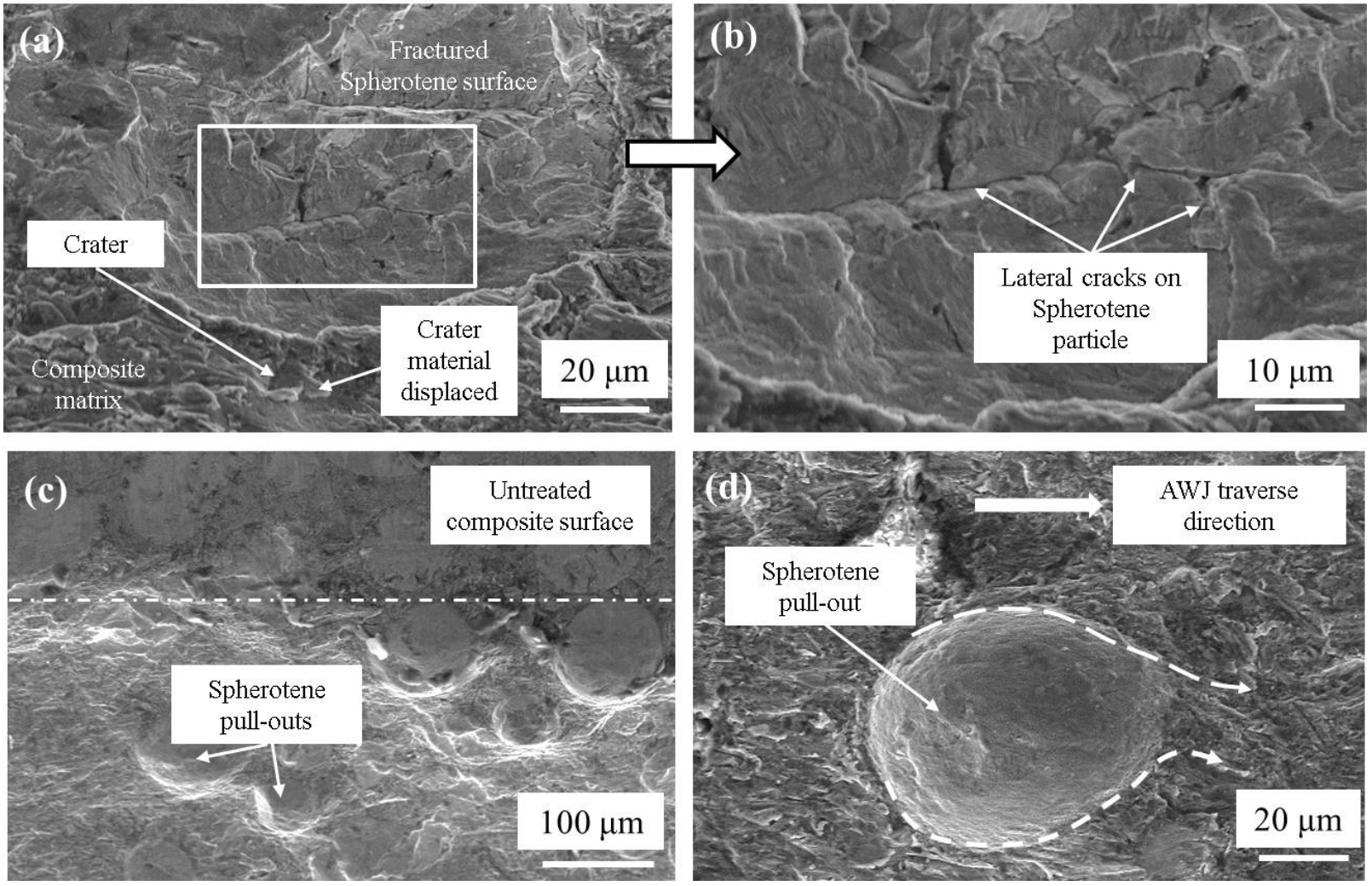

FIGURE 6.5: SE micrographs of AWJ impact damage on Ti-6Al-4V/Spherotene composite (set A) obtained from surface treated with 207 MPa pressure, 200 mm/min traverse speed, 3 mm standoff distance and 0.39 g/s abrasive particle feed rate.

Thus, the Ti-6Al-4V/Spherotene composite possesses significantly enhanced erosion resistant characteristics when compared to the Ti-6Al-4V. It is envisaged that this composite coating will be wear resistant in slurry environment, and will help to save frequent replacement cost of industrial components. In comparison to Ti-6Al-4V erosion resistance, a maximum composite erosion resistance of 13 is observed when 275 MPa head pressure, 20 mm/min jet traverse speed, and 3 mm stand-off distance are employed. Under AWJ test conditions, a maximum erosion resistance of 8 is observed when abrasives are accelerated with fluid against the composite surface at 207 MPa pressure head, 0.39 g/s abrasive feed rate, 200 mm/min jet traverse speed and a stand-off distance of 3 mm employed. The erosion resistances offered by the coating are significant and this performance is dependent on the Spherotene fraction of the laser clad coating. The coating with the highest Spherotene fraction (76±1 wt.%) (Section 4.4.2.1) has the highest resistance to erosion. This shows that the embedded reinforcement particles coupled with the increased hardness of the Ti composite matrix has contributed to the coating performance.

6.2 Discussion

Having subjected the laser clad composites to performance test, the response of the composites can be explained based on their material characteristics and the test characteristics employed. Hence, the discussion focuses on the resistance offered by the Ti-6Al-4V/Spherotene composite against high velocity plain and abrasive waterjet.

6.2.1 Erosion performance of Ti-6Al-4V/Spherotene under PWJ impacts

The erosion damage experienced by the Ti-6Al-4V/Spherotene composites under PWJ impacts have resulted from direct deformation, stress wave propagation, lateral outflow jets, and hydraulic penetration [95]. As the high velocity PWJ exit from the nozzle, the jet is atomised into water droplets due to its aerodynamic interaction with surrounding air [94]. Field [92] explained that the water droplets behave in an incompressible manner and on impact with the solid surface result in a high pressure known as water-hammer

pressure which can be derived from equation (6.1- 6.3).

$$P_h = \frac{1}{2}\rho_o v_o^2 \tag{6.1}$$

$$P_w = 0.78 c_s \rho_o v_o \tag{6.2}$$

$$c_s = c_o + 0.78 k v_o \tag{6.3}$$

Where, P_h = head pressure, (Pa), ρ_o = density of water (998 kg.m^{-3}) at normal temperature and pressure, v_o = jet velocity at orifice exit, P_w = water hammer pressure, (Pa), and c_s = shock velocity in the water droplet, c_o = the acoustic velocity in water at normal temperature and pressure (1480 m.s^{-1}), k is a constant with a value of 2 for water jet in a velocity range up to 1000 m.s^{-1} and the jet velocity coefficient at nozzle exit due to viscosity and turbulence is taken as 0.78 [93].

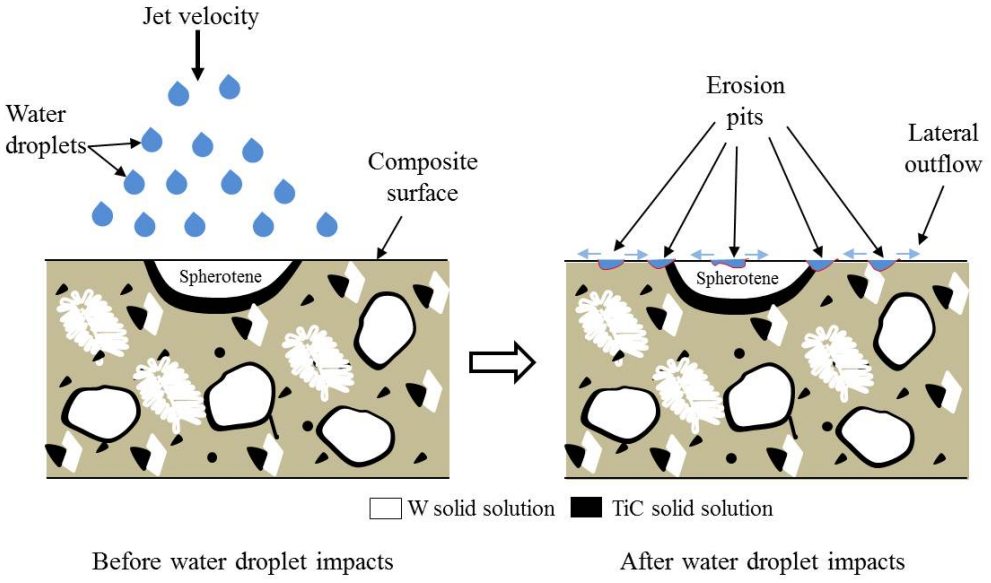

FIGURE 6.6: Schematic of water droplet erosion on the Ti-6Al-4V/Spherotene composite with multiple droplet impacts.

Hence, erosion damage caused by this water hammer pressure is dependent on the material response. As for Ti-6Al-4V/Spherotene composites, the Spherotene reinforcements are expected to possess an elastic-brittle response, while the β-Ti matrix phase is expected to respond plastically as a ductile material. However, the matrix is characterised by TiC and W solid solution precipitates uniformly dispersed in the β-stabilised Ti phase. The impacts of water droplets on the composite surface result in the formation

of erosion pits as shown in Figure 6.6. The coalescence of the erosion pits results in the formation of channels and multiple droplet impacts result in formation of deep cavities on the composite surface as observed in Figure 6.3. Thus, the channels and cavities are developed by the lateral outflow jets and hydraulic penetration of the water droplets. The interfacial layer between the Spherotene reinforcement and the matrix is observed to be severely affected by pitting and tunnelling actions of the jet. This is attributed to poor solubility and bonding strength between a WC/W_2C TiC ceramic system [142] which allows the TiC reaction layer at the interface to be preferentially eroded by lateral outflow jetting. The removal of the TiC interlayer between the composite matrix and the Spherotene reinforcement is envisaged to encourage the subsequent removal of the Spherotene particles [106]. Fractures observed on the reinforcement particle surfaces have been associated with the interaction of the stress wave and lateral outflow jetting with surface asperities and micro-cracks on the surface [95].

However, comparing the composite to the virgin Ti-6Al-4V, the composite matrix significantly contributes to the enhanced erosion resistance of the composite, due to the nano-scale TiC and W solid solution precipitates which reinforce the β-Ti phase [100, 104]. These in-situ synthesized precipitates increase the matrix hardness, thus improving its resistance to impact erosion [105]. Though, all the composites have a significant erosion performance compared to the virgin Ti-6Al-4V, it is worthy to note that composite set A, which had the highest Spherotene composition, has the best erosion resistance. This is followed by composite set B; while composite set C had the least erosion resistance both at water hammer pressures of 1.52 GPa and 1.8 GPa resulting from the applied pressure heads of 275 MPa and 345 MPa respectively. This complements the significance of high reinforcement particle fraction in composite matrix to better erosion resistance reported by Shipway and Gupta [83]. The overall performance of the composite to wrought Ti-6Al-4V under PWJ is significant due to the embedded Spherotene particles and the reaction products uniformly distributed in the β-Ti matrix.

6.2.2 Erosion performance of Ti-6Al-4V/Spherotene under AWJ impacts

When subjected to AWJ impacts, the erosion of the Ti-6Al-4V/Spherotene composite increased due to the simultaneous action of the high energy water droplet and accelerated

garnet particles. Since, the abrasive particles entrained in the high energy jet travel at a slower speed of 0.7 of water droplet speed [143], it is anticipated that the erosion of the surface will be in two stages as illiustrated in Figure 6.7. Firstly, the water droplet impacts would result in pitting and formation of deep cavities on the composite surface, while the abrasive particle impacts lastly erode the surface. This seems to be the valid sequence, as ploughing of the composite matrix is observed in Figure 6.5. The ploughing is indicative of the action of a spherical particle impact on a ductile material [96]. Small craters are observed with crater materials displaced in the direction of the particle incidence [97]. The displaced material is envisaged to fracture at high strain. Despite, the uniform distribution of TiC and W reaction products in the β-Ti phase, the composite matrix exhibits a ductile characteristic even at regions near the embedded Spherotene reinforcement. The direct impact of the accelerated abrasive garnet on the reinforcements results in lateral cracks which are observed on the particle surfaces. This is similar to results presented by Lathabai and Pender [103] and Gant and Gee [105]. In theory, since the abrasive particles employed have spherical morphology, the impact of the abrasive on the reinforcement particles would first result in Hertzian cracks followed by radial cracks, provided that the contact force at impact exceeds a particular threshold value which is material property dependent. The radial cracks formed are responsible for strength degradation, and these cracks propagate to the Spherotene particle surface as lateral cracks which are responsible for chip formation and erosion loss [96].

As earlier observed that PWJ impacts cause pitting and cavities on the composite with preferential removal of the particle/matrix interface, the same phenomenon occurs during the AWJ impacts. Material removal becomes more aggressive as abrasive particles knock out the reinforcement particles with limited metallurgical bond to the composite matrix. The removal of the reinforcement particle by the knock-out actions of the abrasive particles is responsible for the particle pull out indicated by large craters observed in Figure 6.5(c) and (d).

In Figure 6.4, there is a significant material loss in the bulk Ti-6Al-4V when compared to the composite, as the water head pressure increases. This is attributed to the resistance offered by the embedded Spherotene particles and the reaction products reinforcing the composite matrix. Moreover, the erosion loss of the wrought Ti-6Al-4V becomes fairly similar, while that of the composite slightly increase, as the stand-off distance increases. This results in the composite to have a higher resistance at 3 mm SOD compared to

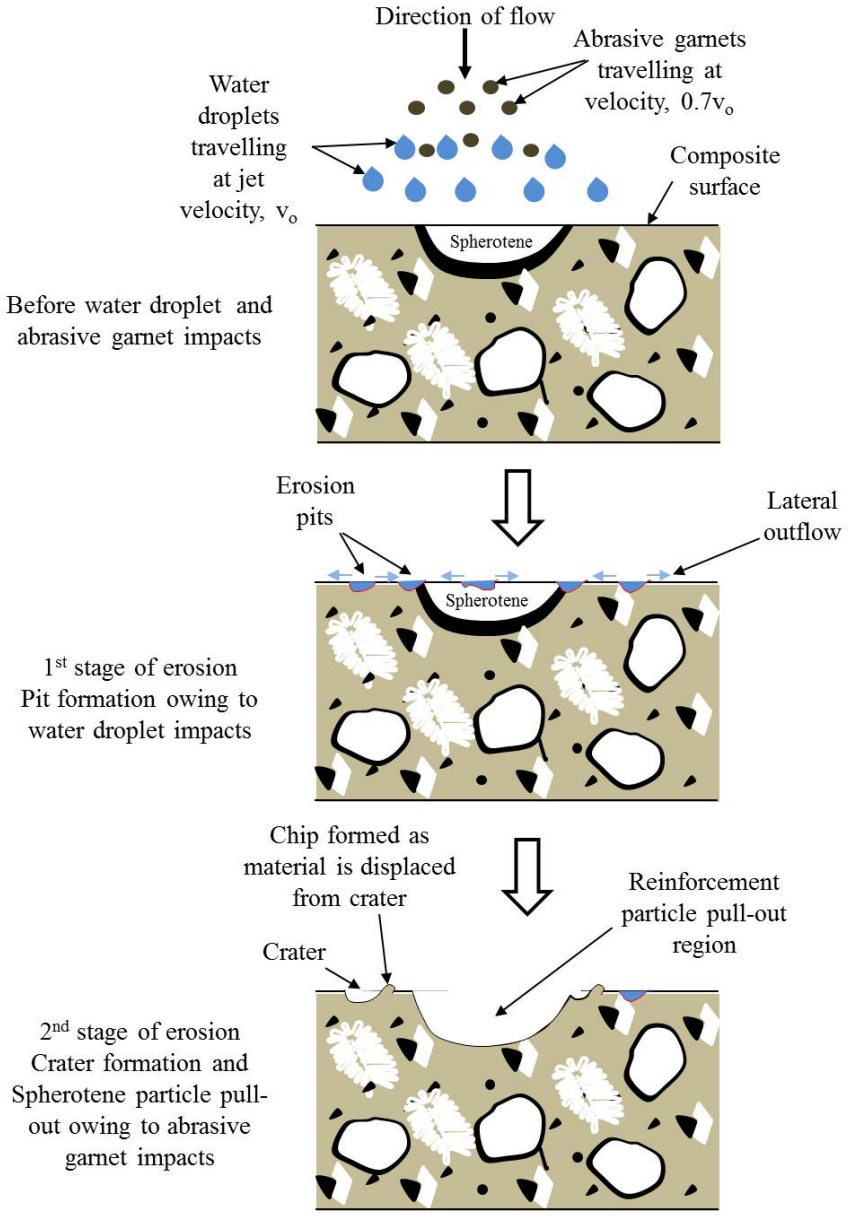

FIGURE 6.7: Schematic of erosion stages by the impacts of water droplets and abrasive garnets on the Ti-6Al-4V/Spherotene composite.

when it is 10 mm. The increase in composite material loss at a higher stand-off distance is attributed to the increased effectiveness of the water droplets and increased potential energy of the abrasive particles in the main region of the flowing jet as explained by Leu et al. [94]. The 3 mm SOD is considered to be in the initial region of the water jet, where the jet is a continuous flow stream which has not been fully discretized into more energetic water droplets. However, at 10 mm SOD, the flowing stream is suggested to have been fully atomised into packets of accelerated droplets which results in a higher water hammer pressure on impact, thus causing increased erosion loss of the composite.

The performance of the composite is also significant under the AWJ impacts and the dominating erosion mechanisms are composite matrix ploughing, particle fracture and lateral cracks resulting into chipping.

6.3 Conclusions

The properties of Ti-6Al-4V have been significantly improved for wear and structural applications by laser cladding the Ti alloy with particulate reinforcements. Ti-6Al-4V/Spherotene composite has displayed an enhanced erosion resistance under both PWJ and AWJ impacts when compared to virgin Ti-6Al-4V. The composite offered erosion resistance as high as 13 and 8 times than bulk Ti-6Al-4V when subjected to high velocity PWJ and AWJ impacts respectively. The composite suffered erosion loss under the action of PWJ by formation of erosion pits, tunnel and deep cavities especially around the reinforcement/matrix interface, while ploughing of the composite matrix, lateral cracking and chipping of embedded particles, and pull-out characterise the erosion mechanism of the composite under AWJ impact. The overall performance of the Ti-6Al-4V/Spherotene composite is attributed to the embedded Spherotene particles and the uniformly distributed nano-sized reaction products (TiC and W) reinforcing the ductile β-Ti composite matrix.

Chapter 7

Conclusions

The aim of this research was to study the laser cladding of Ti-6Al-4V reinforced with carbide and boride particulates to improve material properties. As described in chapter 1, the objectives were to obtain a range of suitable process parameters required for the deposition of Ti-6Al-4V wire with a high Spherotene (WC/W_2C) reinforcement fraction, assess the deposition of Ti-6Al-4V/TiB_2 powder and develop a modified feedstock suitable for a one-stage cladding process, carry out microstructural characterisation of deposits and investigate resulting performance characteristics.

The aim and objectives of this study have been successfully achieved and results obtained have been documented in the previous chapters. Thus, this final chapter contains the conclusions of the study on laser clad Ti-6Al-4V/Spherotene composite (chapter 4), laser clad Ti-6Al-4V/TiB_2 composite (chapter 5) and performance characterisation of deposits reported in chapter 6. Moreover, recommendations are highlighted for the future work that may be conducted based on this study to further the state of the art.

The wire/powder deposition approach for the production of composite coating on substrate for wear applications is advantageous when compare to the use of a pre-blended powder of Ti-6Al-4V and WC in laser processing. It is more economical to use Ti-6Al-4V in the form of wire, as this gives a better material utilisation which is nearly 100%. There is also a better recovery of Spherotene powder which can be recycled and re-use without having to think about the separation of the recovered powder if a pre-blended powder had been used. Also, the resulting composition of the composite microstructure

can be better controlled by feeding the reinforcement powder and the matrix material independently.

The agglomeration approach which allows a fine powder particles to be attached to the surface of a bigger particle is beneficial and further allows powders of different particle size ranges to be processed through cost effective and flexible one-stage laser cladding process. Using this agglomerated powder, a uniform distribution of the reacting elements is promoted in the melt pool, even when the thermo-capillary convection of the melt pool is not strong enough to create an even redistribution of solutes in the pool, which may be an issue when a pre-blended powder without agglomeration is used. The process also becomes more flexible when compared to preplaced deposition process, as cladding conforming to any geometry can be achieved with using the one stage co-deposition process.

In the overall, the benefit-cost ratio of the approaches is anticipated to be higher than other conventional approaches over a short period of time.

7.1 Laser clad Ti-6Al-4V/Spherotene composites

7.1.1 Laser Processing

In this study, it was found that consistent, pore- and crack-free composite deposits of Ti-6Al-4V wire (1.2 mm diameter) and Spherotene powder are achieved using a fibre laser under the conditions of 1400-1800 W laser power, 200-400 mm/min traverse speed, 700-800 mm/min wire feed rate and 10-30 g/min powder feed rate.

The best clad layer, containing as high as 76±1 wt.% reinforcement in the Ti matrix, is achieved via the laser process with an energy density of 150±10 J.mm^{-2}, 275±25 mm/min traverse speed, 700 mm/min wire feed rate and 30 g/min powder feed rate.

Moreover, the design freedoms of laser cladding, which is also an additive manufacturing process, is demonstrated with a functionally graded 3-D cylinder built. This showed that component manufacture and repairs with selective application of functionally graded material is possible with cladding process, which may not have been achievable via traditional manufacturing route.

7.1.2 Microstructure

It is evident that all the laser clad Ti-6Al-4V/Spherotene samples obtained from the range of laser processing conditions employed possess similar phases as confirmed by the XRD traces. Phases identified are WC, W_2C, W, TiC and β-Ti. The dissolution of Spherotene particles enriches the Ti melt with W and C to produce TiC and W in the composite microstructure. These phases serve as reinforcement in the Ti matrix with TiC having a higher hardness (3200 kgf.mm^{-2}) when compared to carbides of tungsten. Within the range of laser processing conditions employed, a 7.5-9 at% W is retained in the Ti solid solution on solidification. This concentration is sufficient to stabilise the Ti as a beta phase and could be considered advantageous as composite matrix may retain its ductility. Increasing laser power is found to decrease the concentration of W retained in the Ti.

Two types of Spherotene particle-matrix interface are identified, these are a mixed and a regular/circular reaction layers. The in-situ synthesized TiC are in blocky, near circular or fine eutectic morphologies, while the W solid precipitates are either blocky or equiaxed. Equiaxed W precipitates with TiC in their interdendritic regions are predominantly featured in the Ti matrix.

The composite matrix hardness is found to range between 410-620 kgf.mm^{-2} and the ratio of composite matrix hardness to the encapsulated Spherotene particles is about 1:5. The uniform dispersion of the TiC and W in the β-Ti matrix phase has increased the matrix hardness (where the matrix is polyphase W + β-Ti + TiC).

7.1.3 Erosion Behaviour

Ti-6Al-4V/Spherotene composites have displayed an enhanced erosion resistance under both PWJ and AWJ impacts when compared to monolithic Ti-6Al-4V. The best clad layer containing as high as 76$\pm$1 wt.% reinforcement exhibited erosion resistance as high as 13 and 8 times that of Ti-6Al-4V when subjected to high velocity PWJ and AWJ impacts respectively. The composite coating suffered erosion loss under the action of PWJ by formation of erosion pits, tunnel and deep cavities especially around the Spherotene particle/matrix interface. The ploughing of the composite matrix, lateral

cracking and chipping of embedded Spherotene particles, and pull-out characterise the erosion mechanism of the composite under AWJ impacts.

The overall performance of the Ti-6Al-4V/Spherotene composite coatings is attributed to the embedded Spherotene particles and the distributed reaction products (TiC and W) reinforcing the ductile β-Ti composite matrix.

7.2 Laser clad Ti-6Al-4V/TiB_2 composites

7.2.1 Powder Feedstock

A new method has been developed to prepare a suitable feedstock from different powders for a one-stage laser cladding process. This is demonstrated by agglomerating fine powder of TiB_2 (10 μm, mean size) on Ti-6Al-4V powder (108 μm, mean size) using an aerosol of a binder solution containing 27 vol.% PVA in water. With suitable choice of original powders and this agglomeration method, it is possible to produce a feedstock suitable for laser cladding process.

7.2.2 Laser Processing

In this study, having modified the feedstock by agglomerating a fine TiB_2 powder on Ti-6Al-4V powder, consistent and crack-free composite deposits of 90 wt.% Ti-6Al-4V/ 10 wt.% TiB_2 are achieved using a fibre laser with processing conditions in the range of 1400-1800 W laser power, 200-400 mm/min traverse speed and 10 g/min powder feed rate. Higher laser powers and higher traverse speed are observed to favour complete dissolution of the feedstock delivered into the melt pool to reduce or eliminate the presence of partially melted particles. In all deposited samples, within the processing range, partially dissolved remnant particles are found mostly in the clad periphery which could have been transported by the Maragoni flow convection in the melt pool. A significant increase in substrate dilution is observed with increasing traverse speed, while increasing laser power is found to reduce dilution.

7.2.3 Microstructure

As confirmed by the XRD results, all samples of the composite deposits with varying laser power and a common speed of 400 mm/min possess TiB and α-Ti phases, while TiB_2 is only identified in sample produced using a lower laser power (1400 W). SEM interrogation confirms the formation of TiB precipitates as eutectic needle-like features in a Ti-rich primary phase microstructure. The composite matrix is characterised by α-Ti phase which is promoted owing to the presence of boron.

Besides the eutectic TiB phase, primary TiB phase is observed in the interlayer regions of composite multilayer wall deposited.

For all samples deposited within the processing conditions, the composite hardness range between 440-480 kgf.mm^{-2} which is about 30% significant improvement when compared to monolithic Ti-6Al-4V with a TiB reinforcement fraction of 12-15 wt.% in Ti matrix.

7.2.4 Tensile Behaviour

The elastic modulus of the composite characterised by 14wt% TiB/86 wt.% Ti is found to be 145 GPa when compared to 114 GPa for monolithic Ti-6Al-4V. Though the fracture surface showed brittle characteristics, typical of composite materials, the formation of a network of TiB reinforcements as they solidify in the composite is advantageous. This helps to intercept the propagation of cracks in the composite when subjected to tensile load. However, process optimisation is further required to improve the quality and properties of the laser clad composite such that partially melted Ti-6Al-4V particles and pores are eliminated.

7.3 Future Work

Having successfully carried out the laser cladding of Ti-6Al-4V/Spherotene and Ti-6Al-4V/TiB_2 to prepare wear resistant coating, the following suggested research opportunities can be further pursued. These include:

- Laser cladding of Ti-6Al-4V/Spherotene could be carried out within the suitable processing range obtained in this work to check whether beads with a reinforcement

fraction higher than 76±1 % wt. can be achieved without significant defects such as, cracks, pores and delamination.

- The erosive wear performance of this coating with higher reinforcement fractions could be compared to check whether there is any significant improvement in its performance compared to the results presented in this study.

- The development of functionally graded parts can be further undertaken with more mechanical testing (destructive or non-destructive) to establish the integrity of graded parts produced.

- The inclusion of particulates or whisker reinforcement in Ti-6Al-4V may reduce its corrosion performance, hence a study of the corrosion performance of the Ti-6Al-4V composite coating and untreated Ti-6Al-4V could be investigated.

- The validity of the modification process employed by attaching the fine TiB_2 on Ti-6Al-4V can be verified by using other material systems. Also, this method can be used to develop new materials with tailored properties for specific applications.

- Moreover, post deposition processing/treatment can be studied with their effect on the properties of composite parts produced. This will allow composites with excellent properties to be developed with little or no defects, such that they can be integrated into a range of materials to be heavily used in the industries.

- In the future, functionally graded MMCs will be more used in ground transport and aerospace applications, however, the challenges of incomplete homogenisation of microstructure and anisotropy of their mechanical properties must be overcome.

Appendix A

Experimental Procedures

TABLE A.1: An L-16 Taguchi Orthogonal Array of process parameters

Track no:	Laser Power (W)	Traverse Speed (mm/min)	Wire Feed Rate (mm/min)	Powder Feed Rate (g/min)	Comment
1	1200	100	500	10	Unstable deposition
2	1200	200	600	20	Unstable deposition
3	1200	300	700	30	Unstable deposition
4	1200	400	800	40	Stable deposition
5	1400	100	600	30	Unstable deposition
6	1400	200	500	40	Unstable deposition
7	1400	300	800	10	Stable deposition
8	1400	400	700	20	Stable deposition
9	1600	100	700	40	Unstable deposition
10	1600	200	800	30	Stable deposition
11	1600	300	500	20	Unstable deposition
12	1600	400	600	10	Unstable deposition
13	1800	100	800	20	Unstable deposition
14	1800	200	700	10	Stable deposition
15	1800	300	600	40	Unstable deposition
16	1800	400	500	30	Unstable deposition

Calibration of the 2-kW Fibre laser at the University of Nottingham, UK using PRIMES Focus Monitor (5th November, 2012)

Fibre diameter [microns]	Set Power [W]	Displayed Power [W]	Measured Power [W]
600	800	790	696
600	1200	1180	1045
600	1600	1560	1380
600	2000	1960	1740

There is a 13% decrease in the measured power when compared to the set laser power.

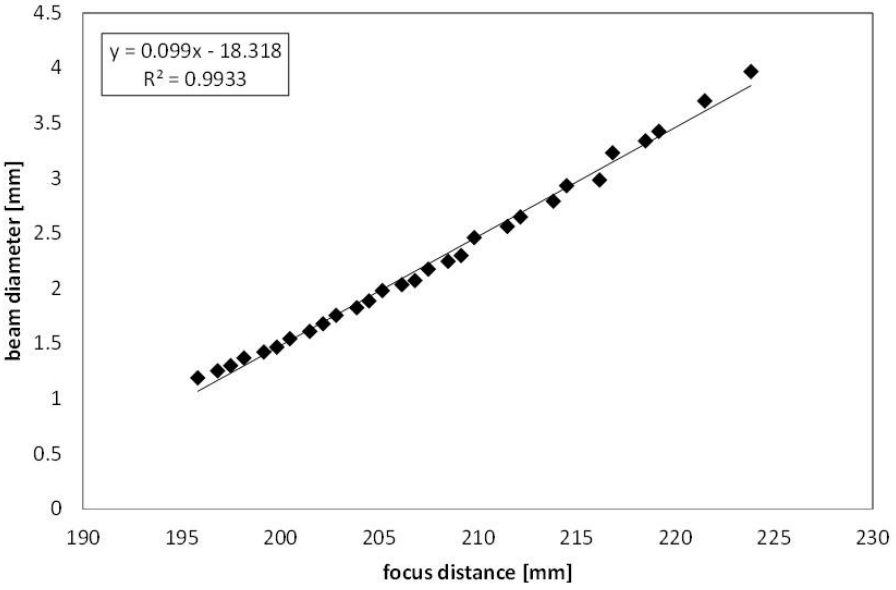

Change in laser beam diameter of the fibre laser as the laser beam is defocussed.

FIGURE A.1: Calibration of the 2-kW Fibre laser at the University of Nottingham.

TABLE A.2: An L-9 Taguchi Orthogonal array for 4 process factors with 3 levels each

Track no	Laser Power (W)	Traverse Speed (mm/min)	Wire Feed Rate (mm/min)	Powder Feed Rate (g/min)	Comment
1	1400	200	700	10	Stable deposition
2	1400	300	750	20	Stable deposition
3	1400	400	800	30	Stable deposition
4	1600	200	750	30	Stable deposition
5	1600	300	800	10	Stable deposition
6	1600	400	700	20	Stable deposition
7	1800	200	800	20	Stable deposition
8	1800	300	700	30	Stable deposition
9	1800	400	750	10	Stable deposition

TABLE A.3: An L 16 orthogonal array for initial hybrid material deposition experiment

Trials	**Process factors**			
	A	**B**	**C**	**D**
T-1	1	1	1	1
T-2	1	2	2	2
T-3	1	3	3	3
T-4	1	4	4	4
T-5	2	1	2	3
T-6	2	2	1	4
T-7	2	3	4	1
T-8	2	4	3	2
T-9	3	1	3	4
T-10	3	2	4	3
T-11	3	3	1	2
T-12	3	4	2	1
T-13	4	1	4	2
T-14	4	2	3	1
T-15	4	3	2	4
T-16	4	4	1	3

TABLE A.4: An L 27 orthogonal array for optimisation of the hybrid deposition

Trials	Process factors			
	A	B	C	D
T-1	1	1	1	1
T-2	1	1	1	1
T-3	1	1	1	1
T-4	1	2	2	2
T-5	1	2	2	2
T-6	1	2	2	2
T-7	1	3	3	3
T-8	1	3	3	3
T-9	1	3	3	3
T-10	2	1	2	3
T-11	2	1	2	3
T-12	2	1	2	3
T-13	2	2	3	1
T-14	2	2	3	1
T-15	2	2	3	1
T-16	2	3	1	2
T-17	2	3	1	2
T-18	2	3	1	2
T-19	3	1	3	2
T-20	3	1	3	2
T-21	3	1	3	2
T-22	3	2	1	3
T-23	3	2	1	3
T-24	3	2	1	3
T-25	3	3	2	1
T-26	3	3	2	1
T-27	3	3	2	1

Appendix B

Ti-6Al-4V/Spherotene composites

TABLE B.1: Mean and Standard error of Ti-6Al-4V bead heights and widths

Laser Power (W)	Traverse Speed, (mm/min)	Wire Feed Rate, (mm/min)	Mean Height, (mm)	Standard Error Height	Mean Width, (mm)	Standard Error Width
1400	200	700	1.46	0.010	3.87	0.042
1400	200	700	1.47	0.003	3.82	0.007
1400	300	750	1.12	0.020	3.6	0.035
1400	300	750	1.15	0.020	3.53	0.003
1400	400	800	0.92	0.015	3.54	0.017
1400	400	800	0.97	0.015	3.56	0.009
1600	200	750	1.38	0.023	4.6	0.038
1600	200	750	1.39	0.015	4.54	0.017
1600	300	800	1.07	0.029	4.17	0.015
1600	300	800	1.09	0.024	4.24	0.026
1600	400	700	0.78	0.010	4.12	0.009
1600	400	700	0.76	0.015	4.06	0.015
1800	200	800	1.39	0.010	5.18	0.062
1800	200	800	1.35	0.013	5.2	0.012
1800	300	700	0.88	0.020	4.85	0.037
1800	300	700	0.91	0.007	4.76	0.018
1800	400	750	0.78	0.012	4.58	0.064
1800	400	750	0.79	0.013	4.44	0.032

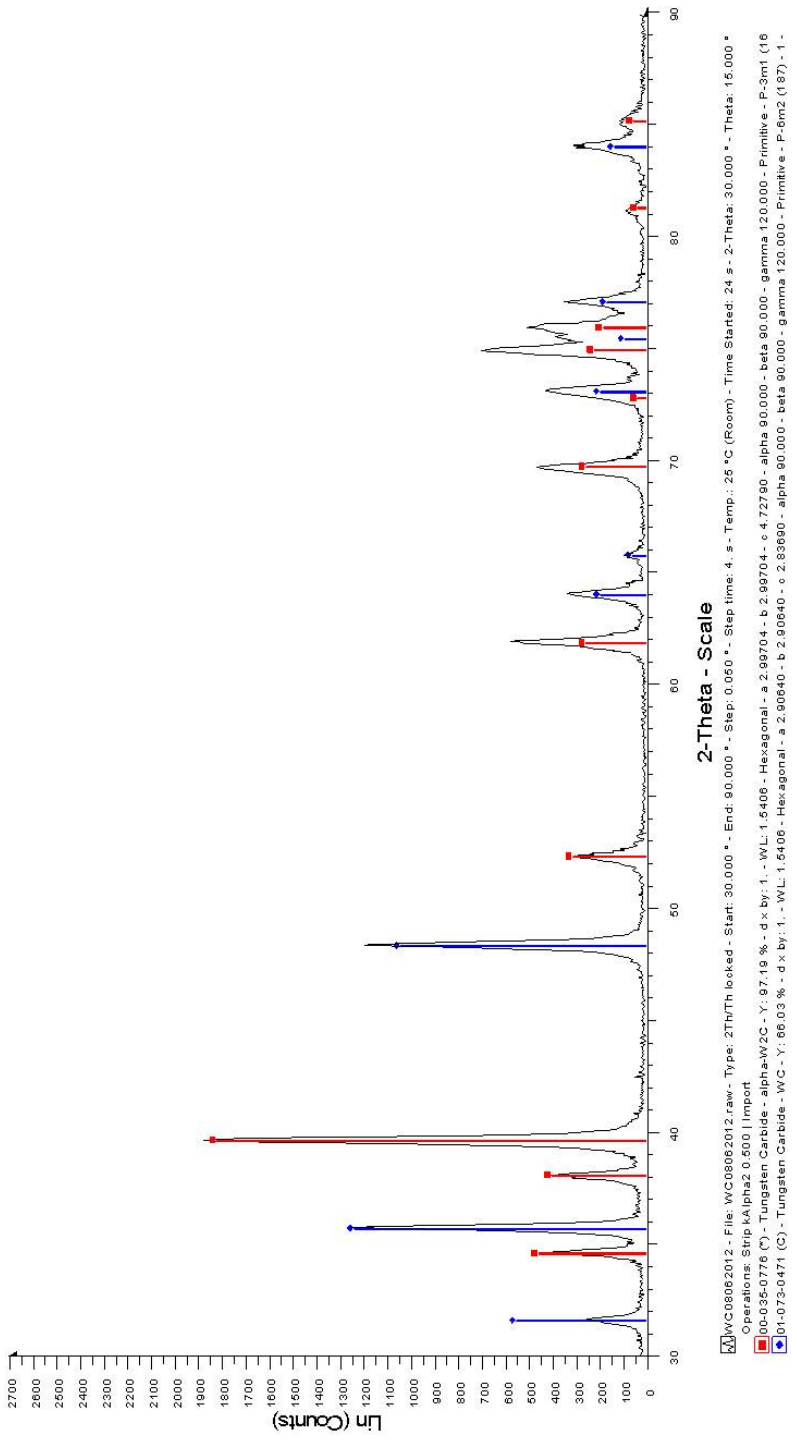

FIGURE B.1: ICDD Patterns for WC and W_2C matching peaks in the experimental XRD spectrum.

TABLE B.2: Mean and Standard Error of Ti-6Al-4V/Spherotene bead heights and widths

Laser Power (W)	Traverse speed (mm/min)	Wire Feed Rate (mm/min)	Powder Feed Rate (g/min)	Mean Height (mm)	Standard Error Height	Mean Width (mm)	Standard Error Width
1400	200	700	10	1.84	0.022	3.66	0.094
1400	200	700	10	1.82	0.015	3.61	0.026
1400	200	700	10	1.85	0.035	3.75	0.077
1400	300	750	20	1.63	0.010	3.24	0.022
1400	300	750	20	1.60	0.035	3.39	0.156
1400	300	750	20	1.60	0.018	3.48	0.143
1400	400	800	30	1.53	0.009	2.89	0.033
1400	400	800	30	1.57	0.061	2.77	0.257
1400	400	800	30	1.53	0.029	3.18	0.060
1600	200	750	30	2.33	0.025	4.09	0.048
1600	200	750	30	2.28	0.023	4.02	0.024
1600	200	750	30	2.29	0.026	4.08	0.110
1600	300	800	10	1.38	0.015	3.86	0.055
1600	300	800	10	1.40	0.006	3.86	0.012
1600	300	800	10	1.39	0.018	3.90	0.055
1600	400	700	20	1.20	0.035	3.61	0.049
1600	400	700	20	1.21	0.035	3.61	0.025
1600	400	700	20	1.17	0.012	3.64	0.032
1800	200	800	20	2.18	0.015	4.29	0.010
1800	200	800	20	2.17	0.063	4.38	0.103
1800	200	800	20	2.11	0.023	4.34	0.035
1800	300	700	30	1.54	0.022	3.96	0.055
1800	300	700	30	1.63	0.030	3.89	0.043
1800	300	700	30	1.53	0.026	3.89	0.042
1800	400	750	10	0.98	0.023	4.29	0.015
1800	400	750	10	0.98	0.019	4.29	0.082
1800	400	750	10	0.93	0.014	4.32	0.030

TABLE B.3: A F-Table to determine the statistical significance of the process the factors

Table B-4. F Table $F_{.01}(f_1,f_2)$, 99% Confidence

f_1 = Number of degrees of freedom of numerator
f_2 = Number of degrees of freedom of denominator

f_2 \ f_1	1	2	3	4	5	6	7	8	9	10	12	15	20	24	30	40	80	120	∞
1	4052.2	4999.5	5403.3	5624.6	5763.7	5859.0	5928.3	5981.6	6022.5	6055.8	6106.3	6157.3	6208.7	6234.6	6260.7	6286.8	6313.0	6339.4	6366.0
2	98.503	99.000	99.166	99.249	99.299	99.332	99.356	99.374	99.388	99.399	99.415	99.432	99.449	99.458	99.466	99.474	99.483	99.491	99.501
3	34.116	30.817	29.457	28.710	28.237	27.911	27.672	27.489	27.345	27.229	27.052	26.872	26.690	26.598	26.505	26.411	26.316	26.221	26.125
4	21.198	18.000	16.694	15.977	15.522	15.207	14.986	14.799	14.659	14.546	14.374	14.198	14.020	13.929	13.838	13.745	13.652	13.558	13.463
5	16.258	13.274	12.060	11.392	10.967	10.672	10.456	10.289	10.158	10.051	9.8883	9.7222	9.5527	9.4665	9.3793	9.2912	9.2020	9.1118	9.0204
6	13.745	10.925	9.7795	9.1483	8.7459	8.4661	8.2600	8.1016	7.9761	7.8741	7.7183	7.5590	7.3958	7.3127	7.2285	7.1432	7.0568	6.9690	6.8801
7	12.246	9.5466	8.4513	7.8467	7.4604	7.1914	6.9928	6.8401	6.7188	6.6201	6.4691	6.3143	6.1554	6.0743	5.9921	5.9084	5.8236	5.7372	5.6495
8	11.259	8.6491	7.5910	7.0060	6.6318	6.3707	6.1776	6.0289	5.9106	5.8143	5.6668	5.5151	5.3591	5.2793	5.1981	5.1156	5.0316	4.9460	4.8588
9	10.561	8.0215	6.9919	6.4221	6.0569	5.8018	5.6129	5.4671	5.3511	5.2565	5.1114	4.9621	4.8080	4.7290	4.6486	4.5667	4.4831	4.3978	4.3105
10	10.044	7.5594	6.5523	5.9943	5.6363	5.3858	5.2001	5.0567	4.9424	4.8402	4.7059	4.5582	4.4054	4.3269	4.2469	4.1653	4.0619	3.9965	3.9090
11	9.6460	7.2057	6.2167	5.6683	5.3160	5.0692	4.8861	4.7445	4.6315	4.5393	4.3974	4.2509	4.0990	4.0209	3.9411	3.8596	3.7761	3.6904	3.6025
12	9.3302	6.9266	5.9526	5.4119	5.0643	4.8206	4.6395	4.4994	4.3875	4.2961	4.1553	4.0096	3.8584	3.7805	3.7008	3.6192	3.5355	3.4494	3.3608
13	9.0738	6.7010	5.7394	5.2053	4.8616	4.6204	4.4410	4.3021	4.1911	4.1003	3.9603	3.8154	3.6646	3.5868	3.5070	3.4253	3.3413	3.2548	3.1654
14	8.8616	6.5149	5.5639	5.0354	4.6950	4.4558	4.2779	4.1399	4.0297	3.9394	3.8001	3.6557	3.5052	3.4274	3.3476	3.2656	3.1813	3.0942	3.0040
15	8.6831	6.3589	5.4170	4.8932	4.5556	4.3183	4.1415	4.0045	3.8948	3.8049	3.6662	3.5222	3.3719	3.2940	3.2141	3.1319	3.0471	2.9595	2.8684
16	8.5310	6.2262	4.2922	4.7726	4.4374	4.2016	4.0259	3.8896	3.7804	3.6909	3.5527	3.4089	3.2588	3.1808	3.1007	3.0182	2.9330	2.8447	2.7528
17	8.3997	6.1121	5.1850	4.5590	4.3359	4.1015	3.9267	3.7910	3.6822	3.5931	3.4552	3.3117	3.1615	3.0835	3.0032	2.9205	2.8348	2.7459	2.6530
18	8.2854	6.0129	4.0919	4.5790	4.2479	4.0146	3.8406	3.7054	3.5971	3.5082	3.3706	3.2273	3.0771	2.9990	2.9185	2.8354	2.7493	2.6597	2.5660
19	8.1850	5.9259	5.0103	4.5003	4.1708	3.9386	3.7653	3.6305	3.5225	3.4338	3.2965	3.1533	3.0031	2.9249	2.8442	2.7608	2.6742	2.5839	2.4893
20	8.0960	5.8489	4.9382	4.4307	4.1027	3.8714	3.6987	3.5644	3.4567	3.3682	3.2311	3.0880	2.9377	2.8594	2.7785	2.6947	2.6077	2.5168	2.4212
21	8.0166	5.7804	4.8740	4.3688	4.0421	3.8117	3.6396	3.5056	3.3981	3.3098	3.1729	3.0299	2.8976	2.8011	2.7200	2.6359	2.5484	2.4568	2.3603
22	7.9454	5.7190	4.8166	4.3134	3.9880	3.7583	3.5867	3.4530	3.3458	3.2576	3.1209	2.9780	2.8274	2.7488	2.6675	2.5831	2.4951	2.4029	2.3055
23	7.8811	5.6637	4.7649	4.2635	3.9392	3.7102	3.5390	3.4057	3.2986	3.2106	3.0740	2.9311	2.7805	2.7017	2.6202	2.5355	2.4471	2.3542	2.2559
24	7.8229	5.6136	4.7181	4.2184	3.8951	3.6667	3.4959	3.3629	3.2560	3.1681	3.0316	2.8887	2.7380	2.6591	2.5773	2.4923	2.4035	2.3099	2.2107
25	7.7698	55.680	4.6755	4.1774	3.8550	3.6272	3.4568	3.3239	3.2172	3.1294	2.9931	2.8502	2.6993	2.6203	2.5383	2.4530	2.3637	2.2695	2.1694
26	7.7213	5.5263	4.6366	4.1400	3.8183	3.5911	3.4210	3.2884	3.1818	3.0941	2.9579	2.8150	2.6640	2.5848	2.5026	2.4170	2.3273	2.2325	2.1315
27	7.6767	5.4881	4.6009	4.1056	3.7848	3.5580	3.3882	3.2558	3.1494	3.0618	2.9256	2.7827	2.6316	2.5522	2.4699	2.3840	2.2938	2.1984	2.0965
28	7.6356	5.4529	4.5681	4.0740	3.7539	3.5276	3.3581	3.2259	3.1195	3.0320	2.8959	2.7530	2.6017	2.5223	2.4397	2.3535	2.2529	2.1670	2.0642
29	7.5976	5.4205	4.5378	4.0449	3.7254	3.4995	3.3302	3.1982	3.0920	3.0045	2.8685	2.7256	2.5742	2.4946	2.4118	2.3253	2.2344	2.1378	2.0342
30	7.5625	5.3904	4.5097	4.0179	3.6990	3.4735	3.3045	3.1726	3.0665	2.9791	2.8431	2.7002	2.5487	2.4589	2.3860	2.2992	2.2079	2.1107	2.0062
40	7.3141	5.1785	4.3126	3.8283	3.5138	3.2910	3.1238	2.9930	2.8876	2.8005	2.6649	2.5216	2.3689	2.2880	2.2034	2.1142	2.0194	1.9172	1.8047
60	7.0771	4.9774	4.1259	3.6591	3.3389	3.1187	2.9530	2.8233	2.7185	2.6318	2.4961	2.3523	2.1978	2.1154	2.0285	1.9360	1.8363	1.7263	1.6006
120	6.8510	4.7865	3.9493	3.4706	3.1735	2.9559	2.7918	2.6629	2.5586	2.4721	2.3363	2.1915	2.0346	1.9500	1.8600	1.7629	1.6557	1.5330	1.3805
∞	6.6349	4.6052	3.7816	3.3192	3.0173	2.8020	2.6393	2.5113	2.4073	2.3209	2.1848	2.0385	1.8783	1.7908	1.6964	1.5923	1.4730	1.3246	1.0000

TABLE B.4: Means and Standard Errors of Spherotene fraction in Ti-6Al-4V/Spherotene beads

Laser Power (W)	Traverse speed (mm/min)	Wire Feed Rate (mm/min)	Powder Feed Rate (g/min)	Mean Spherotene fraction (weight %) in Bead	Mean Spherotene fraction (weight %) per treatment	Standard Error Mean Spherotene fraction
1400	200	700	10	57.40	56.63	0.623
1400	200	700	10	57.10		
1400	200	700	10	55.40		
1400	300	750	20	63.40	64.10	0.379
1400	300	750	20	64.20		
1400	300	750	20	64.70		
1400	400	800	30	67.40	68.73	0.811
1400	400	800	30	68.60		
1400	400	800	30	70.20		
1600	200	750	30	72.70	74.43	0.869
1600	200	750	30	75.20		
1600	200	750	30	75.40		
1600	300	800	10	55.90	53.50	1.200
1600	300	800	10	52.30		
1600	300	800	10	52.30		
1600	400	700	20	65.70	66.90	0.643
1600	400	700	20	67.10		
1600	400	700	20	67.90		
1800	200	800	20	69.00	69.87	0.433
1800	200	800	20	70.30		
1800	200	800	20	70.30		
1800	300	700	30	75.9	76.47	0.296
1800	300	700	30	76.60		
1800	300	700	30	76.90		
1800	400	750	10	55.80	54.83	0.578
1800	400	750	10	53.80		
1800	400	750	10	54.90		

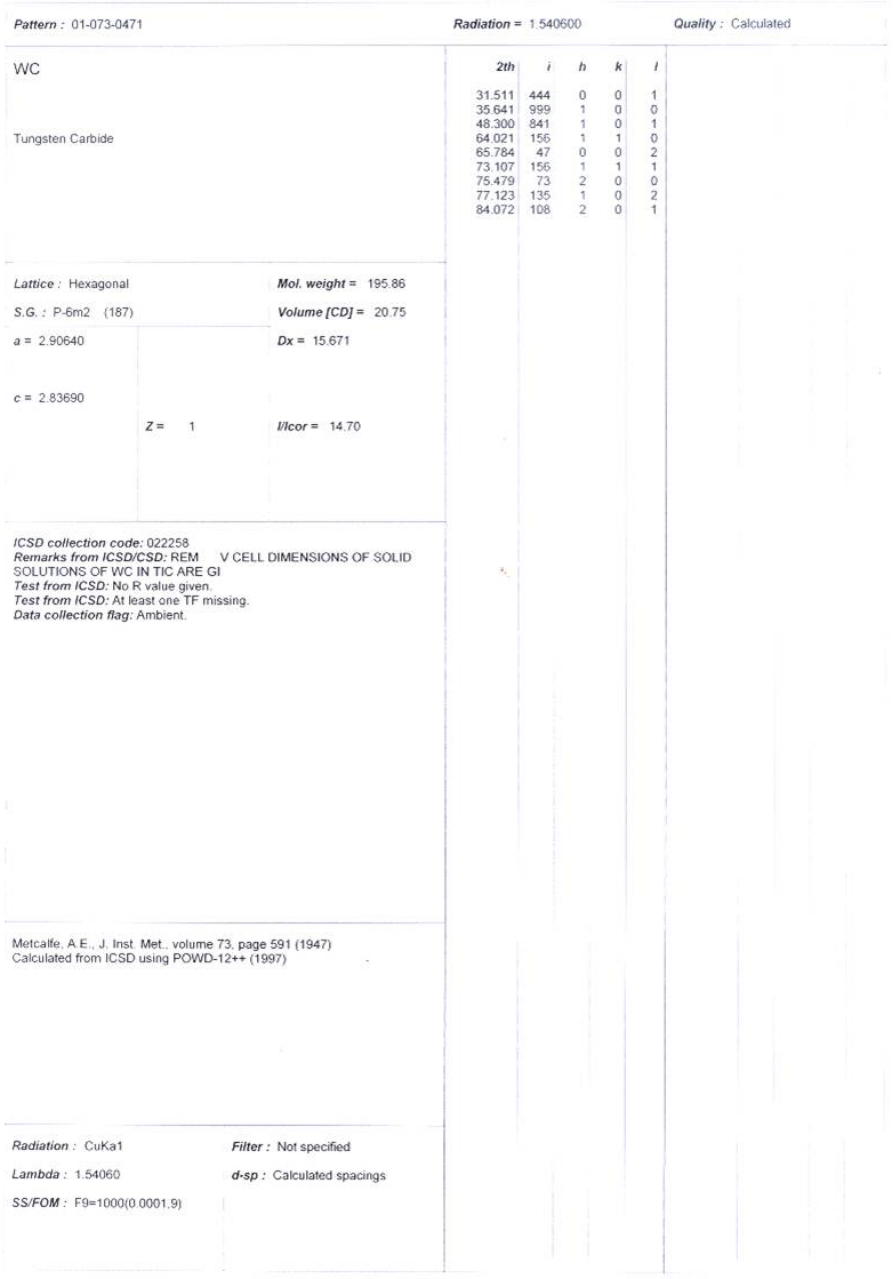

Pattern : 01-073-0471 **Radiation =** 1.540600 **Quality :** Calculated

WC

Tungsten Carbide

2th	i	h	k	l
31.511	444	0	0	1
35.641	999	1	0	0
48.300	841	1	0	1
64.021	156	1	1	0
65.784	47	0	0	2
73.107	156	1	1	1
75.479	73	2	0	0
77.123	135	1	0	2
84.072	108	2	0	1

Lattice : Hexagonal **Mol. weight =** 195.86

S.G. : P-6m2 (187) **Volume [CD] =** 20.75

a = 2.90640 **Dx =** 15.671

c = 2.83690

Z = 1 **I/Icor =** 14.70

ICSD collection code: 022258
Remarks from ICSD/CSD: REM V CELL DIMENSIONS OF SOLID SOLUTIONS OF WC IN TIC ARE GI
Test from ICSD: No R value given.
Test from ICSD: At least one TF missing.
Data collection flag: Ambient.

Metcalfe, A.E., J. Inst. Met., volume 73, page 591 (1947)
Calculated from ICSD using POWD-12++ (1997)

Radiation : CuKa1 **Filter :** Not specified

Lambda : 1.54060 **d-sp :** Calculated spacings

SS/FOM : F9=1000(0.0001,9)

FIGURE B.2: ICDD Pattern information for WC.

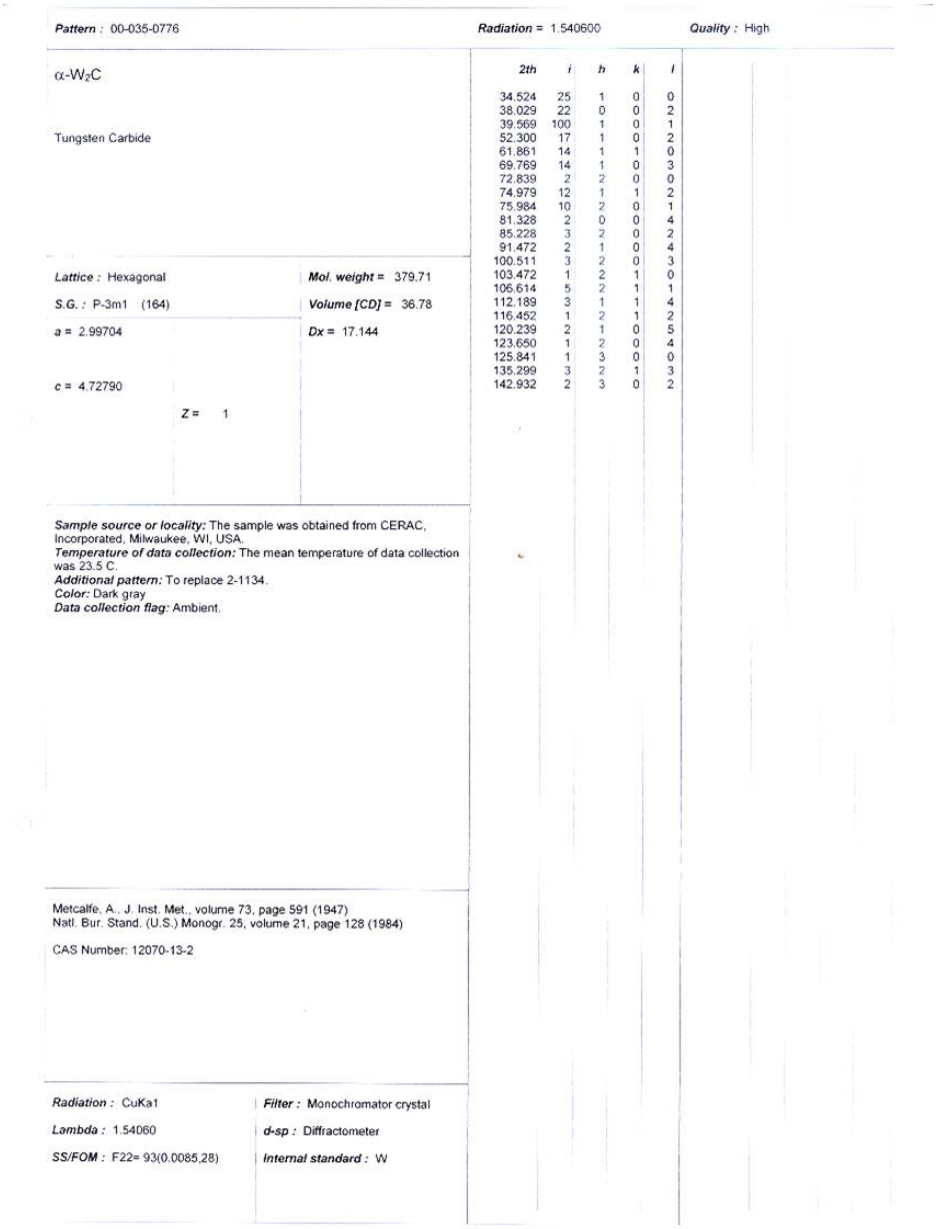

Pattern : 00-035-0776 **Radiation =** 1.540600 **Quality :** High

α-W_2C

Tungsten Carbide

Lattice : Hexagonal ***Mol. weight =*** 379.71

S.G. : P-3m1 (164) ***Volume [CD] =*** 36.78

a = 2.99704 ***Dx =*** 17.144

c = 4.72790

Z = 1

Sample source or locality: The sample was obtained from CERAC, Incorporated, Milwaukee, WI, USA.
Temperature of data collection: The mean temperature of data collection was 23.5 C.
Additional pattern: To replace 2-1134.
Color: Dark gray
Data collection flag: Ambient.

Metcalfe, A., J. Inst. Met., volume 73, page 591 (1947)
Natl. Bur. Stand. (U.S.) Monogr. 25, volume 21, page 128 (1984)

CAS Number: 12070-13-2

Radiation : CuKa1 ***Filter :*** Monochromator crystal

Lambda : 1.54060 ***d-sp :*** Diffractometer

SS/FOM : F22= 93(0.0085,28) ***Internal standard :*** W

2th	i	h	k	l
34.524	25	1	0	0
38.029	22	0	0	2
39.569	100	1	0	1
52.300	17	1	0	2
61.861	14	1	1	0
69.769	14	1	0	3
72.839	2	2	0	0
74.979	12	1	1	2
75.984	10	2	0	1
81.328	2	0	0	4
85.228	3	2	0	2
91.472	2	1	0	4
100.511	3	2	0	3
103.472	1	2	1	0
106.614	5	2	1	1
112.189	3	1	1	4
116.452	1	2	1	2
120.239	2	1	0	5
123.650	1	2	0	4
125.841	1	3	0	0
135.299	3	2	1	3
142.932	2	3	0	2

FIGURE B.3: ICDD Pattern information for W_2C.

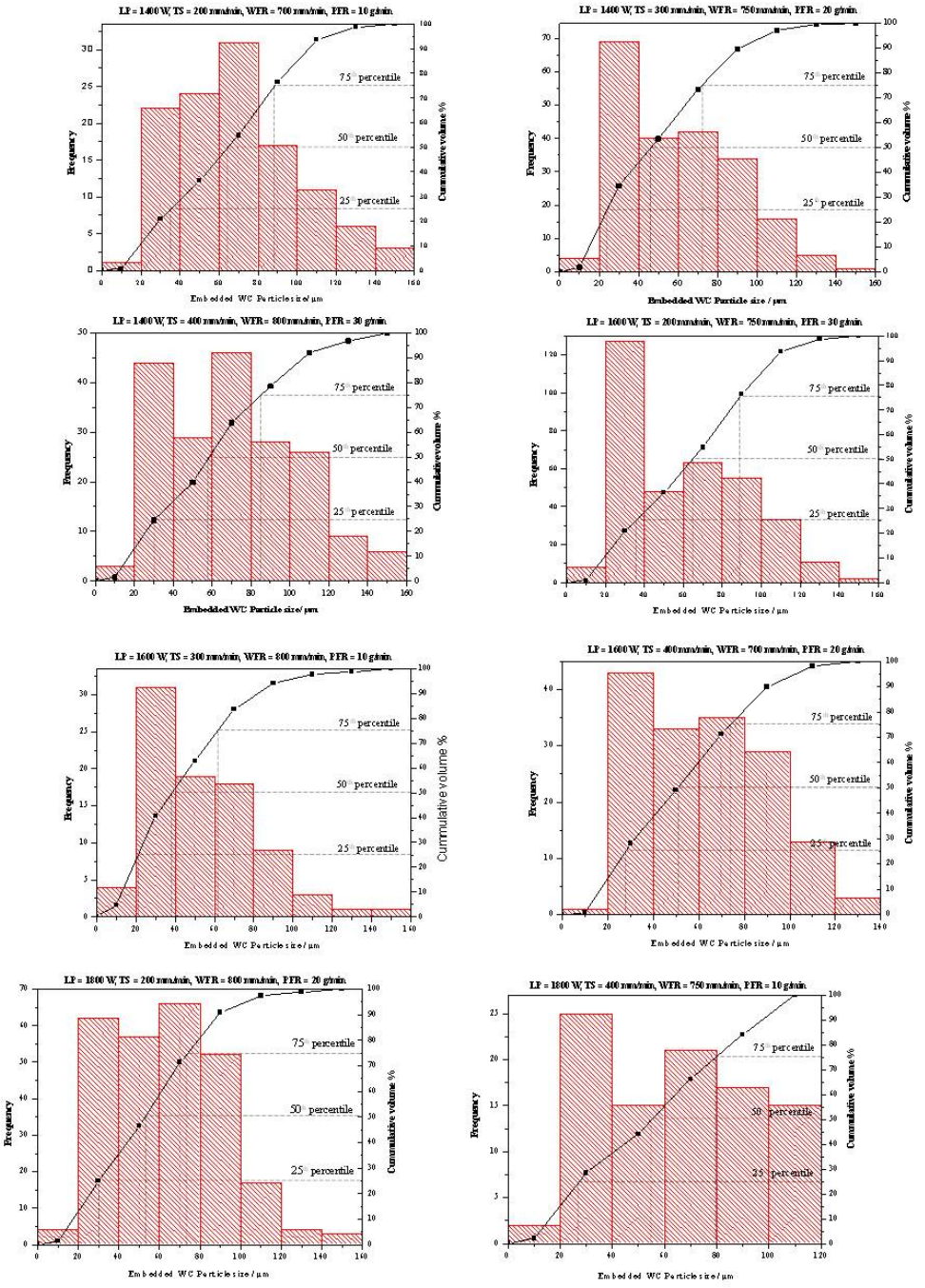

FIGURE B.4: Analysis of the embedded Spherotene particle size in beads.

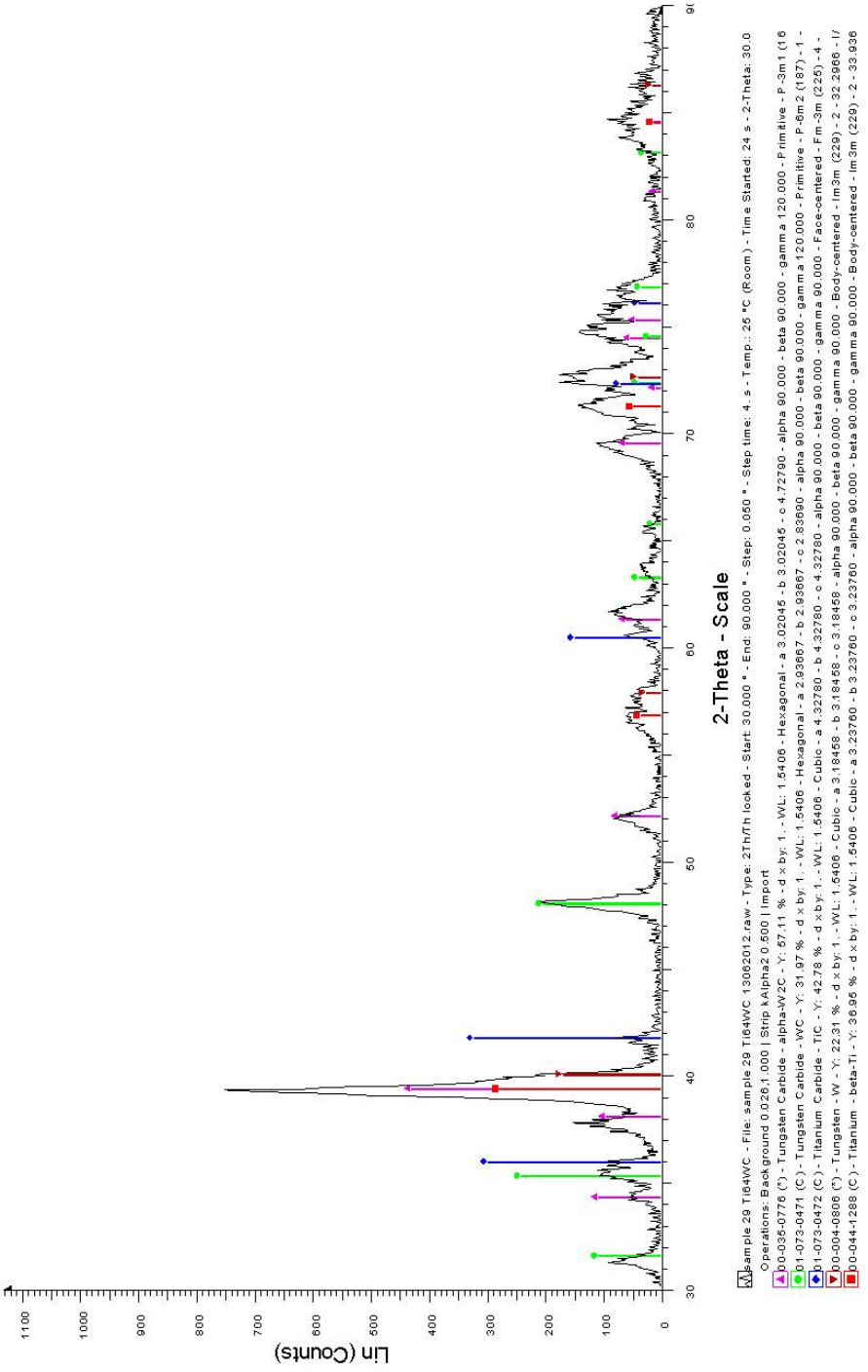

FIGURE B.5: ICDD phase patterns matching the XRD spectrum for the Ti-6Al-4V/Spherotene composite bead.

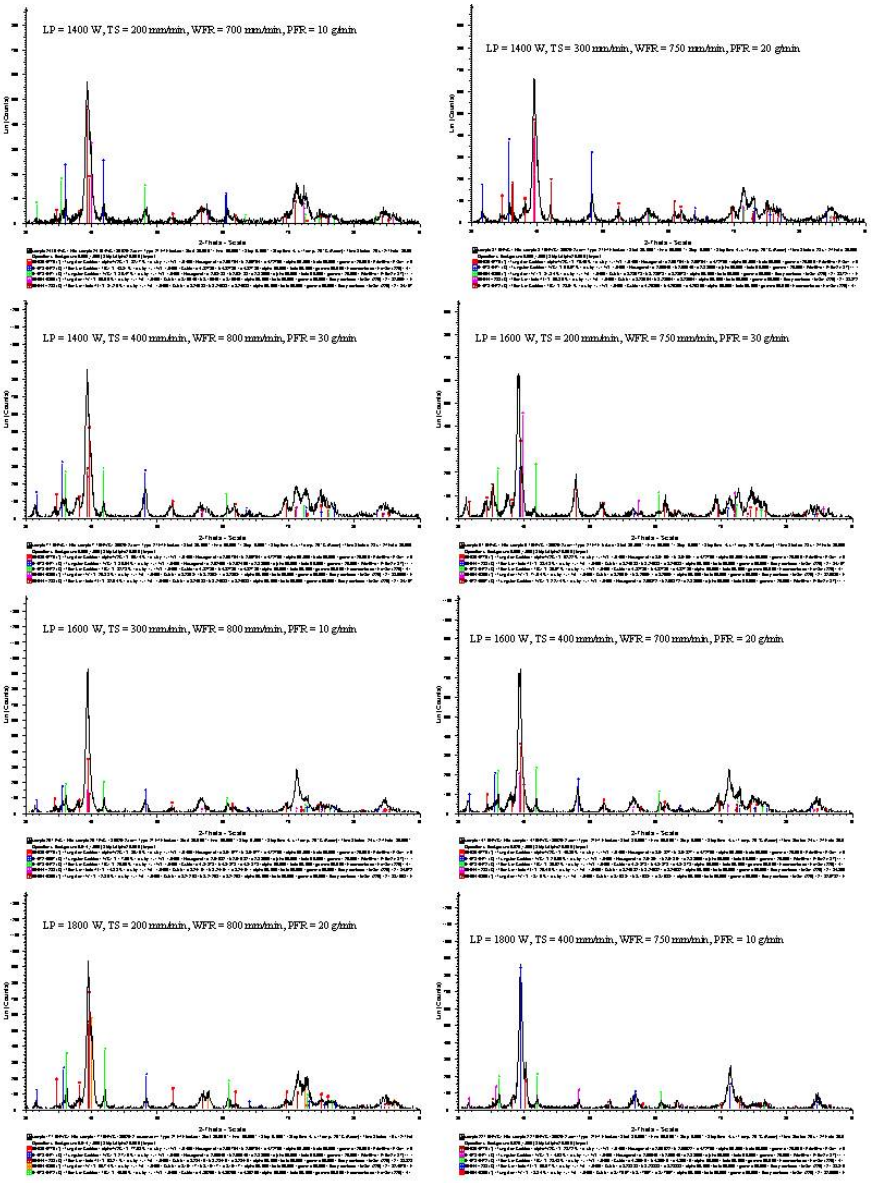

FIGURE B.6: XRD spectrum for Ti-6Al-4V/Spherotene composites.

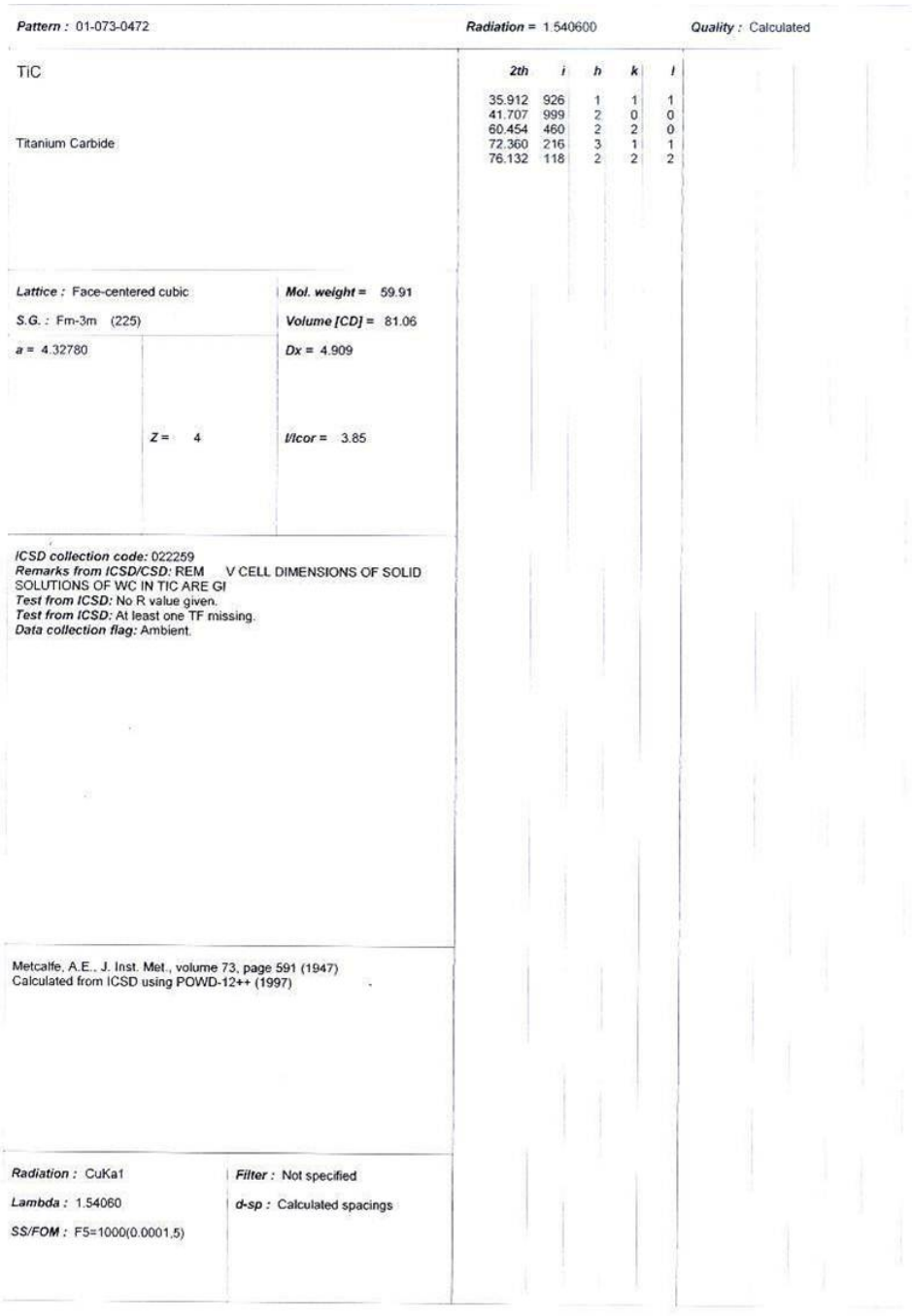

Pattern : 01-073-0472 **Radiation =** 1.540600 **Quality :** Calculated

TiC

Titanium Carbide

2th	i	h	k	l
35.912	926	1	1	1
41.707	999	2	0	0
60.454	460	2	2	0
72.360	216	3	1	1
76.132	118	2	2	2

Lattice : Face-centered cubic
S.G. : Fm-3m (225)
a = 4.32780
Z = 4
Mol. weight = 59.91
Volume [CD] = 81.06
Dx = 4.909
I/Icor = 3.85

ICSD collection code: 022259
Remarks from ICSD/CSD: REM V CELL DIMENSIONS OF SOLID SOLUTIONS OF WC IN TIC ARE GI
Test from ICSD: No R value given.
Test from ICSD: At least one TF missing.
Data collection flag: Ambient.

Metcalfe, A.E., J. Inst. Met., volume 73, page 591 (1947)
Calculated from ICSD using POWD-12++ (1997)

Radiation : CuKa1
Lambda : 1.54060
SS/FOM : F5=1000(0.0001,5)
Filter : Not specified
d-sp : Calculated spacings

FIGURE B.7: ICDD file for TiC phase.

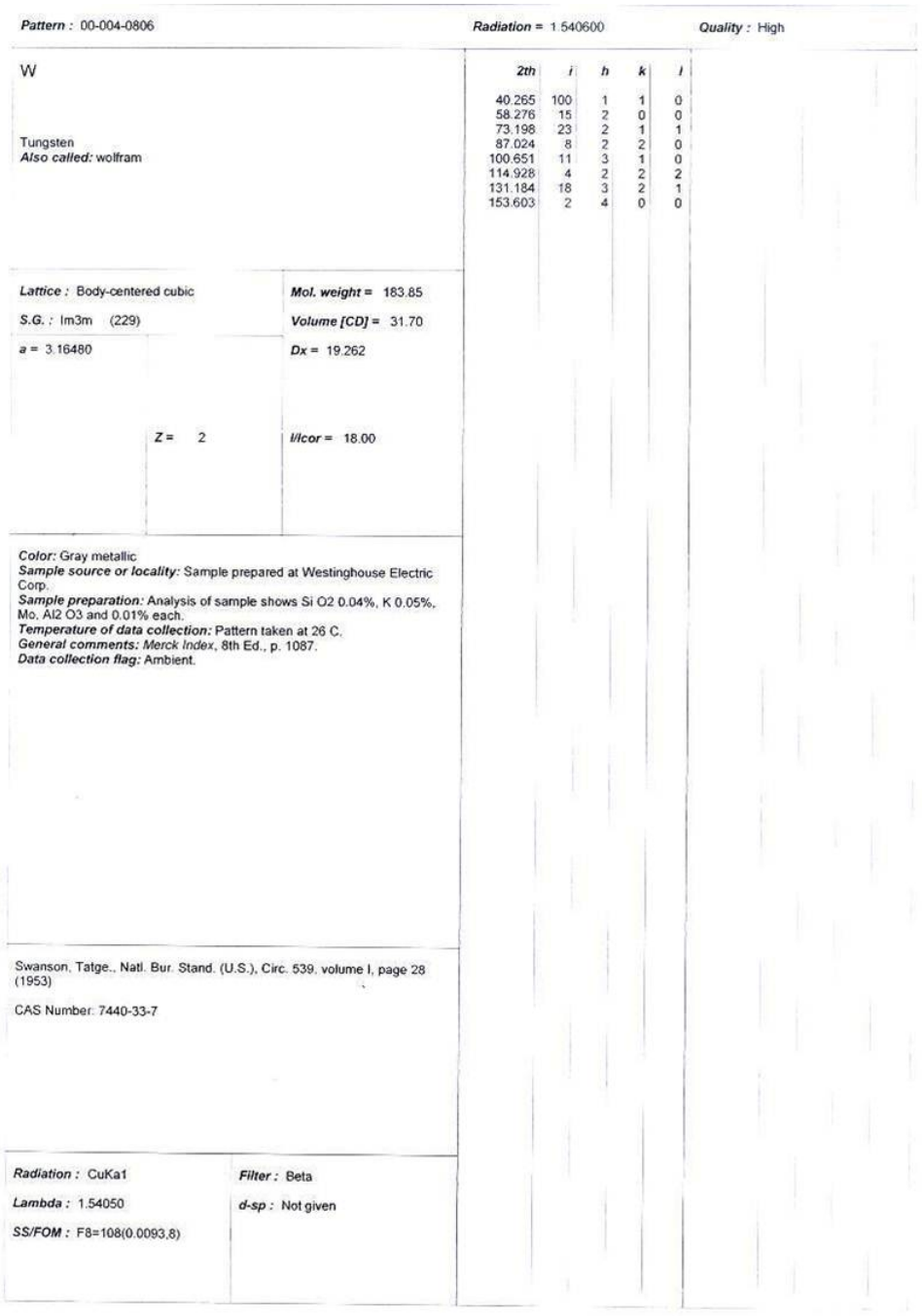

Pattern : 00-004-0806 **Radiation =** 1.540600 **Quality :** High

W

Tungsten
Also called: wolfram

2th	i	h	k	l
40.265	100	1	1	0
58.276	15	2	0	0
73.198	23	2	1	1
87.024	8	2	2	0
100.651	11	3	1	0
114.928	4	2	2	2
131.184	18	3	2	1
153.603	2	4	0	0

Lattice : Body-centered cubic
S.G. : Im3m (229)
a = 3.16480
Z = 2
Mol. weight = 183.85
Volume [CD] = 31.70
Dx = 19.262
I/Icor = 18.00

Color: Gray metallic
Sample source or locality: Sample prepared at Westinghouse Electric Corp.
Sample preparation: Analysis of sample shows Si O2 0.04%, K 0.05%, Mo, Al2 O3 and 0.01% each.
Temperature of data collection: Pattern taken at 26 C.
General comments: *Merck Index*, 8th Ed., p. 1087.
Data collection flag: Ambient.

Swanson, Tatge., Natl. Bur. Stand. (U.S.), Circ. 539, volume I, page 28 (1953)

CAS Number: 7440-33-7

Radiation : CuKa1
Lambda : 1.54050
SS/FOM : F8=108(0.0093,8)
Filter : Beta
d-sp : Not given

FIGURE B.8: ICDD file for W phase.

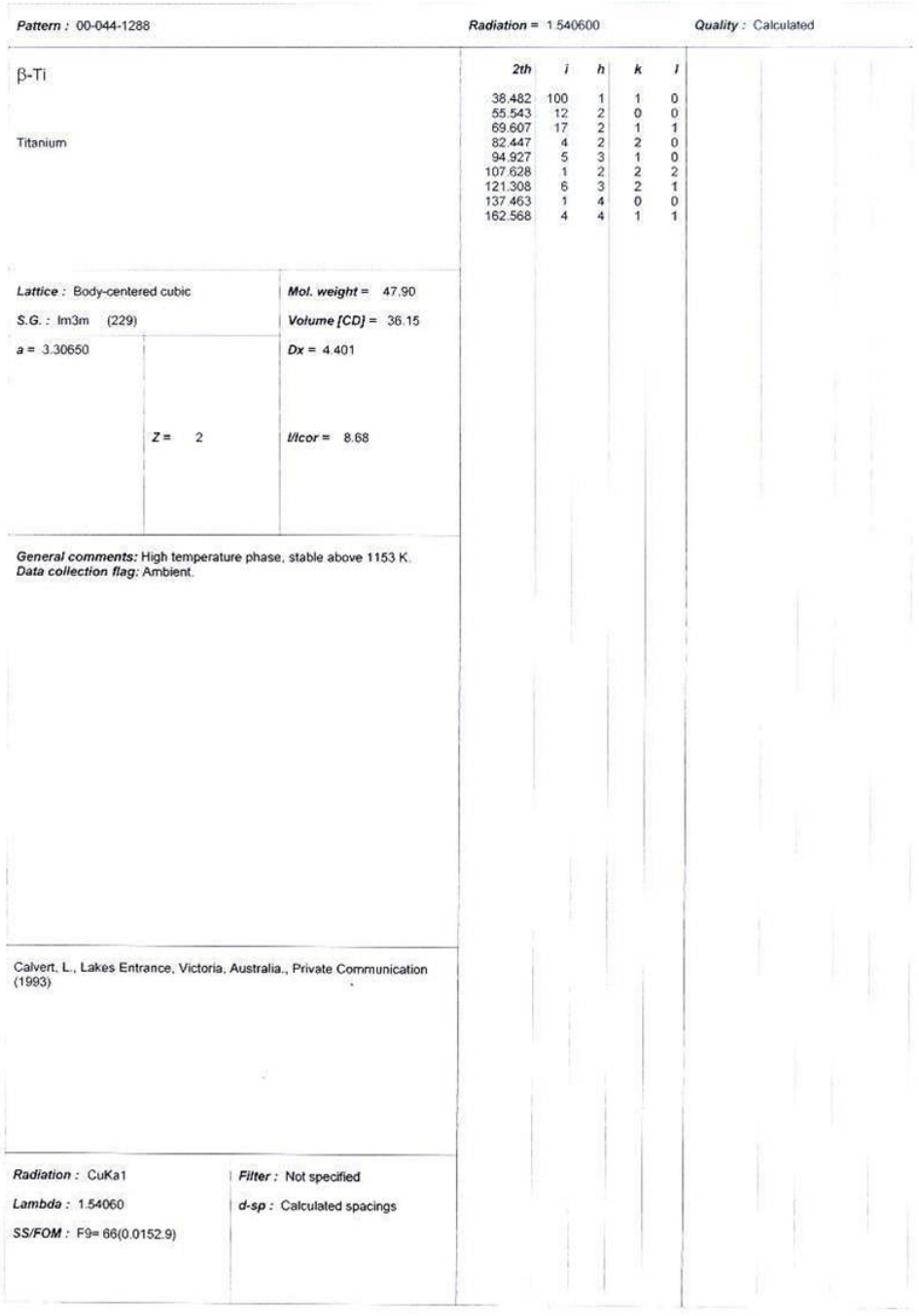

Pattern : 00-044-1288 **Radiation =** 1.540600 **Quality :** Calculated

β-Ti

Titanium

2th	i	h	k	l
38.482	100	1	1	0
55.543	12	2	0	0
69.607	17	2	1	1
82.447	4	2	2	0
94.927	5	3	1	0
107.628	1	2	2	2
121.308	6	3	2	1
137.463	1	4	0	0
162.568	4	4	1	1

Lattice : Body-centered cubic
S.G. : Im3m (229)
a = 3.30650
Z = 2
Mol. weight = 47.90
Volume [CD] = 36.15
Dx = 4.401
I/Icor = 8.68

General comments: High temperature phase, stable above 1153 K.
Data collection flag: Ambient.

Calvert, L., Lakes Entrance, Victoria, Australia., Private Communication (1993)

Radiation : CuKa1
Lambda : 1.54060
SS/FOM : F9= 66(0.0152,9)
Filter : Not specified
d-sp : Calculated spacings

FIGURE B.9: ICDD file for β-Ti phase.

TABLE B.5: Mean value of W (at%) in β-Ti with standard error

Laser Power (W)	Traverse Speed (mm/min)	Powder feed rate (g/min)	Mean W (at. %)	Standard Error
1400	200	10	9.1	0.48
1400	300	20	8.9	1.07
1400	400	30	8.9	0.78
1600	200	30	8.7	0.64
1600	300	10	8.2	0.66
1600	400	20	8.7	0.56
1800	200	20	8.5	0.51
1800	300	30	8.1	0.44
1800	400	10	7.5	0.33

TABLE B.6: Heat Affected Zone depth and Melt pool depth into the substrate

Laser Power (W)	Traverse Speed (mm/min)	Powder feed rate (g/min)	Wire feed rate (mm/min)	HAZ (mm)	Melt depth (µm)
1400	200	10	700	1.6	165
1400	300	20	750	1.32	235
1400	400	30	800	1.18	188
1600	200	30	750	1.76	424
1600	300	10	800	1.37	188
1600	400	20	700	1.27	329
1800	200	20	800	2.02	517
1800	300	30	700	1.41	517
1800	400	10	750	1.27	282

Appendix C

Ti-6Al-4V/TiB_2 composites

TABLE C.1: An L-9 orthogonal arrays for preliminary TiB_2/Ti-6Al-4V deposition trials

Treatment no.	Laser power (W)	Traverse speed (mm/min)
1	600	400
2	600	500
3	600	600
4	800	400
5	800	500
6	800	600
7	1000	400
8	1000	500
9	1000	600

TABLE C.2: An L-9 orthogonal arrays for main cladding experiment of the modified TiB_2/Ti-6Al-4V

Treatment	Laser Power (W)	Traverse speed (mm/min)	Powder Feed Rate (g/min)
T-1	1400	200	10
T-2	1400	300	10
T-3	1400	400	10
T-4	1600	200	10
T-5	1600	300	10
T-6	1600	400	10
T-7	1800	200	10
T-8	1800	300	10
T-9	1800	400	10

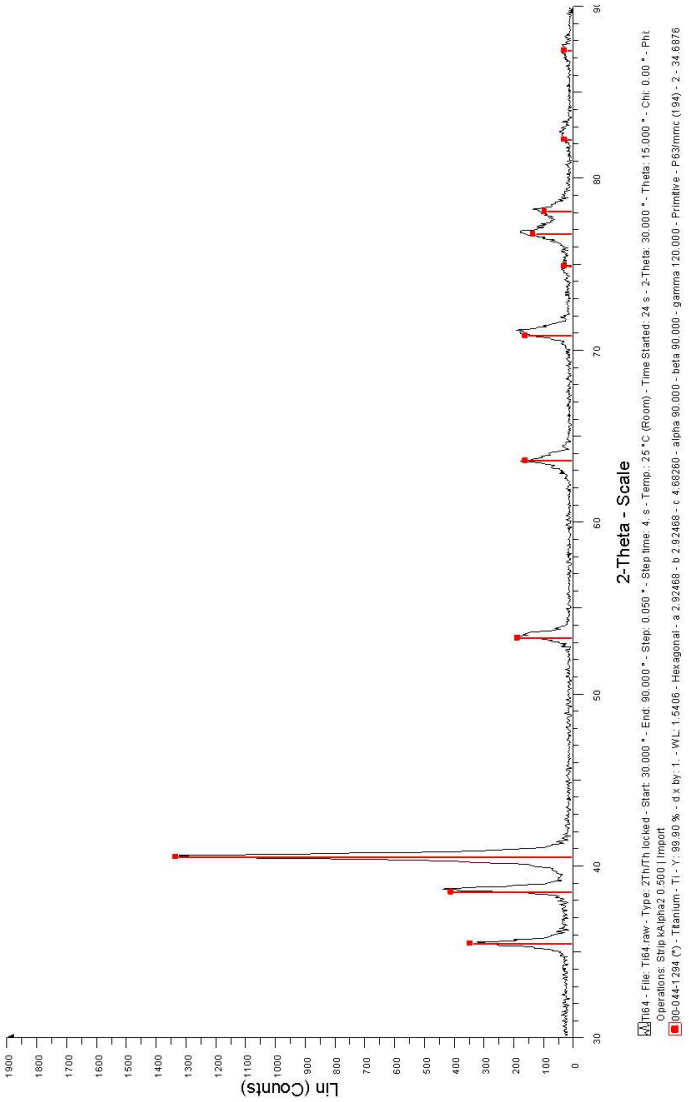

FIGURE C.1: ICDD pattern of αTi phase matching the experimental XRD peaks for the powder.

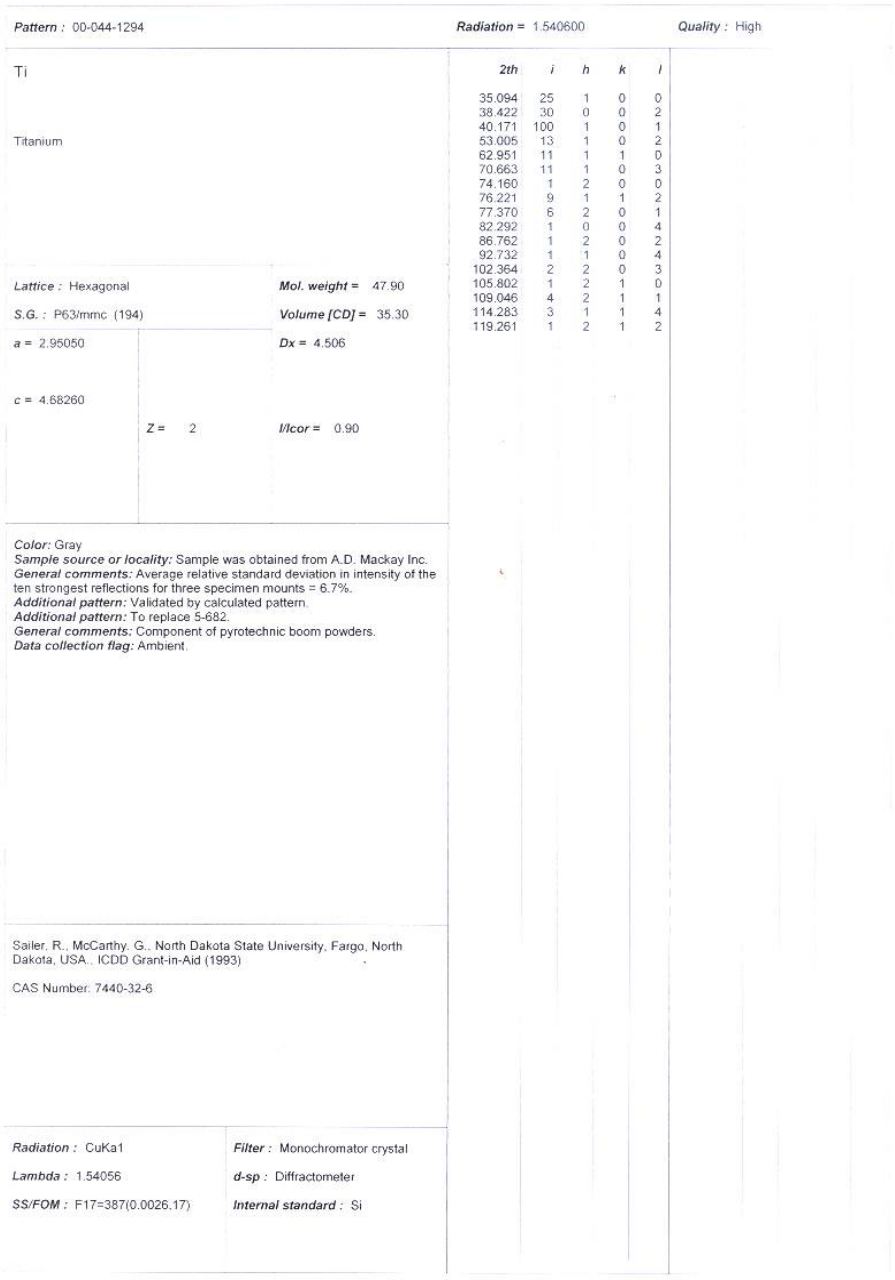

Pattern : 00-044-1294 Radiation = 1.540600 Quality : High

Ti

Titanium

Lattice : Hexagonal
S.G. : P63/mmc (194)
a = 2.95050
c = 4.68260
Z = 2
Mol. weight = 47.90
Volume [CD] = 35.30
Dx = 4.506
I/Icor = 0.90

2th	i	h	k	l
35.094	25	1	0	0
38.422	30	0	0	2
40.171	100	1	0	1
53.005	13	1	0	2
62.951	11	1	1	0
70.663	11	1	0	3
74.160	1	2	0	0
76.221	9	1	1	2
77.370	6	2	0	1
82.292	1	0	0	4
86.762	1	2	0	2
92.732	1	1	0	4
102.364	2	2	0	3
105.802	1	2	1	0
109.046	4	2	1	1
114.283	3	1	1	4
119.261	1	2	1	2

Color: Gray
Sample source or locality: Sample was obtained from A.D. Mackay Inc.
General comments: Average relative standard deviation in intensity of the ten strongest reflections for three specimen mounts = 6.7%.
Additional pattern: Validated by calculated pattern.
Additional pattern: To replace 5-682.
General comments: Component of pyrotechnic boom powders.
Data collection flag: Ambient.

Sailer, R., McCarthy, G., North Dakota State University, Fargo, North Dakota, USA., ICDD Grant-in-Aid (1993)

CAS Number: 7440-32-6

Radiation : CuKa1
Lambda : 1.54056
SS/FOM : F17=387(0.0026,17)
Filter : Monochromator crystal
d-sp : Diffractometer
Internal standard : Si

FIGURE C.2: ICDD pattern file for αTi phase.

TABLE C.3: Means and Standard errors Ti-6Al-4V/TiB_2 bead height and width

Laser Power (W)	Traverse speed (mm/min)	Powder Feed Rate (g/min)	Mean Height (mm)	Standard Error Height	Mean Width (mm)	Standard Error Width
1400	200	10	1.53	0.03	4.47	0.03
1400	300	10	0.97	0.01	4.11	0.06
1400	400	10	0.66	0.01	3.95	0.01
1600	200	10	0.98	0.04	5.16	0.04
1600	300	10	0.72	0.02	4.55	0.02
1600	400	10	0.68	0.02	4.2	0.03
1800	200	10	1.68	0.03	5.4	0.05
1800	300	10	1.09	0.02	4.81	0.09
1800	400	10	0.87	0.04	4.45	0.06

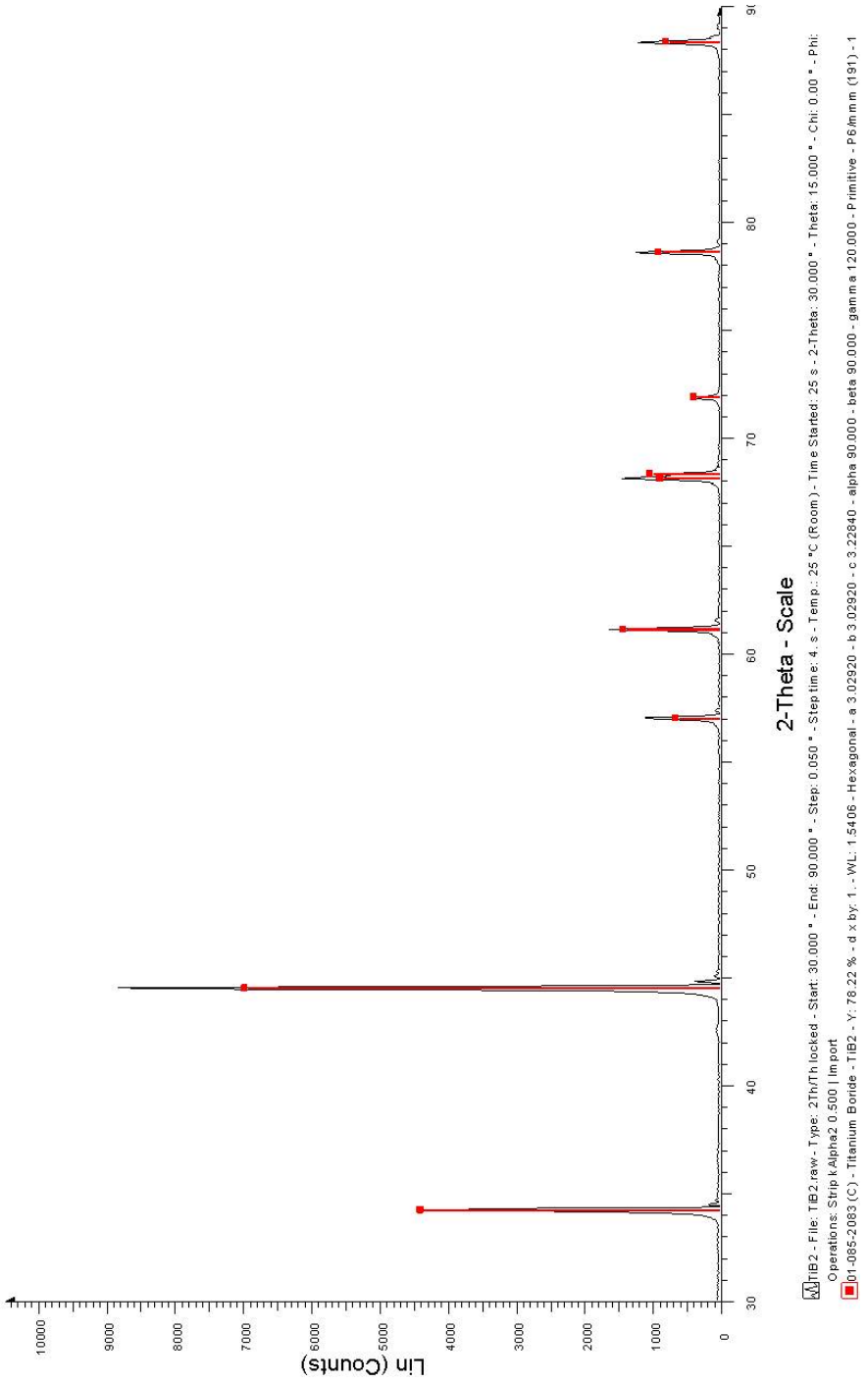

FIGURE C.3: ICDD Pattern for TiB_2 matching peaks in the experimental XRD spectrum.

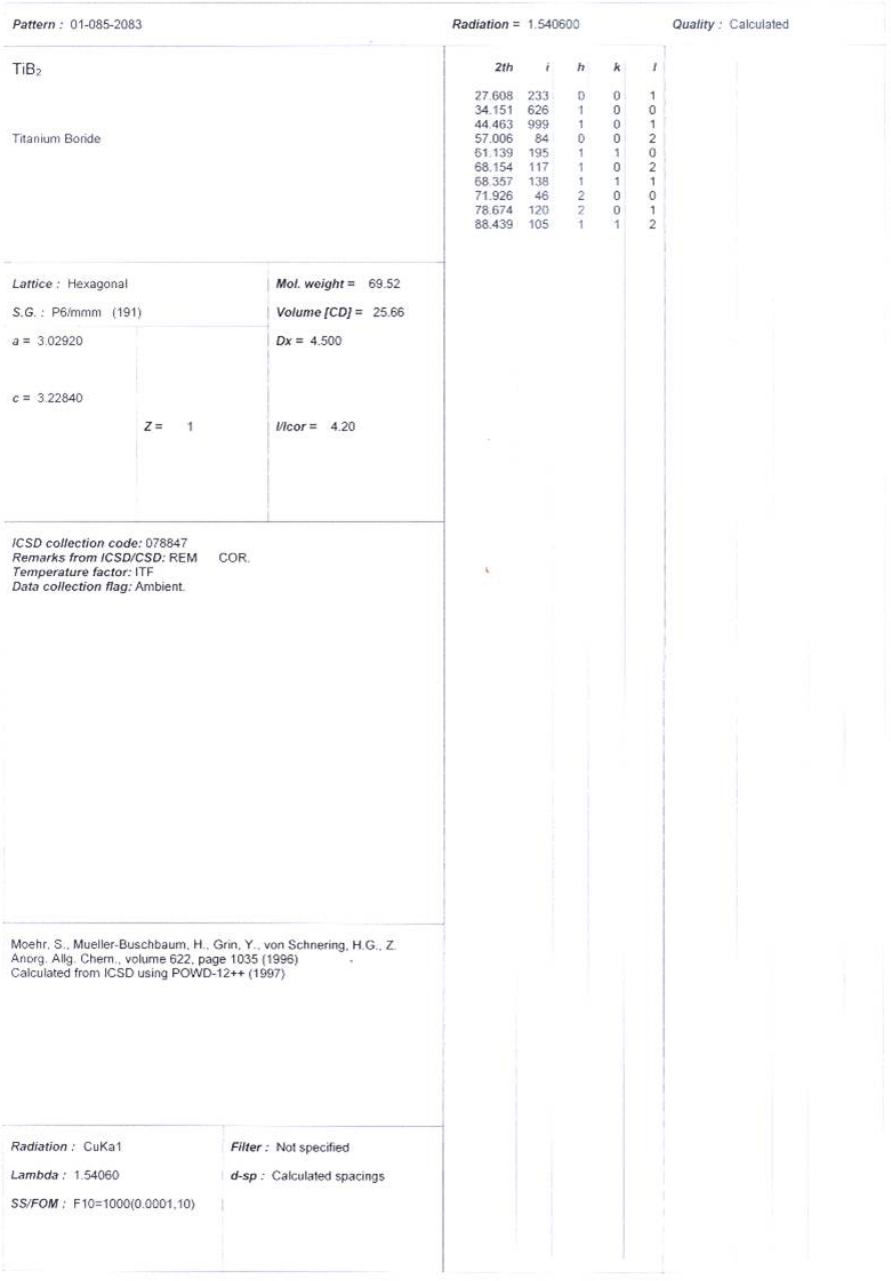

Pattern : 01-085-2083 **Radiation =** 1.540600 **Quality :** Calculated

TiB_2

Titanium Boride

2th	i	h	k	l
27.608	233	0	0	1
34.151	626	1	0	0
44.463	999	1	0	1
57.006	84	0	0	2
61.139	195	1	1	0
68.154	117	1	0	2
68.357	138	1	1	1
71.926	46	2	0	0
78.674	120	2	0	1
88.439	105	1	1	2

Lattice : Hexagonal
S.G. : P6/mmm (191)
a = 3.02920
c = 3.22840
Z = 1
Mol. weight = 69.52
Volume [CD] = 25.66
Dx = 4.500
I/Icor = 4.20

ICSD collection code: 078847
Remarks from ICSD/CSD: REM COR.
Temperature factor: ITF
Data collection flag: Ambient.

Moehr, S., Mueller-Buschbaum, H., Grin, Y., von Schnering, H.G., Z. Anorg. Allg. Chem., volume 622, page 1035 (1996)
Calculated from ICSD using POWD-12++ (1997)

Radiation : CuKa1
Lambda : 1.54060
SS/FOM : F10=1000(0.0001,10)
Filter : Not specified
d-sp : Calculated spacings

FIGURE C.4: ICDD Pattern information for TiB_2.

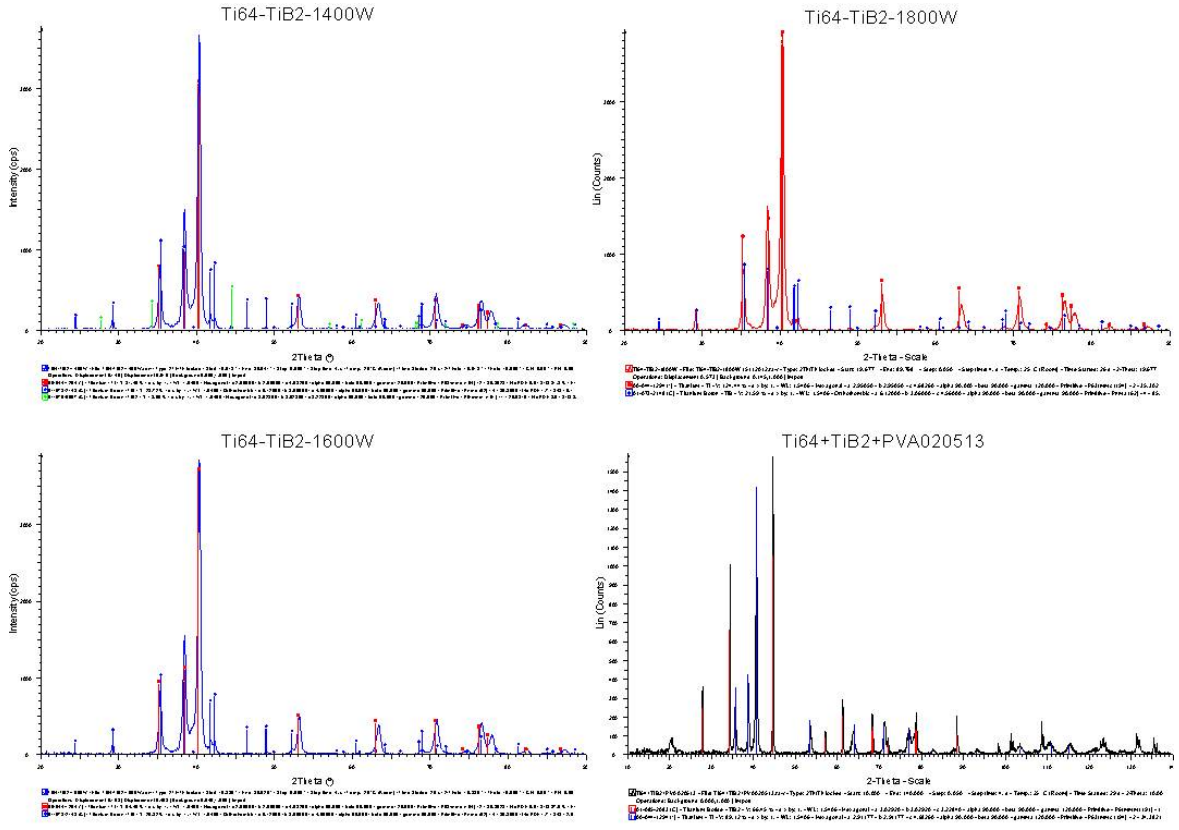

FIGURE C.5: ICDD Pattern information for TiB_2.

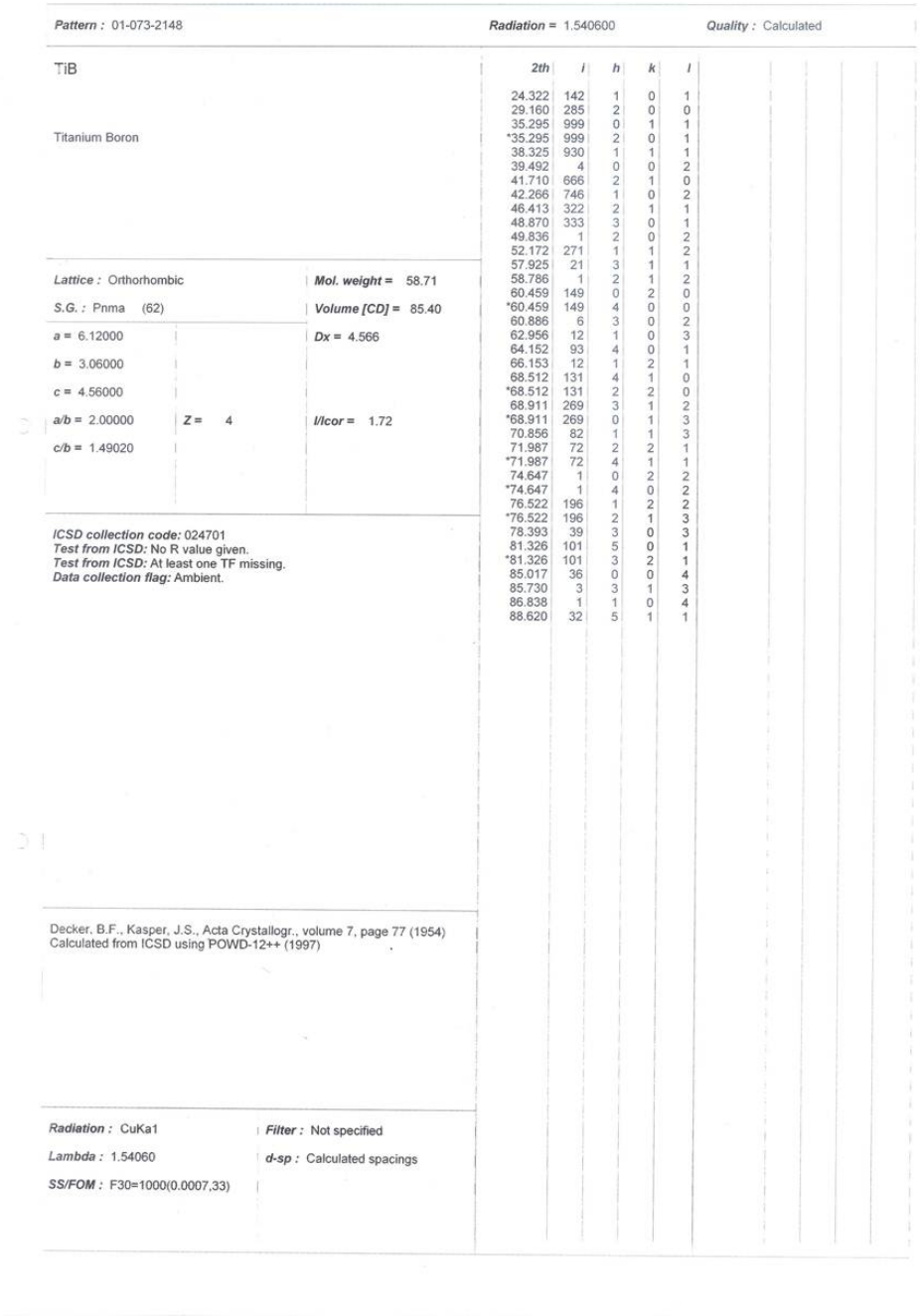

Pattern : 01-073-2148 **Radiation =** 1.540600 **Quality :** Calculated

TiB

Titanium Boron

Lattice : Orthorhombic **Mol. weight =** 58.71

S.G. : Pnma (62) **Volume [CD] =** 85.40

a = 6.12000 **Dx =** 4.566

b = 3.06000

c = 4.56000

a/b = 2.00000 **Z =** 4 **I/Icor =** 1.72

c/b = 1.49020

ICSD collection code: 024701
Test from ICSD: No R value given.
Test from ICSD: At least one TF missing.
Data collection flag: Ambient.

Decker, B.F., Kasper, J.S., Acta Crystallogr., volume 7, page 77 (1954)
Calculated from ICSD using POWD-12++ (1997)

Radiation : CuKa1 **Filter :** Not specified

Lambda : 1.54060 **d-sp :** Calculated spacings

SS/FOM : F30=1000(0.0007,33)

2th	i	h	k	l
24.322	142	1	0	1
29.160	285	2	0	0
35.295	999	0	1	1
*35.295	999	2	0	1
38.325	930	1	1	1
39.492	4	0	0	2
41.710	666	2	1	0
42.266	746	1	0	2
46.413	322	2	1	1
48.870	333	3	0	1
49.836	1	2	0	2
52.172	271	1	1	2
57.925	21	3	1	1
58.786	1	2	1	2
60.459	149	0	2	0
*60.459	149	4	0	0
60.886	6	3	0	2
62.956	12	1	0	3
64.152	93	4	0	1
66.153	12	1	2	1
68.512	131	4	1	0
*68.512	131	2	2	0
68.911	269	3	1	2
*68.911	269	0	1	3
70.856	82	1	1	3
71.987	72	2	2	1
*71.987	72	4	1	1
74.647	1	0	2	2
*74.647	1	4	0	2
76.522	196	1	2	2
*76.522	196	2	1	3
78.393	39	3	0	3
81.326	101	5	0	1
*81.326	101	3	2	1
85.017	36	0	0	4
85.730	3	3	1	3
86.838	1	1	0	4
88.620	32	5	1	1

FIGURE C.6: ICDD Pattern information for TiB.

Bibliography

[1] A. Singh and S. P. Harimkar. *Laser Surface Engineering of Magnesium Alloys: A Review. JOM Journal of the Minerals, Metals and Materials Society*, 64(6): 716–733, 2012.

[2] S.V. Joshi and G. Sundararajan. *Lasers for Metallic and Intermetallic Coatings.* ASM International, Materials Park, OH, 1998.

[3] J.C. Ion. *Laser Processing of Engineering Materials, Principle, Procedure and Industrial Application.* Elsevier Butterworth Heinemann, Linacre House,Jordan Hill, Oxford, UK, 2005.

[4] W. M. Steen. *Laser Material Processing.* Springer-Verlag, London, 3rd edition, 2003.

[5] I. Palcic, M. Balazic, M. Milfelner, and B. Buchmeister. *Potential of Laser Engineered Net Shaping (LENS) Technology. Materials and Manufacturing Processes*, 24(7-8):750–753, 2009.

[6] T.H. Maiman. *Stimulated Optical Raidation in Ruby. Nature*, 187(4736):493–494, 1960.

[7] T.H. Maiman, R.H. Hoskins, I.J. D'Haenens, C.K. Asawa, and V. Evtuhov. *Stimulated Optical Emission in Fluorescent Solids. II. Spectroscopy and Stimulated Emission in Ruby. Physical Review*, 123(4):1151–1157, 1961.

[8] W. M. Steen. Laser material processing - an overview. *Journal of Optics A: Pure and Applied Optics*, 5:3–7, 2003.

[9] T.H. Maiman. Laser applications. *Physics Today*, 20(7):24–28, 1967.

[10] E. Toyserkani, A. Khajepour, and S. Corbin. *Laser Cladding.* CRC Press, Florida, USA, 2005.

[11] E. Kannatey-Asibu. *Principles of Laser Materials Processing.* John Wiley and Sons, Incorporation, Hoboken, New Jersey, 2009.

[12] A. Heralic, A. Christiansson, M. Ottosson, and B. Lennartson. Increased stability in laser metal wire deposition through feedback from optical measurements. *Optics and Lasers in Engineering*, 48(4):478–485, 2010.

[13] R. Banerjee, P. C. Collins, A. Gen, and H. L. Fraser. Direct laser deposition of in situ *Ti-6Al-4V - TiB* composites. *Materials Science and Engineering A*, 358(1-2): 343–349, 2003.

[14] F. Wang, J. Mei, H. Jiang, and X. Wu. Laser fabrication of *Ti-6Al-4V/TiC* composites using simultaneous powder and wire feed. *Materials Science and Engineering: A*, 445-446:461–466, 2007.

[15] F. Wang, J. Mei, and X. Wu. Microstructure study of direct laser fabricated *Ti* alloys using powder and wire. *Applied Surface Science*, 253(3):1424–1430, 2006.

[16] K. Zhang, W. Liu, and X. Shang. Research on the processing experiments of laser metal deposition shaping. *Optics and Laser Technology*, 39(3):549–557, 2007.

[17] S. H. Mok, G. Bi, J. Folkes, and I. Pashby. *Deposition of Ti-6Al-4V using a high power diode laser and wire, Part I: Investigation on the process characteristics. Surface and Coatings Technology*, 202(16):3933–3939, 2008.

[18] O. Verezub, Z. Kalazi, G. Buza, N.V. Verezub, and G. Kaptay. Classification of laser beam induced surface engineering technologies and in situ synthesis of steel matrix surface nanocomposites, 2009.

[19] J. Mazumder. Laser assisted surface coatings. In Kurt H. Stern, editor, *Metallurgical and Ceramic Protective Coatings*, page 341. Chapman and Hall, London, 1996.

[20] J. H. Abboud, A. F. Fidel, and K. Y. Benyounis. Surface nitriding of *Ti-6Al-4V* alloy with a high power CO_2 *laser. Optics and Laser Technology*, 40(2):405–414, 2008.

[21] B. S. Yilbas, C. Karatas, Uslan, O. Keles, I. Y. Usta, and M. Ahsan. *CO_2 laser gas assisted nitriding of Ti6Al4V alloy. Applied Surface Science*, 252(24):8557–8564, 2006.

[22] J. DuttaMajumdar. *Laser Gas Alloying of Ti-6Al-4V. Physics Procedia*, 12, Part A(0):472–477, 2011.

[23] P. Jiang, X. L. He, X. X. Li, L. G. Yu, and H. M. Wang. Wear resistance of a laser surface alloyed *Ti6Al4V* alloy. *Surface and Coatings Technology*, 130(1):24–28, 2000.

[24] A. F. Saleh, J. H. Abboud, and K. Y. Benyounis. Surface carburizing of *Ti6Al4V* alloy by laser melting. *Optics and Lasers in Engineering*, 48(3):257–267, 2010.

[25] J. Senthil S., K. Subramanian, A. K. Nath, H. Kumar, C. Ramachandra, and S. P. Ravindranathan. *Laser boronising of Ti6Al4V as a result of laser alloying with pre-placed BN. Materials Science and Engineering: A*, 260(12):178–187, 1999.

[26] G. C. Onwubolu, J. P. Davim, C. Oliveira, and A. Cardoso. Prediction of clad angle in laser cladding by powder using response surface methodology and scatter search. *Optics and Laser Technology*, 39(6):1130–1134, 2007.

[27] F. Huang, Z. Jiang, X. Liu, J. Lian, and L. Chen. Microstructure and properties of thin wall by laser cladding forming. *Journal of Materials Processing Technology*, 209(11):4970–4976, 2009.

[28] W. J. Suder and S. W. Williams. Investigation of the effects of basic laser material interaction parameters in laser welding. *Journal of Laser Applications*, 24(3): 032009–1–032009–10, 2012.

[29] Z. Xiong, G. Chen, and X. Zeng. Effects of process variables on interfacial quality of laser cladding on aeroengine blade material *GH*4133. *Journal of Materials Processing Technology*, 209(2):930–936, 2009.

[30] G. Chryssolouris, S. Zannis, K. Tsirbas, and C. Lalas. *An Experimental Investigation of Laser Cladding. CIRP Annals - Manufacturing Technology*, 51(1):145–148, 2002.

[31] W. Hofmeister, M. Griffith, M. Ensz, and J. Smugeresky. *Solidifcation in Direct Metal Deposition by LENS Processing. Journal of Minerals, Metals and Materials Society*, 53(9):30–34, 2001.

[32] W. U. H. Syed, A. J. Pinkerton, Z. Liu, and L. Li. *Single-step laser deposition of functionally graded coating by dual wire-powder' or powder-powder' feeding–A comparative study. Applied Surface Science*, 253(19):7926–7931, 2007.

[33] D. F. de Lange, J. T. Hofman, and J. Meijer. Influence of intensity distribution on meltpool and clad shape for laser cladding, 2005. URL http://doc.utwente.nl/52655/1/Wa0997.pdf.

[34] Y. Xiong, J. E. Smugeresky, and J. M. Schoenung. The influence of working distance on laser deposited *WC-Co*. *Journal of Materials Processing Technology*, 209(10):4935–4941, 2009.

[35] L. Dubourg and L. St-Georges. *Optimization of laser cladding process using taguchi and EM methods for MMC coating production. Journal of Thermal Spray Technology*, 15(4):790–795, 2006.

[36] A. G. M Tellez. *Fibre laser metal deposition with Wire: Parameters study and temperature control, PhD Thesis.* PhD thesis, University of Nottingham, 2010.

[37] W. Hu, J. Kang, and T. Huang. *Effect of Processing Parameters on Thermal Phenomena in Direct Laser Metallic Powder Deposition. Tsinghua Science and Technology*, 14(Supplement 1):154–159, 2009.

[38] S. Kou. *Welding Metallurgy.* John Wiley and Sons Inc., 2003.

[39] W. U. H. Syed and L. Li. Effects of wire feeding direction and location in multiple layer diode laser direct metal deposition. *Applied Surface Science*, 248(1-4):518–524, 2005.

[40] U. de Oliveira, V. Ocelk, and J. Th M. De Hosson. Analysis of coaxial laser cladding processing conditions. *Surface and Coatings Technology*, 197(2-3):127–136, 2005.

[41] R. Anandkumar, A. Almeida, R. Vilar, V. Ocelk, and J. Th M. De Hosson. Influence of powder particle injection velocity on the microstructure of *Al-12Si/SiC*$_p$

coatings produced by laser cladding. *Surface and Coatings Technology*, 204(3): 285–290, 2009.

[42] M. Schneider. *Laser Cladding with Powder: Effect of Some Machining Parameters on Clad Properties, PhD Thesis*, March 1998. URL http://doc.utwente.nl/32040/1/t0000007.pdf.

[43] H. Lee. *Effects of the cladding parameters on the deposition efficiency in pulsed Nd:YAG laser cladding. Journal of Materials Processing Technology*, 202(1-3): 321–327, 2008.

[44] E. Brandl, B. Baufeld, C. Leyens, and R. Gault. Additive manufactured *Ti-6Al-4V* using welding wire: comparison of laser and arc beam deposition and evaluation with respect to aerospace material specifications. *Physics Procedia*, 5(Part 2): 595–606, 2010.

[45] M. Alimardani, E. Toyserkani, J. P. Huissoon, and C. P. Paul. On the delamination and crack formation in a thin wall fabricated using laser solid freeform fabrication process: An experimental-numerical investigation. *Optics and Lasers in Engineering*, 47(11):1160–1168, 2009.

[46] J. A. Vreeling, V. Ocelk, Y. T. Pei, D. T. L. van Agterveld, and J. Th M. De Hosson. Laser melt injection in aluminum alloys: on the role of the oxide skin. *Acta Materialia*, 48(17):4225–4233, 2000.

[47] M.J. Donachie. *Titanium: A Technical Guide*. ASM International, Materials Park, OH 44073-0002, USA, 2000.

[48] D. Kopeliovich. Metal crystal structure, 2012. URL http://www.substech.com/dokuwiki/doku.php?id=metals_crystal_structure.

[49] Azom. *Titanium Alloys - Ti6Al4V Grade 5*, 2002. URL http://www.azom.com/Details.asp?ArticleID=1547.

[50] Aerospace Specification Metals. *Titanium Ti-6Al-4V (Grade 5), Annealed*, 2012. URL http://asm.matweb.com/search/SpecificMaterial.asp?bassnum=MTP641.

[51] R. R. Boyer. An overview on the use of titanium in the aerospace industry. *Materials Science and Engineering: A*, 213(1-2):103–114, 1996.

[52] Y. Oshida. *Bioscience and Bioengineering of Titanium Materials*. Elsevier, The Boulevard Langford Lane, Kidlington, Oxford, UK, 2007.

[53] J. M. Amado, M. J. Tobar, J. C. Alvarez, J. Lamas, and A. Yez. *Laser cladding of tungsten carbides (Spherotene) hardfacing alloys for the mining and mineral industry. Applied Surface Science*, 255(10):5553–5556, 2009.

[54] A. Kurlov and A. Gusev. Tungsten carbides and *W-C* phase diagram. *Inorganic Materials*, 42(2):121–127, 2006.

[55] H. Engqvist, S. Ederyd, N. Axn, and S. Hogmark. Grooving wear of single-crystal tungsten carbide. *Wear*, 230(2):165–174, 1999.

[56] J. Li, H. Li, M. Wang, S. Wang, Q. Ji, M. Li, and J. Chi. Applications of *WC*-based composites rapid synthesized by consumable electrode in-situ metallurgy to cutting pick. *International Journal of Refractory Metals and Hard Materials*, 35 (0):132–137, 2012.

[57] B. R. Ross. *Metallic Materials Specification Handbook*. Chapman and Hall, 2-6 Boundary Row, London SE1, 8HN, UK, 4th edition, 1992.

[58] M. D. Demetriou, N. M. Ghoniem, and A. S. Lavine. Kinetic modeling of phase selection during non-equilibrium solidification of a tungsten-carbon system. *Acta Materialia*, 50(6):1421–1432, 2002.

[59] MatWeb. *Tungsten Carbide, WC*, 2012. URL http://www.matweb.com/search/DataSheet.aspx?MatGUID=e68b647b86104478a32012cbbd5ad3ea&ckck=1.

[60] M Jones. *Properties of HVOF sprayed TiC and TiB_2-based cermet coatings, PhD Thesis*. PhD thesis, University of Nottingham, 2001.

[61] D. Vallauri, I. C. Atas Adrin, and A. Chrysanthou. *TiC-TiB_2 composites: A review of phase relationships, processing and properties. Journal of the European Ceramic Society*, 28(8):1697–1713, 2008.

[62] Y. Zhou and Z. Sun. *Crystallographic relations between Ti_3SiC_2 and TiC. Materials Research Innovations*, 3(5):286–291, 2000.

[63] MatWeb. *Titanium Carbide, TiC*, 2012. URL http://www.matweb.com/search/DataSheet.aspx?MatGUID=058d1b70edbd4b2293f298c52bbf9818&ckck=1.

[64] O. Kubaschewski, C. B. Alcock, and P. J. Spencer. *Materials Thermochemistry*, volume 24 of *International Series on Materials Science and Technology*. Pergamon Press, 6th edition, 1993.

[65] B. Haldar, D. Bandyopadhyay, R. Sharma, and N. Chakraborti. *The Ti-W-C (Titanium-Tungsten-Carbon) System. Journal of Phase Equilibria*, 20(3):337–343, 1999.

[66] P. Wanjara, R. A. L. Drew, J. Root, and S. Yue. *Evidence for stable stoichiometric Ti_2C at the interface in TiC particulate reinforced Ti alloy composites. Acta Materialia*, 48(7):1443–1450, 2000.

[67] J. He, W. Wang, Z. Fu, and H. Sun. *Combustion synthesis of TiB_2 Ceramics Powder from B_2O_3-TiO_2-Mg System in Air Atmosphere. Journal of Wuhan University of Technology–Materials Science Edition*, 20(2):90–93, 2005.

[68] R.G. Munro. *Material Properties of Titanium Diboride. Journal of Research of National Institute of Standards and Technology*, 105(5):709–720, 2000.

[69] K. Morsi and V. Patel. Processing and properties of titanium-titanium boride *(TiB_w)* matrix composites-a review. *Journal of Materials Science*, 42(6):2037–2047, 2007.

[70] K. S. Ravichandran, K. B. Panda, and S. S. Sahay. *TiB_w-Reinforced Ti Composites: Processing, Properties, Application Prospects and Research Needs. JOM, Journal of the Minerals, Metals and Materials Society*, 2004.

[71] Calphad. *Titanium - Boron* phase diagram, 2012. URL http://www.calphad.com/titanium-boron.html.

[72] V. Ocelk, D. Matthews, and J. Th M. De Hosson. Sliding wear resistance of metal matrix composite layers prepared by high power laser. *Surface and Coatings Technology*, 197(23):303–315, 2005.

[73] P. Chandrasekar, V. Balusamy, K. S. R. Chandran, and H. Kumar. Laser surface hardening of titaniumtitanium boride *(TiTiB)* metal matrix composite. *Scripta Materialia*, 56(7):641–644, 2007.

[74] J. D. Ayers. Wear behavior of carbide-injected titanium and aluminum alloys. *Wear*, 97(3):249–266, 1984.

[75] J. A. Folkes and K. Shibata. Laser cladding of *Ti-6Al-4V* with various carbide powders. *Journal of Laser Applications*, 6(2):88–94, 1994.

[76] J. A. Vreeling, V. Ocelk, and J. T. M. De Hosson. *Ti6Al4V strengthened by laser melt injection of WC_p particles. Acta Materialia*, 50(19):4913–4924, 2002.

[77] J. Zhang, D. Fan, M. Zheng, Y. Sun, and Y. Zheng. Characterisation of laser cladding *WC-Ti* composite coatings. *Key Engineering Materials*, 368-372:1316–1318, 2008.

[78] Y. Chen, D. Liu, F. Li, and L. Li. *WC_p/Ti-6Al-4V* graded metal matrix composites layer produced by laser melt injection. *Surface and Coatings Technology*, 202(19): 4780–4787, 2008.

[79] D. Liu, Y. Chen, L. Li, and F. Li. In situ investigation of fracture behavior in monocrystalline *WC_p*-reinforced *Ti-6Al-4V* metal matrix composites produced by laser melt injection. *Scripta Materialia*, 59(1):91–94, 2008.

[80] Y. Chen, D. Liu, L. Li, and F. Li. Microstructure evolution of single crystal *WC_p* reinforced *Ti6Al4V* metal matrix composites produced at different cooling rates. *Journal of Alloys and Compounds*, 484(12):108–112, 2009.

[81] N.K. Tolochko, T. Laoui, Y.V. Khlopkov, S.E. Mozzharov, V.I. Titov, and M.B. Ignatiev. Absorptance of powder materials suitable for laser sintering. *Rapid Prototyping*, 6(3):155–160, 2000.

[82] K. Panda and K. Ravi Chandran. *Synthesis of ductile titanium-titanium boride (Ti-TiB) composites with a beta-titanium matrix: The nature of TiB formation and composite properties. Metallurgical and Materials Transactions A*, 34(6):1371–1385, 2003.

[83] P. H. Shipway and K. Gupta. *The potential of WC-Co hardmetals and HVOF sprayed coatings to combat water-droplet erosion. Wear*, 271(910):1418–1425, 2011.

[84] B. J. Kooi, Y. T. Pei, and J. Th M. De Hosson. The evolution of microstructure in a laser clad *TiBTi* composite coating. *Acta Materialia*, 51(3):831–845, 2003.

[85] D. Galvan, V. Ocelk, Y. Pei, B. Kooi, Jeff De Hosson, and E. Ramous. Microstructure and properties of *TiB/Ti-6Al-4V* coatings produced with laser treatments. *Journal of Materials Engineering and Performance*, 13(4):406–412, 2004.

[86] R. Banerjee, A. Gen, D. Hill, P. C. Collins, and H. L. Fraser. Nanoscale *TiB* precipitates in laser deposited *Ti*-matrix composites. *Scripta Materialia*, 53(12): 1433–1437, 2005.

[87] Y. Zhang and J. Li. *Microstructure and Wear Resistance of the Composite Coatings Fabricated on Titanium Alloys by Laser cladding. Advanced Materials Research*, 139-141:398–401, 2010.

[88] J. DuttaMajumdar and L. Li. Development of titanium boride (*TiB*) dispersed titanium (*Ti*) matrix composite by direct laser cladding. *Materials Letters*, 64(9): 1010–1012, 2010.

[89] J. Li, Z. Yu, and H. Wang. Wear behaviors of an *(TiB+TiC)/Ti* composite coating fabricated on *Ti-6Al-4V* by laser cladding. *Thin Solid Films*, 519(15):4804–4808, 2011.

[90] F.C. Ma, P. Liu, W. Li, X.K. Liu, X.H. Chen, and D. Zhang. *Effect of TiB Whiskers Orientation on Mechanical Properties in an In Situ TiB/Ti-1100 Composite. Materials Transactions*, 51(7):1277–1280, 2010.

[91] T. Saito. *The automotive application of discontinuously reinforced TiB-Ti composites. JOM, Journal of the Minerals, Metals and Materials Society*, 56(5):33–36, 2004.

[92] J. E. Field. *ELSI conference: invited lecture: Liquid impact: theory, experiment, applications. Wear*, 233235(0):1–12, 1999.

[93] L. Huang, J. Folkes, P. Kinnell, and P. H. Shipway. Mechanisms of damage initiation in a titanium alloy subjected to water droplet impact during ultra-high pressure plain waterjet erosion. *Journal of Materials Processing Technology*, 212 (9):1906–1915, 2012.

[94] M.C. Leu, P. Meng, E.S. Geskin, and L. Tismeneskiy. Mathematical modeling and experimental verification of stationary waterjet cleaning process. *Journal ofManufacturing Science and Engineering - Transactions of ASME*, 120:571–579, 1998.

[95] W.F. Adler. The mechanics of liquid impact. In C.M. Preece, editor, *Treatise on Materials Science and Technology*, volume 16, pages 127–183. Academic Press Inc. Limited, London, 1979.

[96] A.W. Ruff and S.M. Wiederhorn. *Erosion By Solid Particle Impact.* In C.M. Preece, editor, *Treatise on Materials Science and Technology*, volume 16, pages 69–124. Academic Press Inc. Limited, London, 1979.

[97] V. Ya Karelin, A. I. Denisov, and Y. L. Wu. *Fundamentals of Hydroabrasive Erosion Theory.* In C. G. Duan and V. Y. Karelin, editors, *Abrasive Erosion and Corrosion of Hydraulic Machinery*, volume 2, pages 1–51. Imperical College Press, London WC2H 9HE, 2002.

[98] M. Matsumura and B. E. Chen. Fundamentals of hydroabrasive erosion theory. In C. G. Duan and V. Y. Karelin, editors, *Abrasive Erosion and Corrosion of Hydraulic Machinery*, volume 2, pages 235–312. Imperical College Press, London WC2H 9HE, 2002.

[99] B. S. Mann and V. Arya. An experimental study to corelate water jet impingement erosion resistance and properties of metallic materials and coatings. *Wear*, 253 (56):650–661, 2002.

[100] E. Yarrapareddy and R. Kovacevic. Synthesis and characterization of laser-based direct metal deposited nano-particles reinforced surface coatings for industrial slurry erosion applications. *Surface and Coatings Technology*, 202(10):1951–1965, 2008.

[101] V. A. Pugsley and C. Allen. Microstructure/property relationships in the slurry erosion of tungsten carbidecobalt. *Wear*, 225229, Part 2(0):1017–1024, 1999.

[102] E. J. Wentzel and C. Allen. Erosion-corrosion resistance of tungsten carbide hard metals with different binder compositions. *Wear*, 181183, Part 1(0):63–69, 1995.

[103] S. Lathabai and D. C. Pender. Microstructural influence in slurry erosion of ceramics. *Wear*, 189(12):122–135, 1995.

[104] T. S. Castberg, R. Johnsen, and J. Berget. *Erosion of hardmetals: Dependence of WC grain size and distribution, and binder composition. Wear*, 300(12):1–7, 2013.

[105] A. J. Gant and M. G. Gee. Structure-property relationships in liquid jet erosion of tungsten carbide hardmetals. *International Journal of Refractory Metals and Hard Materials*, 27(2):332–343, 2009.

[106] A. Momber and R. Kovacevic. Fracture of brittle multiphase materials by high energy water jets. *Journal of Materials Science*, 31(4):1081–1085, 1996.

[107] Malvern Instruments. Laser diffraction: Particle size distribution from nanometers to millimetres, 2012. URL http://www.malvern.com/labeng/technology/laser_diffraction/laser_diffraction.htm.

[108] R. Roy. *A Primer on the Taguchi Method*. Van Nostrand Reinhold International Company Limited, New York, 1990.

[109] B.D. Culity and S.R. Stock. *Elements of X-Ray Diffraction*. Prentice Hall, Upper Saddle River, New Jersey, third edition edition, 2001.

[110] D Harrison. *The Electromagnetic Spectrum*, 2008. URL http://www.glyndwr.ac.uk/harrisond/science_three/emag_spectrum.html.

[111] H.E. Exner. *Scanning Electron Microscopy*. In ASM Handbook Committee, editor, *Metallography and Microstructures*, volume 9. ASM International, USA, 1992.

[112] Laser Cladding Technology. *Spherotene - Laser Cladding Technology*, 2013. URL http://www.lasercladding.co.uk/Spherotene.aspx.

[113] T. Prater. *Solid-State Joining of Metal Matrix Composites: A Survey of Challenges and Potential Solutions. Materials and Manufacturing Processes*, 26(4):636–648, 2011.

[114] V. Giuliani, R.J. Hugo, and P. Gu. Powder particle temperature distribution in laser deposition technologies. *Rapid Prototyping*, 15(4):244–254, 2009.

[115] B. Lotfi, P. H. Shipway, D. G. McCartney, and H. Edris. *Abrasive wear behaviour of Ni(Cr)TiB_2 coatings deposited by HVOF spraying of SHS-derived cermet powders. Wear*, 254(34):340–349, 2003.

[116] D. A. Stewart, P. H. Shipway, and D. G. McCartney. Microstructural evolution in thermally sprayed (wc-co.

[117] X. Zeng, B. Zhu, Z. Tao, and K. Cui. Analysis of energy conditions for laser cladding ceramic-metal composite coatings. *Surface and Coatings Technology*, 79 (1-3):162–169, 1996.

[118] K. Van Acker, D. Vanhoyweghen, R. Persoons, and J. Vangrunderbeek. Influence of tungsten carbide particle size and distribution on the wear resistance of laser clad *WC/Ni* coatings. *Wear*, 258(1-4):194–202, 2005.

[119] Z. Xiaoyan, T. Zengyi, Z. Beidi, Z. Erhua, and C. Kun. Investigation of laser cladding ceramic-metal composite coatings: processing modes and mechanisms. *Surface and Coatings Technology*, 79(13):209–217, 1996.

[120] C. F. Yolton. The pre-alloyed powder metallurgy of titanium with boron and carbon additions. *JOM*, 56(5):56–59, 2004.

[121] F.C. Ma, W. Lu, J. Qin, and D. Zhang. *Effect of Carbon Element on Mechanical Properties of In Situ 5 Vol% TiC/Ti-1100 Composite. Materials Transactions*, 47 (4):1135–1139, 2006.

[122] V. Ocelk, U. de Oliveira, M. de Boer, and J. Th M. de Hosson. *Thick Co-based coating on cast iron by side laser cladding: Analysis of processing conditions and coating properties. Surface and Coatings Technology*, 201(12):5875–5883, 2007.

[123] J. Mazumder. Overview of melt dynamics in laser processing. *Optical Engineering*, 30(8):1208–1219, 1991.

[124] K. Shah, A. J. Pinkerton, A. Salman, and L. Li. *Effects of Melt Pool Variables and Process Parameters in Laser Direct Metal Deposition of Aerospace Alloys. Materials and Manufacturing Processes*, 25(12):1372–1380, 2010.

[125] F. Moures, E. Cical, P. Sallamand, D. Grevey, B. Vannes, and S. Ignat. Optimisation of refractory coatings realised with cored wire addition using a high-power diode laser. *Surface and Coatings Technology*, 200(7):2283–2292, 2005.

[126] X. He, J. W. Elmer, and T. DebRoy. Heat transfer and fluid flow in laser microwelding. *Journal of Applied Physics*, 97(084909):1–9, 2005.

[127] R. Baboian. *Corrosion tests and standards: application and interpretation.* ASTM International, 7th January, 2011 2005.

[128] C. Yang and G. M. Wu. Study of microporous PVA/PVC composite polymer membrane and it application to MnO_2 capacitors. *Materials Chemistry and Physics*, 114(23):948–955, 2009.

[129] M. Picasso, C.F. Marsden, J.D. Wagniere, A. Frenk, and M. Rappaz. *A Simple but Realistic Model for Laser Cladding. Metallurgical and Materials Transactions B*, 25:281–291, 1994.

[130] M. Alimardani, E. Toyserkani, and J. P. Huissoon. Three-dimensional numerical approach for geometrical prediction of multilayer laser solid freeform fabrication process. *Journal of Laser Applications*, 19(1):14–25, 2007.

[131] S. Tamirisakandala, R. B. Bhat, D. B. Miracle, S. Boddapati, R. Bordia, R. Vanover, and V. K. Vasudevan. Effect of boron on the beta transus of $Ti6Al4V$ alloy. *Scripta Materialia*, 53(2):217–222, 2005.

[132] J. Zhu, A. Kamiya, T. Yamada, W. Shi, and K. Naganuma. Influence of boron addition on microstructure and mechanical properties of dental cast titanium alloys. *Materials Science and Engineering: A*, 339(12):53–62, 2003.

[133] W. Kurz and D.J. Fisher. *Fundamentals of Solidification.* Trans Tech Publications Limited, Aedermannsdorf, Switzerland, 1989.

[134] M.J; Berminghan, S.D.; McDonald, M.S.; Dargusch, and D.H. StJohn. *Microstructure of Cast Titanium Alloys. Materials Forum*, 31:84–89, 2007.

[135] V. Fallah, M. Alimardani, S. F. Corbin, and A. Khajepour. *Impact of localized surface preheating on the microstructure and crack formation in laser direct deposition of Stellite 1 on AISI 4340 steel. Applied Surface Science*, 257(5):1716–1723, 2010.

[136] M. Alimardani, V. Fallah, A. Khajepour, and E. Toyserkani. The effect of localized dynamic surface preheating in laser cladding of *Stellite 1. Surface and Coatings Technology*, 204(23):3911–3919, 2010.

[137] W. U. H. Syed, A. J. Pinkerton, Z. Liu, and L. Li. Coincident wire and powder deposition by laser to form compositionally graded material. *Surface and Coatings Technology*, 201(16-17):7083–7091, 2007.

[138] J.M.; Drezet, S.; Pellerin, C.; Bezencon, and S. Mokadem. *Modelling the Marangoni convection in laser heat treatment. Journal de Physique. IV*, 120:299–306, 2004.

[139] S. Gorsse and D. B. Miracle. Mechanical properties of *Ti-6Al-4V / TiB* composites with randomly oriented and aligned *TiB* reinforcements. *Acta Materialia*, 51(9): 2427–2442, 2003.

[140] A. F Liu. *Mechanics and Mechanisms of Fracture: An Introduction.* ASM International, Materials Park, Ohio, USA, 2005.

[141] R. J. Parrington. Fractography of metals and plastics. *Practical Failure Analysis*, 2(5):16–19, 2002.

[142] G.S. Upadhyaya. *Cemented Tungsten Carbides: Production, Properties and Testing.* Elsevier Science, 1998.

[143] P. Roth, H. Looser, K.C. Heiniger, and S. Bhler. *Determination of Abrasive Particle Velocity Using Laser-Induced Fluorescence and Particle Tracking Methods in Abrasive Water Jets*, August 21-23, 2005 2005.